

Cover Page



Universiteit Leiden



The handle <http://hdl.handle.net/1887/24094> holds various files of this Leiden University dissertation.

Author: Iacobelli, Marco

Title: Exploring the magnetic, turbulent Milky Way through radio waves

Issue Date: 2014-02-25

Exploring the magnetic, turbulent Milky Way through radio waves

Proefschrift

ter verkrijging van de
graad van Doctor aan de Universiteit Leiden,
op gezag van de Rector Magnificus, prof. mr. C.J.J.M. Stolker,
volgens besluit van het College vor Promoties
te verdedigen op dinsdag 25 february 2014
klokke 15.00 uur

door

Marco Iacobelli
geboren te Rome, Italië
in 04 november 1977

Promotor: Prof. dr. H. J. A. Röttgering

Co-promotor: Dr. M. Haverkorn (Radboud Universiteit, Nijmegen)

Overige leden: Prof. dr. M. Garrett (Stichting ASTRON, Dwingeloo;
Universiteit Leiden)
Dr. M. Ehle (European Space Agency
XMM-Newton Science Operations Centre, Madrid)
Prof. dr. F. Israel
Prof. dr. P. van der Werf

ISBN: 978-94-6259-051-9

Front Cover: The 2.3 GHz radio map depicting the large- and small-scale structures associated with turbulent motions in the diffuse and ionized interstellar medium in the southern sky.

“What sowed wrath grew up in a night luxuriantly but the rain destroyed it.
What sown with love germinated slowly matured later but blessed in abundance.”

– Peter Rosegger

Table of Contents

1	Introduction	1
1.1	Introduction	2
1.2	The physics of the diffuse ISM	2
1.3	The Galactic magnetic field	4
1.4	MHD turbulence	6
1.5	Radio observational methods	8
1.6	This thesis	11
2	Rotation measure synthesis at the 2 m wavelength of the FAN region	17
2.1	Introduction	18
2.2	Data analysis	19
2.2.1	RM-synthesis	20
2.2.2	RM-synthesis data cubes	21
2.3	Observational results	22
2.3.1	Total intensity	22
2.3.2	Polarized intensity	22
2.4	The polarization cube in Faraday depth space	25
2.4.1	Noise properties and errors	26
2.4.2	Cross-correlation in ϕ space	28
2.5	Definition and description of structures	30
2.5.1	Diffuse foreground polarized emission	32
2.5.2	Polarized extragalactic background sources	33
2.6	Model for the diffuse polarized emission	35
2.6.1	Distance estimates to the structures	37
2.6.2	The foreground “curtain” component	40
2.6.3	The background “ring” component	41
2.6.4	The “bubble” component	41
2.6.5	The model in physical space	45
2.6.6	Possible associations	46
2.6.7	Comparison of the model at other wavelengths	50
2.7	Summary and conclusion	51
3	Studying Galactic interstellar turbulence through fluctuations in synchrotron emission – First LOFAR Galactic foreground detection	55
3.1	Introduction	56
3.2	Observations and data reduction	59
3.2.1	Subtraction of Cas A and Cyg A visibilities	60
3.2.2	BBS calibration	61

3.2.3	Removal of bad data	62
3.2.4	Self-calibration and imaging	62
3.3	Observational results	62
3.3.1	Continuum emission maps	62
3.3.2	Comparing LOFAR with WSRT data	65
3.3.3	Power spectral analysis	67
3.4	Turbulence of the diffuse Galactic foreground	72
3.4.1	The outer scale of fluctuations	73
3.4.2	Constrain B_o/B_r from L_{out}	73
3.5	Discussion	75
3.6	Summary & Conclusions	79
4	Galactic interstellar turbulence in the southern sky seen through spatial gradients of the polarization vector – Interstellar turbulence in the southern sky	85
4.1	Introduction	86
4.2	Data overview	88
4.2.1	Radio polarization gradients	89
4.3	Observational results	90
4.3.1	The polarization horizon	94
4.3.2	Galaxy-scale variations in $ \nabla\mathbf{P} / \mathbf{P} $	95
4.3.3	Thermal electron density and magnetic features	96
4.4	ISM turbulent regimes	100
4.4.1	Moments of $ \nabla\mathbf{P} $ and the Sonic Mach Number	103
4.5	Discussion	108
4.6	Summary and Conclusions	109
5	The all-sky structure function portrait of Galactic MHD turbulence	115
5.1	Introduction	116
5.2	RM data overview	117
5.2.1	The observations	118
5.2.2	Catalogue filtering: the outliers issue	120
5.2.3	RM comparison with the Mao catalogue	123
5.2.4	RM comparison with the NVSS catalogue	124
5.3	Structure function calculations	127
5.3.1	The size of the sampling regions, and the width of the structure function bins	127
5.3.2	Comparison with NVSS structure functions	128
5.4	Observational results	130
5.4.1	Structure functions contour maps	131
5.4.2	Comparison with the SGPS structure functions	132
5.4.3	Contour maps and ISM turbulence	134
5.5	Summary and Conclusions	137

6 Final remarks and perspectives	141
6.1 Summary	142
6.2 The LOFAR Magnetism key science project	144
Nederlandse Samenvatting	149
Sommario in Italiano	159
English Summary	169
Publications	177
Curriculum Vitae	179
Acknowledgements	181

Introduction

1

1.1 Introduction

The matter in the Universe is hierarchically structured over a huge range of spatial scales. The most popular structures are galaxies, which were initially thought of as a large collection of stars. Over the past century however it has been clear that galaxies are massive, gravitationally bound systems and are permeated by a complex and turbulent medium spreading between the stars, namely the interstellar medium (ISM). The importance of the ISM originates because of its intermediate role between stellar and galactic scales, connecting the life cycle of a galaxy and its stars. Indeed the interplay between stars and the ISM affects both the physical and chemical processes, driving the evolution of the Galaxy. In addition, the Universe is filled by magnetic fields from planetary up to cosmological scales. Observations of Galactic magnetic fields are fundamental to understand the origin as well as basic mechanisms such the amplification and maintenance of these fields. Furthermore understanding the magnetic field structure is necessary to explain the confinement and the propagation in the Galaxy of relativistic cosmic ray particles. The relevance of both the magnetism and turbulence in the ISM of our Galaxy is reviewed in the following. In Sect. 1.2 we introduce the three basic ingredients of the ISM: the ordinary matter (made of gas and dust), magnetic fields, and cosmic rays. We present their observed physical characteristics as well as their spatial distributions at large and small scales. In Sect. 1.3 the Galactic magnetic field is briefly described. Then a summary of the current theoretical description of magnetohydrodynamic (MHD) turbulence and the link with the interstellar turbulence is given in Sect. 1.4. Finally, the radio observational methods relevant for this thesis are briefly discussed in Sect. 1.5.

An overview of the Galactic ISM and its magnetic fields can be found in the papers by Ferrière (2001) and Beck et al. (2013), a review of the key role of astrophysical MHD turbulence in Brandenburg & Lazarian (2013), while a recent discussion on the relevance of radio observation as a diagnostic of the MHD turbulent ISM is provided by Haverkorn & Spangler (2013).

1.2 The physics of the diffuse ISM

Plasma processes are a critical component for most of astrophysical environments (e.g. planetary environments, stars and stellar winds, accretion disks, nebulae and remnants, the intergalactic medium). It is therefore not surprising that the ISM is a complex, dynamic and multi-phase plasma. The multi-phase nature of the ISM plasma is usually described by a few parameters: the temperature, the density and the ionization state. Both neutral and ionized phases are considered in the description of the ISM, but note that the neutral and cold phase of the ISM is partially ionized at a degree larger than the typical laboratory plasma standards (Spangler 2001). At large-scales the spatial distribution of the ISM is peaked towards the Galactic plane and along the spiral arms, while at small scales the turbulent state of the ISM determines an inhomogeneous and highly contrasted distribution. Compact clouds occupying only $\sim 1\text{--}2\%$ of the interstellar volume collect up to half of the ISM mass, explaining why the interstellar space appears to be almost empty. However the

Table 1.1 – Phases of the diffuse ISM and main parameters: temperature, gas density (Tielens 2005) and degree of ionization (Leahy 1987).

Phase	T [K]	n_H [cm ⁻³]	ξ
Hot coronal gas	$\sim 10^6$	0.003	~ 1
Warm ionized gas	~ 8000	0.1	~ 0.9
Warm neutral gas	~ 8000	0.5	~ 0.2
Cold neutral medium	~ 80	50	$\lesssim 10^{-3}$

diffuse ISM accounts for $\sim 10\text{--}15\%$ of the total mass of the Galactic disk. Most ($\sim 99\%$) of the ISM mass is in gas form, with only a marginal ($\sim 1\%$) mass contribution from dust. The chemical composition of the gas in the ISM is dominated by hydrogen (89%) and helium (9%), with traces (2%) of heavier elements called “metals”. While the filling factors of the gas phases are poorly known, the warm ionized gas phase is the more pervasive.

In addition, characteristics of the ISM plasma are defined by fundamental plasma parameters, such as the ion gyroradius (i.e. the radius of the circular motion of an ion in the plane perpendicular to the magnetic field), the plasma β (i.e. the ratio of thermal to magnetic pressure), the Debye length (i.e. the spatial distance within which the mobile electric charges shield the electric field inside a plasma), the Alfvén velocity (i.e. the speed of the waves resulting from the mass of the particles and the restoring force of the magnetic field) and the sound velocity (i.e. the speed of the longitudinal waves resulting from the mass of the particles and the pressure of the electrons). As a consequence of the large range of observed values of the basic ISM parameters, the diffuse phases of the ISM are characterized by different values of the plasma parameters and host prominent interstellar objects: photodissociation regions, dark and reflection nebulae, H II region complexes and supernova remnants. The presence of these objects in the gas phases is relevant because it reflects the cycle of energy/matter from the ISM to stars and finally to the ISM.

Along with the (dust and) gas phases, the space between the stars is occupied by pervasive magnetic fields and relativistic particles called cosmic-rays. Gas, magnetic fields and cosmic-rays interact and influence each other, creating the complex dynamics of the ISM plasma which is described in the framework of the magnetohydrodynamics (MHD). Indeed both the dynamics and the spatial distribution of the gas are affected by cosmic-rays and magnetic fields, with the turbulent motions of the gas supporting the amplification of magnetic fields and the acceleration of cosmic-rays. The corresponding energy densities are:

THERMAL

$$U_{th} \left[\frac{eV}{cm^{-3}} \right] = \frac{3}{2} P \approx 0.78 \frac{P/k}{6 \times 10^3 cm^{-3} K^{-1}} \quad (1.1)$$

TURBULENT

$$U_{turb} \left[\frac{eV}{cm^{-3}} \right] = \frac{1}{2} \rho \langle v^2 \rangle \approx 0.52 \left(\frac{n_H}{cm^{-3}} \right) \left(\frac{\sigma_{1D}}{10 km s^{-1}} \right)^2 \quad (1.2)$$

MAGNETIC

$$U_{magn} \left[\frac{eV}{cm^{-3}} \right] = \frac{B^2}{8\pi} \approx 0.88 \left(\frac{B}{6 \mu G} \right)^2 \quad (1.3)$$

COSMIC-RAYS

$$U_{cr} \left[\frac{eV}{cm^{-3}} \right] \approx 0.8 \quad (1.4)$$

with P , n_H , σ_{1D} and B being the thermal pressure, the gas density, the one-dimensional velocity dispersion and the magnitude of the magnetic field, respectively. A fundamental observational result is the energy stored in these components exhibits similar values of about $1 eV cm^{-3}$ in the ISM, indicating a global equilibrium state of the plasma. However the ISM is locally far from thermodynamic equilibrium, and different heating and cooling mechanisms determine the temperature of the gas.

For this research project the warm ionized phase of the Galaxy has a special role (see below) so we briefly focus on its characteristics, while a comprehensive review is given by Haffner et al. (2009). The warm ionized phase is a major constituent of galaxies (in particular of star-forming), consisting of mostly ionized hydrogen. The origin of this ISM plasma is due to the feedback of massive stars. In the Galactic ISM it accounts for about the 90 % of the H^+ and about 1/4 of the total mass of $H I$. Observations in nearby galaxies of the diffuse optical recombination line of hydrogen (the so called $H\alpha$ emission) suggest this plasma to extend up to height larger than 1 kpc above the disk. Spectroscopic investigations indicate a separation of the diffuse, warm and ionized plasma from the $H II$ region complexes (Madsen et al. 2006), in terms of temperatures (9000 and 6000 K, respectively) as well as ionization rate. Observations of this plasma in the Galaxy reveal a turbulent state (see e.g. Armstrong et al. 1995) and a clumpy structure, in agreement with theoretical predictions (Rickett 1990). Turbulence in the warm and ionized gas phases is almost isothermal and incompressible, while the neutral warm and cold ISM phases are highly compressible due to both thermal instability in the atomic gas and of supersonic motions in the cold atomic and molecular components. Furthermore turbulence is expected to be a key parameter to answer major open questions about the mechanism for sustaining the heating and ionization of the warm and ionized ISM.

1.3 The Galactic magnetic field

Galactic magnetic fields are a key component of the ISM of galaxies. Magnetic fields control the origin and the propagation of charged cosmic-rays. In the Galaxy, large-scale magnetic fields contribute to the overall stability of the ISM (Boulares & Cox 1990),

while at small scales (i.e. in molecular clouds) magnetic fields regulate the star formation process (see e.g. Heiles & Crutcher 2005). Insights of Galactic magnetic fields are usually derived by measuring one or more of the following tracers: the Zeeman splitting of spectroscopic lines, diffuse synchrotron emission, Faraday rotation of (galactic and extragalactic) polarized sources, far-infrared polarimetry of thermal emission from aligned dust grains and optical linear polarization of starlight. The first three diagnostics are used in radio astronomy and will be illustrated in the next section.

The origin and growth of the Galactic magnetic field is debated, but scenarios involving dynamo processes are favoured. The large-scale structure of the Milky Way's magnetic field is also poorly known and three basic spatial regions are usually identified: the halo, the disk and the Galaxy centre. Large-scale vertical components of the magnetic field have been claimed only towards the south Galactic pole, with a vertical field of strength $+0.31 \pm 0.03 \mu\text{G}$ (Mao et al. 2010). However, vertical magnetic fields are also seen towards the Galactic Center.

Magnetic field strength is about $6 \mu\text{G}$ in the local neighbourhood, increasing towards the Galactic center and with a radial exponential scale length of the total field of about 12 kpc (see e.g. Beck et al. 2013). A lower limit of $H_B \gtrsim 1.5$ kpc for the scale height of the total magnetic field in the local neighbourhood is derived from the observed radio synchrotron emission (Beuermann et al. 1985). These values are similar to those found in external galaxies, but a peculiar feature of the Galactic magnetic field is the presence of field reversals (for a discussion see Beck 2001). An increase of field strength with the gas density is observed for large (i.e. $n \gtrsim 300 \text{ cm}^{-3}$) densities (Crutcher et al. 2010) as expected from flux freezing and it is explained in the framework of the MHD turbulence (Passot & Vázquez-Semadeni 2003). This behaviour is typically observed in molecular clouds, protostellar regions, as well as in compressed regions associated with and/or produced by star formation (Heiles & Haverkorn 2012).

The Galactic magnetic field is usually described by two components: the regular (or ordered) and the random (turbulent), the ratio of these components being of interest in the context of dynamo theory. The regular component is oriented along the large-scale structures present in the Galactic plane, in agreement with symmetric dynamo models. Its magnitude is of a few μG ($2\text{--}4 \mu\text{G}$ at the Sun (Beck 2001)) and decreases away from the plane. However, the strongest regular fields are detected towards the Galactic center region, showing a filamentary morphology oriented perpendicular to the plane. The scale height of the regular magnetic field in the Galaxy is found to be about 1.5 kpc (Han & Qiao 1994), similar to the one of the thermal electrons (Schnitzeler et al. 2012).

The random component has a magnitude of about $4\text{--}6 \mu\text{G}$ and its turbulent fluctuations extend over a range of spatial scales related to that of the MHD turbulent cascade (see e.g. Rand & Kulkarni 1989, Ohno & Shibata 1993). The scales over which the random field fluctuates are smallest (i.e. a few parsec) towards the arms in the Galactic plane, while increase towards the interarms and are largest in the halo to about 100 pc (Haverkorn et al. 2008).

The analysis of available data (see e.g. Brown et al. 2007, Fauvet et al. 2011, Van Eck et al. 2011, Jansson & Farrar 2012a,b) allows to constrain the structure of the Galactic magnetic field. The overall structure suggested by observations agrees with an axi-

symmetric spiral magnetic field configuration, thus favouring the presence of Galactic dynamo processes. Towards the Perseus arm the magnetic field is clockwise, while a large-scale magnetic field reversal is present between the Scutum-Crux-Sagittarius arm and the Carina-Orion arm (Beck et al. 2013).

1.4 MHD turbulence

Turbulence is a major feature of astrophysical plasmas as well as of many astrophysical processes, by enhancing transport of mass, momentum, energy and magnetic fields. Its fundamental role in the different phases of the ISM concerns both the structure formation, the evolution and the magnetization. Indeed turbulence is necessary to generate structure over a huge range of spatial scales and to set up dynamo mechanisms in order to convert a fraction of kinetic to magnetic energy. Therefore one deals with MHD turbulence in astrophysical plasmas, which is a complex and non-linear phenomenon. As a consequence, the characteristic signature of MHD turbulence is the presence of highly-irregular, fractal and magnetized flows.

Of course turbulence is not just observed in extraterrestrial environments. However there exist important differences between astrophysical and laboratory turbulence:

- the driving, which is often determined by intrinsic instabilities;
- the non-negligible magnetization;
- the huge range spanned by fundamental parameters, such as length scales and velocities;
- no direct in-situ measurements are usually possible.

The first two features suggest the anisotropic nature of astrophysical MHD turbulence, while the latter two features suggest the difficulties to investigate this topic.

MHD turbulence is not yet completely understood. It deals with two vectorial fields, the velocity (\vec{v}) and magnetic (\vec{B}) fields, whose evolution is described by a set of MHD equations for the momentum (i.e. the Navier-Stokes equation), the induction and the solenoidity for \vec{v} and \vec{B} . Turbulence develops in a flow when the ratio of the advective term to the viscous term in the Navier-Stokes equation is very large.

The basic parameters to describe an MHD turbulent plasma are:

- the plasma beta parameter (β), i.e. the ratio of gas pressure to magnetic pressure in a plasma: the evolution of a plasma with small or high β will be determined by electromagnetic or hydrodynamic fluid forces, respectively;
- the driving and dissipation spatial scales (L_{out}, l_{diss});
- the sonic Mach number (M_S), which relates to the compressibility;
- the Alfvénic Mach number (M_A), which relates to the magnetization;

- the Reynolds number (Re), which measures the strength of viscous processes relative to diffusion;
- the magnetic Reynolds number (Re_M), which measures the strength of inductive processes relative to diffusion;
- the magnetic Prandtl number (Pr_M), i.e. the ratio of magnetic to kinetic Reynolds number indicating the strength of kinematic viscosity relative to magnetic diffusivity. It is important to characterize the onset of dynamo processes in a plasma (Schekochihin et al. 2005).

Typical values for the diffuse, warm ISM plasma are: $\beta_{ISM} \sim 1 - 4$, $M_S \sim 0.5 - 2$, $M_A \lesssim 1$, $Re_M \sim Re \gtrsim 10^8$, $Pr_M \gg 1$, along with extreme density and temperature contrasts. The phenomenology is qualitatively depicted by the concept of a turbulent cascade (see Fig. 6.4), where the energy is injected around a large scale L_{out} and then is transferred without dissipation by non-linear processes to smaller scales down to a typical scale (l_{diss}) where dissipation takes places. In the ISM the MHD turbulent cascade is driven by several sources (e.g. supernova explosions, strong stellar winds) and the energy is injected at different spatial scales (likely in the range 1–100 pc), the supernova explosions providing the major contribution, while the dissipation scale (perhaps at scales ~ 500 Km) and mechanisms are still debated.

Over the past few decades, research on astrophysical MHD turbulence has taken advantage of the use of both analytical, numerical and observational studies. The use of high-resolution numerical simulations allowed to confirm theoretical predictions over a large portion of the parameter space and compare these with the observational results. As a result, three regimes of MHD turbulence have been identified depending on the relative magnitude of the magnetic and kinetic fluctuations. To this aim a comparison is made between the magnitude of velocity fluctuations $v_{L_{out}}$ at the injection scale and the Alfvén speed $v_A = B_{rms} / \sqrt{4\pi\rho_0\mu_0}$, associated with the random magnetic field B_{rms} :

$v_A \ll v_{L_{out}}$ this is the case of weak magnetic fields and turbulence is described by the isotropic approximation proposed by Iroshnikov (1964) and Kraichnan (1965). The transfer of energy via the turbulent cascade is characterized by the Alfvénic interactions.

$v_A \gg v_{L_{out}}$ this is the case of strong magnetic fluctuations and highly anisotropic turbulence, with the explicit dependence to the local direction of the magnetic field, for which a wave description is possible (i.e. *weak* turbulence).

$v_A \sim v_{L_{out}}$ this is the case of balanced turbulence, treated by the model of Goldreich & Sridhar (1995). The turbulent cascade is anisotropic and dominated by non-linear interactions (i.e. *strong* turbulence).

Table 1.2 provides a summary of the main properties for the three regimes of MHD turbulence. For negligible magnetic fields an almost isotropic MHD turbulent cascade is generated. Note the different degree of anisotropy for the *strong* and *weak* cases: the

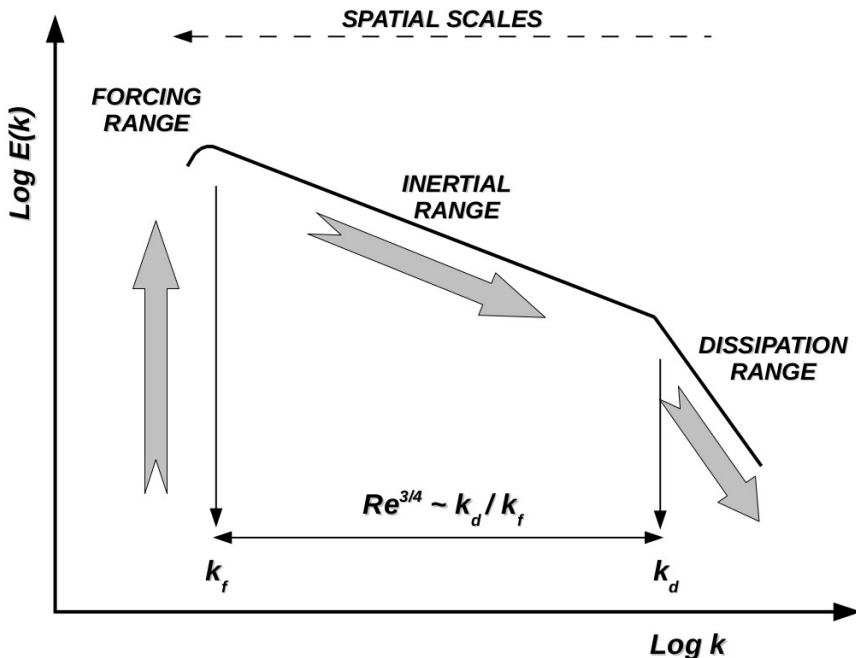


Figure 1.1 – Schematic representation of the spatial energy spectrum of a turbulent cascade. The forcing ($k_f \sim 1/L_{out}$) and dissipation ($k_d \sim 1/l_{diss}$) wave-numbers defining the extension of the inertial range are also marked. The energy flow is from large to small scales as indicated by the arrows.

turbulent cascade becomes more and more anisotropic toward smaller scales in the limit of *strong* MHD turbulence, while it is fully anisotropic at all scales in the limit of *weak* MHD turbulence.

1.5 Radio observational methods

Radio observations are a major probe of the interstellar magnetic fields as well as turbulence. Indeed the motion of cosmic-rays electrons in the Galactic magnetic fields give rise to copious emission of electromagnetic radiation, which is bright in the radio domain, displays a broad spectrum and is linearly polarized: synchrotron radiation. The synchrotron emissivity of the isotropic distribution of cosmic-rays electrons with a power-law energy spectrum $N(E) = N_0 E^{-\alpha}$ in a magnetic field with a component perpendicular to the line of sight of strength B_{\perp} is:

$$I(\nu) \propto N_0 B_{\perp}^{(\alpha+1)/2} \nu^{-(\alpha-1)/2} \quad , \quad (1.5)$$

Table 1.2 – Summary of the main properties for the three regimes of MHD turbulence (adapted from Brandenburg & Nordlund (2011)): the degree of anisotropy, the cascade rate and the energy spectrum, respectively.

Parameter	Iroshnikov-Kraichnan	Strong turbulence	Weak turbulence
$v_A/v_{L_{out}}$	$\ll 1$	~ 1	$\gg 1$
k_{\perp}/k_{\parallel}	1	$\propto k_{\perp}^{1/3}$	$\rightarrow \infty$
ϵ	$(\epsilon v_A)^{1/2}$	$C_{GS} \epsilon^{2/3}$	$(\epsilon v_A k_{\parallel})^{1/2}$
$E(k_{\parallel}, k_{\perp})$	$C_{IK} (\epsilon v_A)^{1/2} k^{-3/2}$	$C_{GS} \epsilon^{2/3} k_{\perp}^{-5/3}$	$(\epsilon v_A k_{\parallel})^{1/2} k_{\perp}^{-2}$

with ν being the frequency of the emitted photons. Therefore B_{\perp} can be obtained, by measuring the synchrotron spectrum at different frequencies and having knowledge of the cosmic-ray electrons energy spectrum. Moreover because of the energy equipartition between cosmic rays and magnetic fields, it is also possible to estimate the total magnetic field strength (B_{eq}) (Beck & Krause 2005) and indeed the radial variation of B_{eq} in the Galaxy was obtained from the radial variation of the total synchrotron emission (Beuermann et al. 1985). The intrinsic degree of linear polarization of synchrotron emission is:

$$p_{0,\alpha} = \frac{3\alpha + 3}{3\alpha + 7} \quad , \quad (1.6)$$

with the electric-field (i.e. the polarization) vector being oriented perpendicular to the projection of the magnetic field in the emitting region, onto the plane of the sky. For typical values of α , a high level of linear polarization ($p_{0,\alpha} \sim 75\%$) is expected. However the observed degree of polarization is much lower due to depolarization mechanisms (Sokoloff et al. 1998):

- depolarization due to turbulent fluctuations within the synchrotron emitting volume (intrinsic depolarization), and /or within the plasma where the propagation takes place (Faraday depolarization);
- instrumental depolarization due to beam or bandwidth limitations.

In the extreme case of just isotropic, turbulent and randomly oriented magnetic fields unpolarized synchrotron emission would be detected and $p_{0,\alpha} \rightarrow 0$. Thus, it appears that the linearly polarized emission traces ordered magnetic fields, while the intensity of the synchrotron emission provides a measure of the strength of the total (ordered and turbulent) magnetic field components in the sky plane weighted by the density number of cosmic-ray electrons. Finally, the ratio of the observed and the intrinsic degree of polarization (i.e. the depolarization) relates to the magnitude of turbulent fluctuations in and the coherence of the total field.

In addition, since the ISM is a plasma the propagation of electromagnetic waves is characterized by three fundamental effects: total reflection, dispersion and Faraday rotation. In an unmagnetized plasma free electrons oscillate at the characteristic frequency $\omega_p \propto \sqrt{n_e}$ (i.e. the plasma frequency), with n_e the number density of electrons. The dielectric constant of the plasma (neglecting the ions motion) is:

$$\epsilon = 1 - \frac{\omega_p^2}{\omega^2} \quad , \quad (1.7)$$

with ω the frequency of the incoming electromagnetic wave. For frequencies $\omega < \omega_p$ the dielectric constant is negative and the refractive index $n = \sqrt{\epsilon}$ is imaginary, implying the reflection of the wave by the plasma. This reflection effect is also used on Earth for low-frequency radio signals transmission. Indeed the outermost layer of the Earth's atmosphere (i.e. the ionosphere) is partially ionized with a plasma frequency of ~ 1 MHz, allowing signals in the long-wave band to be reflected off the ionosphere. Substituting the dielectric constant in the phase velocity of electromagnetic waves in a dielectric medium $v_p = c/n = c/\sqrt{\epsilon}$, we obtain the dispersion relation:

$$\omega^2 = k^2 c^2 + \omega_p^2 \quad , \quad (1.8)$$

where c is the speed of light and k the wave-number of the wave. From equation 1.8 we can determine how fast the electromagnetic wave propagates in the plasma (i.e. the group velocity):

$$v_g = \frac{d\omega}{dk} = c \sqrt{1 - \frac{\omega_p^2}{\omega^2}} \quad . \quad (1.9)$$

Thus, electromagnetic waves of different frequencies propagate through a plasma with different speeds, indicating the dispersive nature of plasma refraction and implying different arrival times at the detectors as observed in e.g. dynamic spectra of pulsars.

Finally, because the ISM is a magnetized plasma the propagation of electromagnetic waves is characterized by a birefringence effect called Faraday Rotation. Now the dielectric constant of the plasma is:

$$\epsilon = 1 - \frac{\omega_p^2}{\omega(\omega \pm \Omega_e)} \quad , \quad (1.10)$$

with $\Omega_e \propto B$ being the gyro-frequency of the electrons in the magnetic field. Therefore both the electron density and the magnetic field affect the propagation of the waves and different phase velocities characterize right- and left-hand circularly polarized waves. Because a linearly polarized wave can be represented as the combination of right and left-hand circularly polarized waves, the direction of the polarization vector rotates as the wave propagates through the interstellar medium. The measure of this effect is a primary tool to estimate plasma density and magnetic fields (along the line of sight) in the interstellar medium, the observable being the Faraday depth (Burn 1966):

$$\phi = 0.81 \int_{source}^{observer} n_e \vec{B} \cdot d\vec{s} \quad . \quad (1.11)$$

Two regimes need to be considered:

- the synchrotron emission and the Faraday rotation do not take place in the same plasma; in this case ϕ can be quantified by the slope of the polarization angles (χ) as a function of the wavelength squared (λ^2), which is called rotation measure (RM).
- the synchrotron emission and the Faraday rotation take place in the same plasma or the synchrotron emission and the Faraday rotation take place in multiple spatially separated plasmas along the line of sight; in this case a spectrum of ϕ (i.e. a Faraday spectrum) can be obtained by Fourier transforming the polarization vector as a function of λ^2 , which is the base of the RM synthesis technique (Brentjens & de Bruyn 2005).

Note that the theory of the propagation of radio waves through the turbulent interstellar medium is still incomplete and several observational evidences related to e.g. the interstellar scintillation measurements need to be addressed (Rickett 2007).

By using radio observations it is also possible to detect line emission from e.g. the atomic hydrogen (H I) and perform measurements of the Zeeman splitting of atomic levels. The presence of a magnetic field along the line of sight (B_{\parallel}) causes a line at a frequency ν_0 to split into two components and the separation ($\Delta\nu$) is $\Delta\nu \propto B_{\parallel}$. By this method a direct measure of the ordered B_{\parallel} in the source is possible and it is currently used to investigate magnetic fields in stars (e.g. the Sun), molecular clouds and maser spots.

Fluctuations of thermal electron density and magnetic field amplitude determine spatial and temporal fluctuations of the synchrotron emissivity and the refractive index of the ISM plasma. The interpretation of these fluctuations is done in the framework of MHD turbulence. The general approach to investigate astrophysical MHD turbulence in both numerical simulations and observations consists of statistical studies. In order to study interstellar MHD turbulence there exist several diagnostics (see Fig. 1.2) that can be applied to radio observations, depending on the ISM phase: for instance, power spectra of both velocity and column density of the neutral hydrogen can be used to probe turbulence in the neutral ISM phase, while radio polarization maps of either the diffuse Galactic synchrotron emission or structure functions of RMs of radio sources probe turbulence in the ionized ISM phase. Note that observations are usually more sensitive to density fluctuations, while the primary fluctuating quantities are the velocity and the magnetic fields. However, a new diagnostic with a better sensitivity to the influence of the magnetic field has been developed to investigate the turbulent fluctuations in the ISM affecting the radio polarization measurements: the spatial gradient of the polarization vector (Gaensler et al. 2011).

1.6 This thesis

Radiative heating and cooling, magnetic fields, self-gravity, and turbulence are major physical processes playing a role in the ISM, thus investigations of their role and interplay are required to understand the Galaxy evolution. The goal of this research project has been

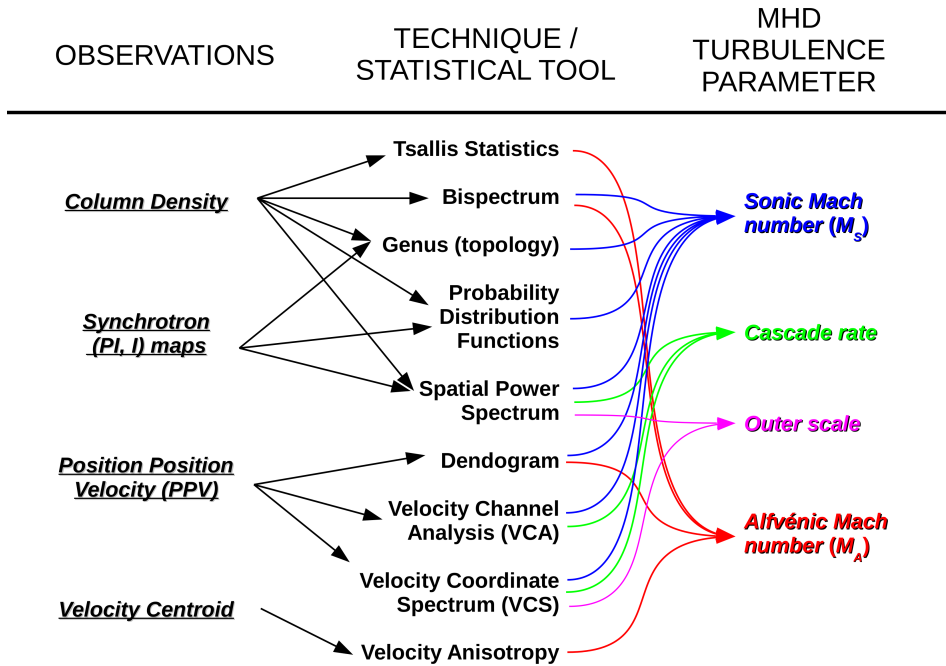


Figure 1.2 – Radio observational signatures of interstellar MHD turbulence and common statistical tools providing basic characteristics of interstellar MHD turbulence. Adapted from Burkhart & Lazarian (2012).

to perform observational studies on the interstellar turbulence in the warm ionized ISM regarding two complementary science cases: mapping of the magneto-ionic structures in the ISM (Chapter 2) and characterizing the MHD turbulence of the diffuse warm ionized ISM (Chapters 3, 4 and 5).

In this thesis, I present these four investigations and the results obtained in the framework of the following major scientific questions:

1. the ISM structure cartography; three dimensional spatial mapping of the Galactic matter and magnetic fields is still missing, the local ISM being the only region approximatively depicted (Lallement et al. 2013). Beside providing a description of the spatial distribution of the matter, a main aim is to reveal how matter is structured in the turbulent, ionized interstellar medium. Recent radio observations have proven RM synthesis to be an effective diagnostic of structures in the magneto-ionic ISM otherwise undetectable, although it does not provide a direct spatial mapping.
2. the characterization of the interstellar turbulent cascade in the ionized ISM; estimates of fundamental parameters such the outer scale, the ratio of magnetic fields

components and the sonic Mach number are provided in Chapter 3 and 4. The knowledge of these parameters as well as their spatial variations is of interest to model the propagation of cosmic rays and the Galactic dynamo.

3. the spatial structure of the interstellar MHD turbulence; several observations suggest turbulent fluctuations in the ISM to be produced in localized sheets (2D) structures, rather than uniformly distributed (3D) structures. As a consequence, observations of turbulent fluctuations in the electron density and the magnetic field throughout the ISM may discriminate the 2D and 3D scenarios. Our investigation (Chapter 5) of RM structure functions on angular scales $\gtrsim 1^\circ$ show flat ($\lesssim 0.6$) logarithmic slopes, marginally consistent with 2D turbulence.

In the framework of this Ph.D. project scientific results were obtained by using several data-sets from different facilities and over a broad range of radio frequencies: polarization data at 150 MHz from the Westerbork Synthesis Radio Telescope (WSRT) in the Netherlands (Chapter 2), continuum and polarization data at 150 MHz from the LOw Frequency ARray (LOFAR) in the Netherlands (Chapter 3), continuum and polarization data at 2.3 GHz from the Parkes radio telescope in Australia (Chapter 4) and polarization data at 2.3 GHz from the Australia Telescope Compact Array (ATCA) in Australia (Chapter 5). Furthermore, we make use of complementary data such as optical starlight polarization, $H\alpha$ diffuse emission and pulsars.

Both recently developed as well as standard techniques were applied to analyse and interpret these radio data. In Chapter 2 we adopt RM synthesis on the low frequency polarization data, to image the distribution of Faraday rotating and/or synchrotron emitting regions along the line of sight. In Chapter 3 we perform a power spectral analysis of the synchrotron fluctuations at 150 MHz detected by LOFAR, while in Chapter 4 the novel technique of spatial gradients of polarization is applied to image the southern all-sky MHD turbulence in the warm ionized ISM and the moments analysis is used to constrain the spatial variations of the sonic Mach number. Finally, in Chapter 5 structure function of RMs is adopted to highlight density and magnetic fluctuations in the warm ionized ISM and provide the first all-sky portrait of Galactic MHD turbulence.

In Chapter 2 we present a study of the local, warm ionized ISM towards the Galactic anti-centre. The target field is a peculiar synchrotron bright Galactic region (called the Fan region) and we detect diffuse, low-frequency synchrotron emission from several Faraday thin (i.e. with negligible internal Faraday depolarization) structures with different morphologies, in agreement with earlier RM synthesis studies of the Galactic diffuse synchrotron emission. We associate a faint foreground component with the Local Bubble and investigate the nature of a bubble structure, favouring the scenario of a Strömrgren sphere relic. The turbulent state of both the bubble and the background component is suggested by the spatial power spectrum of the polarized emission.

In Chapter 3 we characterize the interstellar MHD turbulent cascade towards the highly polarized Fan region, by studying the spatial fluctuations in synchrotron emission. We obtain the deepest image at low radio frequencies of the Fan region to date and

find diffuse continuum emission within the primary beam, which constitutes the first LO-FAR detection and imaging of the Galactic fluctuations of diffuse synchrotron emission around 160 MHz. An upper limit of ~ 20 pc for the outer scale of the interstellar MHD turbulent cascade is derived, which matches with previous estimates in literature. Lower limits of the ratio of random to ordered magnetic field strength consistent with magnetic field ratios at other places in the ISM are also found and we claim a variation of the ratio of random to ordered field as a function of Galactic coordinates.

Chapter 4 discusses the spatial variations of the sonic Mach number (M_s) of the interstellar MHD turbulence. The first map of the spatial gradient of the linearly polarized synchrotron emission ($|\nabla\mathbf{P}|/|\mathbf{P}|$) of the entire southern sky is shown, revealing rapid changes of the density and magnetic fluctuations in the warm and ionized phase of the ISM due to magnetic turbulence as a function of Galactic position. The elongated structures with typical widths down to the angular resolution are associated with turbulence in the warm, ionized ISM. In order to constrain the sonic Mach number we apply a high order moments analysis to the observations and to the simulated diffuse, isothermal ISM with ideal magneto-hydrodynamic turbulence. An upper limit of $\lesssim 2$ for the sonic Mach number is found, supporting the view of a turbulent ISM in a transonic regime. Moreover no systematic variations of the sonic Mach number are observed as a function of Galactic coordinates. A major feature of this investigation is that the adopted approach is mainly sensitive to the magnetic field fluctuations in a plasma with low- M_s .

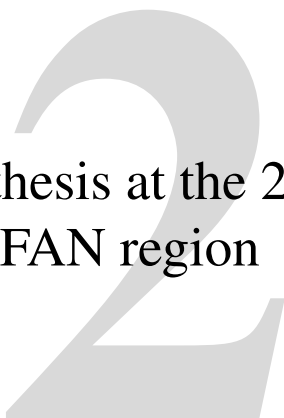
Finally, in Chapter 5 a study of the all-sky thermal electron density and (to a lesser extent of the) magnetic field fluctuations is presented. We study turbulence in the Galactic magnetized interstellar medium by measuring fluctuations between the rotation measures (RMs) of extragalactic sources along different lines of sight and we show an all-sky map of rotation measures of extragalactic sources as well as maps for both the structure function amplitudes and slopes. A systematic flattening is found in both the NVSS and S-PASS samples away from the Galactic plane. In some fields of view, the structure function slopes are consistent with 2D turbulence, while none of them correspond to 3D turbulence.

Bibliography

- Armstrong J.W., Rickett B.J., Spangler S.R. 1995, *ApJ*, 443, 209
- Beck R. 2001, *Space Sci. Rev.*, 99, 243
- Beck R., Krause M., 2005, *AN* 326, 414
- Beck R. & Wielebinski R. 2013, in *Planets, Stars and Stellar Systems Vol.5*, eds. D.T. Oswalt & G. Gilmore (Dordrecht: Springer), 641
- Beuermann K., Kanbach G. and Berkhuijsen E.M. 1985, *A&A*, 153, 17
- Boulares A., Cox D.P. 1990, *ApJ*, 365, 544
- Brandenburg A., Lazarian A. 2013, *Space Sci. Rev.*, 178, 163
- Brandenburg A., Nordlund Å 2011, *Rep. Prog. Phys.* 74, 046901
- Brentjens M.A. and deBruyn A.G. 2005, *A&A*, 441, 1217
- Brown J.C., Haverkorn M., Gaensler B.M. et al. 2007, *ApJ*, 663, 258
- Burn B.J. 1966, *MNRAS*, 133, 67
- Burkhart B., Lazarian A. 2012, *Proceedings of the International Astronomical Union*, 8, 325
- Crutcher R.M., Wandelt B., Heiles C., Falgarone E., Troland T.H. 2010, *ApJ*, 725, 466
- Fauvet L., Macías-Pérez J.F., Aumont J., Désert F.X., Jaffe T.R., Banday A.J., Tristram M., Waelkens A.H., Santos D. 2011, *A&A*, 526, 145
- Ferrière K.M. 2001, *Rev. Mod. Phys.*, 73, 1031
- Gaensler B.M., Haverkorn M., Burkhart B., et al. 2011, *Nature*, 478, 214
- Goldreich P., Sridhar S. 1995, *ApJ*, 438, 763
- Hafner L.M., Dettmar R.J., Beckman J.E. et al. 2009, *RvMP*, 81, 969
- Han J.L., Manchester R.N., Lyne A.G., Qiao G.J., van Straten W. 2006, *ApJ*, 642, 868
- Han J.L., Qiao G.J. 1994, *A&A*, 288, 759
- Haverkorn M., Brown J.C., Gaensler B.M., McClure-Griffiths N.M. 2008, *ApJ*, 680, 362
- Haverkorn M., Spangler S.R. 2013, *Space Sci. Rev.*, 178, 483
- Heiles C., Crutcher R.M. 2005, in *Cosmic Magnetic Fields*, eds. R. Wielebinski & R. Beck (Berlin: Springer Verlag), *Lecture Notes in Physics*, 664, 137
- Heiles C., Haverkorn M. 2012, *Space Sci. Rev.*, 166, 293
- Iroshnikov P.S. 1964, *Soviet Ast.*, 7, 566
- Jansson R., Farrar G.R. 2012a, *ApJ*, 757, 14
- Jansson R., Farrar G.R. 2012b, *ApJ*, 761, 11
- Kraichnan R.H. 1965, *Phys. Fluids* 8, 1385
- Lallement R., Vergly J.-L., Valette B., Puspitarini L., Eyer L., Casagrande L. 2013, *A&A*, in press 2013arXiv1309.6100L
- Leahy J.P. 1987, *MNRAS*, 226, 433
- Madsen G.J., Reynolds R.J., Haffner L.M. 2006, *ApJ*, 652, 401
- Mao S.A., Gaensler B.M., Haverkorn M., Zweibel E.G., Madsen G.J., McClure-Griffiths N.M., Shukurov A., Kronberg P.P. 2010, *ApJ*, 714, 1170
- Ohno H., Shibata S. 1993, *MNRAS*, 262, 953

- Passot T., Vázquez-Semadeni A. 2003, *A&A*, 398, 845
- Rand R.J., Kulkarni S.R. 1989, *ApJ*, 343, 760
- Rickett B.J. 1990, *ARA&A*, 28, 561
- Rickett B.J. 2007, *Astron. Astrophys. Trans.*, 26, 429
- Schnitzeler D.H.F.M. 2012, *MNRAS*, 427, 664
- Schekochihin A.A., Haugen N.E.L., Brandenburg A., Cowley S.C., Maron J.L. and McWilliams J.C. 2005, *ApJ*, 625, 115
- Sokoloff D.D., Bykov A.A., Shukurov A., Berkhuijsen E.M., Beck R., Poezd A.D. 1998, *MNRAS*, 299, 189
- Spangler S.R. 2001, *Space Sci. Rev.*, 99, 261
- Tielens A.G.G.M. 2005, *The Physics and Chemistry of the Interstellar Medium* (Cambridge University Press)
- Spangler S.R. 2007, *PASP*, 265, 307
- Van Eck C.L., Brown J.C., Stil J.M., Rae K., Mao S.A., Gaensler B.M., Shukurov A., Taylor A.R., Haverkorn M., Kronberg P.P., McClure-Griffiths N.M. 2011, *ApJ*, 728, 97
- van Haarlem M.P., Wise M.W., Gunst A.W., Heald G., McKean J.P., Hessels J.W.T., de Bruyn A.G., Nijboer R., Swinbank J., Fallows R. et al. 2013, *A&A*, 556, 2

Rotation measure synthesis at the 2 m wavelength of the FAN region



M. Iacobelli, M. Haverkorn and P. Katgert

A&A, 2012, 549, 56

Abstract

Aims. Rotation Measure synthesis of the Westerbork Synthesis Radio Telescope (WSRT) observations at $\lambda \sim 2$ m of the FAN region at $l=137^\circ$, $b=+7^\circ$ shows the morphology of structures in the ionized interstellar medium. We interpret the diffuse polarized synchrotron emission in terms of coherent structures in the interstellar medium and the properties of the interstellar magnetic field.

Methods. We performed statistical analysis of the polarization data cube obtained through Rotation Measure synthesis. For the first time, cross-correlation is applied to identify and characterize polarized structures in Faraday depth space. Complementary information about the medium are derived from H α emission, properties of nearby pulsars, and optical polarized starlight measurements.

Results. We find an overall asymmetric Faraday dispersion function in a Faraday depth range of $[-13,+5]$ rad m $^{-2}$, which is peaked around -1 rad m $^{-2}$. Three morphological patterns are recognized, showing structures on scales from degrees down to the beam size. The first structure is a nearby synchrotron emission component with low Faraday depth, filling the entire field of view. The second pattern is a circular polarization structure with enhanced (negative) Faraday depth, which has the same morphology as a low-emission region within the third component. This third component is interpreted as the background in which the circular structure is embedded. At low Faraday depth values, a low gradient across the imaged field is detected, almost aligned with the Galactic plane. Power spectra of polarized structures in Faraday depth space provide evidence of turbulence.

Conclusions. A sign reversal in Faraday depth from the nearby component to the circular component indicates a reversal of the magnetic field component along the line of sight, from towards the observer and nearby to away from the observer at large distances. The distance to the nearby, extended component is estimated as $\lesssim 100$ pc, which suggests that this structure corresponds to the Local Bubble wall. For the circular component, various physical interpretations are discussed. The most likely explanation is that the circular component seems to be the presence of a nearby (~ 200 pc away) relic Strömgren sphere, associated with an old unidentified white dwarf star and expanding in a low-density environment.

2.1 Introduction

The study of the magneto-ionic properties of the interstellar medium (ISM) by multi-frequency polarimetry started in 1960 with the Dwingeloo radio telescope (Westerhout et al. 1962). A breakthrough came much later when Wieringa et al. (1993) acknowledged the importance of small angular scale structures (down to a few arcmins) in polarized intensity (PI) or polarization angle with no detection in total intensity. Such a fine structure was explained in terms of Faraday rotation of the diffuse, linearly polarized, Galactic synchrotron radiation background by a highly structured foreground magneto-ionic medium. The cosmic rays propagating through the Galactic magnetic field are responsible for the radio synchrotron emission, and the magneto-ionic medium is primarily the warm ionized

ISM. As a result polarimetric observations of the Galaxy provide insight into the ionized ISM and the Galactic magnetic field.

The FAN region is a highly polarized, extended region in the second Galactic quadrant at low Galactic latitudes. Its polarization properties were first investigated by Bingham & Shakeshaft (1967), who discovered a circular structure in the rotation measure (RM) map. From higher angular resolution observations, Verschuur (1969) suggested a connection of the observed structure with the B2 IV:e star HIP 15520 that is located close to the centre of the circular structure.

Haverkorn et al. (2003) presents multi-frequency polarimetry radio observations at five wavelengths in the range of $\lambda = 0.80 - 0.88$ m. They point out a ring structure in PI along with an extended pattern of depolarization canals in maps of polarized intensity. They constructed an RM map from these five wavelengths and interpret the ring as a purely magnetic flux tube.

Bernardi et al. (2009) observed the FAN region at $\lambda = 1.93 - 2.16$ m in order to characterize the properties of the foreground for epoch of re-ionization experiments. They detected total intensity and polarization fluctuations for the first time in the Galactic diffuse foreground emission at this wavelength. Rotation measure synthesis (RM-synthesis) was used to image this region in the sky revealing a complex and structured distribution of polarized signals.

In this paper, we re-analyse the data from Bernardi et al. to study the diffuse Galactic polarized emission. In Section 2 we present the data and illustrate the working principle of RM synthesis technique. In Section 3 we describe the main properties of total and polarized intensity. In Section 4 the polarized data in Faraday depth space are discussed. In Section 5 we describe the main components and their properties. In Section 6 we present a simple model to explain the observed structures and their features. Finally in Section 7 we summarize and conclude.

2.2 Data analysis

The data were collected with the east-west Westerbork Synthesis Radio Telescope (WSRT) array in 2007. Baselines between 36 m and 2.7 km were used to obtain good uv -coverage. Data reduction was performed by Gianni Bernardi using the AIPS++ package, and for a description of their reduction we refer to Bernardi et al. (2009). The corresponding main properties are given in Table 1. Ionospheric propagation effects are direction- and time-dependent and affect the phase of the signal received by the interferometer. They also affects the polarization, giving rise to time-variable Faraday rotation. Moreover, differential Faraday rotation by the ionosphere will alter Stokes Q and U, which could lead to depolarization but could also lead to spurious extra polarization, thus affecting the results of the polarization imaging. Over the six days of observation the mean total electron content (TEC) value (provided by the Center for Orbit Determination in Europe (CODE)) and the mean intensity of the geomagnetic field (calculated using the International Geomagnetic Reference Field (IGRF10)) give us a typical $RM_{ion} \lesssim 0.3$ rad m⁻², which implies a phase shift of about 80 degrees at the lower observed frequency. The spread of the RM_{ion}

Table 2.1 – Observational set up and basic properties of the RM-synthesis cube, from Bernardi et al. (2009)

Data		
l, b	$137^\circ + 7^\circ$	Galactic coordinates
N_{bands}	8	Number of spectral bands
$\nu_{0,band}$	139.3, 141.5, 143.7, 145.9, 148.1, 150.3, 152.5, 154.7 MHz	Central frequency of each band
$\Delta\nu_{0,band}$	2.5 MHz	Width of each band
$\delta\nu_{ch}$	9.8 kHz	Frequency resolution
$\Delta\theta_0$	$2' \times 2.2'$	Beam size
(α, δ, ϕ) -cube		
$\Delta\phi$	3 rad m^{-2}	RMSF width
$\delta\phi_{scale}$	0.85 rad m^{-2}	Max scale in ϕ
$\delta\theta$	$4.2'$	Beam size
ξ	$1 \text{ mJy beam}^{-1} = 1 \text{ K}$	Conversion factor

over days of observation is 0.1 rad m^{-2} . Since the resolution in Faraday depth is about 3 rad m^2 (see Table 1), ionospheric Faraday rotation will hardly change the analysis or conclusions, so that corrections for the ionospheric Faraday rotation were not applied. To enhance sensitivity for diffuse emission, the resolution of the Stokes Q and U maps was decreased. In this paper we use the full angular resolution Stokes I map (i.e. $\Delta\theta_0 = 2 \text{ arcmin}$) and Stokes Q,U maps with angular resolution $\Delta\theta = 4.2 \text{ arcmin}$. No correction was performed for the primary beam attenuation in order to preserve a uniform noise level across the images. In the following section, we summarize the principle of the RM-synthesis technique.

2.2.1 RM-synthesis

Low frequency polarimetric studies of the diffuse Galactic radio emission are a valuable tool to investigate the ionized and magnetized components of the interstellar medium. Generally, these studies have been based on RM measurements calculated as the slope of a linear fit to the polarization angle as a function of the wavelength squared. However, a new analysis technique has recently been applied, the so-called RM-synthesis (Burn 1966). This technique has only recently become practically applicable due to technical and computational advances, and was developed and used for the first time by Brentjens & de Bruyn (2005). Its main advantages with respect to the standard RM technique are that it provides a mapping of the linearly polarized emission as a function of Faraday depth (ϕ), the Faraday dispersion function ($F(\phi)$), and that bandwidth depolarization and depth depolarization are much less severe. RM-synthesis is implemented as a weighted (by the sampling function $W(\lambda^2)$) Fourier transform between $F(\phi)$ and the measured complex

polarization vector $P(\lambda^2)$:

$$P(\lambda^2) = W(\lambda^2) \int_{-\infty}^{+\infty} F(\phi) e^{2i\phi\lambda^2} d\phi, \quad (2.1)$$

with the Faraday depth

$$\phi = 0.81 \int_{d_1[\text{pc}]}^{d_2[\text{pc}]} n_e \vec{B} \cdot d\vec{l} \quad (2.2)$$

where the electron density n_e and the magnetic field \vec{B} are given in cm^{-3} and μG , respectively. Since we can only sample a finite positive range of wavelengths, the inversion of the Fourier transform is incomplete, and we only get an approximation of $F(\phi)$. However, three physical quantities directly linked to the experimental set up (the channel width $\delta\lambda^2$, the width of the λ^2 distribution $\Delta\lambda^2$, and the shortest wavelength squared λ_{\min}^2) can be used to characterize the detection capability:

- the maximum detectable Faraday depth, constrained by the channel width $\delta\lambda$: $\phi_{\max} \approx \sqrt{3}/\delta\lambda^2$;
- the maximum scale detectable in Faraday depth to which the sensitivity is reduced to 50%, which is constrained by the lowest observed wavelength λ_{\min} : $\delta\phi_{\text{scale}} \approx \pi/\lambda_{\min}^2$;
- the resolution in Faraday depth space defined as the half power width of the rotation measure spread function¹ (RMSF), constrained by the total wavelength range $\Delta\lambda^2$: $\Delta\phi \approx 2\sqrt{3}/\Delta\lambda^2$. This defines the minimum separation between separate synchrotron emitting structures that is detectable.

For our frequency coverage, $\phi_{\max} \approx 2650 \text{ rad m}^{-2}$, $\delta\phi_{\text{scale}} \approx 0.85 \text{ rad m}^{-2}$, and $\Delta\phi \approx 3 \text{ rad m}^{-2}$. With these data we can therefore only detect Faraday thin structures, since the resolution is greater than the maximum detectable scale. Since the polarized radiation is a vector quantity, astrophysical information is stored in both intensity and angle. However, due to the generally low signal-to-noise ratio (S/N) per resolution element, the solution of the $n\pi$ -ambiguity is challenging so we do not use polarization angle maps for a quantitative derivation, but only to infer some basic properties. For this reason, we focus on polarized intensity maps and maps of Stokes U. Maps of Stokes Q show similar characteristics to Stokes U.

2.2.2 RM-synthesis data cubes

Maps for Stokes Q,U, and PI were obtained in Faraday depth space by applying the RM-synthesis technique to the 4.2 arcmin Stokes Q,U maps in the frequency domain. No bias correction was applied to the polarized intensity maps but owing to the high side lobe level of the RMSF, an RM CLEAN (Heald et al. 2009) was performed with a threshold of 5 mJy. The polarized emission from our Galaxy is expected at low Faraday depth values

¹ The point spread function in Faraday depth space is generally called the rotation measure spread function.

$|\phi| \lesssim 10^2 \text{ rad m}^{-2}$ (see Clegg et al. 1992). Inspection of this range of Faraday depth reveals the presence of significant polarized emission only within a few tens of frames around $\phi = 0 \text{ rad m}^{-2}$ Bernardi et al. (2009). The PI content of the data out of this range of Faraday depths has not been checked. For the data analysis, we limited the Faraday depth range of this data set to $[-50, +50] \text{ rad m}^{-2}$.

2.3 Observational results

Two well known basic properties of the diffuse polarized emission (see Wieringa et al. 1993) are visible in the images (see e.g. Figs. 2.2 and 2.8):

- the intensity attenuation due to the WSRT primary beam (about 2.5° at 150 MHz). This is a strong argument for excluding an instrumental origin of the polarization fluctuations, and it suggests a wider extent on the sky of the detected patterns of polarized emission;
- the absence of a correlation between total intensity and polarized intensity, which indicates that the polarization fluctuations are caused by Faraday rotation of the diffuse synchrotron emission background by the intervening magneto-ionized medium.

In the following sections, we describe the global properties of the signals detected in polarized intensity and total intensity.

2.3.1 Total intensity

The Stokes I map displayed in Fig. 2.1 has a size of about 12° in declination and 12° in right ascension, and its dynamic range is about 1450:1 at an angular resolution of $2' \times 2.2'$ FWHM. The only extended Galactic object detected is the H II region complex W3/W4/W5 in the south-west corner, approximately from $(\alpha, \delta)_{J2000} \approx (02^h 25^m, 62^\circ.0)$ to $(\alpha, \delta)_{J2000} \approx (02^h 53^m, 60^\circ.4)$. Faint Stokes I emission is also seen from the spiral galaxy IC 342 at $(\alpha, \delta)_{J2000} \approx (03^h 47^m, 68^\circ.0)$ and from the giant double radio galaxy WNB 0313+683 at $(\alpha, \delta)_{J2000} \approx (03^h 18^m, 68^\circ.3)$. No large-scale diffuse emission in the primary beam is seen at 150 MHz because the interferometer filters away power on the largest scales. However, Bernardi et al. (2009) detected extended faint, mottled, small-scale total intensity emission from the Galactic foreground. From the power spectrum these authors suggest a minimum spatial scale of ~ 12 arcmin for these Stokes I fluctuations.

2.3.2 Polarized intensity

Figure 2.2 shows the polarized intensity at a Faraday depth $\phi = -1 \text{ rad m}^{-2}$. Grating rings are seen around brighter compact sources, but owing to their multiplicative nature, such error patterns are only visible around bright Stokes I sources, so their effect is negligible in the map except in the direct vicinity of bright point sources. Unwanted instrumental

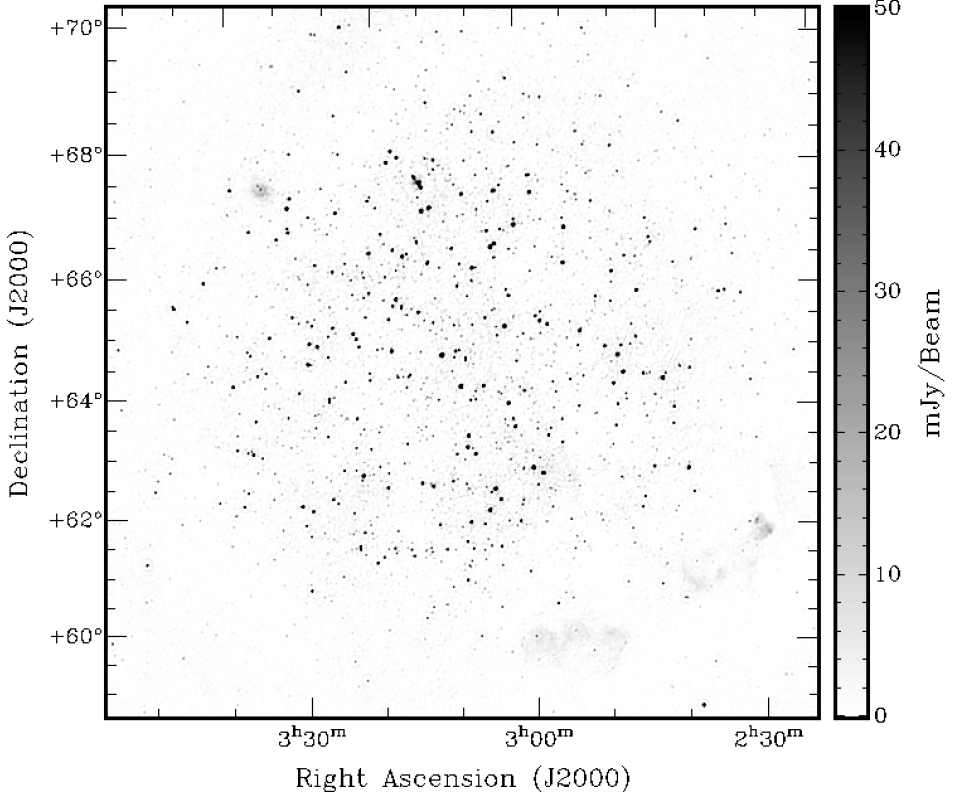


Figure 2.1 – Total intensity map at 150 MHz with an angular resolution of $\approx 2' \times 2.2'$. The diffuse structures towards the upper left and lower right corner are the galaxy IC 342 and the H II region complex W3/W4/W5 respectively.

signals are visible in the Stokes Q, U, and PI maps as elongated stripes and/or waves crossing the field. As pointed out by de Bruyn & Brentjens (2005) and Pizzo et al. (2011), the WSRT off axis polarization has a strong frequency dependence with a period of 17 MHz, which causes peaks in the Faraday spectrum at about 42 rad m^{-2} . At our frequency range, this 17 MHz ripple appears as a broad peak at the edges of the selected Faraday depth range (see Fig. 2.4). These are due to sources Cas A and Cyg A entering the telescope side lobes.

The overall properties of the polarized signal distribution as a function of Faraday depth are shown in Figure 2.4 and an example of Faraday dispersion spectrum is displayed

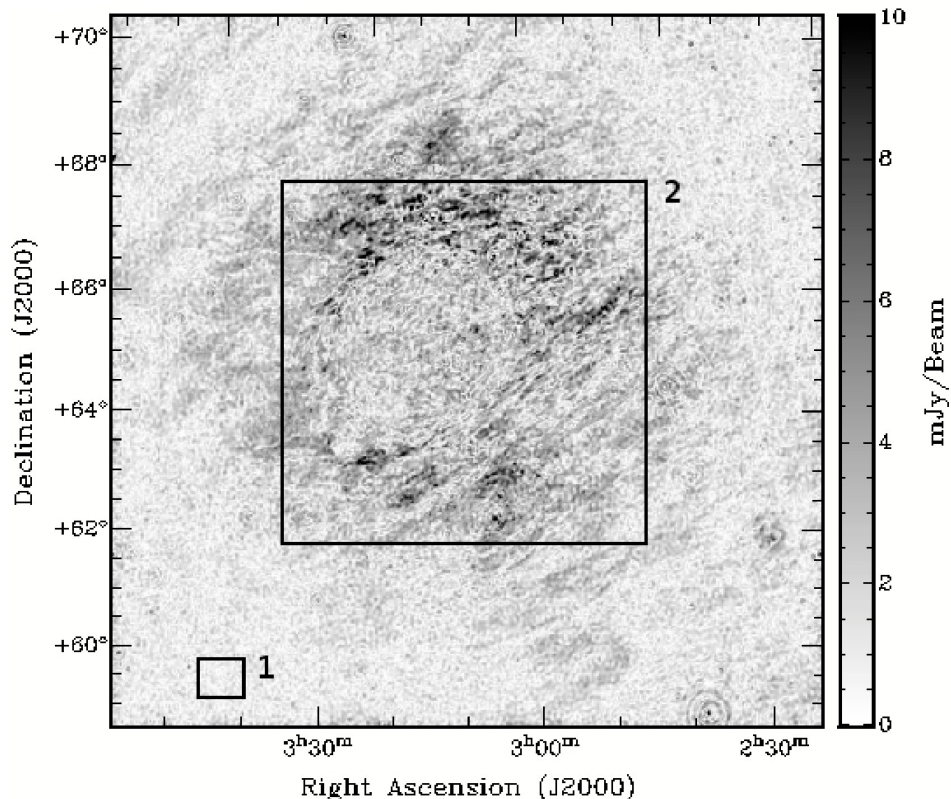


Figure 2.2 – Frame of the RM-synthesis cube at Faraday depth $\phi = -1 \text{ rad m}^{-2}$ displaying the extended polarized emission. Grating rings can be seen around the bright point sources at $(\alpha, \delta)_{J2000} \approx (02^{\text{h}}38^{\text{m}}, 59^{\circ}.1)$ (close to the edge of the image), and $(\alpha, \delta)_{J2000} \approx (03^{\text{h}}06^{\text{m}}, 62^{\circ}.5)$. The drawn boxes are chosen to infer the noise behaviour (box 1) and derive the cross-correlation profile (box 2), see text.

in Figure 2.3. The distribution of polarized signal includes the whole field, i.e. 480×480 lines of sight. We counted at each Faraday depth the number of pixels having a polarized intensity above a 5 mJy beam^{-1} threshold (~ 5 times the PI mean noise level). Polarized emission is detected over a wide range from positive to negative ϕ values. Two main features are clearly seen:

- a central peak at slightly negative ϕ where the most of polarized emission is,

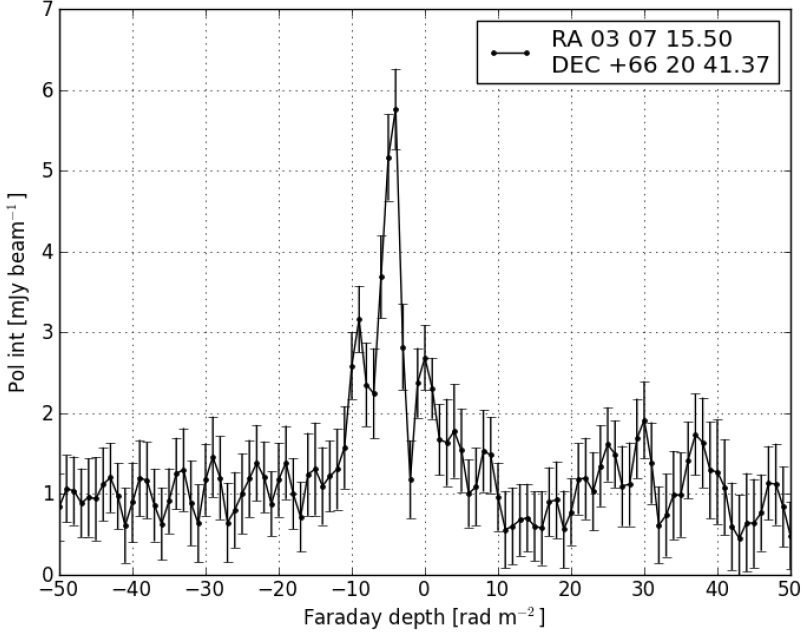


Figure 2.3 – Example of Faraday dispersion spectrum with emission at a single Faraday depth along the line of sight, averaged over a beam-sized box region. The noise level is indicated by 1σ error bars.

- two wings towards the edges of our ϕ range, due to the residuals from Cas A and Cyg A.

Figure 2.4 makes it evident that the Galactic emission from this region is concentrated in a very narrow ϕ range from about -10 to $+5$ rad m^{-2} . The main central feature in the distribution is clearly asymmetric; we interpret this as an evidence of a multi-component signal and we discuss this in Sects. 5 and 7.

2.4 The polarization cube in Faraday depth space

In this section we discuss the noise properties and the connection between RMSF width and cross-correlation in Faraday space.

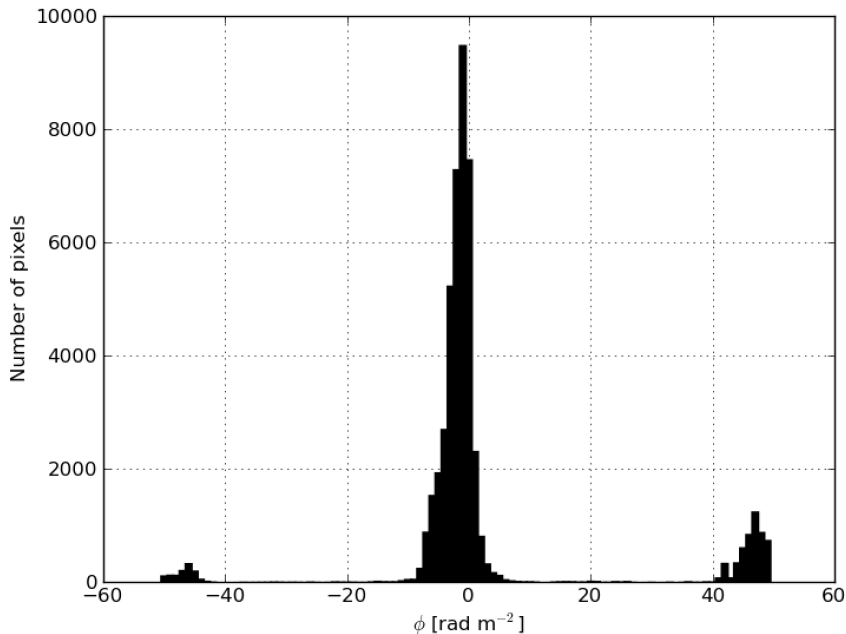


Figure 2.4 – *Distribution of polarized intensity as a function of Faraday depth, above a threshold of 5 mJy. At $|\phi| \geq 40 \text{ rad m}^{-2}$ the residual signal from side lobes of Cyg A and Cas A are visible, while the Galactic emission occurs around -1 rad m^{-2} and has an asymmetric profile.*

2.4.1 Noise properties and errors

Since we are dealing with the measurement of a pseudo-vector - i.e. the polarization - in the presence of random noise we look at noise behaviour. While the two Stokes Q and U parameters are Gaussian distributed, the linearly polarized intensity

$$PI = \sqrt{Q^2 + U^2} \quad (2.3)$$

follows an asymmetric positive definite distribution: the Rice distribution, which is dependent on signal-to-noise and responsible for a bias towards too high values of PI at low S/N Wardle & Kronberg (1974).

We tested the Gaussian behaviour of Stokes Q and U maps and estimated the noise in PI as a function of Faraday depth under the assumption of a Rayleigh distribution of polarized intensities. The noise was determined from a small region assumed to contain no emission from the sky, so that all detected emission is noise (see box 1 in figure 2.2). We assume uniformity of the noise across the field. Since in every Faraday depth frame

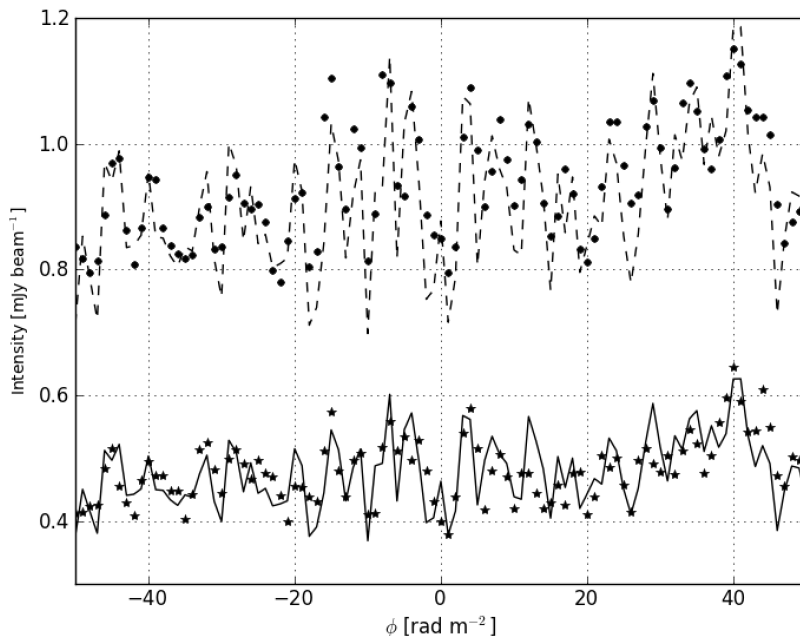


Figure 2.5 – Noise behaviour in the PI map derived from a region denoted by box 1 in figure 2.2 as a function of Faraday depth under the assumption of Rayleigh distribution statistics. The expected mean and variance values of the noise are indicated by the dashed and solid lines, while the measured values indicated by circles and stars refer to the noise mean and variance, respectively.

we detect emission (either from the ISM or from grating lobes from strong out-of-field sources), this uniformity could not be tested. Noise values in Stokes Q and U are similar; also, the assumption of Gaussian noise in Stokes components Q and U is satisfied, because the standard deviation of the sample and the width of fitted normal distribution agree with each other.

The noise properties of PI as a function of the Faraday depth under the assumption of Rayleigh distribution statistics are shown in figure 2.5. Good agreement is found for the expected (i.e. $\sigma_{PI} = 0.66\sigma_U$) and the measured noise variance, as well as for the expected (i.e. $\langle \mu_{PI} \rangle = 1.25\sigma_U$) and the measured noise mean value. A mean noise level of ≈ 1 mJy beam $^{-1}$ is found in PI over a ϕ range of $[-50, +25]$ rad m $^{-2}$ while an increase in the mean and variance values is seen in the Faraday depth range above $+25$ rad m $^{-2}$ due to the presence of residual signal from side lobes of Cyg A and Cas A. Because the Rayleigh statistics a clipping of PI values at 3σ allows to mitigate the impact of Ricean bias below 10% level. Since our analysis does not depend on exact values of polarized intensity, but rather uses rough estimates of ISM parameters, bias corrections were not

applied.

No corrections for the off-axis instrumental polarization were applied. We estimated its magnitude and radial dependence from the fractional polarization values at $\phi = 0 \text{ rad m}^{-2}$, where instrumental polarization is expected. We found a mean level of $\simeq 2\%$ within 3° (primary beam), which rises to $\simeq 9\%$ at the edges of the field of view. There are not enough sources left in the maps after the subtraction to derive the angular dependence of the antenna pattern.

In analogy to radio interferometric observations, the standard errors in Faraday depth measurements can be obtained in an RM-synthesis cube as:

$$\sigma_\phi = 0.5\Delta\phi/(S/N) \sim 1.5/(S/N) \quad [\text{rad m}^{-2}], \quad (2.4)$$

where $\Delta\phi$ is the RMSF width and S/N the PI signal-to-noise ratio. Because we mostly deal with spatially extended emission over several ranges of Faraday depths, we prefer to provide a general upper limit for the ϕ uncertainty at each frame as set by the mean S/N of the emission across the maps. Because the chosen 3σ clip level (i.e. $S/N \gtrsim 3.0$): $\sigma_\phi \lesssim 0.50 \text{ rad m}^{-2}$. Therefore the total Faraday depth estimation error in our 2 m data consists of two main contributions: the systematic error due to the ionospheric Faraday rotation (as discussed in Section 5.2) and the standard error (as shown in Figs. 2.3 and 2.9), having comparable amplitudes.

2.4.2 Cross-correlation in ϕ space

In RM-synthesis the standard estimator for the nominal resolution in Faraday space is the RMSF width. However, as in aperture synthesis, there is some information present on scales smaller than the beam size, as can be seen in figure 2.7. This figure shows polarized intensity changes between neighbouring frames (i.e. $\Delta\phi = 1 \text{ rad m}^{-2}$), about one third of the RMSF width. An effective approach to investigating ϕ -resolution is cross-correlation. Cross-correlation between frames can be used as a probe to infer the presence of structures in the data and their Faraday thickness. We calculate the cross-correlation coefficient for the frames a and b with a frame gap $\delta\phi$ ($C_{\delta\phi}$) as

$$C_{\delta\phi} = \frac{1}{N-1} \sum_{i,j} \frac{(a_{ij} - \bar{a})(b_{ij} - \bar{b})}{\sigma_a \sigma_b}, \quad (2.5)$$

where N is the total number of pixels, (\bar{a}, \bar{b}) are the mean values of the frame, and (σ_a, σ_b) are their standard deviations. The frame gap $\delta\phi = |a - b|$ is the distance between frames a and b in rad m^{-2} .

We studied the correlation length in Faraday depth space of the PI data by considering the whole field of view and by focussing on a square region in the centre of the field (given by box 2 in figure 2.2). In figure 2.6 we show the cross-correlation coefficients for different frame gaps ($\delta\phi$).

For a fixed convolving RMSF, the reference level for data correlation/anti-correlation is shifted from zero to a certain positive value. This offset is due to the convolution of

the noise of each frame with the RMSF, which introduces a degree of correlation of the noise in the frames. The cross-correlation of frame gaps $\delta\phi = 1, 2, 3 \text{ rad m}^{-2}$ for noise-dominated frames convolved with an RMSF of 3 rad m^{-2} is approximately 0.68, 0.22 and 0.1, respectively. Therefore the average levels in Fig. 2.6 correspond to a convolving function with a width of $\approx 2.95 \text{ rad m}^{-2}$, in good agreement with the width of the RMSF. This means that outside the range of Galactic signal of the Faraday depth, from about -10 to $+5 \text{ rad m}^{-2}$, the cross-correlation profile is consistent with a pure noise signal. Therefore for $\delta\phi = 1 \text{ rad m}^{-2}$, a correlation coefficient above 0.68 indicates a positive correlation between two frames, a correlation coefficient of about 0.68 indicates no correlation while a correlation coefficient below 0.68 indicates an anti-correlation.

Several features in the cross-correlation profile for $\delta\phi = 1$ can be seen, which disappear as the frame gap increases. Therefore they are not broader than the RMSF width, which means these structures are Faraday thin. For a frame gap of $\delta\phi = 1 \text{ rad m}^{-2}$, prominent peaks are seen at $\phi \approx -5 \text{ rad m}^{-2}$ and $\phi \approx -2 \text{ rad m}^{-2}$. Three more tentative, small peaks, possibly related to fainter extended emission, are observed around $\phi \approx -10 \text{ rad m}^{-2}$, $\phi \approx +1 \text{ rad m}^{-2}$, $\phi \approx +5 \text{ rad m}^{-2}$.

Calculating the cross-correlation coefficients with the same frame gap of $\delta\phi = 1 \text{ rad m}^{-2}$ in the smaller box indicated as **2** in Figure 2.2 shows interesting results. Correlated peaks at $\phi \approx -10, -6, -2 \text{ rad m}^{-2}$ are still seen, although their amplitudes have changed. However, the most conspicuous changes are seen in the range of Faraday depth $\phi \sim [-2, +4] \text{ rad m}^{-2}$ where the cross-correlation profile is turned into anti-correlation, with two possible small peaks at $\phi \approx 0 \text{ rad m}^{-2}$ and $\phi \approx +2 \text{ rad m}^{-2}$. The polarized emission in this ϕ -range is spatially anti-correlated. Simple simulations show that qualitatively this behaviour can be caused by a spatial gradient in Faraday depth space across these frames. The presence of multiple Faraday components within the peak was also confirmed by comparing the width of the peaks in the spectrum with the width of the RMSF. We checked the behaviour of some representative lines of sight through the “bubble”, “ring”, and “curtain” components. From the fitting of the limited sample of Faraday dispersion spectra, we find clues of multiple poorly separated components, in agreement with the cross correlation result.

- the RM peaks associated with the noise or artefacts (e.g. due to the lobes of the RMSF) show a systematically low $FWHM < 2.7 \text{ rad m}^{-2}$, while RM peaks associated with the three components have $FWHM \sim [2.9, 3.2] \text{ rad m}^{-2}$, in agreement with the expected RMSF width;
- Some lines of sight show excess of widths or complex morphology (see e.g. spectrum of line of sight 4 in Figure 2.9), which make them unsuitable for a single component fitting step. These cases can be found in all three components, but are more evident for the “curtain” component;
- Often spectra also have associated main lobes that are higher than the $\sim 35\%$ level expected from the RMSF profile. In conclusion we find agreement between the result of this test and the cross-correlation.

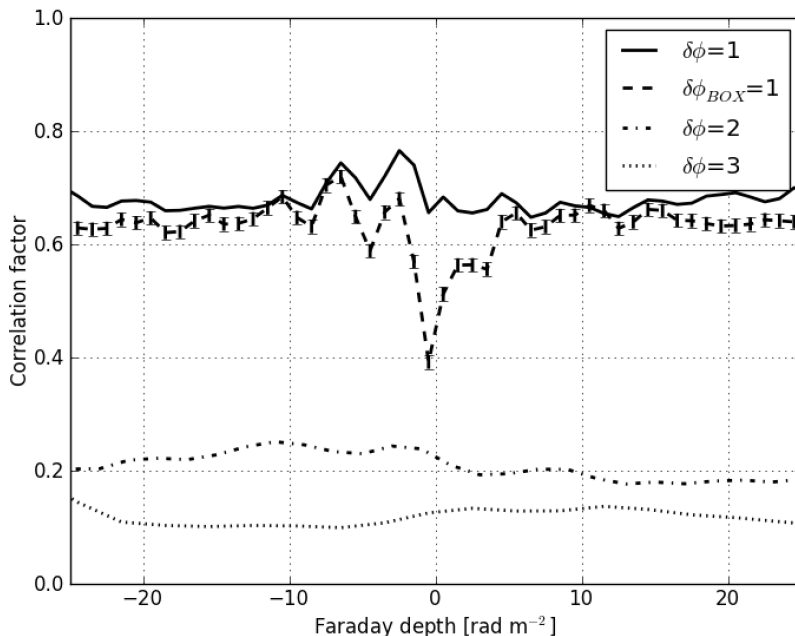


Figure 2.6 – Cross-correlation coefficients as function of Faraday depth for different frame gaps $\delta\phi = 1 \text{ rad m}^{-2}$ (solid), $\delta\phi = 2 \text{ rad m}^{-2}$ (dash-dotted), and $\delta\phi = 3 \text{ rad m}^{-2}$ (dotted). The cross-correlation at $\delta\phi = 1 \text{ rad m}^{-2}$ for only the emission within box 2 in figure 2.2 is shown by the dashed line. The uncertainties are shown by 1σ error bars.

2.5 Definition and description of structures

The (α, δ, ϕ) -cube contains a wealth of structures. In this section we briefly describe the main morphological features in the PI and Stokes U maps as a function of Faraday depth. First, there are spatially compact and isolated structures, such as Galactic and extragalactic Stokes I sources. These objects primarily “illuminate” the intervening Galactic ISM, and reveal its Faraday depth. If their structure is multi-component, then internal Faraday dispersion can be significant and they may actually show emission over a range of Faraday depths. Their definition is based on their compactness in (α, δ) and, occasionally, on association with known objects. The second class of structure is the spatially (very) extended emission detected in polarization. These can be characterized by their properties of PI, Q, or U in Faraday space, in combination with the distribution of polarization angles.

We identified various components in the RM-synthesis cube based on morphological consistency and coherence in Faraday depth and name these components the “bubble”,

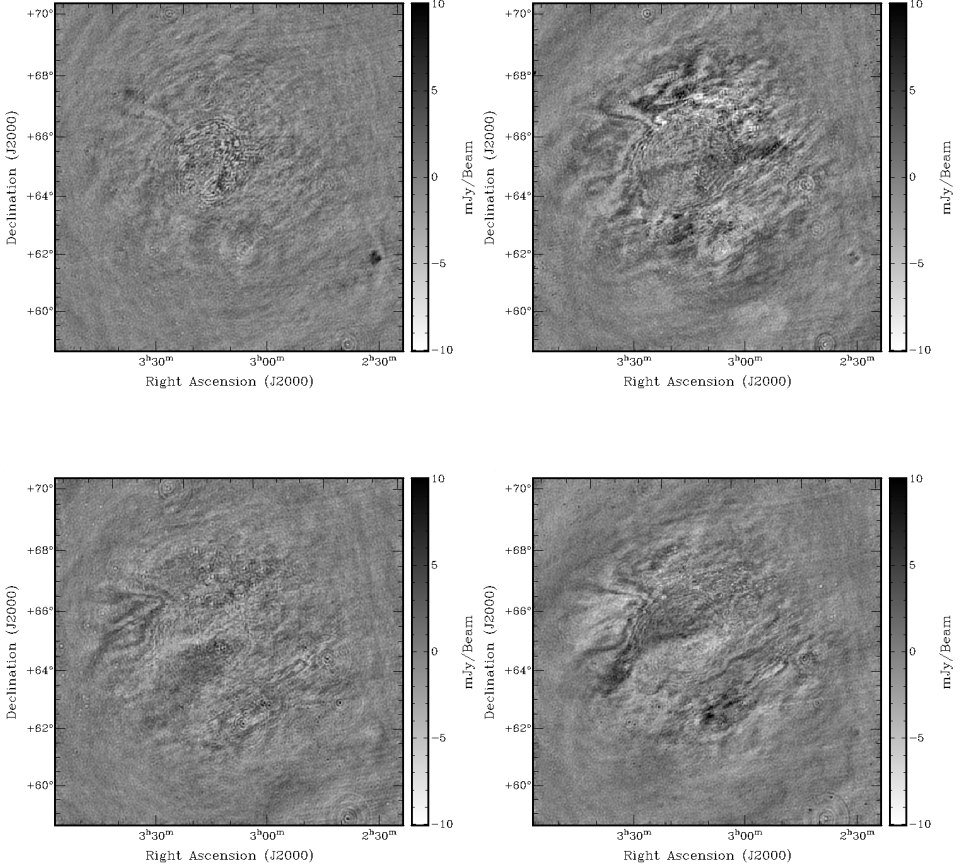


Figure 2.7 – Stokes U emission at four representative Faraday depth values. The images correspond to $\phi = -5 \text{ rad m}^{-2}$ (upper left panel), $\phi = -1 \text{ rad m}^{-2}$ (upper right panel), $\phi = 0 \text{ rad m}^{-2}$ (lower left panel) and $\phi = +1 \text{ rad m}^{-2}$ (lower right panel).

the “ring”, and the “curtain”. These components are shown in polarized intensity in Figure 2.8.

- The discrete PI emission from the “bubble” appears at $\phi \sim -10 \text{ rad m}^{-2}$ in the centre of the field of view. A circular filled structure develops and expands with a maximum of polarized intensity at $\phi \sim -5 \text{ rad m}^{-2}$ and an angular diameter of $\sim 3^\circ$. Also, close to the center a hole in the emission develops and expands until the next structure - the “ring” - comes up. The Stokes U map (see Fig. 2.7 upper left panel) depicts a complex pattern of small-scale wrapped structures surrounded by larger

and smoother ones.

- The “ring” structure consists of extended emission combined with narrow canals of low polarized intensity around a central, almost circular, edge. The “ring” can be considered as a smooth transition from the “bubble”. Its polarized emission reaches a maximum around $\phi \sim -1 \text{ rad m}^{-2}$ and shows bright PI emission occurring in the north-western part of the field with longer depolarization canals (Haverkorn et al. 2000), with lengths up to a few degrees. The orientation of these canals is mostly parallel to the Galactic plane, in agreement with the observation of Haverkorn et al. (2003). The Stokes (Q and) U maps (see Fig. 2.7, upper right panel) show a rapid sinusoidal behaviour at the edge of the “ring”, corresponding to a gradient in polarization angle.
- Finally, a significant pattern of faint, extended polarized emission -the “curtain”- is found at $\phi \sim [0, +5] \text{ rad m}^{-2}$. A fast transition is seen around $\phi \approx +2 \text{ rad m}^{-2}$ from the previous “ring” component to the “curtain”. We interpret this as a spatial gradient of polarized emission in Faraday space around $\phi \sim -2 \text{ rad m}^{-2}$ and $\phi \sim 0 \text{ rad m}^{-2}$, which is responsible for the abrupt decrease in correlation. Stokes U emission (Fig. 2.7 lower panels) reveals extended features on larger scales than the “bubble” and “ring” components. Also, whereas the “bubble” and “ring” show morphological correspondences, these are not present for the “curtain”.

These three components in the RM-synthesis cube correspond to the peaked features seen in the cross-correlations profiles (Figure 2.6) around $\phi \sim -6, -2, +2 \text{ rad m}^{-2}$, respectively.

2.5.1 Diffuse foreground polarized emission

To emphasize properties of linearly polarized emission in ϕ space, the PI emission was integrated in the frames from -13 rad m^{-2} to -5 rad m^{-2} , from -4 rad m^{-2} to -1 rad m^{-2} , and from 0 rad m^{-2} to $+5 \text{ rad m}^{-2}$ as (Brentjens 2007)

$$P(\Delta\phi) = B^{-1} \sum_{\phi_{min}}^{\phi_{max}} (PI(\phi) - \sigma_{PI}) \sqrt{\frac{\pi}{2}}, \quad (2.6)$$

where the normalization factor B is the area of the RMSF beam after RM-CLEAN divided by the interval between two frames of the data cube, and σ_{PI} is the noise in PI estimated from figure 2.5. These maps were clipped at a level of 3σ and then combined into a composite false-colour image as shown in the left-hand upper plot in figure 2.8.

Figure 2.9 shows a sample of Faraday depth spectra, obtained averaging over a beam-sized box region, for several lines of sight. The lines of sight were selected to show widely varying spectra, with a strong main peak (e.g. spectrum 7) or with double and multiple peaks (e.g. spectra 1, 3, and 5 respectively). A peak in the Faraday depth spectrum indicates an emission component in Faraday space. However, due to the limited frequency

Table 2.2 – Properties of the three components.

Structure	Colour	ϕ range [rad m ⁻²]	ϕ_{peak} [rad m ⁻²]	$\langle P \rangle$ [Jy beam ⁻¹]
Bubble	<i>Red</i>	8.0	-5	$(1.72 \pm 0.58) \times 10^{-3}$
Ring	<i>Green</i>	4.0	-2	$(1.78 \pm 0.26) \times 10^{-3}$
Curtain	<i>Blue</i>	5.0	+2	$(1.53 \pm 0.22) \times 10^{-3}$

The columns denote: 1) Name of component, 2) Colour in figure 2.8, 3) Range in Faraday depth in which component is visible, 4) Faraday depth of peak, 5) Polarized surface brightness averaged over Faraday depth range.

coverage, components in Faraday space may be represented in the Faraday depth spectrum incompletely or not at all.

We estimated the mean polarized surface brightness for each component (see Table 2). These mean values are of the same order of magnitude. Interestingly the “bubble” and “ring” components have comparable polarized surface brightness, slightly higher than the “curtain”. The mean polarized brightness temperature over the range $\phi \in [-13, +5]$ is $T_b \sim 5.6$ K.

2.5.2 Polarized extragalactic background sources

Although we are primarily interested in the Galactic emission we briefly point out a few interesting discrete extragalactic objects within 5° of the field centre. These are

- The spiral galaxy IC 342, which is visible both in polarized and total intensity. Large scale disk/halo emission at $\phi = (-3.0 \pm 0.5)$ rad m⁻² is observed, in agreement with Krause et al. (1989) who find RM values between -10 rad m⁻² and 10 rad m⁻².
- The giant double-lobe radio galaxy WNB 0313+683, which shows prominent linearly polarized emission from the south lobe (at $(\alpha, \delta)_{J2000} \approx (03^h 17^m, 68^\circ.2)$) and the core (at $(\alpha, \delta)_{J2000} \approx (03^h 18^m, 68^\circ.3)$) in a range $\phi \approx [-17, -5]$ rad m⁻² consistent with values reported by Schoenmakers et al. (1998) and Haverkorn et al. (2003). However, no polarized emission is detected from the north lobe, which is pointing away from the observer. Since the Stokes I map shows a sharp difference in brightness for the lobes (the north to south lobe mean brightness ratio is ~ 0.2), the non-detection of polarized emission from the north lobe can be explained as a consequence of relativistic beaming and/or additional Faraday depolarization (Heald et al. 2009).

We used discrete polarized background sources to search for a latitude and/or longitude dependence of the Faraday depth across the field of view. From the NVSS RM catalogue (Taylor et al. 2009) we selected a sample of polarized sources with known RM, which covers the observed field of view and its surroundings (see Fig. 2.10). To average out intrinsic RM components of the extragalactic sources, we re-sampled the data over

Chapter 2 Rotation measure synthesis at the 2 m wavelength of the Fan region: Unveiling screens and bubbles.

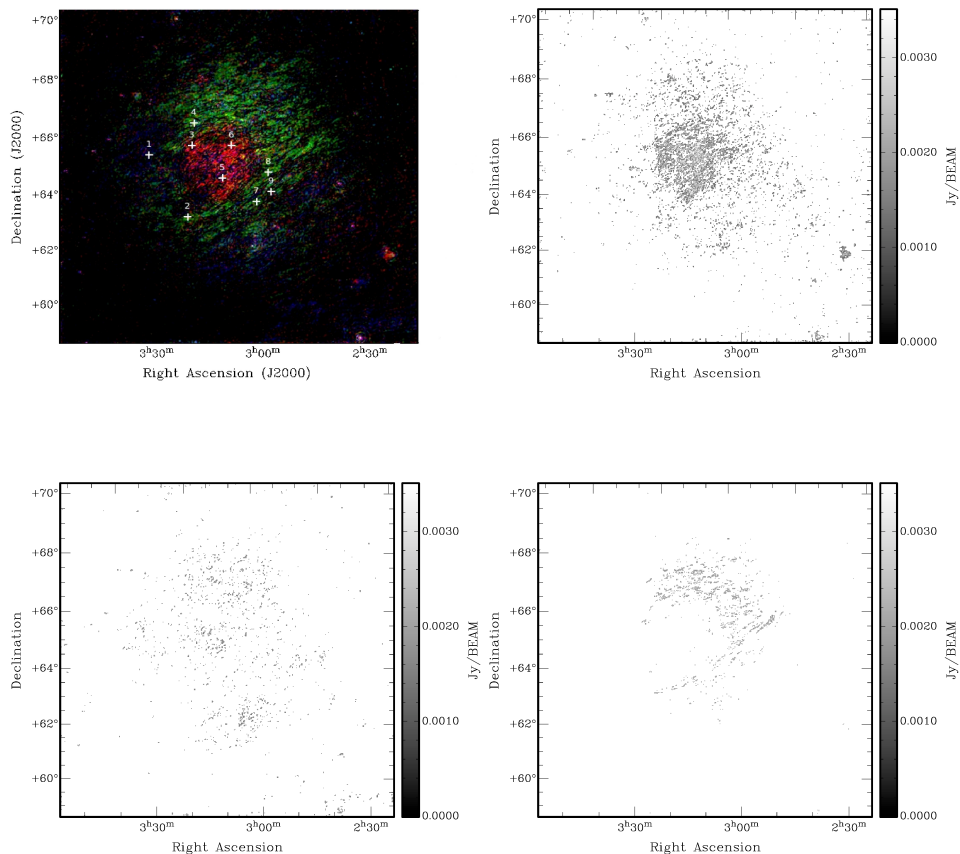


Figure 2.8 – Composite image showing in the upper left panel a colour coded image of polarized intensity emission clipped at 3σ at three main Faraday depth ranges, where the white crosses denote the lines of sight used to extract the Faraday dispersion spectra in figure 2.9. PI clipped maps averaged over ranges in Faraday depth depicting the “bubble”, the “ring” and the “curtain” are shown clockwise in grey scale; Red (upper right panel) is averaged PI over a range of $\phi \in [-13, -5]$ rad m^{-2} , Green (lower right panel) is averaged PI over a range of $\phi \in [-4, -1]$ rad m^{-2} and Blue (lower left panel) is averaged PI over a range of $\phi \in [0, +5]$ rad m^{-2} .

square bins with an angular scale of 5° (about half the size of the imaged field). We find a clear gradient in Galactic latitude of $\Delta RM/\Delta b \approx 4.6 \text{ rad m}^{-2} \text{ deg}^{-1}$, while no evident Galactic longitude dependence is found. The dominant negative RM values imply overall negative B_{\parallel} values, in accordance with the observed negative Faraday depths. A systematic increase in RM values for sources below $b = 5^\circ$ is observed as expected because

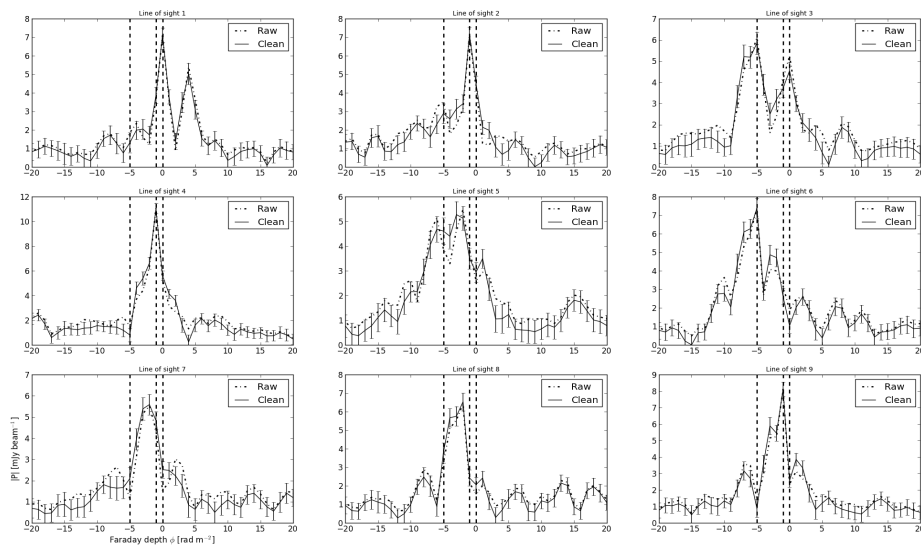


Figure 2.9 – Faraday dispersion spectra of selected lines of sight labelled from 1 to 9 as in figure 2.8. The three dashed black lines point out the position of the histogram peak for the “bubble”, the “ring” and the “curtain” components. For each spectrum the “Clean” line is obtained from the “Raw” one by applying an RMCLEAN session with a threshold of 3 mJy beam^{-1} . The noise level is shown by 1σ error bars.

of the presence of the Galactic disk. In the longitude range $l \in [125^\circ, 140^\circ]$ the presence of extended H II regions (i.e. the W3/W4/W5/HB3 H II region/supernova remnant (SNR) complex in the Perseus arm), as well as the H α maps (Haffner et al. 2003) suggests that the increase in RM towards lower latitudes is at least partially a consequence of enhanced thermal electron density. We note that both the diffuse emission and polarized point sources show predominantly negative Faraday depth and RM, respectively. However, RMs from the extragalactic point sources are much more negative than the Faraday depths of the diffuse emission, suggesting that (a) the diffuse emission is nearby and does not span the full line of sight through the Galaxy, and (b) that $|\text{RM}|$ increases through the outer Galaxy without large-scale magnetic field reversals.

2.6 Model for the diffuse polarized emission

In this section, we discuss plausible sources in the ISM that correspond to the three polarized components identified in Section 5. Interpretation of these polarized components in terms of synchrotron emitting and/or Faraday rotating regions is not straightforward for a number of reasons. First, these are interferometric data, which are missing short spacings in the uv-plane and are therefore insensitive to structure on scales larger than two degrees. This explains why a large amount of polarized emission is observed, but only very weak

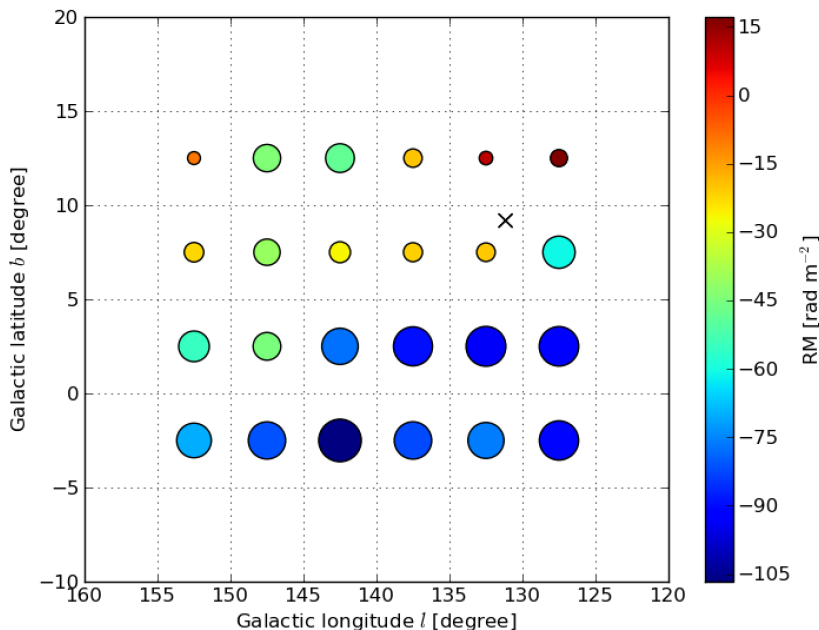


Figure 2.10 – *Distribution of polarized extragalactic point sources and rotation measure values from the NVSS catalogue after binning over 5 degrees spatial scale across the imaged field and its surroundings. The position of pulsar B0226+70, which is used in section 7 to constrain the spatial distance of observed polarized structures is indicated by a cross.*

total intensity (Bernardi et al. 2009), providing an apparent polarization degree far above 100%. This indicates that the synchrotron radiation is emitted on large scales, but its polarization is altered on smaller scales by Faraday effects. In this case we can calculate the missing large-scale structure contribution for Stokes Q and U for a uniformly polarized background propagating through a small-scale Faraday screen (Haverkorn 2002). The expected offset for Stokes Q and U (Q_0 and U_0) depends on the wavelength (λ) and the width of the Faraday depth distribution (σ_ϕ) as

$$e^{-2\sigma_\phi^2\lambda^4} \rightarrow 0 \Rightarrow Q_0 = U_0 = 0. \quad (2.7)$$

At low frequency this condition is typically well satisfied and we do not expect large-scale undetected Stokes Q and U structures. Although there is missing large-scale structure in total intensity Stokes I, there is no missing large-scale structure in Stokes Q and U, therefore the polarization data are reliable. Second, the limited frequency range of the data set precludes the detection of Faraday depth components that have a width $\delta\phi > 1 \text{ rad m}^{-2}$ (Section 2.2.1). Therefore, by definition, the Faraday depth components that we observe

are unresolved in Faraday depth. Analogously to the missing short-spacing problem, this indicates that there likely is Faraday-thick polarized emission (e.g. emission over a wide range of Faraday depths), which we cannot detect. Last, depolarization effects can decrease the polarized intensity of the observed structures.

First, we calculate some properties of the global interstellar medium in the direction of the FAN region, below. Then we discuss what information is available on the absolute and relative distances of the three components in Section 2.6.1. Finally, we present our model in Section 2.6.5.

From the mean dust-corrected $H\alpha$ surface brightness across the (half upper part of the) field of view ($I_{H\alpha} \approx 3.3$ R) and adopting an electron temperature in the diffuse ionized interstellar medium $T = 8000$ K, we derive the related emission measure $EM_{field} = 7.43$ pc cm⁻⁶. This corresponds to a large-scale mean free electron density of $n_e \approx 3 \times 10^{-2}$ cm⁻³ over an assumed total path length of 7 kpc, a value, which is in good agreement with the literature (Hill et al. 2008, Ferrière 2001, de Avillez et al. 2012).

The Fan region has a high degree of polarization, which indicates a relatively regular, large-scale magnetic field topology. This can be either uniform or anisotropically random magnetic fields.

The uniform magnetic field component following the spiral arms is almost perpendicular to the line of sight in this direction. Therefore, the impact of the large-scale interstellar magnetic field on Faraday depth values toward the Fan region is expected to be small. We can test this assumption by estimating the path-averaged magnetic field amplitude along the line of sight up to a few hundred parsecs. We consider a sample of nearby pulsars around the imaged field (see Table 2.3) and apply the general relation:

$$\langle B_{\parallel} \rangle = 1.24 \frac{RM}{DM} . \quad (2.8)$$

With the exception of object 1, all pulsars have estimated distances lower than ≈ 600 pc. The scatter in B_{\parallel} is high, and its sign changes for different pulsars, confirming that the uniform magnetic field component is much smaller than the random component in this direction. We calculate a mean parallel magnetic field $\langle B_{\parallel} \rangle \approx 1.2$ μ G.

2.6.1 Distance estimates to the structures

Most of the polarized emission can be found at slightly negative Faraday depths, consistent with earlier observations (Brouw & Spoelstra 1976, Taylor et al. 2009), which suggests that the radiation is emitted at a short distance from the observer. Wilkinson & Smith (1974) and Uyaniker et al. (2003) deduce that this polarized emission and the low RM values in the second quadrant around $l \sim 150^\circ$ must be nearby, possibly at a distance $\lesssim 500$ pc.

Also, the NVSS gradient show a mean RM value at the FAN latitude of $\overline{RM}_{b=7^\circ} \approx -32$ rad m⁻², which is higher than the observed Faraday depths. We conclude that the detected structures are not representative of the general behaviour through the entire line of sight; as a consequence, these structures must be close.

Table 2.3 – Parameters of nearby pulsars located in the direction of the FAN region. For each object the inferred magnetic field component along the line of sight $\langle B_{\parallel} \rangle$ is also listed. Data are taken from the ATNF Pulsar Database (Manchester et al. 2005).

Object	Name	l,b [deg,deg]	DM [cm ⁻³ pc]	RM [rad m ⁻²]	Dist ^a [kpc]	Dist DM ^b [kpc]	$\langle B_{\parallel} \rangle$ [μ G]
1	B0450+55	152.62, 7.55	14.495 ± 7	10.0 ± 3	1.19	0.79	+0.8555
2	B0655+64	151.55, 25.24	8.771 ± 5	-7.0 ± 6	0.48	0.48	-0.9896
3	B0809+74	140.00, 31.62	6.116 ± 18	-11.7 ± 13	0.43	0.33	-2.3721
4	B1112+50	154.41, 60.36	9.195 ± 8	3.2 ± 5	0.54	0.54	+0.4315

^a (a) Dist is the best estimate to the pulsar distance (kpc).

^b (b) Dist DM is the distance based on the Taylor & Cordes (1993) electron density model.

We can roughly estimate the distance to the “bubble”, assuming uniform conditions for the medium along the entire line of sight, as

$$d_D = \frac{\phi_{OBS}}{\phi_{REF}} D_{REF} [pc], \quad (2.9)$$

where ϕ_{OBS} is the measured Faraday depth, and ϕ_{REF} the reference value of Faraday depth (or rotation measure) corresponding to the line of sight total length D_{REF} . We consider the rotation measure of nearby radio pulsar B0226+70 at $(\alpha, \delta)_{J2000} \approx (02^h 31^m, 70^\circ.26)$ as a reference. The distance of this pulsar is $d_{PSR} = (2.25 \pm 0.56)$ kpc and its rotation measure $RM_{PSR} = (-56 \pm 21)$ rad m^{-2} from the ATNF Pulsar Database² (Manchester et al. 2005). Equation (8) then gives $d_{BUBBLE} \approx (201 \pm 90)$ pc, which is consistent with a previous estimate (Haverkorn et al. 2003). At such a distance and considering the angular size of the “bubble” ($\approx 3^\circ$), a physical size in the plane of the sky of ≈ 10 pc is obtained.

Considering the intrinsic Faraday depth for the “curtain” and “ring” components along with the large-scale electron density field and magnetic field component estimated above along the line of sight, we obtain an estimate of the distance needed to build up this Faraday depth. We find ranges of ≈ 70 pc and ≈ 140 pc for the “curtain” and the “ring”, respectively. These distance estimates do have considerable error margins due to the strong assumptions.

These distance estimates can be tested by comparing the amount of polarized intensity built up over that distance to the observed polarized intensity in the component. At 408 MHz, the total intensity emissivity is $\epsilon_I^{408} \sim (11 \pm 3)$ K kpc^{-1} or 0.011 K pc^{-1} (Beuermann et al. 1985). With a spectral index of -2.5 , the conversion factor from 408 to 150 MHz is ~ 12.2 . Thus the total intensity emissivity at 150 MHz is $\epsilon_I^{150} \sim 12.2 \times \epsilon_I^{408} = (134 \pm 37)$ K kpc^{-1} or 0.13 K pc^{-1} . If we assume a polarization degree of $\sim 8\%$ (Haverkorn et al. 2008), then $\epsilon_{PI}^{150} \sim \epsilon_I^{150} \times 0.08 = (10.72 \pm 2.96)$ K kpc^{-1} or 0.0094 K pc^{-1} . Therefore, for a constant ϵ_{PI}^{150} (which implies a constant polarization degree of 7%) over the line of sight through the “curtain” component, we need about (140 ± 39) pc to build up the polarized intensity of the “curtain” of ~ 1.2 K. This estimate is higher than our estimate above, probably because the “curtain” component is likely to show enhanced synchrotron emission in a narrow emission region (see Section 2.6.2). The “ring” component would need about (168 ± 46) pc to build up the proper polarized intensity, consistent with the estimate above.

We can also give information about the relative positions and distances of the components. The “curtain” component is the nearest component. Since it does not show any imprint of the “bubble”, it has to be located in front of it. The observation of small Faraday depths in this component suggests that it is the nearest layer of ISM with respect to the observer.

The Faraday depths corresponding to these three components are in adjacent ranges, suggesting that their relative distances are small. In particular, the “bubble” has to be located close behind the “curtain”. This is because an additional synchrotron emission component would build up in a large distance between “bubble” and “curtain”, which

² <http://www.atnf.csiro.au/research/pulsar/psrcat/>

would have been observable. The morphology of PI patterns, as well as the very similar mean polarized surface brightness (see Table 2), point to a clear link between the “bubble” and the “ring”.

2.6.2 The foreground “curtain” component

The change in sign of Faraday depth between the “curtain” and the other components indicates a reversal of the magnetic field component along the line of sight B_{\parallel} behind the “curtain”. A plausible magnetic field configuration of how this can be achieved is, e.g., a localized, ordered, magnetic field in the Galactic plane perpendicular to the observer, which fans out locally to produce oppositely directed parallel field components. This magnetic field configuration has a maximum synchrotron emission at the location of the perpendicular magnetic field lines, possibly corresponding to the synchrotron emission from the “curtain”.

We propose that this component corresponds to the wall of the Local Bubble. The above size estimates for this foreground component roughly agree with the dimension of the Local Bubble in this direction (Snowden et al. 1998). A tomography of the interstellar gas within 250 pc was recently obtained by Welsh et al. (2010) combining interstellar absorption data for stars with a Hipparcos measured parallax. Maps of spatial distribution for the neutral gas and neutral plus ionized gas components were derived from Na I, Ca II tracers, displaying the Local Bubble as a region that is poor in neutral gas (and dust) but with several diffuse and highly ionized clouds. A visual inspection of both Na I and Ca II galactic projected maps (see their Figs. 12 and 15) toward the direction $l = 137^{\circ}$, $b = +7^{\circ}$ reveals the presence of an extended and high-density wall of partially ionized medium at about 100 pc of the Sun, as well as a rarefied medium inside the wall, in agreement with our estimate. Moreover, optical starlight measurements in the Fan region from Heiles (2000) show a rise in polarization degree from a distance ~ 100 pc, as shown in Fig. 2.11. This can be explained by an increase in the dust density, denoting the edge of the Local Bubble. The few high polarization degrees at ~ 10 pc can be explained by a compact and cold cloud in the very local interstellar medium. In this picture, the magnetic field would be aligned with the Local Bubble wall, i.e. mostly perpendicular to the line of sight, which indicates enhanced synchrotron emission in the Bubble wall. The Faraday rotation of that emission by the Local Bubble interior is small, i.e. $\lesssim 2$ rad m^{-2} . Using the computed mean parallel magnetic field component of $\langle B_{\parallel} \rangle \approx 1.2 \mu\text{G}$ and a path length of 70 pc, the mean electron density is $n_e^{LB} \approx 1.5 \times 10^{-2} \text{ cm}^{-3}$ in the Local Bubble, which agrees with literature (Spangler 2009).

Previously, an association of the extended polarized Galactic radio synchrotron foreground with the Local Bubble was made by Brentjens (2011), who observed the area around the Perseus cluster near $l = 150^{\circ}$, $b = -13^{\circ}$ at $\lambda = 0.80 - 0.88$ m. In this region, negative Faraday depth values are expected from the inferred direction of the large-scale magnetic field, while he finds a positive Faraday depth component at $\phi = +6$ rad m^{-2} and estimates its size of approximately 200 pc. These values differ from our estimations by about a factor two and may indicate density variations and irregular shape of the Local Bubble wall.

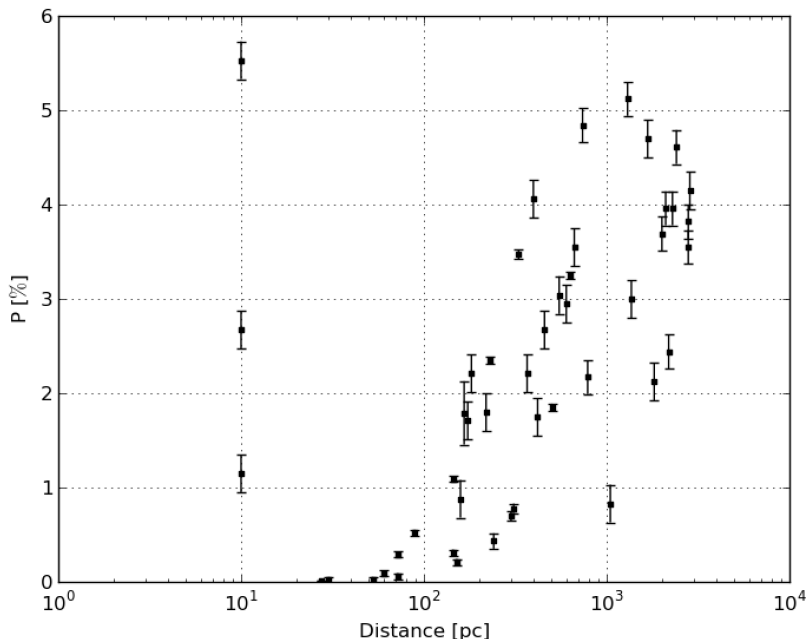


Figure 2.11 – Increase in the polarization degree of optical starlight from stars within the Fan field, closer than 3 kpc.

2.6.3 The background “ring” component

The “ring” component shows a small south-east to north-west gradient in Faraday depth ($\lesssim 1 \text{ rad m}^{-2} \text{ degree}^{-1}$). This gradient does not correspond to the large-scale gradient in RM expected from the NVSS data (Taylor et al. 2009), but is directed almost perpendicular to that. If, as we argue below, the “bubble” component is just an additional Faraday rotation of synchrotron emission in the “ring” component, we would expect this gradient across the field to also be present in the “bubble”. However, since the Faraday depth gradient of $\sim 2 \text{ rad m}^{-2}$ is measured over the entire imaged field, the expected ϕ gradient over the bubble size (about 1/3 of the entire field) turns out to be less than $1 \text{ rad m}^{-2} \text{ degree}^{-1}$ (i.e. less than 1/3 of RMSF width), hence undetectable with our observational set up.

2.6.4 The “bubble” component

The “bubble” component is detected in polarized intensity, but not in total intensity. This could be due to the lack of short spacings. However, if the bubble were significantly emitting, its polarized intensity would be higher than the ring component. Instead, their polarized brightness temperatures are comparable, suggesting that the “bubble” is a Fara-

day rotating structure, retro-illuminated by the synchrotron emission from the “ring”.

We interpret these observations as a consequence of the configuration with the “bubble” located in the spatially extended “ring” structure. Two configurations are possible for the “bubble”: it can be assumed to be either a filled sphere or a shell surrounding a density depletion. We prefer the first configuration because PI emission at the greatest Faraday depths is observed in the centre of the “bubble”. Indeed under the assumption of pressure balance a depletion of warm ionized medium relative to its surroundings may imply an enhancement of neutral gas or dust, which is not observed (e.g. the total H I or IRAS 100 μm maps). Instead since the early work of Verschuur (1969), a considerable lack of H I is observed, as well a very good agreement between higher RM / Faraday depth values and lack of H I. Also, for a filled sphere it is easier to build up the higher Faraday depths observed through the “bubble”

The additional Faraday rotation in the “bubble” component can be caused by increased B_{\parallel} , increased n_e , or a combination of these two options. Observations of H α emission measures set an upper limit for the increase in n_e in the bubble. The bubble is not detected (Haverkorn et al. 2003) in the WHAM Northern Sky Survey (Haffner et al. 2003), which has a sensitivity of 0.05 R. For the emission not to be detected at 3σ (i.e. 0.15 R), the emission measure has to be $EM_{3\sigma} \lesssim 0.34 \text{ pc cm}^{-6}$.

Assuming that the bubble is spherical, the magnetic field component along the line of sight B_{\parallel} can be estimated as

$$\Delta\phi_{max,Bubble} \approx 0.81 \times n_{e,Bubble} \times B_{\parallel,Bubble} \times \Delta L_{Bubble} . \quad (2.10)$$

We can express both the size and the free electron density as a function of the distance to the “bubble”: $\Delta L_{Bubble} \approx \tan 3^\circ \times d_{Bubble}$ and $n_{e,Bubble} = \sqrt{EM/\Delta L_{Bubble}}$. By using these expressions we can check the variation in the magnetic field component along the line of sight, the free electron density and the size of the “bubble” as a function of its distance, indeed indicating an enhancement (with respect to the mean values computed above) of both the free electron density and magnetic field strength along the line of sight by a factor of a few as shown in figure 2.12. A reference distance of about 200 pc implies a path length through the “bubble” of $\lesssim 11$ pc and the corresponding electron density and magnetic field strength within the bubble feature are $n_{e,Bubble} \sim 0.18 \text{ cm}^{-3}$ and $B_{\parallel,Bubble} \sim 5.25 \mu\text{G}$, respectively.

Extra morphology information is obtained from the polarization angle maps. A highly structured configuration for the projected field is observed in the $\phi \in [-10, 0] \text{ rad m}^{-2}$ range. As can be seen from figure 2.13, the polarization angles (also in Stokes Q,U) show very ordered structures around the edge of the bubble. The circular, rapid variations in angle are due to a large angle gradient, displayed in a fixed angle range of $[-0.5\pi, 0.5\pi] \text{ rad}$. Each “ripple” corresponds to an angle gradient over ~ 8 arcmin, followed by an abrupt jump across ~ 2 arcmin, which is due to the $n\pi$ -ambiguity. The polarization angle thus varies by π radians over ~ 10 arcmin. On average four or five of these ripples are visible, which indicates an angle gradient of $\Delta\theta \sim 5\pi \text{ rad}$ over 50 arcmin. At a wavelength of two metres, this indicates a gradient in Faraday depth $\Delta\phi = \Delta\theta/\lambda^2 \approx 3.9 \text{ rad m}^{-2}$ over 50 arcmin, corresponding to ≈ 2 pc at the estimated distance of the “bubble”.

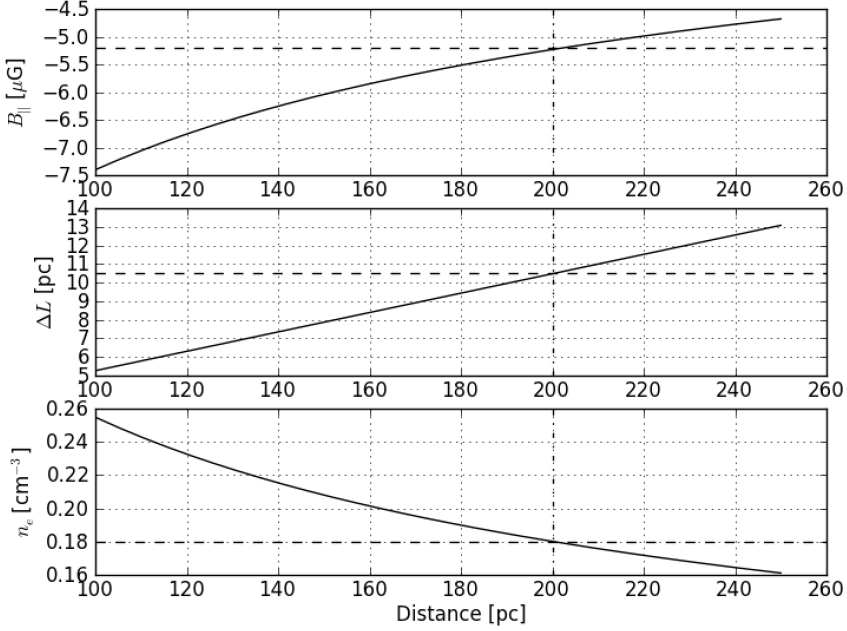


Figure 2.12 – Variation in $B_{\parallel, \text{Bubble}}$, $n_{e, \text{Bubble}}$, and ΔL_{Bubble} as a function of “bubble” distance. Also, for a reference distance of ~ 200 pc (vertical dot dashed black lines) the upper limit for the “bubble” electron density ($n_{e, \text{Bubble}} \sim 0.18 \text{ cm}^{-3}$), the magnetic field component along the line of sight $B_{\parallel, \text{Bubble}} \sim 5.25 \mu\text{G}$ and its size $\Delta L_{\text{Bubble}} \sim 10.5$ pc are indicated by the horizontal black dashed lines.

Moreover, we can use the Faraday depth gradient derived from the rippled features in the polarization angle map to estimate the maximum ϕ value through the “bubble”. Assuming uniform conditions within the “bubble” for the magnetic field and the thermal electron density, we find the total amount of Faraday depth to be $\sim 5 \text{ rad m}^{-2}$, which agrees with the observed value. Finally a lower Faraday depth value for the nearby surrounding “Fan” medium is well supported by previous observations (Brouw & Spoelstra 1976).

The chaotic and patchy appearance of observed features both in polarized intensity and polarization angle imply a large amount of depolarization and may be the result of the turbulent state of the probed magnetized medium. The power-law behaviour of the power spectrum indicates a turbulent medium. In figure 2.14 we show power spectra of the bubble and background components; the spectral energy distributions are close to, but slightly flatter than, a Kolmogorov spectrum. Furthermore, the presence of an inertial

Chapter 2 Rotation measure synthesis at the 2 m wavelength of the Fan region:
Unveiling screens and bubbles.

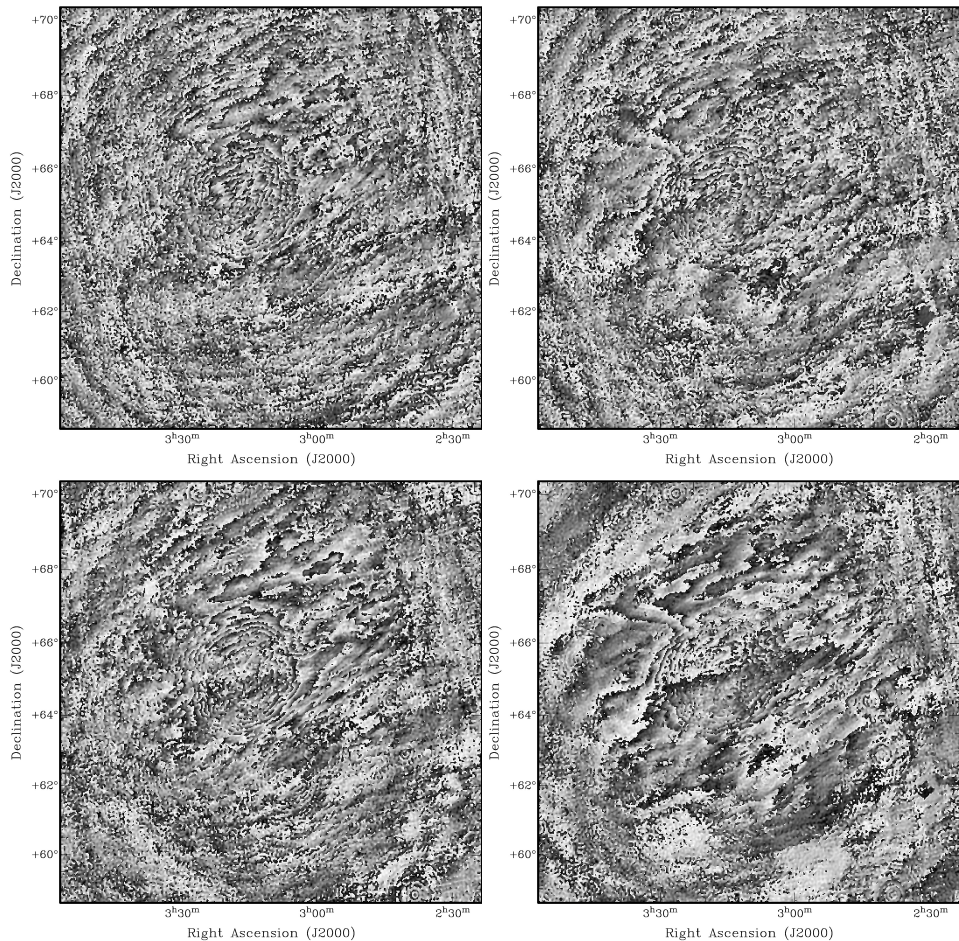


Figure 2.13 – Grey scale images of polarization angle at selected Faraday depths at $\phi = [-7, -5, -3, -1]$ rad m^{-2} from top left to bottom right. The gray scale runs from $+90^\circ$ (black) to -90° (white).

range is apparent, which extends for more than a decade³ and flattens at modes $k \gtrsim 10^3$. Such an increase in power on small scales agrees with the expected large amount of depolarization.

³ Due to the finite size of the field of $\sim 12^\circ$, the smallest mode we can consider is $k_{\min} \sim 10^2$, while the largest mode $k_{\max} \sim 2.6 \times 10^3$ is defined by the angular resolution.

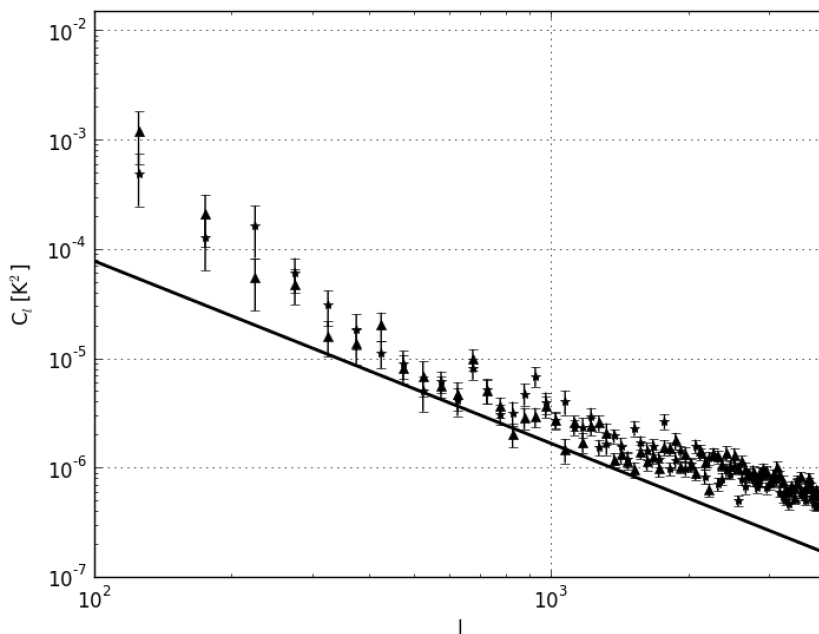


Figure 2.14 – Power spectral density of polarized intensity of the “ring” (stars) and “bubble” (circles) components as derived from a 6 degree inner square of the PI images integrated over the relevant Faraday depths. Also statistical errors and the Kolmogorov spectral slope are shown by 1σ error bars and a black solid line, respectively.

2.6.5 The model in physical space

These considerations lead us to a qualitative model in physical space as depicted in figure 2.15. The region nearest to the observer is bordered by a synchrotron emission layer that corresponds to the Local Bubble wall, about 70 pc away (the “curtain”). This region has a small Faraday depth and is therefore (partially) ionized and has a parallel magnetic field component towards the observer. The border region has enhanced synchrotron emission, which points to an increase in magnetic field perpendicular to the observer.

Behind this region is an extended, magnetized region corresponding to the “ring”, a volume of warm partially ionized and weakly emitting medium which contains the “bubble” component. The parallel component of the large-scale magnetic field in this direction is expected to point slightly away from us (Sun et al. 2008), in agreement with these two components at negative Faraday depths. Since most of the diffuse synchrotron emission is thought to be emitted in the spiral arms and the spatial distances we infer are within a few hundreds of parsec, we conclude that the overall detected PI emission originates primarily in the Local arm.

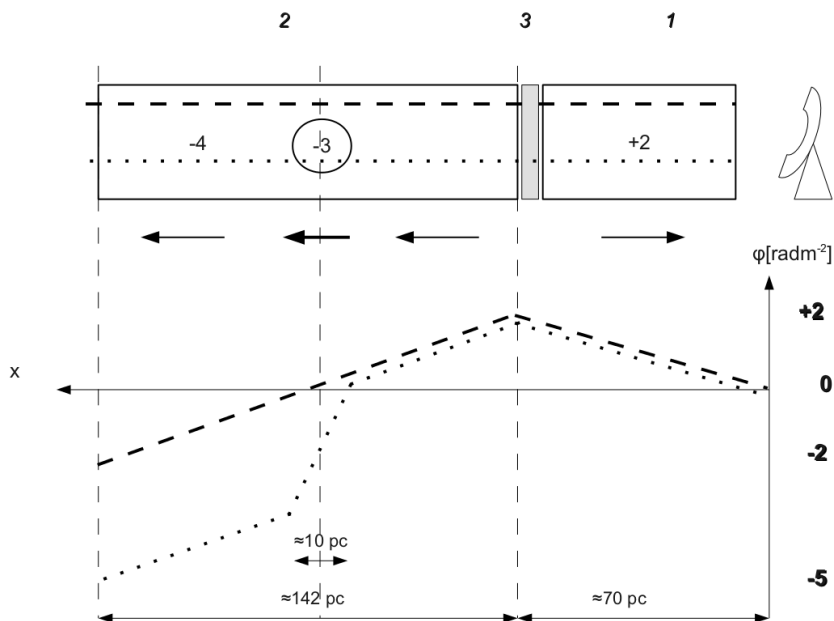


Figure 2.15 – Cartoon illustrating the proposed model for the observed distribution of Faraday depths. Grey areas indicate only emitting regions, and white blocks indicate regions both emitting and Faraday rotating. Intrinsic Faraday depth values are shown within each structure in the top panel, and observed Faraday depth profiles are built up in the lower panel for two representative lines of sight: the dotted line crosses all the detected structures, the dashed line misses the “bubble”. Arrows in the top panel point out the magnitude and sign of $n_e B_{\parallel}$

2.6.6 Possible associations

Circularly shaped, polarized objects without counterparts in other tracers have been observed before (e.g. Gray et al. 1998, Uyaniker & Landecker 2002). These observations differ in two ways from the previous one.

Firstly, we observe much more small-scale fluctuations in the polarization angle patterns. However, this can be caused by the different observing frequencies: Faraday effects are much stronger at low frequencies, so that angle variations are expected to be more evident. Secondly, Gray et al. (1998) and Uyaniker & Landecker (2002) explain their polarization structures in terms of enhancement in electron density, while we (and Haverkorn et al. 2003) argue that some of the structure must be due to enhanced magnetic field. The importance of the magnetic effects and their coupling with the particle density is supported by the ratio of thermal to magnetic pressure β_{pr} which is given by

$$\beta_{pr} = \frac{16\pi n_e k T_e}{B^2} \quad (2.11)$$

Table 2.4 – Main properties of selected stars within the “bubble”. Data are taken from the SIMBAD database.

Star ID	Spectral type	α (J2000)	δ (J2000)	Distance [pc]	Prop. motions [mas/yr]	Radial vel. [km/s]
WD 0314+64	DA	03 18 35.07	+65 00 01.2		110.0, -169.0	
HIP 15520	B2 IV:e	03 19 59.273	+65 39 08.250	234±24	11.25, -14.56	-3.4

where $B \gtrsim B_{\parallel}$ is the total magnetic field strength, k the Boltzmann constant, and T_e the electron temperature in K. For the background “ring” component, with $T_e = 8000$ K, $B_{\parallel,ring} \sim 1.2 \mu\text{G}$, and $n_e \sim 3 \times 10^{-2} \text{ cm}^{-3}$, we find $\beta_{pr} \lesssim 1.15$, which indicates a non-negligible role played by the magnetic field with respect the thermal motion. For the bubble (with $n_e \lesssim n_{e,Bubble}$ and $B_{\parallel} \lesssim B_{\parallel,Bubble}$) we find a lower value $\beta_{pr} \lesssim 3.62 \times 10^{-1}(T_e/8000 \text{ K})$, indicating that magnetic effects dominate thermal effects over a wide range of temperatures (i.e. $T_e \lesssim 2.2 \times 10^4 \text{ K}$); therefore the observed morphology can be shaped by the magnetic pressure of the surrounding ISM. Because of the low thermal electron density, the estimated β_{pr} value is far outside the commonly observed range ($\beta_{pr} > 1$) for an H II region (Harvey-Smith et al. 2011) unless a strong gradient of temperature with respect to the surrounding is considered.

To address the origin of the bubble we now examine several possible origins of this component: an old supernova remnant, an old planetary nebula, and a photo-ionized region.

2.6.6.1 Old supernova remnant

The presence of a Faraday depth gradient across the bubble, the abundance of small scales and an evident polarized intensity pattern could indicate a supernova remnant. The absence of Stokes I emission, as well as the low ratio of thermal to magnetic pressure could be explained by a very old remnant. However, no traces of shocks are found at other wavelengths, and the radial Faraday depth gradient within the bubble does not agree with the expected ϕ -profile for supernova remnants (Uyaniker et al. 2002, Harvey-Smith et al. 2010). Finally, a supernova remnant is a shell, while the bubble is thought to be a filled spherical structure.

2.6.6.2 H II region

We consider the case of an H II region in an unusually low-density medium and a possible association with the nearby B-type star HIP 15520 $d_{LOS} \approx (234 \pm 24) \text{ pc}$ (Van Leeuwen 2007). The distance, position and proper motion of this star (see Table 4 and figure 2.16) lie within the constraints for the bubble. A link between this star and the Fan region was first suggested by Verschuur (1969), who pointed out the neutral gas depletion around the position of this star. He explained the disturbance in the H I by the motion of this star through the interstellar medium.

However, an active H II region is a strong source of H α . We calculated the estimates H α flux from the bubble if it is an H II region. The ionization flux (Q_0) for a B2 type is $Q_0 \lesssim 10^{45} \text{ ph s}^{-1}$ (Sternberg et al. 2003), which can be used to constrain the density in the Strömgren sphere as

$$n_s \approx 10^3 \text{ cm}^{-3} \left(\frac{1.2 \text{ pc}}{R_s} \right)^{3/2} \times \left(\frac{Q_0}{5 \times 10^{49} \text{ photons s}^{-1}} \right)^{1/2}. \quad (2.12)$$

At a distance of 234 pc and for an angular size of $\sim 3^\circ$, we find a corresponding radius of 3.9 pc, a density of $\sim 0.4 \text{ cm}^{-3}$ and an emission measure of $EM_{HIP 15520} \sim 5.25 \text{ pc cm}^{-6}$.

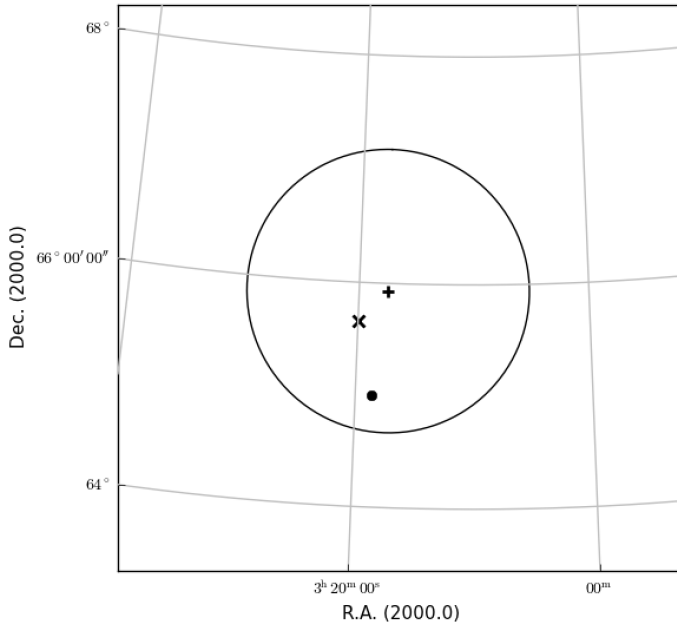


Figure 2.16 – Relative position of selected stars (HIP 15520 is given by the cross, WD 0314+64 by the dot) with respect to the polarized bubble here indicated by the circle. The offsets from the bubble centre (indicated by a plus) are $\sim 0.23^\circ$ and $\sim 0.83^\circ$, respectively, while the bubble radius is $\sim 1.15^\circ$.

This expected emission measure value is well above the WHAM sensitivity, thus it appears that a steady H II region is not likely to be responsible for the observed bubble.

2.6.6.3 Old planetary nebula

A more likely scenario would be provided by the final stage of the life of a star, forming a compact object. For a white dwarf star, some outer shells of materials have to be expelled in the surrounding ISM before the collapse by a weak shock. After this ISM sweeping stage, the hot star can ionize the surrounding medium quickly, producing a photo-ionized region. Indeed evolved planetary nebula nuclei can have Lyman continuum photon luminosities comparable to those of early B stars (Reynolds 1986), enabling rapid ionization of the surroundings. The observational work of Tweedy & Kwitter (1996), focussed on old planetary nebulae, indicates there is a class of nebulae that appear to be filled, in agreement with the bubble.

Indeed, the white dwarf star WD 0314+648 (see Table 4 and figure 2.16) on the edge of the bubble, moving outwards, is an obvious first candidate. Its distance and radial

motion are not known. However, the white dwarf has a high proper motion, which can be due to a small distance to the observer, or due to a kick acceleration at its formation. If we assume that this white dwarf was born at the approximate centre of the bubble, we can obtain an estimate of its age as the time needed for the star travelling from the bubble centre. We find an age of $\gtrsim 15000$ yr for the star WD 0314+648 close to the edge of the bubble (for a proper motion and an estimated radial distance from the bubble centre of $\mu^* \sim 0.2$ arcsec yr $^{-1}$ (Lepine & Shara 2005) and $r^* \sim 0.83^\circ$, respectively). This age is much shorter than the recombination time, thus supporting the inferred high ionization degree.

The effective temperature for white dwarf WD 0314+648 is 17500 K (Sion et al 1988). This temperature is so low that the white dwarf will not ionize its surroundings, in agreement with the lack of any bubble features around WD 0314+648. However, for it to be able to explain the bubble, it must have been much hotter and ionizing its surroundings when it was located near the centre of the current bubble.

From the above reasoning, it is possible that the bubble is a fossil Strömngren sphere created out of an old planetary nebula and associated with a white dwarf star. Owing to the old age of the relic, interaction with the surrounding interstellar medium is expected, and the high symmetry of the observed morphology suggests that the surrounding medium is rather uniform. For a white dwarf at a distance of 200 pc, with a density of the bubble of $n_e \lesssim 0.18$ cm $^{-3}$, the required ionization flux Q_0 is $Q_0 \lesssim 10^{44}$ ph s $^{-1}$. This corresponds to an emission measure $EM \lesssim 0.34$ pc cm $^{-6}$, consistent with observations.

From the Lyman continuum fluxes of Panagia (1973) and the white dwarf temperature and radius, we estimate the minimum temperature needed for sustaining the bubble: $T_{min}^{WD} \gtrsim 26000$ K. The time needed for the white dwarf to cool from T_{min}^{WD} to the current value is $\Delta t \sim 10^7$ yr (roughly estimated from the cooling time in Mestel (1952)), which does not agree with the age estimated from its proper motion. Therefore, this particular white dwarf is probably not the cause of the bubble. However, other white dwarfs, at even greater angular distances from the centre of the bubble, may have created the bubble.

2.6.7 Comparison of the model at other wavelengths

We compare our model to two radio observations of this field at higher frequencies, the 85 cm WSRT observation by Haverkorn et al. (2003) and the PI survey at 21 cm by Wolleben et al. (2006). In our framework the bulk of the emission must build up within and beyond the foreground “ring” component, at a few hundred parsec from the observer, in agreement with the conclusion of Wolleben et al. (2006). Also, in agreement with their claim of multiple emitting components over a wide range of spatial scales, we suggest there are at least two emitting and Faraday thin components: the very nearby “curtain” component and the “ring” component; however, the “bubble” component is not seen in their polarized intensity map. We explain this lack of detection as due to the low synchrotron emissivity of the “bubble” feature at this frequency (the “bubble” does not manifest in emission) and to the low depolarizing impact it has on the background emission. For a maximum $\phi_{bubble} \sim 8$ rad m $^{-2}$ the expected modulation of the polarization angle at 21 cm is ~ 21 degrees, but over the beam of the map the mean ϕ_{bubble} is $\lesssim 4$ rad m $^{-2}$

providing a variation in the polarization angle $\lesssim 10$ degrees. Interesting is also the comparison with the 85 cm data of Haverkorn et al. (2003). Indeed, the standard RM values estimated by Haverkorn et al. (2003) are in good agreement with the Faraday depths of the “bubble” and “ring” components we present in this paper. Moreover, the spatial distribution of RM values matches the observed Faraday depths observed at 2 m. However, the PI map at 85 cm displays a ring-like feature instead of a filled one. This difference is not likely to be explained by beam or depth depolarization (the resolution of PI maps is similar at 1 m and 2 m) but may be the consequence of the missing short spacing on Stokes Q and U maps at 85 cm, as also noted by Bernardi et al. (2009). Finally, we note the similarity of our model with the one provided by Bernardi et al. (2009), who consider the presence of three separated components: a synchrotron-emitting plus a separated Faraday-rotating components beyond the “bubble”, which correspond to our spatially extended, synchrotron-emitting and Faraday-rotating “ring” component, which surrounds the “bubble”. The main differences from their model are the absence of the very nearby “curtain” component and the position of the “bubble” with respect to the “ring” component.

2.7 Summary and conclusion

We used the RM-synthesis technique on WSRT radio polarization data at ~ 2 m to reveal a complex Galactic synchrotron-emission foreground in a field in the Fan Region centred at $(l, b) = (137^\circ, 7^\circ)$. We detected polarized signals with Faraday depth between -13 and $+5$ rad m^{-2} , which can be separated into three distinct components around -5 , -2 , and $+2$ rad m^{-2} , based on morphological consistency and coherence in Faraday depth space. For the first time, cross-correlation was applied to identify and characterize these polarized structures in Faraday depth space. The low Faraday depth values of all components suggest nearby locations of the emission.

The structure at $[0, +5]$ rad m^{-2} (called the “curtain”) very likely corresponds to enhanced synchrotron emission due to compressed magnetic fields in the Local Bubble wall at around 70 pc distance, in agreement with the location of the wall from optical polarized starlight data. The low but positive Faraday depth of this component suggests a parallel magnetic field component directed towards the observer.

The second component centred at -1 rad m^{-2} (called the “ring” component) is located just behind the Local Bubble. It is expected to be spatially extended and Faraday-thick, and therefore only partially detected in these data.

The third component (the “bubble”) is located within the extended “ring”. Its regular circular shape suggests relatively uniform electron density and magnetic field structure, as is expected within the Fan region. The Faraday depth of the “bubble” in combination of its non-detection in $H\alpha$ indicates that it cannot be created by density enhancement alone, but needs to have enhanced magnetic field strength as well, contrary to earlier detected regular polarization structures (Gray et al. 1998, Uyaniker & Landecker 2002, Uyaniker et al. 2003). Several possible associations of the bubble with ISM objects we discussed, but the most likely explanation is the presence of a nearby (~ 200 pc) relic Strömgren

sphere, associated with old unidentified white dwarf star and expanding in a low-density environment.

Polarized intensity from both the “ring” and the “bubble” components show a power spectrum that has a power law, which is indicative of turbulence. Also, the discrete Faraday depth components suggest discrete, small-scale synchrotron emitting structures in the ISM, as noted earlier by Brentjens (2011).

This analysis shows that radio-polarimetry can detect magnetized objects in the ISM that is not detectable in any other means. If fainter and Faraday thin structures lie along the line of sight toward the Fan region, this will be seen by deeper low-frequency observations. In the near future, the higher sensitivity and resolution of modern low-frequency arrays, such as the LOw Frequency ARray (LOFAR, Heald et al. 2011) may reveal these new components. The study of these spatially very extended and polarized foreground components will benefit from accurate Faraday rotation measurements (e.g. to separate the low ϕ “curtain” and “ring” components), as well as from the wide-field and accurate polarimetric imaging capabilities. A LOFAR observation over its full bandwidth (about 200 MHz from LBA to HBA high) will improve the RM-synthesis maximum scale sensitivity in Faraday depth space, allowing to be detected also the eventually Faraday thick components along the line of sight. The low-frequency arrays of next generation will sensitively probe weak magnetic fields with low Faraday depths, which may reveal more (“bubble”-like) magnetized objects.

Acknowledgments The Westerbork Synthesis Radio Telescope is operated by the Netherlands Foundation for Research in Astronomy (ASTRON) with financial support from the Netherlands Organization for Scientific Research (NWO). The research leading to these results has received funding from the European Union’s Seventh Framework Programme (FP7/2007-2013) under grant agreement number 239490. This work is part of the research programme 639.042.915, which is (partly) financed by the Netherlands Organisation for Scientific Research (NWO). This research has made use of the SIMBAD database, operated at the CDS, Strasbourg, France. We thank Gianni Bernardi for providing the data and helpful discussions.

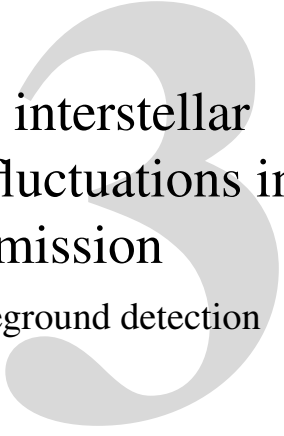
Contributions M.I. led the writing of the paper and the interpretation of results. All authors discussed the results and commented on the manuscript. Data have been provided by Gianni Bernardi.

Bibliography

- Bernardi G., de Bruyn A.G., et al. 2009, A&A, 500, 965
- Beuermann K., Kanbach G. and Berkhuijsen E.M. 1985, A&A, 153, 17
- Bingham R.G. & Shakeshaft J.R. 1967, MNRAS, 136, 347
- Brentjens M.A. & de Bruyn A.G. 2005, A&A, 441, 1217
- Brentjens M.A., PhD thesis, 2007, University of Groningen
- Brentjens M.A. 2011, A&A, 526, 9
- Brouw W.N. & Spoelstra T.A.T. 1976, A&A, 26, 139
- Burn B.J. 1966, MNRAS, 133, 67
- Clegg A.W., Cordes J.M., Simonetti J.-H. & Kulkarni S. R. 1992, ApJ, 386, 143
- de Avillez M.A., Asgekar A., Breitschwerdt D., Spitoni E. 2012, MNRAS, 423, 450
- de Bruyn A.G., brentjens M.A. 2005, A&A, 441, 931
- Ferrière K.M. 2001, Rev. Mod. Phys., 73, 1031
- Frèmat Y., Zorec J., Hubert A.M., Floquet M. 2005 A&A, 440, 305
- Gray A.D., Landecker T.L., Dewdney P.E. & Taylor A.R. 1998, Nature393, 660
- Haffner L.M., Reynolds R.J., Tuft S.L., Madsen G.J., Jaehnig K.P., & Percival J.W. 2003, ApJ, 149, 405
- Harvey-Smith L., Gaensler B.M., Kothes R., Townsend R., Heald G.H., Ng C.-Y., Green A.J. 2010, ApJ, 712, 1157
- Harvey-Smith L., Madsen G.J. & Gaensler B.M. 2011, ApJ, 736, 83
- Haslam C.G.T., Salter C.J., Stoffel H. & Wilson W.E. 1982, A&A, 47, 1
- Haverkorn M., Katgert P. and de Bruyn A.G. 2000, A&A, 356, 13
- Haverkorn M. 2002, PhD thesis Leiden University
- Haverkorn M., Katgert P. and de Bruyn A.G. 2003, A&A, 404, 233
- Haverkorn M., Brown J.C., Gaensler B.M. and McClure-Griffiths N.M. 2008, ApJ, 680, 362
- Heald G., Braun R. and Edmonds R. 2009, A&A, 503, 409
- Heald G., Bell M.R., Horneffer A. et al. 2011, J. Astrophys. Astron., 32, 589
- Heiles C. 2000, AJ, 119, 923
- Hill A.S., Benjamin R.A., Kowal G., Reynolds R.J., Haffner L.M., & Lazarian, A. 2008, ApJ, 686, 363
- Krause M., Hummel E. and Beck R. 1989, A&A, 217, 4
- Lepine S., Shara M.M. 2005, AJ, 129, 1483L
- Manchester R.N., Hobbs G.B., Teoh A. & Hobbs M. 2005, AJ, 129, 1993-2006
- Mestel L. 1952, MNRAS, 112, 583
- Ohno H. & Shibata S. 1993, MNRAS, 262, 953
- Panagia N. 1973, AJ, 78, 929
- Pizzo R.F., de Bruyn A.G., Bernardi G., Brentjens M.A. 2011, A&A, 525 104
- Schoenmakers A.P., Mack K.H., Lara L., Rottgering H.J.A., de Bruyn A.G., van der Laan H., Giovannini G. 1998, A&A, 336, 455

Chapter 2 Rotation measure synthesis at the 2 m wavelength of the Fan region: Unveiling screens and bubbles.

- Spangler S.R. 2009, *Space Sci. Rev.*143, 277
- Reynolds R.J. 1986, *AJ*, 92, 653
- Sion E. M., Fritz M. L., McMullin J.P., Lallo M.D. 1988, *AJ*, 96,251
- Snowden S., Egger R., Finkbeiner D., Freyberg M. & Plucinsky P. 1998, *ApJ*, 493, 715
- Sternberg A., Hoffmann T.L., Pauldrach A.W.A. 2003, *ApJ*, 599, 1333
- Sun X.H., Reich W., Waelkens A. & Enblin T.A. 2008, *A&A*, 477, 573
- Taylor J.H., Cordes J.M. 1993, *ApJ*, 411, 674
- Taylor A.R., Stil J.M., Sunstrum C. 2009, *ApJ*, 702, 1230
- Tweedy R.W., Kwitter K.B. 1996, *ApJ*, 107, 255
- Uyaniker B., Kothes R. & Brunt C.M. 2002 *ApJ*, 565, 1022
- Uyaniker B. & Landecker T.L. 2002, *ApJ*, 575,225
- Uyaniker B., Landecker T.L. Gray A.D. & Kothes R. 2003, *ApJ*, 585,785
- van Eck C.L., Brown J.C. 2010, *ASPC* 438, 236
- van Leeuwen F. 2007, *A&A*, 474, 653
- Verschuur G.L. 1969, *AJ*, 74, 597
- Wardle J.F.C. & Kronberg P.P. 1974, *ApJ*, 194, 249
- Westerhout G., Seeger C.L., Brouw W.N. & Tinbergen J. 1962, *Bull. Astron. Inst.*
- Wieringa M.H., de Bruyn A.G., Jansen D., Brouw W.N. and Katgert P. 1993, *A&A*, 268, 215
- Wilkinson A. & Smith F.G. 1974, *MNRAS*, 167, 593
- Welsh B.Y., Lallement R., Vergely J.-L. & Raimond S. 2010, *A&A*, 510, 54
- Wolleben M., Landecker T.L., Reich W. & Wielebinsky R. 2006, *A&A*, 448, 411



Studying Galactic interstellar turbulence through fluctuations in synchrotron emission

First LOFAR Galactic foreground detection

M. Iacobelli, M. Haverkorns, E. Orrú, R. F. Pizzo and 84 authors

A&A, 2013, 558, 72

Abstract

Aims. The characteristic outer scale of turbulence (i.e. the scale at which the dominant source of turbulence injects energy to the interstellar medium) and the ratio of the random to ordered components of the magnetic field are key parameters to characterise magnetic turbulence in the interstellar gas, which affects the propagation of cosmic rays within the Galaxy. We provide new constraints to those two parameters.

Methods. We use the LOw Frequency ARray (LOFAR) to image the diffuse continuum emission in the Fan region at $(l, b) \sim (137.0^\circ, +7.0^\circ)$ at $80'' \times 70''$ resolution in the range [146,174] MHz. We detect multi-scale fluctuations in the Galactic synchrotron emission and compute their power spectrum. Applying theoretical estimates and derivations from the literature for the first time, we derive the outer scale of turbulence and the ratio of random to ordered magnetic field from the characteristics of these fluctuations.

Results. We obtain the deepest image of the Fan region to date and find diffuse continuum emission within the primary beam. The power spectrum displays a power law behaviour for scales between 100 and 8 arcmin with a slope $\alpha = -1.84 \pm 0.19$. We find an upper limit of ~ 20 pc for the outer scale of the magnetic interstellar turbulence toward the Fan region, which is in agreement with previous estimates in literature. We also find a variation of the ratio of random to ordered field as a function of Galactic coordinates, supporting different turbulent regimes.

Conclusions. We present the first LOFAR detection and imaging of the Galactic diffuse synchrotron emission around 160 MHz from the highly polarized Fan region. The power spectrum of the foreground synchrotron fluctuations is approximately a power law with a slope $\alpha \approx -1.84$ up to angular multipoles of $\lesssim 1300$, corresponding to an angular scale of ~ 8 arcmin. We use power spectra fluctuations from LOFAR as well as earlier GMRT and WSRT observations to constrain the outer scale of turbulence (L_{out}) of the Galactic synchrotron foreground, finding a range of plausible values of 10 – 20 pc. Then, we use this information to deduce lower limits of the ratio of ordered to random magnetic field strength. These are found to be 0.3, 0.3, and 0.5 for the LOFAR, WSRT and GMRT fields considered respectively. Both these constraints are in agreement with previous estimates.

3.1 Introduction

The Galactic interstellar medium (ISM) is a complex and diffuse thermodynamic system with physical properties such as temperature and density spanning many orders, which define three main phases: the “hot”, the “warm”, and the “cold” phase. Moreover, the ISM is both magnetised and turbulent. Many efforts have been made over the past decades to characterise the magnetic fields and the turbulence in the ISM as well as their mutual dependence. However, fundamental parameters regarding both the Galactic magnetic field structure (e.g. the number and spatial location of large-scale reversals, the structure in the halo) and turbulence (e.g. the physical scale of energy injection, the sonic and Alfvénic Mach numbers) are still poorly constrained.

In this paper, we focus on the interplay of the Galactic magnetic field with turbulence

in the ISM by estimating the physical scale of energy injection, L_{out} . This parameter defines the largest linear scale of the turbulent component of the Galactic magnetic field. Towards high Galactic latitudes an injection scale of about 140 pc is found by Chepurnov et al. (2010), who were studying the velocity spectrum of the 21 cm line. Using structure functions of rotation measures, Ohno & Shibata (1993) found a large $L_{out} \lesssim 100$ pc when averaging over large parts of the sky. Haverkorn et al. (2008) confirmed this large outer scale for interarm regions in the Galactic plane using the same method; however, they found a much smaller outer scale $L_{out} \lesssim 10$ pc in the spiral arms. This is in agreement with Clegg et al. (1992), who quote values of 0.1 – 10 pc in the Galactic disk mostly towards the Sagittarius arm. Also, arrival anisotropies in TeV cosmic ray (CR) nuclei can be best explained by a magnetised, turbulent ISM on a maximum scale of about 1 pc (Malkov et al. 2010).

In principle, one could expect multiple scales of energy injection in the ISM (Nota & Katgert 2010). However, MacLow (2004) showed from energy arguments that supernova remnants are expected to be the dominant energy source of the turbulence. Instead, the wide range of estimates of L_{out} can be explained by a non-uniform spatial distribution of sources powering turbulence at the same scale of energy injection (see e.g. Haverkorn et al. 2008). In addition, the typical linear scale of turbulent regions in the ISM is an important parameter in the modelling of CR propagation. Anisotropies in the distribution of Galactic CR arrival directions on the sky have been measured by several experiments both on large (i.e. dipolar anisotropy) and small (i.e. between $10^\circ - 30^\circ$) scales in the TeV-PeV energy range. Anisotropic magneto-hydrodynamic (MHD) turbulence in the interstellar magnetic field has also been proposed to explain such large-scale (Battaner et al. 2009) and small-scale (Malkov et al. 2010) anisotropies in the CR arrival directions at Earth. Recently Giacinti & Sigl (2012a) have proposed the observed anisotropies to be the result of the scattering of TeV-PeV CR across the local magnetic turbulence, and thus within a few tens of parsecs from Earth.

Different observational methods and tracers can be used to study the properties of turbulence and/or magnetic fields in the ISM (see e.g. Elmegreen & Scalo 2004, Scalo & Elmegreen 2004) because they affect both the particle density as well as the emission, absorption, and propagation of radiation. Most of the observations about large-scale Galactic magnetic fields rely on Faraday rotation measures (RMs), where the imprints of magnetic fields and thermal electron density fluctuations are mixed; therefore, RM data allow direct study of fluctuations in the Galactic magnetic field only with a reliable electron density model. But the radio synchrotron continuum of our Galaxy should also contain imprints of the magnetised turbulence in the ISM (see e.g. Eilek 1989a,b, Waelkens et al. 2009, Junklewitz et al. 2011, Lazarian & Pogosyan 2012). Below $\nu \lesssim 1$ GHz, Galactic CR electrons involved in synchrotron emission can be assumed to be uniformly distributed over the scales of magnetic field inhomogeneities (see e.g. Regis 2011). As a consequence, the fluctuations of synchrotron radiation emitted over a large volume and detected in total intensity radio maps directly reflect the spectrum of magnetic fluctuations. Indeed, high dynamic range radio maps of spatially extended ISM features display fluctuations in both total (Haslam et al. 1982) and polarized intensity (Wieringa et al. 1993, Carretti et al. 2009) over a wide range of spatial scales. The advantage of this

method is that it relies on total intensity data that are not affected by depolarization and hence by the thermal electron density distribution. As a result, it is a powerful tool to look at spatial fluctuations of magnetic fields. An analysis of total power synchrotron fluctuations both in the Galaxy and in the nearby spiral galaxy M 33 was recently performed by Stepanov et al. (2012) in order to study magnetic turbulence.

Also, the characterisation of the diffuse synchrotron foreground at arcminute angular scales is fundamental for cosmological studies, such as e.g. extracting the highly red-shifted 21 cm signal from the epoch of reionisation from low-frequency observations. At these frequencies, the Galactic diffuse non-thermal radiation dominates over all other Galactic emission components (i.e. dust and free-free emission), thus forming a Galactic foreground screen and constituting a limiting factor for precise cosmology measurements.

The 408 MHz (Haslam et al. 1982) all-sky map is the most comprehensive map of Galactic diffuse synchrotron emission at about one-meter wavelength. However due to its poor angular resolution ($\sim 0.85^\circ$), it is not adequate for the investigation of small-scale fluctuations in the Galactic foreground emission. Moreover, the radio emission from our Galaxy at lower frequencies is still poorly known. The new generation of radio interferometers operating below $\lesssim 300$ MHz will provide high-quality interferometric data at high ($\sim 1''$) angular resolution, thus overcoming this present limitation. The LOw Frequency ARray (LOFAR) (see e.g. van Haarlem et al. 2012 A&A submitted and Heald et al. 2011) is one of the first of the new generation radio telescopes already in operation in the frequency range $\nu \lesssim 240$ MHz. Due to its large collecting area, the dense uv -coverage at short spacings, and the high sensitivity, LOFAR can perform sensitive observations as well as wide-field and high dynamic range imaging, allowing for detailed studies of the diffuse radio continuum.

Located mostly in the second quadrant at low positive Galactic latitudes, the Fan region is a spatially extended ($\sim 100^\circ \times 30^\circ$), highly polarized, and synchrotron bright region. A small field in the Fan region, which contains a conspicuous circular polarized feature (Bingham & Shakeshaft 1967, Verschuur 1968, Haverkorn et al. 2003b), was recently studied in detail both in total (Bernardi et al. 2009) and polarized (Iacobelli et al. 2013) intensity. We used this field to probe the relationship of Galactic magnetic field and turbulence by studying the Galactic radio synchrotron foreground. Moreover, we had the advantage that there exists a previous observation of this field with the Westerbork telescope (WSRT) at comparable frequencies (Bernardi et al. 2009), which enables a comparison with the new LOFAR results.

In this paper we summarize results obtained from a 12-hour LOFAR observation of part of the Fan region. In Sect. 4.2 we describe the data processing. In Sect. 4.3 we present the frequency-averaged total intensity map, displaying the amplitude fluctuations and its power spectral analysis. Then in Sect. 3.4 we derive an upper limit for the minimum size of the turbulent cells toward the Fan region and constrain the ratio of the random to total components of the Galactic magnetic field. Finally, we discuss our results in Sect. 4.5, and a summary of our results and conclusions is presented in Sect. 5.5.

3.2 Observations and data reduction

The target field was observed with LOFAR in the framework of commissioning activities. The observation was performed on 2012 January 07-08th for 12 hours (mostly during night time), using the LOFAR high band antennas (HBAs) arranged into 57 stations. The array configuration consisted of 48 core stations (CS) and 9 remote stations (RS). The phase centre was set at right ascension $\alpha=03:10:00.00$ and declination $\delta=+65:30:00.0$ (J2000), and no flux calibrator was observed for the adopted single-beam observing mode. Data were recorded over the frequency range 110-174 MHz with an integration time of 2 s. This frequency range was divided into 244 subbands (each with a bandwidth of about 0.18 MHz). The longest and shortest baselines recorded correspond to ~ 81 km and ~ 36 m respectively, although we used baselines only up to about 12 km for better calibratability, resulting in a resolution of about $60'' - 80''$. radio frequency interference (RFI) flagging was done for each subband with the Default Pre-Processing Pipeline (DPPP) using the algorithm described by Offringa et al. (2010, 2012).

Table 3.1 – Observational properties of our LOFAR data set.

Phase centre ^a (J2000)	$\alpha: 03:10:00.0 (\pm 0.''2)$ $\delta: +65:30:00.0 (\pm 0.''1)$
Start date (UTC)	07-Jan-2012/14:00:10.0
End date (UTC)	08-Jan-2012/02:00:10.0
Frequency range	110–174 MHz
Wavelength range	172–273 cm
CS primary beam FWHM at 160 MHz	4.3°
RS primary beam FWHM at 160 MHz	2.8°

A visual inspection of the visibilities revealed some time-dependent emission from the brightest radio sources in the sky, outside the field of view and modulated by the station beam side lobes. We find that only Cassiopeia A and Cygnus A cause significant spurious emission. Therefore our data reduction strategy consists of:

- removal of the two sources Cas A and Cyg A,
- (single direction) calibration of the target field visibilities,
- identification and removal of bad data per station,
- self-calibration to correct for direction-dependent effects,
- imaging.

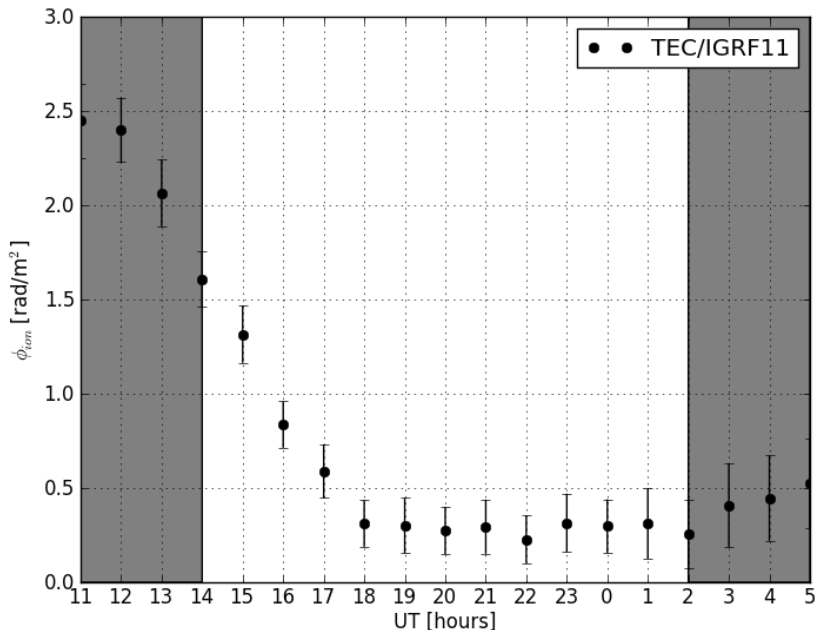


Figure 3.1 – Diagnostic plot of the predicted ionospheric Faraday rotation and its time variation for this observation. Uncertainties are based only on the RMS values of the CODE global TEC maps.

Each data reduction step was performed using software tools of the LOFAR standard imaging pipeline (for a description see e.g. Pizzo et al. 2010, Heald et al. 2010). Both the subtraction of A-team visibilities and the single direction calibration were performed with the BlackBoard Self-calibration (BBS) package (Pandey et al. 2009), which is based on the measurement equation (see e.g. Hamaker et al. 1996). In order to solve and correct for directional dependent effects we used the SAGEca1 software (Kazemi et al. 2011). We now discuss each of these steps individually.

3.2.1 Subtraction of Cas A and Cyg A visibilities

The removal of Cas A and Cyg A visibilities was done from the time-averaged data because subtraction of visibilities from full-time resolution data provided maps with a noise level about 2.5 times higher due to the lower signal-to-noise ratio (S/N) per visibility. Increasing the integration time of the gain solutions from 1 s to 20 s improved the subtraction and decreased the size of the data set. First, the direction-dependent complex gain solutions were calculated for each subband and each of the two A-team sources. Inspection of gain solutions indicated a higher impact of Cas A than Cyg A, likely due to its

higher apparent luminosity. Then the two A-team sources were subtracted from the visibility data using their direction- dependent gain solutions. To remove residual RFI and bad data appearing after this first calibration step, another DPPP flag step was performed on the subtracted data.

3.2.2 BBS calibration

The BBS calibration needs a sky model, which was extracted from a primary beam-corrected Stokes I map obtained in the previous WSRT observations at 150 MHz of the same field (Bernardi et al. 2009). It consists of a list of clean components describing the point sources only. Furthermore, no information related to the Stokes Q, U, or V parameters was included, and a constant spectral index of $\alpha = -0.8$ was used for all sources¹.

Low-frequency observations are affected by ionospheric propagation effects, introducing differential phase delays and Faraday rotation. Both these effects are time and direction dependent and are proportional to the total electron content (TEC) of the Earth ionosphere along the line of sight. Therefore differential Faraday rotation appears between array elements that probe different lines of sight, resulting in a phase rotation of the measured visibilities. Differential ionospheric phase rotations cause image plane effects (e.g. smearing and source deformation), while the related differential Faraday rotation affects polarization. We estimated the global TEC time variations for this observation by predicting the amount of ionospheric Faraday rotation and its time variability. To this aim we ran the `ionFR` code (Sotomayor et al. 2013) and show in Fig. 3.1 the prediction for the RM variations during the time of the observation. With the exception of the first three hours (i.e. observation during the sunset), a steady amount of ionospheric Faraday rotation of $\sim 0.3 \text{ rad m}^2$ was predicted. At 146 MHz, the lowest frequency used for the next imaging step, such an RM implies a change in polarization angle of $\sim 121^\circ$. Because we did not have any (point-like) phase reference calibrator observed, we could not directly inspect the visibility (amplitude and phase) profiles in order to search for signatures of differential ionospheric Faraday rotation. However, estimates of differential Faraday rotation in the HBA indicated phase variations of about ten degrees for baselines comparable to or larger than ours (Wucknitz, priv. comm. on LOFAR Users Forum). Moreover, we found no signal from point sources in Stokes V maps, which indicates a very limited role of differential Faraday rotation. Therefore, we performed corrections of the visibility phases for differential phase delays using BBS and decided to not apply Faraday rotation corrections in this analysis.

A modelled estimate of the station beam was taken into account when calculating the model visibilities. We applied the calibration solutions and corrected the data for each station beam response in the phase centre.

¹ We tested the impact of the assumption of a constant spectral index by comparing results obtained for a sample of five subbands. We did this by adopting a sky model with a spectral index of $\alpha = -1.0$; however, the visual inspection of the maps pointed out no differences.

3.2.3 Removal of bad data

Due to limited receiver synchronization at the time of the observation, the performance of some stations was not optimal, causing decorrelation of signals and, especially around 100 MHz, beam-shape deformation. These effects were visible in the solutions of the calibration step in these faulty stations, showing up as systematically lower gains or noisier phase patterns. This occurred in 15 stations (12 CS and 3 RS), which were subsequently flagged. Next a further flagging step was carried out and in order to minimize the beam-shape deformation effect, which is primarily present at the lower frequencies, we used only the 144 subbands at frequencies higher than 145 MHz.

3.2.4 Self-calibration and imaging

Once the direction-independent calibration step was completed, an intermediate imaging step was done using CASA² imager. A $16^\circ.7 \times 16^\circ.7$ total power sky map of each subband was imaged and cleaned using CASA imager with w-projection (Cornwell et al. 2005, 2008), but without primary beam corrections. These wide-field Stokes I maps with a resolution of $86'' \times 74''$ were used to update the sky model in the next self-calibration step. Therefore, to mitigate direction-dependent errors seen in the wide-field maps we ran SAGEcal with a solution interval of five minutes. To match our sky model, which consisted of point sources only, and to exclude extended emission from the model, we also excluded baselines shorter than 50 lambda in the creation of a clean component model from the CASA images. Finally, a flagging of the corrected data was done.

The final imaging step of the self-calibrated dataset was performed using both the CASA and AW imagers. The sky maps for each subband were imaged with uniform weighting, allowing high resolution. Again, the CASA imager provided us with a wide-field mapping, while the AW imager (Tasse et al. 2013), which is part of the LOFAR software, provided us with primary beam-corrected sky maps to be used when comparing the LOFAR and WSRT fluxes. Moreover, the AW imager is tailored to perform corrections for direction-dependent effects (e.g. the LOFAR beam and the ionosphere) that vary in time and frequency. Finally, each clean model sky map was convolved with a nominal Gaussian beam, and the SAGEcal solutions were applied to the residual sky maps in order to properly restore the fluxes.

3.3 Observational results

3.3.1 Continuum emission maps

The main features of the calibrated maps for a single subband are summarised in Tab. 3.2. Maps obtained with the CASA imager have a noise level measured out of the main beam that varies from about $4.0 \text{ mJy beam}^{-1}$ (i.e. about four times the expected thermal noise level of 1 mJy beam^{-1}) at $\sim 146 \text{ MHz}$ to about $3.2 \text{ mJy beam}^{-1}$ at $\sim 165 \text{ MHz}$, rising up

² Common Astronomy Software Applications, <http://casa.nrao.edu>

Table 3.2 – Properties of individual subband (top) and frequency-averaged (bottom) Stokes I maps.

	CASA imager	AW imager
Dynamic range:	~ 500	~ 500
Rms noise ^a :	4.0 – 3.2	3.8 – 3.1
Beam size:	86'' × 74'', PA=92°	80'' × 70'', PA=88°
Field size:	16.7° × 16.7°	10.0° × 8.0°
Dynamic range:	5.08 × 10 ³	5.80 × 10 ³
Rms noise ^b :	0.40	0.45
Beam size:	86'' × 74'', PA=92°	80'' × 70'', PA=88°
Field size:	16.7° × 16.7°	10.0° × 8.0°

a) Flux density unit is mJy beam⁻¹. The values refer to the frequency range 146 – 174 MHz.

b) Flux density unit is mJy beam⁻¹.

about 3.4 mJy beam⁻¹ at ~174 MHz as shown in Fig. 3.2. An evident spike is found around 169 MHz, and four related subbands of the CASA imaging were discarded. Maps of each subband were inspected visually after the imaging step with AW imager; 17 primary beam-corrected maps displaying an extended pattern of artifacts propagating from the source 4C+63.05 at the south-west edge of the field had to be discarded.

In a single subband map of total intensity, many extragalactic point sources are visible as well as artifacts around bright sources, but no Galactic diffuse emission is detected. In order to increase the S/N ratio, the individual subbands were combined into one frequency-averaged map. The LOFAR main beam, frequency-averaged map after the imaging step with AW imager, which is primary beam corrected, is given in Fig. 3.3. Fig. 3.4 depicts the full bandwidth-averaged map covering 16°.7 × 16°.7, which has a measured noise level out of the main beam of ~ 0.4 mJy beam⁻¹ and a dynamic range of 5080. The imaging step with the AW imager after the self-calibration results in a slightly higher noise level of ~ 0.45 mJy beam⁻¹ and a slightly higher dynamic range ~ 5800. The resulting maps are confusion dominated toward its centre; indeed at 160 MHz and with a beam size of about 1', the expected confusion noise level is about 1 mJy beam⁻¹ (Brown 2011).

The CASA imaged map (Fig. 3.4) clearly shows hundreds of point sources and a few extended extragalactic sources within the primary beam as well as a significant number of extragalactic unresolved sources out of the primary beam. Furthermore, artifacts are evident around bright sources spread within the imaged field, indicating a limited accuracy of calibration. The brightest sources in the imaged field are 4C+58.08, 4C+72.06, and 4C+64.02 with fluxes at 178 MHz of about 19.9, 9.6, and 7.6 Jy respectively. All these sources are located out of the main beam, but only 4C+58.08 and 4C+64.02 show evident

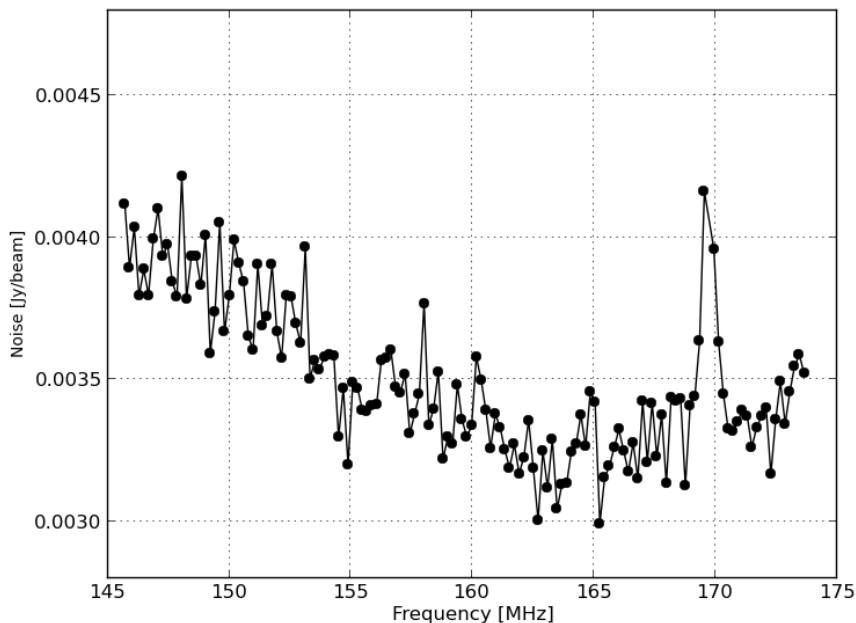


Figure 3.2 – The behaviour of the noise as a function of frequency in maps obtained with CASA imager. A prominent peaked feature in the noise level is seen around 169 MHz. A thermal noise level of about 1 mJy beam^{-1} is expected for each subband over the range 146–174 MHz for this observation.

artifacts. This is likely because the sky model treats these sources as single point sources, while their structure is partially resolved at the adopted angular resolution.

The primary beam-corrected Stokes I map imaged with AW imager also displays hundreds of point sources as well as artifacts around bright sources, but now the noise dominates towards the edges. Intriguingly, we detect diffuse and faint continuum in both frequency-averaged maps toward the Fan region, at a level of about 3 mJy beam^{-1} . The complex spatial morphology agrees with Stokes I structure seen in the WSRT map at lower resolution (see Fig.5 of Bernardi et al. 2009). In what follows we focus on this faint, very extended, Galactic emission. Since the detected diffuse emission is relevant for both cosmological and foreground studies, we describe its spatial properties statistically through its angular power spectrum.

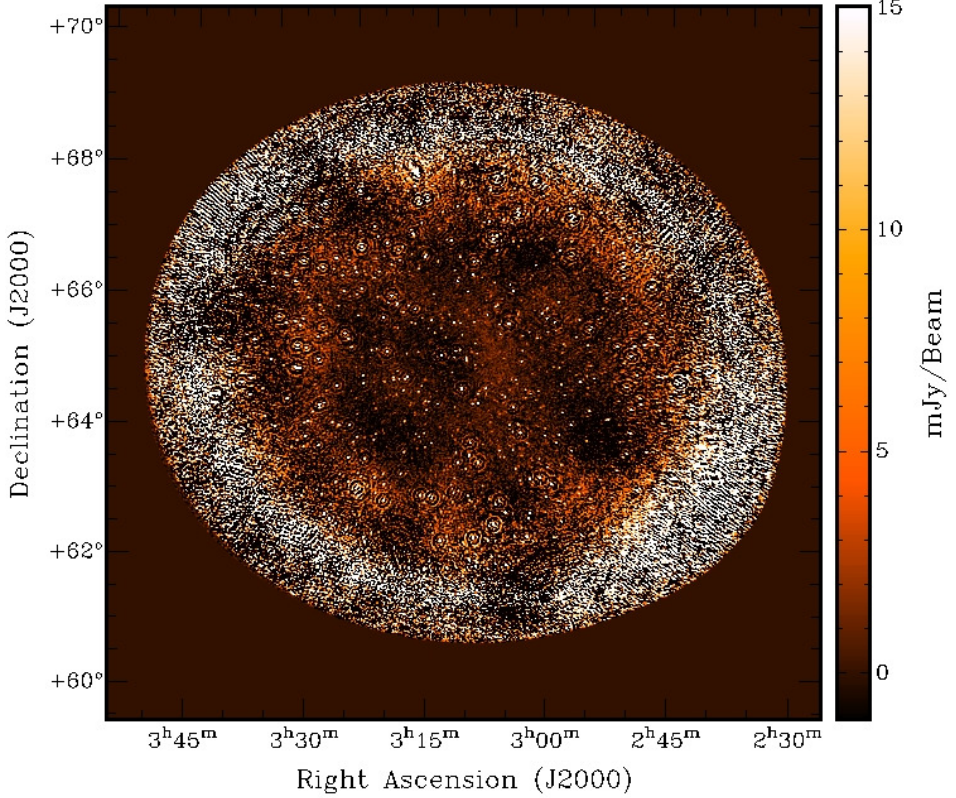


Figure 3.3 – Frequency-averaged Stokes I map of the Fan region field, as obtained with the AW imager with a resolution of $80'' \times 70''$.

3.3.2 Comparing LOFAR with WSRT data

We test the quality of the LOFAR flux calibration by comparing the point sources in the frequency-averaged Stokes I map to sources detected at this frequency with the WSRT (Bernardi et al. 2009). We select sources stronger than 20 mJy beam^{-1} in a $3^\circ \times 3^\circ$ region centred at the phase centre in the LOFAR map. We rescale the LOFAR fluxes measured at a reference frequency of 160 MHz to the WSRT reference frequency of 150 MHz, using a constant spectral index of $\alpha = -0.8$. The error in the WSRT flux density is 5% (Bernardi et al. 2009) and the LOFAR flux uncertainty was assumed at a level of 10%. The fluxes of point sources measured in the LOFAR and WSRT maps are compared in Fig. 3.5.

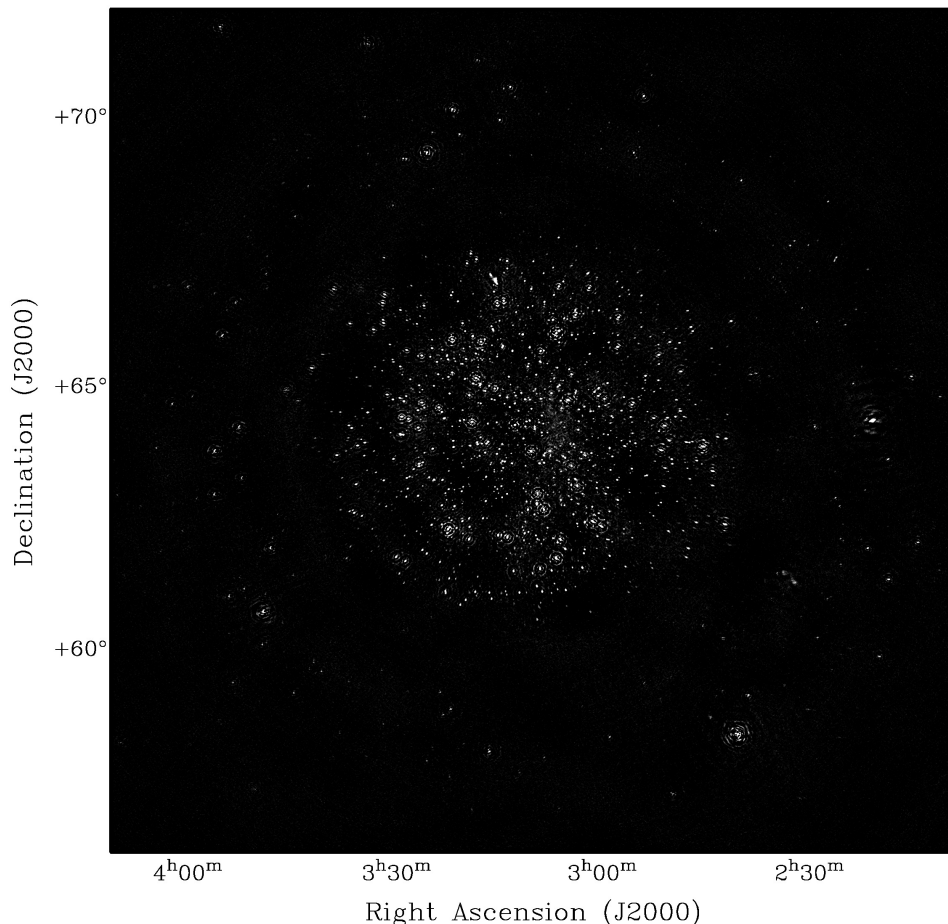


Figure 3.4 – Frequency-averaged Stokes I map of the Fan region field, as obtained with the CASA imager with a resolution of $86'' \times 74''$. The bright sources out of the main beam showing artifacts are 4C+58.08, 4C+72.06, and 4C+64.02.

The LOFAR fluxes of this sample of sources are mostly consistent with WSRT ones. Small deviations from the reference flux ratio may reflect either residuals of calibration or a different spectral behaviour. However, the differences in LOFAR and WSRT flux of these point sources seem to be systematic in position. We compare the LOFAR peak fluxes above a threshold of 20 mJy beam^{-1} within a $3^\circ \times 3^\circ$ box centred at the phase centre rescaled to the WSRT reference frequency to those from the WSRT primary beam-corrected map. The corresponding peak fluxes are used as a reference for the calculation

of the relative flux difference $\frac{\Delta F}{F}$:

$$\frac{\Delta F}{F} = \frac{F_{WSRT} - F_{LOFAR}}{F_{LOFAR}}. \quad (3.1)$$

The relative flux difference as a function of the radial distance from the field centre is shown in Fig. 3.6. Out to a radius of about one degree from the phase centre, the LOFAR and WSRT fluxes agree well (slightly worse for the weakest sources) and a flat $\Delta F/F$ profile is seen, while at larger radii the LOFAR fluxes are increasingly lower than the WSRT fluxes. We explain this systematic effect in the image plane as due to the combination of core and remote stations having different beams with a size of about 4.6 and 3.0 degrees FWHM at 150 MHz respectively. Therefore, out of a region with a radius of about 1.5 degrees, the resolution is expected to decrease (by about a factor 4) because of the smaller contribution to the visibilities of the remote stations, thus affecting the measured peak fluxes. In the following, we use the inner (3×3 degrees) part of the field of view only to mitigate this systematic effect. Also, an evident scatter of data points is found over the entire range of radial distances, which may indicate a limited accuracy of the LOFAR beam model (e.g. a non-negligible azimuthal dependence), but we note that the errors in the WSRT beam model, which is poorly known at such low frequencies, are also present in the comparison.

3.3.3 Power spectral analysis

To perform the angular power spectral analysis two approaches are feasible, namely working in the image plane or directly in the visibilities' uv -space. The first allows calculation of the angular power spectrum of a selected sky region, thus permitting the contributions of different astrophysical sources to be separated from the bulk of detected power; however, it is affected by systematics due to the imaging step. The latter provides a proper errors estimate and investigation of data quality and systematics effects but does not allow contributions towards different directions in the sky to be distinguished. In this study, both these issues are relevant and the approaches are complementary.

In order to evaluate the distribution of detected power in the uv -plane we consider the calibrated, residual visibilities. To convert the power to squared temperature brightness, we need to estimate the size of the main beam seen at station level. Indeed, the sensitivity in the plane of the sky of a receiving LOFAR station is a function of the observing frequency and the size of the station, and LOFAR has stations of two types and sizes, the CS and RS stations respectively. Therefore a main beam with different angular sizes is formed by core-core core-remote and remote-remote baselines, and we correct for this effect by assuming a cylindrical approximation for the beam shape. The power at angular scales we are interested is mainly detected by CS. Thus we select the visibilities from CS-CS baselines only as a function of the uv -distance with a maximum uv -range of $10 k\lambda$, calculate the Stokes I parameter and finally the power spectrum.

As a result, we obtain the multi-frequency angular power spectrum shown in Fig. 3.7, where an evident excess of power at short baselines (i.e. at large angular scales) is displayed. Also, a frequency dependence of this large scale emission is seen, the larger

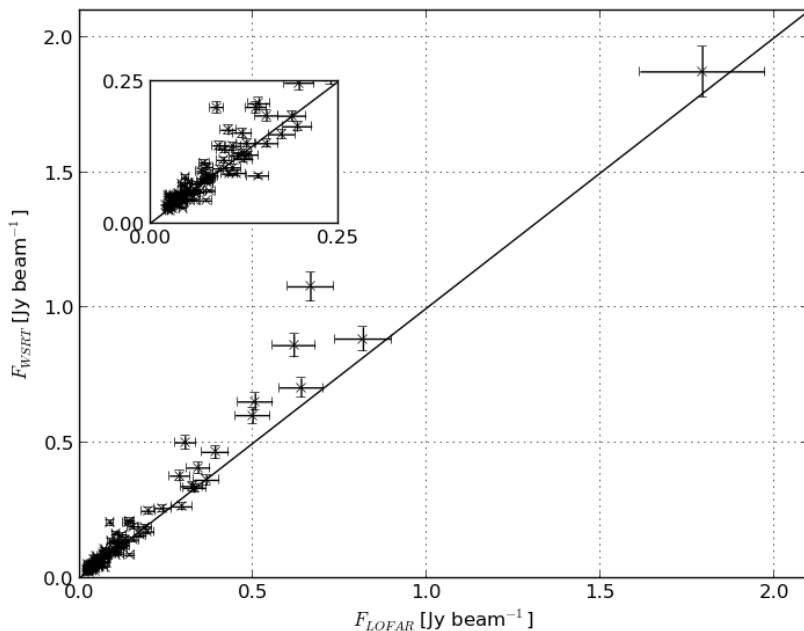


Figure 3.5 – Comparison between the LOFAR fluxes rescaled to 150 MHz and the WSRT fluxes at 150 MHz of point sources detected above a threshold of 20 mJy beam^{-1} within a $3^\circ \times 3^\circ$ box centred at the phase centre. The reference flux ratio of unity is indicated by the solid line.

amount of power being towards long wavelengths. The systematic excess of power over the entire range of uv -distances indicates the presence of instrumental effects corrupting the data, and therefore we exclude SB 233.

The angular total power detected by LOFAR from the observed target field is the sum of several contributions. The diffuse Galactic foreground (which is not modelled), consists of the synchrotron fluctuations due to MHD turbulence spread across the field of view, the presence of an extended and nearby (Iacobelli et al. 2013) Galactic object close to the phase reference, the extended W3/4/5 H II region complex, and the Galactic plane emission towards the lower west edge of the observed field at a radial distance of ~ 5.6 and ~ 6.4 degree from the phase reference. Also, at sub-degree scales, the spiral galaxy IC 342 and the giant double lobe radio galaxy WBN 0313+683, which are located at ~ 4.4 and ~ 3.7 degrees from the phase reference respectively, produce power excess.

The only way to perform spatial selection in the uv -domain is to tune the station field of view by selecting a proper frequency range. In this way we can minimize power contributions due to the Galactic plane and the extended W3/4/5 H II region complex, the price being the use of only a fraction of the data.

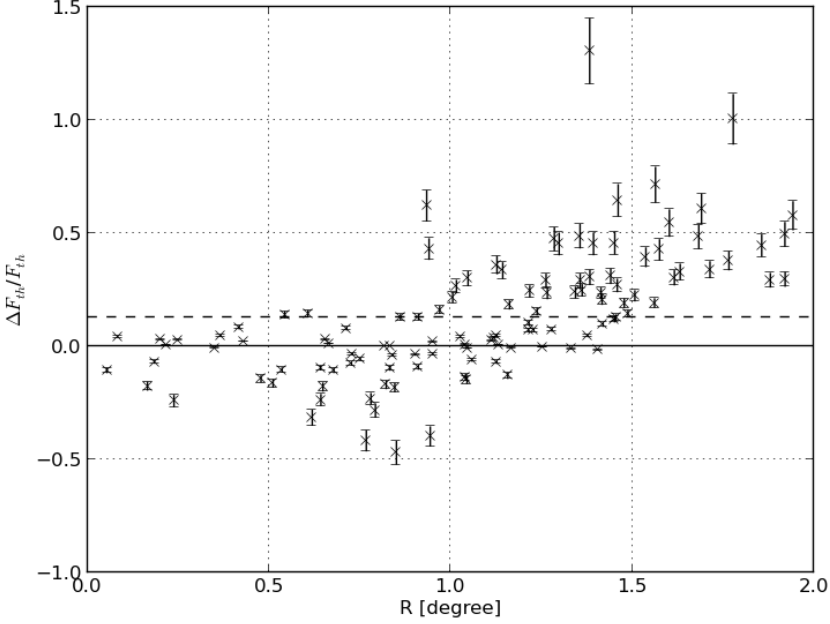


Figure 3.6 – The normalized peak flux differences between point sources in the LOFAR and WSRT observations as a function of radial distance. The LOFAR peak fluxes were rescaled to 150 MHz and both maps were corrected for primary beam attenuation. The mean value (dashed line) of these fractional variations is $(\Delta F/F) = (0.128 \pm 0.014)$, indicating the presence of a bias.

To avoid this drawback and discard the unwanted power contributions, we use the prescription by Bernardi et al. (2009) to calculate the power spectrum. However, instead of identifying the point sources by making sky images with only the long baselines and subtracting these directly from the visibilities, as Bernardi et al. did, we identify and extract point sources from the frequency-averaged total intensity map down to $\lesssim 5 \text{ mJy beam}^{-1}$ using the PyBDSM source extraction software³. We obtain the residual image shown in Fig. 3.8, where an extended pattern of fluctuations is seen, along with evident artifacts around bright sources; only very faint sources are left.

From this residual map we calculate the power spectrum as in Seljak (1997) and Bernardi et al. (2009) over a region of $3^\circ \times 3^\circ$ degrees centred on the field centre:

$$C_\ell^I = \left\{ \frac{\Omega}{N_\ell} \sum_\ell I(\vec{\ell}) I^*(\vec{\ell}) - \frac{\Omega(\sigma_{\text{noise},\ell}^I)^2}{N_b} \right\} b^{-2}(\vec{\ell}), \quad (3.2)$$

³ <http://tinyurl.com/PyBDSM-doc>

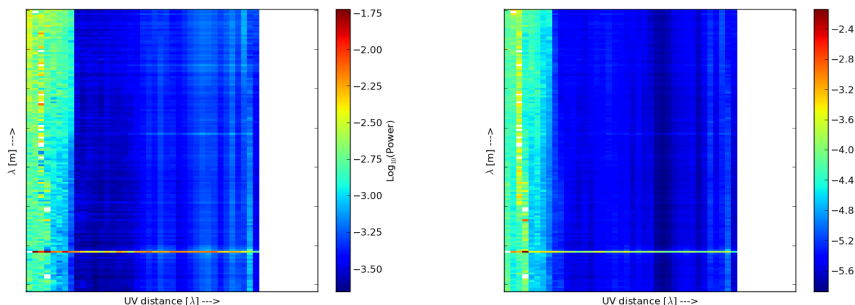


Figure 3.7 – Distribution of the power (left panel) and its error (right panel) as a function of the uv -distance (up to 10 $k\lambda$) and frequency, detected by CS stations only. The row showing a systematic excess of power over the entire uv -distance range corresponds to the corrupted and discarded SB 233.

where I indicates the Fourier transform of the total intensity, ℓ is the multipole (i.e. $\ell = 180/\theta$ where θ is the angular scale in degrees), Ω is the solid angle in radians, N_ℓ is the number of Fourier modes around a certain ℓ value, $\sigma_{\text{noise},\ell}$ is the noise per multipole, and N_b is the number of independent synthesized beams in the map. In the case of negligible calibration errors, the factor $b^2(\ell)$ is the power spectrum of the window function (Tegmark 1997), which in the case of interferometric images corresponds to the power spectrum of the dirty beam. However, this is not the case for the LOFAR data, as indicated by the presence of artifacts in the image plane. Therefore, taking into account only the dirty beam provides just approximate corrections to the power spectrum. Thus, instead of being able to measure angular size scales down to the synthesized beam size from the interferometry, we are limited to the largest size scale ($\sim 8'$) of the imaging artifacts shown in Fig. 3.8.

The largest angular scale of emission measured by an interferometer, i.e. the smallest multipole ℓ_{\min} , is fixed by the shortest (u,v) spacings of the interferometer. For LOFAR $\ell_{\min} \gtrsim 50$. In principle, a constraint on the smallest scale suitable for the investigation of the data is given by the size of the point spread function (PSF), which attenuates the angular power; at LOFAR angular resolution ($\sim 1'$) attenuation would be negligible up to $\ell_{\max} \lesssim 3700$. As noted above, because of the artifacts affecting the image plane due to non-negligible calibration errors we practically limit our investigation up to $\sim 8'$, corresponding to a multipole $\ell_{\max} \lesssim 1350$. We used a least square method to fit a power law ($C_\ell \propto \ell^\alpha$) to the angular power spectrum, giving a spectral index $\alpha = -1.84 \pm 0.19$ for $\ell \in [100, 1300]$ in agreement within 2 sigma with the previous slope estimate from WSRT data (Bernardi et al. 2009). The power spectrum down to scales of about $2'$ is shown in Fig. 3.9. The uncertainties were calculated as the standard deviation of the signal within one multipole bin. At low ℓ the power spectrum shows a power law behaviour, while at high multipoles (i.e. $\ell > 10^3$) a flat power spectrum is seen. Bernardi et al. (2009) inter-

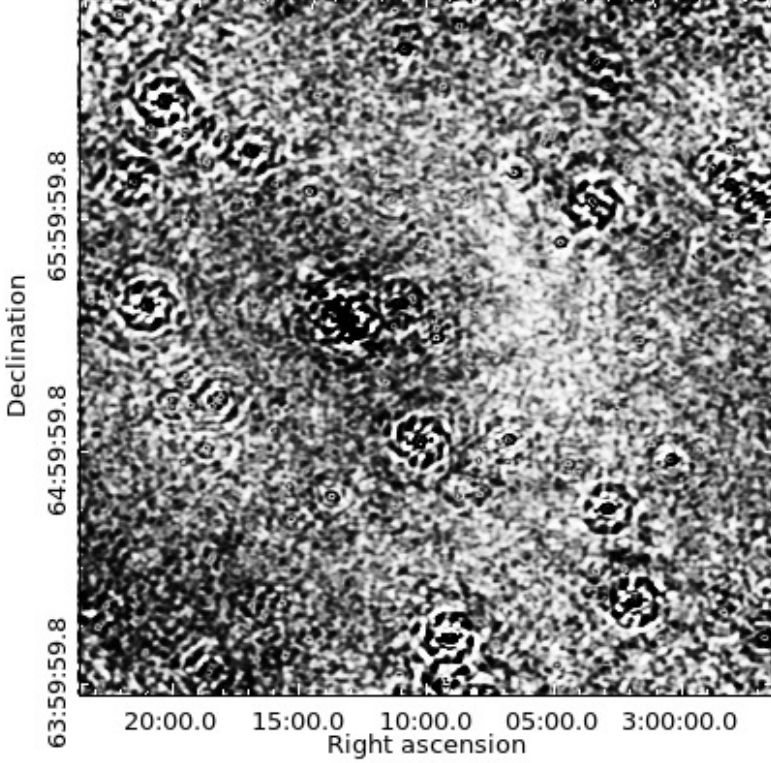


Figure 3.8 – The inner $3^\circ \times 3^\circ$ region of the primary beam-corrected Stokes I map with point sources subtracted.

preted this power law as the large-scale foreground emission from the Galaxy toward the Fan region and the flattening of the spectrum as the rms confusion noise (σ_c) due to the point source contamination. As in Brown (2011), we can estimate σ_c as

$$\frac{\sigma_c}{\text{mJy beam}^{-1}} \approx 0.2 \times \left(\frac{\nu}{\text{GHz}}\right)^{-0.7} \times \left(\frac{\theta}{\text{arcmin}}\right)^2, \quad (3.3)$$

where ν is the reference frequency and θ is the FWHM of the Gaussian beam. The confusion noise level for the LOFAR data is $\sigma_c \sim 0.85 \text{ mJy beam}^{-1}$, which corresponds to a power of $C_\ell^c \sim 4 \times 10^{-5} \text{ K}^2$.

For comparison, the WSRT power spectrum obtained by Bernardi et al. (2009) is overplotted in Fig. 3.9. The shapes of the power spectra from the LOFAR and WSRT data

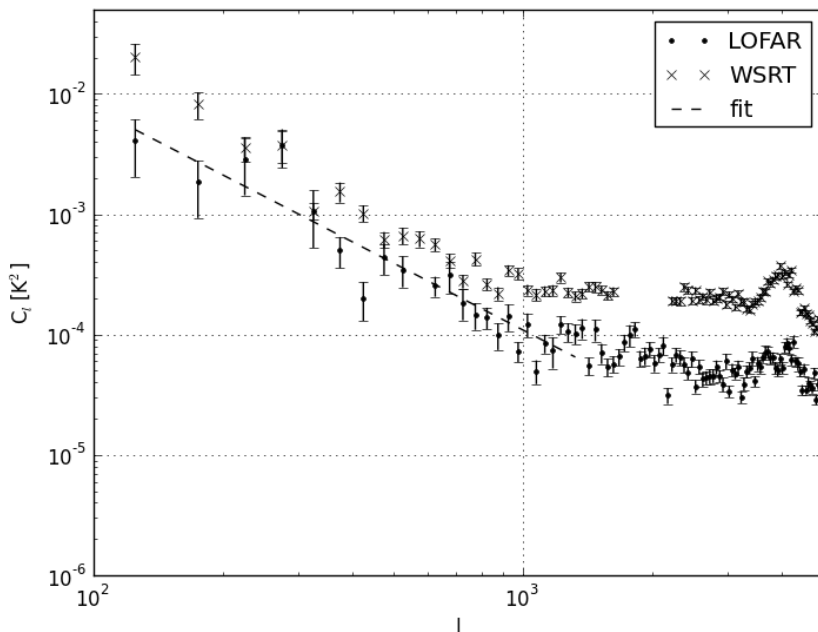


Figure 3.9 – Power spectra of total intensity from the LOFAR (dots) and WSRT (crosses) observations. The error bars indicate statistical errors at 1σ . The fitted power law (dashed line) with a spectral index $\alpha = -1.84 \pm 0.19$ for $\ell \in [100, 1300]$ is also shown.

match very well, indicating that the diffuse emission in the LOFAR data probes the same total intensity fluctuations as the WSRT. However, the amplitude of the LOFAR data is a factor 3 or so lower, a plausible reason being the applied weighting scheme. In order to clarify this point we performed an imaging step with a natural weighting scheme, thus not changing the power distribution at different angular scales. Now we obtain an amount of power in LOFAR profile that was consistent with the WSRT one, with no change of the spectral shape in the multipoles' range of interest (i.e. $\ell \lesssim 1300$). However, the beam is about three times worse and more diffuse emission is recovered, thus implying a less accurate source subtraction step with PyBDSM. Because of the higher rms confusion noise, a lower maximum ℓ value characterizing the power law is obtained and we decided to use the uniform weighting scheme.

3.4 Turbulence of the diffuse Galactic foreground

In the following, we use power spectra fluctuations to constrain the outer scale of turbulence (L_{out}) of the Galactic synchrotron foreground (Sec. 3.4.1). In Sec. 3.4.2, we use

this information to deduce the ratio of the regular to random field strength (B_o/B_r) as a function of L_{out} .

3.4.1 The outer scale of fluctuations

Magnetic turbulence in the Galactic disk and the halo dictates the power spectral behaviour of synchrotron intensity. Based on earlier results of Lazarian & Shutenkov (1990), Cho & Lazarian (2002) modelled the synchrotron emissivity in two different regimes: where the angle between the lines of sight is so small that they travel mostly through the same turbulent cells (i.e. $\theta < L_{out}/L_{max}$, with L_{max} being the path length to the farthest turbulent cells), and where the angle between the lines of sight is large, so that these lines of sight mostly probe independent cells. They conclude that on the small scales the synchrotron power spectrum should show the same (Kolmogorov) slope as the magnetic field power spectrum. On the large scales, however, the slope will be shallower and a function of the Galactic latitude. The latter effect occurs because at higher Galactic latitudes there will be more emissivity near the disk than further away in the halo. The scale at which the power spectrum transits from Kolmogorov to a shallower slope is the critical scale $\ell_{cr} \sim \pi L_{max}/L_{out}$.

For a characteristic scale height of the Galactic synchrotron emission of $H_{sync} = 1.0 \pm 0.4$ kpc (see e.g. Page et al. 2007), the path length L_{max} through the Galactic synchrotron layer is $L_{max} = H_{sync}/\sin b$, with b the Galactic latitude. At the latitude $b = +7^\circ$ of the Fan region, the distance up to the boundary of the probed volume is $L_{max} = 8.2 \pm 1.6$ kpc. This path length indicates an average emissivity of $\epsilon_{b=7^\circ} = 5.5 \pm 1.1$ K/kpc, in agreement with the synchrotron emissivity of ~ 7 K/kpc at 408 MHz in the solar neighborhood (Beuermann et al. 1985). The LOFAR power spectrum corresponds to the shallow (large angular scale) regime of the model by Cho & Lazarian (2002), which means that the critical multipole ℓ_{cr} is a multipole larger than the higher multipole of the power law before the spectrum flattens to noise. The higher multipole of the power law is $\ell \sim 1300 \pm 300$, indicating an outer scale of turbulence of $L_{out} \lesssim 20 \pm 6$ pc.

3.4.2 Constrain B_o/B_r from L_{out}

The importance of statistical investigations of the Galactic MHD turbulence and its properties has been recently exploited by Lazarian & Pogosyan (2012), providing an accurate and quantitative description of the synchrotron fluctuations for an arbitrary cosmic ray spectral index. However, because the artefacts affecting the accuracy of the data and the calculated power spectrum do not allow us to aim with such a precision, we adopt the earlier model of Eilek (1989a,b) with a fixed cosmic ray spectral index of about three. The effects of MHD turbulence in subsonic and transonic regimes on the total and polarized intensity of an extended radio source were explored by Eilek (1989a,b) under the assumptions that the characteristic outer scale (L_{out}) is much smaller than the source size (L_{max}) and the fluctuations obey a Gaussian statistics. This author shows how (strong) MHD turbulence produces detectable fluctuations in total intensity and how the mean ($\langle I \rangle$) and variance (σ_I) of the total intensity of an extended synchrotron source can be interpreted

in terms of the total intensity source function

$$S_I = S_0 \left(\frac{B_\perp}{B_o} \right)^{\frac{\gamma+1}{2}} \quad (3.4)$$

and its standard deviation σ_{S_I} , where B_\perp is the magnetic field component perpendicular to the line of sight, B_o is the ordered field component, and γ is the spectral index of the electron energy distribution $N(E) = N_0 E^{-\gamma}$. Then the fractional source-function variance $((\sigma_{S_I}^2)^{1/2}/S_I)$ is given by

$$\frac{(\sigma_{S_I}^2)^{1/2}}{S_I} \approx \sqrt{\frac{L_{max}}{L_{out}}} \frac{\sigma_I}{\langle I \rangle}, \quad (3.5)$$

(Eilek 1989a). Because variations of S_I reflect variations in the random magnetic field, the ratio of source-function variance and mean points to an estimate of the ratio of the random to ordered magnetic field strengths within the extended source. For subsonic turbulence, the fluctuations in synchrotron emission are likely predominantly caused by magnetic field fluctuations, with only slightly varying relativistic electron and positron densities, so that $(\sigma_{S_I}^2)^{1/2}/\langle S_I \rangle \approx B_r^2/(B_r^2 + B_o^2)$. However, for transonic turbulence, density fluctuations will also be important and the source function behaviour can be approximately represented as $S \propto B^4$ (Eilek 1989b), so that $(\sigma_{S_I}^2)^{1/2}/\langle S_I \rangle \approx B_r^4/(B_r^2 + B_o^2)^2$. A major dependence by density fluctuations is also expected for supersonic turbulence, but this case is not treated by Eilek (1989b).

We compute the ratio of random to ordered magnetic field B_o/B_r for our LOFAR data set using the prescriptions above. Since this is an interferometric measurement, short spacing information is missing and we cannot estimate $\langle I \rangle$ from our data. Instead, we obtain $\langle I \rangle$ from the absolute flux calibrated all-sky map at 408 MHz (Haslam et al. 1982): the Stokes I brightness temperature at 408 MHz is about $T_{408}^I = 45.0 \pm 4.5$ K around $(l, b) \approx (137.0^\circ, +7.0^\circ)$. The frequency dependence of the spectral index for the synchrotron brightness temperature has been investigated by several authors, e.g. de Oliveira-Costa et al. (2008) and recently Kogut (2012). For a spectral index of $\beta = -2.64 \pm 0.03$ (Kogut 2012), the corresponding sky temperature at 150 MHz is $T_{150}^I = 632 \pm 32$ K. Next the isotropic extragalactic background component is subtracted. We scale the value of about 28 K at 178 MHz of Turtle et al. (1962) to 150 MHz, obtaining a contribution of about 45 K. Therefore the final sky temperature at 150 MHz is $T_{150}^I = 587 \pm 30$ K, which is in agreement with the sky temperature of about 600 K around $(l, b) \approx (137.0^\circ, +7.0^\circ)$ of the Landecker & Wielebinski (1970) survey at 150 MHz (Reich priv. comm.). From the residual map after source subtraction, we estimate the Stokes I variance from the FWHM to be about 2.9 mJy beam $^{-1}$, which corresponds to about 22 K. Suitably scaled at 150 MHz, this value corresponds to a Stokes I variance of 25 K.

Observational studies of turbulence in the warm ionised medium indicate a transonic (Hill et al. 2008, Gaensler et al. 2011, Burkhart et al. 2012) regime. Rewriting Eq. 3.5 for the transonic case gives

$$\frac{B_o}{B_r} = (A^{1/2} - 1)^{1/2} \quad \text{where} \quad A = \frac{\langle I \rangle}{\sigma_I} \left(\frac{L_{out}}{L_{max}} \right)^{1/2} \quad (3.6)$$

For a turbulent outer cell size $L_{out} \lesssim 20$ pc, the ratio of magnetic field strengths $B_o/B_r \gtrsim 0.3$.

3.5 Discussion

In the following we interpret the detected total power fluctuations as being due to turbulence in the magnetic field. However, we note the Fan region to be peculiar, characterised by a high polarization degree, whose origin is still debated, and implying that the regular component of the magnetic field is dominant over the turbulent one. Therefore the comparison of total power and polarisation is a major point to associate the Stokes I fluctuations with turbulence in the magnetic field. A simple explanation is obtained by considering the different spatial depths probed by the low-frequency Stokes I and PI emission. At low frequencies, polarisation data are constrained by the polarization horizon ($d_h \lesssim 1$ kpc), while the total power data can probe a larger volume and the Stokes I fluctuations may probe different conditions along the line of sight. The polarised emission would originate in a nearby volume with a dominant ordered field, in agreement with the model of Wilkinson & Smith (1974), while the total power fluctuations would arise in a farther and disordered region.

Many theoretical and numerical simulation results suggest the MHD turbulence in the ISM to be Alfvénic, with an angular power spectrum matching the Kolmogorov one (i.e. a spectral index $\alpha_K \approx -3.7$). Observational results from investigations of H α emission (see e.g. Chepurnov & Lazarian 2010) support the Kolmogorov spectrum for the electron density fluctuations, in agreement with a weakly compressible and low Mach number turbulence. However, spectral indices steeper than α_K are inferred from the velocity fluctuations in the neutral cold phase of the ISM (Chepurnov et al. 2010), indicating a high Mach number turbulence. The analysis of synchrotron fluctuations deals with magnetic fluctuations, and previous studies of the angular power spectrum of the Galactic radio diffuse synchrotron emission (see e.g. Giardino et al. 2001, La Porta et al. 2008) have shown it can be fitted by a power law, $C_l \propto l^\alpha$, with $\alpha \sim [-3.0, -2.5]$ and $l \lesssim 200$. Moreover, strong local variations in the index exist. However, the lower values of α typically correspond to the higher latitudes in both total intensity and polarized intensity (Haverkorn et al. 2003a), indicating a latitude dependence of Galactic turbulence. Indeed, over the range $100 \lesssim \ell \lesssim 800$ Baccigalupi et al. (2001) find that regions at low and medium Galactic latitudes show total intensity fluctuations with slopes displaying large variations (from ≈ -0.8 to ≈ -2), and steeper slopes corresponding to regions where diffuse emission dominates. The synchrotron spectral index ($\alpha \approx -1.84$) that we find in the Fan region is smaller than the sky-averaged spectral index of about -2.4 (Giardino et al. 2001) but consistent with the range of slopes found by Baccigalupi et al. (2001). The origin of such spatial variations of the angular power spectral features of the Galactic diffuse emission was addressed by Cho & Lazarian (2002, 2010) in the framework of MHD turbulence with a Kolmogorov spectrum, as a result of the inhomogeneous distribution of synchrotron emissivity along the line of sight arising from the structure of the Galactic

disk and the halo. We note that the aforementioned framework is consistent with the Goldreich & Sridhar (1995) theory of Alfvénic turbulence for both a weakly compressible and a supersonic compressible (Cho & Lazarian 2003) medium because a Kolmogorov spectrum is also predicted by the Goldreich & Sridhar (1995) model of turbulence. To our knowledge, earlier angular power spectra of the Galactic radio diffuse synchrotron fluctuations at sub-degree angular scales and at a frequency of 150 MHz are only provided by Bernardi et al. (2009), Bernardi et al. (2010), and Ghosh et al. (2012), obtained with the WSRT and Giant Metrewave Radio Telescope (GMRT) respectively. The LOFAR and WSRT (Bernardi et al. 2009) studies both discuss the Fan region at low Galactic latitude $b \approx +7.0^\circ$, while Ghosh et al. (2012) focused on two sky patches at Galactic latitudes of $b \approx +25^\circ$ and $b \approx +30^\circ$ respectively. However, due to baselines corruptions the quality of the power spectra is not as good as for the Fan region field at lower Galactic latitude. Because the power law behaviour is not well sampled, we decide to not use these WSRT data for our analysis. Ghosh et al. (2012) discuss four fields of view in their paper, but only their FIELD I at $(l, b) = (151.80^\circ, 13.89^\circ)$ was used for foreground analysis because it provided the best sensitivity and point source subtraction. At $b = +7^\circ$ and $b = +14^\circ$, the distances up to the boundary of the Galactic synchrotron disk as defined above are $L_{max} = 8.2 \pm 1.6$ kpc and $L_{max} = 4.1 \pm 0.8$ kpc respectively. These path lengths indicate an average emissivity of $\epsilon_{b=7^\circ} = 5.5 \pm 1.1$ K/kpc and $\epsilon_{b=14^\circ} = 9.7 \pm 2.0$ K/kpc, which match with the synchrotron emissivity of ~ 7 K/kpc at 408 MHz and at the solar position (Beuermann et al. 1985).

The WSRT power spectrum by Bernardi et al. (2009) does not show any break up to $\ell = 900$; therefore $\ell_{cr} > 900$ and $L_{out} \lesssim 29 \pm 6$ pc. Ghosh et al. (2012) derived an angular power spectrum in the GMRT field that does not show any break up to $\ell = 800$, thus implying $L_{out} \lesssim 16 \pm 3$ pc. We summarize the upper limits for L_{out} derived from the available data in Tab. 3.3.

These upper limits are consistent with previous measurements of the outer scale in the Galaxy, as summarised in Fig. 3.10 and discussed in the Introduction. In particular, the earlier lower limit for L_{out} of Wilkinson & Smith (1974) allows the cell size towards the Fan region to be constrained in the range $\sim 5 - 20$ pc. While this range of values for L_{out} is inconsistent with the large outer scales found in the Galactic interarms or halo (see e.g. Chepurnov et al. 2010) and with the small ($L_{out} \lesssim 1$ pc) outer scale reported by Malkov et al. (2010), it agrees with the estimate for the spiral arm regions of Haverkorn et al. (2008). This suggests that turbulent fluctuations in the spiral arms dominate the gas density and magnetic field strength along these lines of sight. If so, for a nearest distance to the Perseus arm of 1.95 ± 0.04 kpc (Xu et al. 2006), this could indicate that spiral arms would extend at least up to 320 pc from the Galactic disk for the Fan region field or even up to 540 pc for the Ghosh field (Fig. 3.11). Actually, the complete high-polarisation Fan region stretches out over $(l, b) \approx (90^\circ - 190^\circ, -5^\circ - 25^\circ)$ and therefore also encompasses the Ghosh field. Indeed, Wolleben et al. (2006) argue from depolarisation arguments that the Fan region has to extend over a range of distances out to the Perseus arm. As concerns the disagreement with the small ($L_{out} \lesssim 1$ pc) outer scale reported by Malkov et al. (2010), we note that the lower limit of Wilkinson & Smith (1974) varies with the assumed total path length. These authors derived the 5 pc lower limits assuming a total path of 500 pc,

Table 3.3 – Summary of upper limits for L_{out} and B_o/B_r obtained from available data at 150 MHz.

Reference	Telescope	(l, b) coordinates	L_{max} [kpc]	ℓ_{cr}	L_{out} [pc]	$\langle l \rangle$ [K]	σ_l [K]	B_o/B_r
This paper	LOFAR	137.00°, 7.00°	8.2 ± 1.6	> 1300	$< 20 \pm 6$	587 ± 30	> 25	> 0.28
Bernardi et al. (2009)	WSRT	137.00°, 7.00°	8.2 ± 1.6	> 1000	$< 29 \pm 6$	587 ± 30	> 30.5	> 0.26
Ghosh et al. (2012)	GMRT	151.80°, 13.89°	4.1 ± 0.8	> 800	$< 16 \pm 3$	516 ± 26	> 20	> 0.51

but lower values are obtained when a deeper origin for the polarised emission (Wolleben et al. 2006) is considered, thus mitigating the disagreement.

Furthermore, we compare our estimates of the outer scale of magnetic turbulence in the Galaxy to the case of the nearby spiral galaxies M 51 and NGC 6946. As noted above, turbulent fluctuations in the spiral arms dominate in our Galaxy and turbulent (and compressed) magnetic fields also play a major role in M 51, as shown by Fletcher et al. (2011) and Houde et al. (2013). However, they find a typical size of 50 pc for the turbulent cells in the magneto-ionic medium of M 51, about a factor 2 larger than our upper limits towards the outer Galactic spiral arm regions. Such a factor might result from several reasons: a statistical effect because of the averaging over a different sample of probed regions (most of the halo of M 51 and only three fields for the Galaxy disk), the uncertainties (and assumptions) involved in the estimates and different turbulent parameters in the ISM of the Milky Way and M 51. The uncertainties involved in the estimates are relevant only for the estimate of Fletcher et al. (2011); thus a difference between the turbulence scale in the Milky Way and in M 51 may indeed be the major contributor. Finally we consider the case of the galaxy NGC 6946, for which a turbulent scale of about 20 ± 10 pc was estimated by Beck et al. (1999), which is in good agreement with the result of this paper.

We compute the ratio of random to ordered magnetic fields for the WSRT and GMRT data following the procedure above, where the relevant parameters are given in Table 3.3. The GMRT data claim a tentative $\sim 5\sigma$ detection of diffuse Galactic foreground at a resolution of $10'$ and a $\sim 10\sigma$ detection at a resolution of $16'$. We use the latter value of 20 K as a rough approximation of σ_I in this field. The numbers quoted for Stokes I fluctuations are lower limits, since there may be additional fluctuations on scales larger than the ones probed in these studies. However, this will contribute only to more stringent upper limits to the magnetic field ratio.

The resulting ratios of magnetic field components are consistent with earlier estimates in the literature: starlight and synchrotron polarisation data constrain the ratio of regular to turbulent field strengths to $\sim 0.6 - 0.9$ (Beck 2001, Fosalba et al. 2001), and rotation measures of distant pulsars give an even smaller value ~ 0.3 (Ohno & Shibata 1993). The lower limits indicate that the actual ordered magnetic field component may be even larger, which is not unexpected in the extended Fan region. Due to the extremely high degree of polarization in this region, the regular magnetic field component is believed to dominate over the turbulent component in this field (Haverkorn et al. 2003b, Wolleben et al. 2006). This would account for the deviating ratios of regular to random magnetic field.

In addition, the structure of the Galactic magnetic field affects the motion of CRs across it. The CR electrons are most efficiently scattered and diffused if their gyro radii $r_g(E) \simeq 1 pc (E_{PeV}/Z) \times B_{\mu G}^{-1}$ are similar to the outer scale of magnetic turbulence. For the range of L_{out} values we present in this paper and a total magnetic field strength of $5 \mu G$, CR protons with an energy of 65-130 PeV, which is slightly above the “knee”, are most efficiently scattered. This is consistent with the idea that the transition from Galactic to extragalactic CRs starts at the “knee”.

Another consequence of a small outer scale of turbulence in this direction is the possibility of observing anisotropies in gamma-ray flux around young CR sources. Giacinti et al. (2012b) describe that young CR sources should emit CRs anisotropically close to the

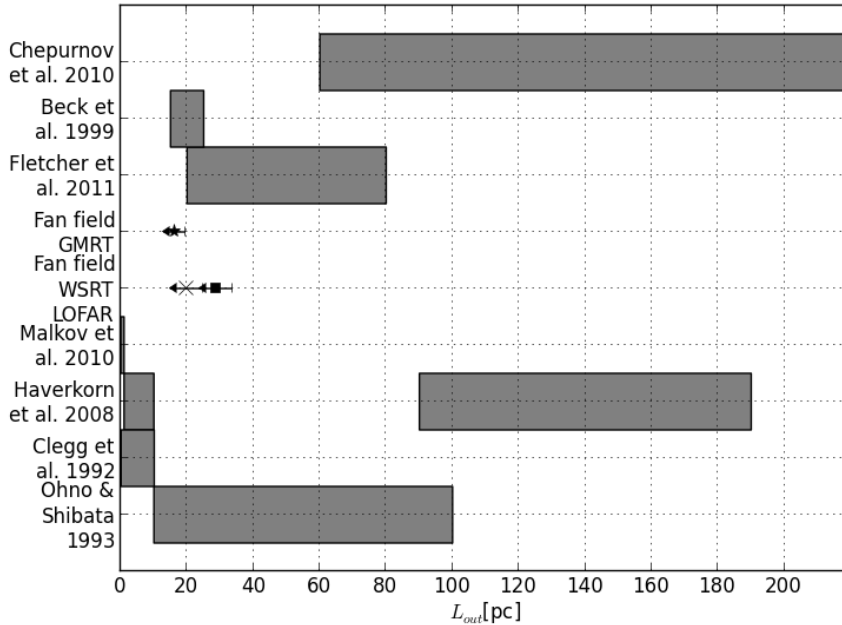


Figure 3.10 – Comparison of the LOFAR, WSRT (Bernardi et al. 2009), and GMRT (Ghosh et al. 2012) estimates of the outer scale of turbulence of the Galaxy towards the second Galactic quadrant with earlier observations from Ohno & Shibata (1993), Clegg et al. (1992), Haverkorn et al. (2008), Malkov et al. (2010), and Chepurinov et al. (2010). The turbulence scale derived by Fletcher et al. (2011) and Beck et al. (1999) for the nearby spiral galaxies M 51 and NGC 6946 respectively are also shown.

source, up to distances comparable to the outer scale of the turbulent Galactic magnetic field. This should be visible in the gamma-ray flux. For a turbulent outer scale of about 20 pc, this means that these anisotropies would only be visible if the source was located at distances smaller than this, which is very unlikely.

3.6 Summary & Conclusions

In the framework of the commissioning activities to characterise the LOFAR performance, we present results from a LOFAR HBA observation of a field in the Fan region centred at $(l, b) = (137^\circ, +7^\circ)$, between 110 and 174 MHz, using currently available LOFAR data processing software. We show in this paper that fluctuations in the diffuse synchrotron emission can be used to characterise turbulence scales and magnetic field strengths in the ISM. LOFAR is a breakthrough instrument for this work due to its low frequencies

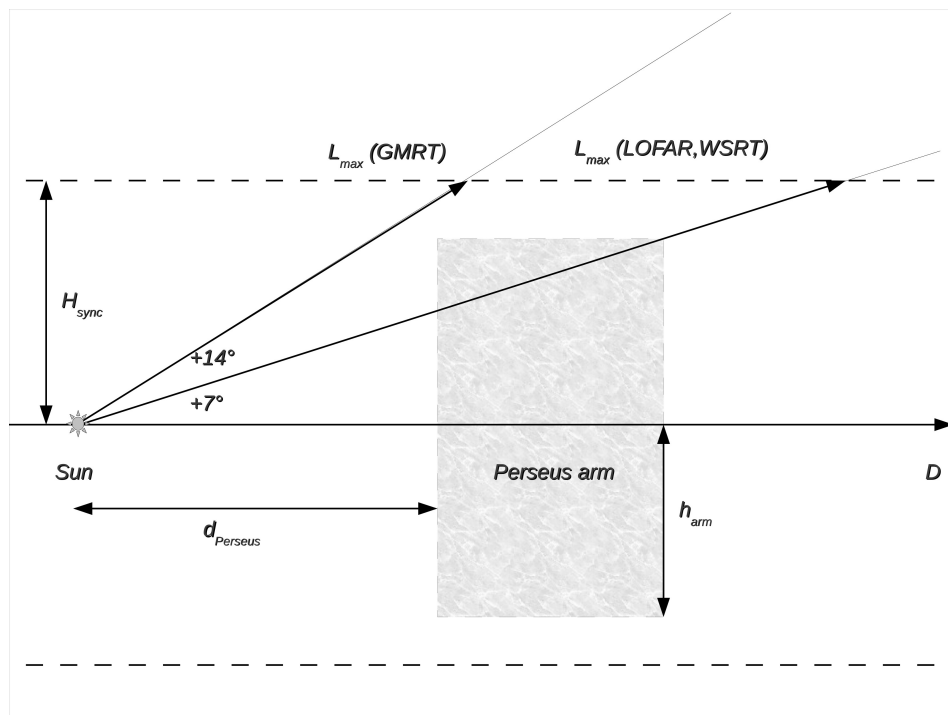


Figure 3.11 – Sketch of the projected spatial configuration for the lines of sight probed by the GMRT, LOFAR, and WSRT observations as a function of distance and Galactic latitude. The Galactic synchrotron scale height (H_{sync}) and the Perseus arm scale height (h_{arm}) are also shown.

(providing high sensitivity for synchrotron emission) and good uv -coverage for imaging extended emission. Summarizing the process:

1. For the first time we detect and image Galactic diffuse synchrotron emission with LOFAR in total intensity, at an angular resolution of about $1'$ and in a wide frequency range around 160 MHz.
2. Data of the target field were carefully calibrated and imaged, and we find faint and complex spatial morphology from the highly polarised Fan region in agreement with the detection by Bernardi et al. (2009) using the WSRT.
3. Comparing the LOFAR data of the Fan field to the WSRT data, we find the total intensity angular power spectrum of LOFAR in agreement with that of WSRT. Due to the higher resolution of LOFAR, we characterise for the first time the statistical properties of the foreground synchrotron fluctuations as a function of the

angular multipole up to $l \sim 1300$. The power spectrum of the synchrotron diffuse foreground is approximately a power law up to angular multipoles $\lesssim 1300$, corresponding to an angular scale of about $8'$. The slope we find is in agreement with the one reported by Bernardi et al. (2009) within 2 sigma.

4. We estimate the outer scale (L_{out}) of ISM magnetic turbulence from theoretical arguments that a break in the power spectrum should be observed at a certain critical scale (Cho & Lazarian 2002). We find a range of plausible values in the LOFAR and WSRT data sets and in a third low-frequency field with diffuse synchrotron fluctuations observed with the GMRT of 16 – 29 pc. This value is in agreement with previous estimates of outer scales of turbulence in spiral arms, although it is a factor of a few too small to be consistent with outer scale values in the Galactic halo or interarm regions. This suggests that towards the Fan region observed fluctuations are at least in part due to synchrotron emission in the Perseus arm.
5. We constrain the ratio for the magnetic field components B_o/B_r from theoretical estimates of allowed magnetic field strength ratios based on the relative strength of the synchrotron fluctuations with respect to the mean total intensity (Eilek 1989a,b). Lower limits of the ratio of random to ordered magnetic field strength are found to be 0.3, 0.3, and 0.5 for the three fields considered. These are consistent with magnetic field ratios at other places in the ISM and may indicate a higher than average ordered magnetic field in the Fan region.

Even though the presented LOFAR observations only show a moderate improvement in both resolution and sensitivity over existing WSRT data, they do reveal for the first time the feasibility of imaging interstellar turbulence with LOFAR through fluctuations in synchrotron emission. Furthermore, we prove the usefulness of theoretical estimates of characteristics of interstellar turbulence as applied to these data.

We present indications of a limited accuracy in the flux recovering in the field. This may indicate either that the current LOFAR calibration procedures for complex fields like this one, with extended and point source emission, could not yet be sufficiently accurate for precise flux calibration or a limited instrumental performance at station level at the time of the observation. We expect that the ongoing technical improvements of the array stations will largely increase sensitivity and decrease artifacts. Moreover, a better accuracy of the recovering of source fluxes may also be achieved by adopting a different observing strategy (e.g. using a multi-beam observing mode).

Future sensitive and high-resolution LOFAR observations in a mosaic mode will allow a wider portion of the Galaxy to be covered in order to check the spatial dependence of synchrotron fluctuations and the related variation of the turbulent cell size L_{out} . Furthermore, mapping the angular power spectrum of synchrotron fluctuations will benefit understanding of the Galactic magnetic field structure, its relation to the turbulence, and the transport of the CR across the magnetised and turbulent ISM.

Acknowledgments The authors wish to thank M. Brentjens for his help with the power spectral analysis of LOFAR data analysis. Chiara Ferrari and Giulia Macario acknowledge financial support by the “*Agence Nationale de la Recherche*” through grant ANR-09-JCJC-0001-01. LOFAR, the LOw Frequency ARray designed and constructed by AS-TRON, has facilities in several countries, which are owned by various parties (each with their own funding sources), and are collectively operated by the International LOFAR Telescope (ILT) foundation under a joint scientific policy. The research leading to these results has received funding from the European Union’s Seventh Framework Programme (FP7/2007-2013) under grant agreement number 239490. This work is part of the research programme 639.042.915, which is (partly) financed by the Netherlands Organisation for Scientific Research (NWO). This research has made use of the SIMBAD database, operated at CDS, Strasbourg, France.

Contributions E.O., R.F.P., M.H. and M.I. contributed to observation planning. E.O., R.F.P. and M.I. contributed to data analysis. M.I. and M.H. performed the discussion and interpretation of the results. M.I. led the writing of the paper. All other authors have made various contributions to development and construction of the LOFAR telescope.

Bibliography

- Baccigalupi C., Burigana C., Perrotta F., De Zotti G., La Porta L., Maino D., Maris M., Paladini R. 2001, *A&A*, 372, 8
- Battaner E., Castellano J. and Masip M. 2009, *ApJ*, 703, 90
- Beck R., Berkhuijsen E.M. and Uyaniker, B. 1999, in *Plasma Turbulence and Energetic Particles in Astrophysics*, eds. M. Otrowski and R. Schlickeiser (Kraków: Obs. Astron. Univ. Jagiellonski), 5
- Beck R. 2001, *Space Sci. Rev.*, 99, 243
- Bernardi G., de Bruyn A.G., Brentjens M.A., et al. 2009, *A&A*, 500, 965
- Bernardi G., de Bruyn A.G., Harker G., et al. 2010, *A&A*, 522, 67
- Beuermann K., Kanbach G. and Berkhuijsen E.M. 1985, *A&A*, 153, 17
- Bingham, R.G., & Shakeshaft, J.R. 1967, *MNRAS*, 136, 347
- Brown S. 2011, *JApA* 32, 577
- Burkhart B., Lazarian A., Gaensler B.M. 2012, *ApJ*, 749, 145
- Carretti E., Haverkorn M., McConnell D., Bernardi G., Cortiglioni S., McClure-Griffiths N.M., Poppi S. 2009, *Rev. Mexicana Astron. Astrofis.*, 36, 9
- Chepurnov A., Lazarian A., Staminirović S., Heiles C., & Peek, J.E.G. 2010, *ApJ*, 714, 1398
- Chepurnov A., Lazarian A. 2010, *ApJ*, 710, 853
- Cho J., Lazarian A. 2002, *ApJ*, 575, 63
- Cho J. & Lazarian A. 2003, *MNRAS*, 345, 325
- Cho J., Lazarian A. 2010, *ApJ*, 720, 1181
- Clegg, A.W., Cordes, J.M., Simonetti, J.M., & Kulkarni, S.R. 1992, *ApJ*, 386, 143
- Cornwell T.J., Golap K. & Bhatnagar S. 2005, *ASP Conf. Ser.* 347, 86
- Cornwell T.J., Golap K. & Bhatnagar S. 2008, *IEEE J. Selected Topics in Signal Processing* 2, 647
- de Oliveira-Costa A., Tegmark M., Gaensler B. M., Jonas J., Landecker T. L., Reich P. 2008, *MNRAS*, 388, 247
- Eilek J.A., *AJ*, 98, 244 (Paper a)
- Eilek J.A., *AJ*, 98, 256 (Paper b)
- Elmegreen B.G. & Scalo J. 2004, *ARA&A*, 42, 211
- Fosalba P., Lazarian A., Prunet S. & Tauber J.A. 2001, *ApJ*, 564, 762
- Fletcher A., Beck R., Shukurov A., Berkhuijsen E.M., Horellou C. 2011, *MNRAS*, 412, 2396
- Gaensler B.M., Haverkorn M., Burkhart B., et al. 2011, *Nature*, 478, 214
- Giacinti G. & Sigl G. 2012, *PhRvL* 109, 1101 (Paper a)
- Giacinti G., Kachelrieß M., Semikoz D.V. 2012, *PhRvL* 108, 1101 (Paper b)9cm
- Giardino G., Banday A.J., Fosalba P., Górski K.M., Jonas J.L., O'Mullane W., Tauber J. 2001, *A&A*, 371, 708
- Ghosh A., Prasad J., Bharadwaj S., Ali S.S., Chengalur J.N. 2012, *MNRAS*, 426, 3295
- Goldreich P. & Sridhar S. 1995, *ApJ*, 438, 763
- Haslam C.G.T., Salter C.J., Stoffel H. & Wilson W.E. 1982, *A&A*, S 47, 1

- Haverkorn M., Brown J.C., Gaensler B.M. and McClure-Griffiths N.M. 2008, *ApJ*, 680, 362
- Haverkorn, M., Katgert, P., & de Bruyn, A.G. 2003, *A&A*, 403, 1045, Paper a
- Haverkorn, M., Katgert, P., & de Bruyn, A.G. 2003, *A&A*, 404, 233, Paper b
- Hamaker J.P., Bregman J.D. & Sault R.J. 1996, *A&AS*, 117, 137
- Heald G., McKean J., Pizzo R., van Diepen G., van Zwieten J.E., et al. 2010, *PoS(ISKAF2010)*, 57
- Heald G., Bell M.R., Horneffer A. et al. 2011, *JApA* 32, 589
- Hill, A.S., Benjamin, R.A., Kowal, G., et al. 2008, *ApJ*, 686, 363
- Houde M., Fletcher A., Beck R., Hildebrand R.H., Vaillancourt J.E., Stil J.M. 2013, *ApJ*, 766, 49
- Iacobelli M., Haverkorn M. and Katgert P. 2013, *A&A*, 549, 56
- Junklewitz H. and Enßlin T. A. 2011, *A&A*, 530, 88
- Kogut A. 2012, *ApJ*, 753, 110
- Landecker T.L. & Wielebinski R. 1970, *Austr. J. Phys. Supp.*, 16, 1
- Lazarian A. and Pogosyan D. 2012, *ApJ*, 747, 5
- Lazarian A. & Shutenkov V.P. 1990, *PAZh*, 16, 690 (translated *Sov. Astron. Lett.*, 16, 297)
- La Porta L., Burigana C., Reich W., Reich P. 2008, *A&A*, 479, 641
- Kazemi S., Yatawatta S., Zaroubi S., et al. 2011, *MNRAS*, 414, 1656
- Mac Low M.-M. 2004, *Ap&SS*, 289, 323
- Malkov M.A., Diamond P.H., Drury L., and Sagdeev R. Z. 2010, *ApJ*, 721, 750
- Nota T. & Katgert P. 2010, *A&A*, 513, 65
- Offringa A.R., de Bruyn A.G., Biehl M., Zaroubi S., Bernardi G. & Pandey V.N. 2010, *MNRAS*, 405, 155
- Offringa A.R., van de Gronde J.J. & Roerdink J.B.T.M. 2012, *A&A*, 539, A95
- Ohno H. & Shibata S. 1993, *MNRAS*, 262, 953
- Page L., Hinshaw G., Komatsu E., et al. 2007, *ApJS*, 170, 335
- Pandey V.N., van Zwieten J.E., de Bruyn A.G., Nijboer R. 2009, *ASPC* 407, 384
- Pizzo R.F. et al. 2010, "The Lofar Imaging Cookbook", internal ASTRON report
- Regis M. 2011, *Aph* 35, 170
- Scalo J. & Elmegreen B.G. 2004, *ARA&A*, 42, 275
- Seljak U. 1997, *ApJ*, 482, 6
- Sotomayor-Beltran C., Sobey C., Hessels J.W.T., de Bruyn G. et al. 2013, *A&A*, 552, 58
- Stepanov R. Shukurov A., Fletcher A., Beck R., La Porta L., Tabatabaei F.S. 2012, *arXiv* 1205.0578S
- Tasse C., van der Tol S., van Zwieten J., van Diepen G., Bhatnagar S. 2013, *A&A*, 553, 105
- Tegmark M. 1997, *PRD* 56, 8
- Turtle A.J., Pugh J.F., Kenderdine S., Pauliny-Toth I.I.K. 1962, *MNRAS*, 124, 297
- Verschuur, G. L. 1968, *The Observatory*, 88, 15
- Waelkens A. H., Schekochihin A. A. and Enßlin T. A. 2009, *MNRAS*, 398, 1970
- Wieringa M.H., de Bruyn A.G., Jansen D., Brouw W.N. and Katgert P. 1993, *A&A*, 268, 215
- Wilkinson A., Smith F.G. 1974 *MNRAS*, 167, 593
- Wolleben, M., Landecker, T. L., Reich, W., & Wielebinski, R. 2006, *A&A*, 448, 411
- Xu, Y., Reid, M.J., Zheng, X.W., & Menten, K.M. 2006, *Science*, 311, 54

Galactic interstellar turbulence in the southern sky seen through spatial gradients of the polarization vector

Interstellar turbulence in the southern sky

M. Iacobelli, B. Burkhart, M. Haverkorn, A. Lazarian, E. Carretti, L. Staveley-Smith,
B.M. Gaensler, G. Bernardi, M.J. Kesteven, S. Poppi

submitted to A&A

Abstract

Aims. Radio synchrotron polarization maps of the Galaxy can be used to infer the properties of interstellar turbulence in the diffuse warm ionized medium (WIM). In this paper, we investigate the spatial gradient of linearly polarized synchrotron emission ($|\nabla\mathbf{P}|/|\mathbf{P}|$) as a tracer of turbulence, the relationship of the gradient to the sonic Mach number of the WIM, and changes in morphology of the gradient as a function of Galactic position in the southern sky.

Methods. We use data from the S-band Polarization All Sky Survey (S-PASS) to image the spatial gradient of the linearly polarized synchrotron emission ($|\nabla\mathbf{P}|/|\mathbf{P}|$) of the entire southern sky at 2.3 GHz. The spatial gradient of linear polarization reveals rapid changes of the density and magnetic fluctuations in the WIM due to magnetic turbulence as a function of Galactic position; we make comparisons of these data to ideal MHD numerical simulations. In order to constrain the sonic Mach number (M_s), we apply a high order moments analysis to the observations and to the simulated diffuse, isothermal ISM with ideal magneto-hydrodynamic turbulence.

Results. We find that polarization gradient maps reveal elongated structures, which we associate with turbulence in the ISM. Our analysis corroborates the view of a turbulent WIM in a transonic regime $M_s \lesssim 2$. Filamentary structures with typical widths down to the angular resolution are seen and the observed morphologies match closely with numerical simulations and in some cases H α contours. The $|\nabla\mathbf{P}|/|\mathbf{P}|$ intensity is found to be approximately log-normal distributed. No systematic variations of the sonic Mach number are observed as a function of Galactic coordinates, which is consistent with turbulence in the WIM inferred by the analysis of H α data. We conclude that the sonic Mach number of the diffuse WIM appears to be spatially uniform towards the Galactic plane and the Sagittarius-Carina arm, but local variations induced by nearby extended objects are also found.

4.1 Introduction

Galactic magnetic fields and matter (i.e. atoms, ions and molecules) spread between the stars constitute a complex dynamic plasma, the interstellar medium (ISM). The density and temperature of the particles and the magnitude of the fields are fundamental parameters which shape the structure of the interstellar environment and characterize its evolution. Earlier studies (for a review see e.g. Ferrière 2001, Cox 2005) have pointed out the presence of magnetohydrodynamic (MHD) turbulence in the ISM, which is responsible for the distribution and the dissipation of energy through a wide range of spatial scales. MHD turbulence plays an essential role for many key interstellar processes (for a review see e.g. Elmegreen & Scalo 2004), including star formation (see McKee & Ostriker 2007), cosmic ray propagation (see Schlickeiser 2011, Lazarian et al. 2011) and magnetic reconnection (see Lazarian & Vishniac 1999). Additionally, astrophysical MHD turbulence is an integral part of the dynamics of the Galaxy, providing a significant pressure (and energy density) to support the diffuse ISM (Boulares & Cox 1990). Many efforts have

been made over the past decades to characterize magnetic fields and turbulence in the ISM as well as their mutual dependence (see review by Burkhart & Lazarian 2012a). The presence of a turbulent cascade in the ISM was obtained by tracing density variations in the warm ionized medium (Armstrong et al. 1995, Chepurnov & Lazarian 2010). However MHD turbulence is traced in the different phases of the ISM by several typical signatures, such as density, velocity (Pogosyan & Lazarian 2009, Chepurnov et al. 2010) and synchrotron intensity (Lazarian & Pogosyan 2012, Iacobelli et al. 2013) variations. Because observations of astrophysical MHD turbulence and magnetic fields are challenging, the fundamental parameters of ISM turbulence such as the sonic and Alfvénic Mach numbers, the magnetic field structure and strength, the Prandtl and Reynolds numbers and the physical scale of energy injection are still poorly constrained. Therefore observational studies of MHD turbulence in the ISM, combined with analytic predictions and numerical simulations, are essential. Radio observations are a fundamental tool to gain insights about magnetic fields, density of the ionized gas and their turbulent fluctuations. In particular, radio polarization maps constitute a useful diagnostic to study turbulence and magnetic fields in the diffuse, ionized ISM (see e.g. Wieringa et al. 1993, Gaensler et al. 2001, Haverkorn et al. 2004a,b, Schnitzeler et al. 2007). Surveys covering a large part of the sky add information on spatial dependence of these fields as well. Previous surveys of the southern sky are affected by several limitations such as incomplete sky coverage (e.g. the survey at 2.4 GHz by Duncan et al. 1995, 1997), the absence of polarimetric data (e.g. the survey at 2.3 GHz by Jonas et al. 1985, 1998) as well as a limited resolution (e.g. the survey at 1.4 GHz by Testori et al. 2008). The S-band Polarization All Sky Survey (S-PASS) (Carretti et al. 2010) is a recent single-dish survey of the entire southern sky at 2.3 GHz which bypasses the aforementioned limitations, its main aim being to map the total intensity and polarized continuum emission with higher resolution and sensitivity and at higher frequency to reveal the polarised emission from the Galactic disc, otherwise depolarised up to 1.4 GHz. The use of the spatial gradient of the polarization vector to image the small-scale structure associated with ISM turbulence has been recently discovered by Gaensler et al. (2011) and exploited by Burkhart et al. (2012). They show how to map the magnetized turbulence in diffuse ionized gas from the gradient of the Stokes Q and U pseudo-vectors. In a 18 deg^2 patch of the Galactic plane, they find an intricate filamentary network of discontinuities in gas density and magnetic field. In agreement with Hill et al. (2008), these authors find turbulence in the warm ionized medium to be transonic, with a sonic Mach number $M_s \lesssim 2$ and therefore weakly compressible. These results were partially derived from the ability of statistical moments to characterize the sonic Mach numbers from spatial gradient maps of linear polarization by testing the sensitivity of statistical methods to different regimes of turbulence. Analyses of Gaensler et al. (2011) and Burkhart et al. (2012) find correlations between the spatial morphology, the higher order moments of the distribution of the spatial gradients of polarized emission and the sonic and Alfvénic Mach number.

In this paper we present the first mapping of different regimes of turbulence in the diffuse, ionized ISM over the entire southern sky by applying the statistical moments analysis to several regions. In particular, by comparing the analysis of high order moments in both simulations of MHD turbulence and observations we search for spatial variations of

Table 4.1 – Observational properties of S-PASS data.

System temperature	$T_{sys} = 20$ K
Reference frequency	$\nu = 2307$ MHz
Bandwidth	$\Delta\nu = 184$ MHz
Gridded beamwidth	$FWHM = 10.75'$
Stokes Q,U maps rms	$\sigma \gtrsim 1$ mJy beam ⁻¹
Gain (Jy/K) at 2307 MHz	1 mJy beam ⁻¹ = 0.55 mK

the sonic Mach number. Galactic coordinates are used throughout the following sections.

In Sect. 4.2 we present an overview of both the data and the gradient method. In Sect. 4.3 we present the spatial gradient map of the polarization vector displaying an extended network of filaments and in Sect. 4.4 different regimes of MHD turbulence in the ISM are characterized from the moment maps analysis. Finally, we discuss our results and present conclusions in Sect. 5.5.

4.2 Data overview

The S-band Polarization All Sky Survey (S-PASS) is a single dish polarimetric survey of the entire southern sky at 2.3 GHz, performed with the Parkes 64 m Radio Telescope and its S-band Galileo receiver, which is a circular polarization system suitable for Stokes Q and U measurements. S-PASS observational parameters are given in Table 5.1, while a description of S-PASS observations and analysis is given by Carretti et al. (2010) and Carretti et al. (2013, in preparation). In order to realize absolute polarization calibration of the data, an innovative observing strategy based on long scans along the horizon towards the east and west of the Parkes telescope was adopted. A system temperature of about 20 K was reached, with an improvement of a factor of 2 with respect to the previous continuum survey at the same frequency (see e.g. Duncan et al. 1997). Another main feature of the survey is its high angular resolution; due to a telescope beam width of 8.9', final maps were obtained with a beam of $FWHM = 10.75'$ with an improvement of about a factor of 4 with respect to a previous continuum all-sky survey at 1.4 GHz (see e.g. Reich 2001). The final maps of the Stokes parameters resulting from the S-PASS survey will be fully presented by Carretti et al. (2013, in preparation). In this paper we use the Stokes Q and U maps to image the spatial gradients of the linearly polarized emission for our analysis of ISM turbulence.

4.2.1 Radio polarization gradients

Variations in polarized intensity and polarization angles of radio synchrotron radiation are related to magnetic turbulence in the ISM. However both these quantities are not invariant to rotations and translations in the Q–U plane, e.g. due to Faraday rotation by a uniform foreground screen and incomplete interferometric sampling respectively, making their interpretation difficult. A new diagnostic to investigate the turbulent fluctuations in the ISM affecting the radio polarization measurements is the spatial gradient of the polarization vector (Gaensler et al. 2011).

The radio polarization gradient ($\nabla\mathbf{P}$) indicates the variation of the polarization vector (\mathbf{P}) as a function of position in the image plane. In addition, the spatial gradient of the polarization vector acts as a high-pass filter, allowing one to recover interesting features from a map with a strong DC offset (see e.g. Schnitzeler et al. 2009). To calculate the gradient of the polarization vector we follow Gaensler et al. (2011), determining the magnitude as:

$$|\nabla\mathbf{P}| = \sqrt{\left(\frac{\partial Q}{\partial x}\right)^2 + \left(\frac{\partial U}{\partial x}\right)^2 + \left(\frac{\partial Q}{\partial y}\right)^2 + \left(\frac{\partial U}{\partial y}\right)^2}. \quad (4.1)$$

Gradients in the polarization vector can be caused by fluctuations in different quantities, as detailed below.

1. fluctuations in Stokes I only. Even in the case of no Faraday rotation or depolarization, variations in Stokes I will cause variations in the polarized intensity ($|\mathbf{P}|$) and therefore a non-zero $|\nabla\mathbf{P}|$. In this case, $|\mathbf{P}| \propto I$ and $|\nabla\mathbf{P}| \propto \nabla I$. Maps of $|\nabla\mathbf{P}|$ will act as an edge detection algorithm for fluctuations in synchrotron emission.
2. fluctuations in polarization angle only. This is the case of a Faraday screen, which alters the direction of the polarization vector but not its amplitude. Then, $|\mathbf{P}| \propto I$, but $|\nabla\mathbf{P}|$ is not correlated with either $|\mathbf{P}|$ or Stokes I. In this case, $|\nabla\mathbf{P}|$ directly traces gradients in rotation measure (RM), and therefore turbulence in the magneto-ionic ISM. This situation can be divided into two special cases:

- (a) A Faraday screen in front of spatially constant synchrotron emission. In this case, both Stokes I and $|\mathbf{P}|$ are constant, but $|\nabla\mathbf{P}|$ is not constant. Then (Burkhart et al. 2012):

$$|\nabla RM| = \frac{|\nabla\mathbf{P}|}{2\lambda^2|\mathbf{P}|} \quad (4.2)$$

and the quantity $|\nabla\mathbf{P}|/|\mathbf{P}|$ should be used to track fluctuations in RM, i.e. to track magnetic turbulence. This is also the case in the simulations we use to compare to the data.

- (b) The Faraday screen emits thermal, unpolarized radiation, such as e.g. an H II region. In this case, some correlation between Stokes I and $|\nabla\mathbf{P}|$ may exist.
3. fluctuations in the polarized intensity and polarization angle, as caused by depolarization. In this case, equation 4.2 does not hold. Turbulence, as traced by $|\nabla RM|$, is

tracked by $|\nabla\mathbf{P}|$. This is the situation for which the polarization gradient method was originally created (Gaensler et al. 2011): RM fluctuations that cause depolarization canals are masked by foreground/background polarized emission, but the polarization gradient method makes these RM fluctuations visible even in the presence of a polarized emission foreground/background.

In the observations, gradients in the polarization vector will be caused by a combination of these three effects. In the following, we estimate the importance of each of these three effects by investigating correlations between Stokes I, polarized intensity $|\mathbf{P}|$ and polarization gradient $|\nabla\mathbf{P}|$. In fields where the Faraday screen approximation is reasonable, the normalized gradient map $|\nabla\mathbf{P}|/|\mathbf{P}|$ traces fluctuations in RM. However, in fields where this approximation does not hold, the unnormalized map $|\nabla\mathbf{P}|$ should be considered.

Both the magnitude of the polarization spatial gradient ($|\nabla\mathbf{P}|$) and of the polarization vector ($|\mathbf{P}|$) follow an asymmetric positive distribution, while the Stokes Q and U parameters follow Gaussian distributions. The positive definite distributions are signal-to-noise (S/N) dependent and are thus affected by a bias towards high values at low S/N (Vinokur 1965). Wardle & Kronberg (1974) suggested a widely used correction for the bias of a positive defined distribution $P(R)$ as:

$$R \sim R'_M \left[1 - \left(\frac{\sigma'}{R'_M} \right) \right]^{1/2}, \quad (4.3)$$

where R'_M is the measured magnitude, σ' the measured noise level and R the intrinsic magnitude of the signal vector. We confirmed the Gaussian behaviour of Stokes Q and U maps and determined a noise level of 1 mJy beam⁻¹ from a small region assumed to contain no emission from the sky. We also assumed uniformity of the noise across the entire field. Finally, we calculated the normalized gradient of the polarization vector and we discarded lines of sight where \mathbf{P} is at the level of the bias $|\mathbf{P}_R| = 1.25\sigma_{Q,U}$, resulting in a fraction of blanked pixels of about 1% in the final $|\nabla\mathbf{P}|/|\mathbf{P}|$ map.

In order to quantify the impact of the foreground Faraday rotation effects for these data, we look at the correspondence between total intensity and polarised intensity, by determining the degree of correlation between the Stokes I and the $|\mathbf{P}|$ maps. If the polarization signal is due to foreground Faraday rotation, little linear correlation between the fluctuations of $|\mathbf{P}|$ and Stokes I is expected. Thus, we adopt the Pearson correlation coefficient (ρ_p) and we consider the range of weak correlation to be $|\rho_p| \leq 0.35$ and we find a mild positive correlation $\rho_p = 0.38$, so the bulk of the $|\nabla\mathbf{P}|/|\mathbf{P}|$ fluctuations are not intrinsic to the sources of polarized emission and can be interpreted in the framework of MHD turbulence in the ionized ISM. In the following we will select regions of low correlation where the $|\nabla\mathbf{P}|/|\mathbf{P}|$ fluctuations can be interpreted in the framework of MHD turbulence.

4.3 Observational results

Fig. 4.1 shows the final de-biased $|\nabla\mathbf{P}|/|\mathbf{P}|$ sky map, clipped at 3σ for displaying purpose. The spatial gradient of the astrophysical polarized synchrotron emission of the diffuse

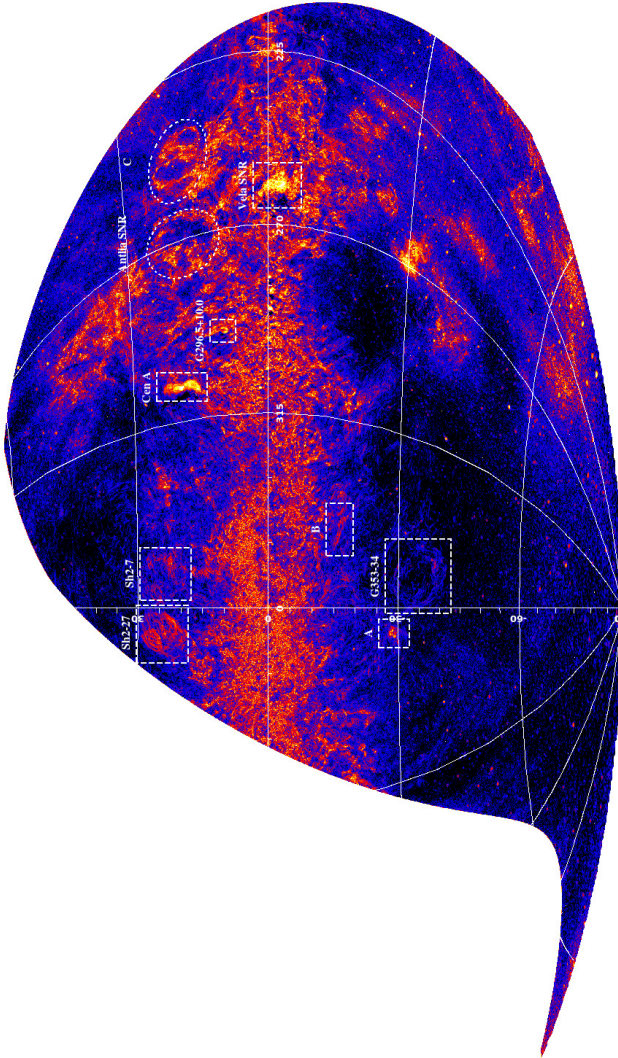


Figure 4.1 – The map of the normalized spatial gradient of linearly polarized emission in Aitoff projection of the entire southern sky at a reference frequency of 2.3 GHz and a resolution of $1''$. The noise level in the map was obtained by averaging intensity over a small region with no signal and intensity is clipped at 3σ . The scaling runs from 0.2 (black) to 1000 (white). Intensity unit is $\text{beam}^{-0.5}$.

Table 4.2 – List of unambiguously identified SNRs in all of Stokes I, polarized intensity and polarization gradient S-PASS maps, by cross-checking radio data taken from the Green (2009) database.

Name	Other names	Distance ^a [kpc]
G261.9+5.5		2.9
G263.9–3.3	Vela (XYZ)	0.29
G296.5+10.0	PKS 1209-51/52	2.1
G327.6+14.6	SN 1006	2.2

a) The listed distance values are taken from Milne (1970), Dodson et al. (2003), Giacani et al. (2000) and Ghavamian et al. (2002) respectively.

Galactic foreground is depicted in this image at 2.3 GHz, producing a wealth of structures. Faint artefacts are also present around the equatorial south-pole due to the scanning strategy. We now describe the main morphological features in the de-biased $|\nabla\mathbf{P}|/|\mathbf{P}|$ map.

First, there are spatially compact and isolated structures, corresponding to bright extragalactic synchrotron sources. Several hundreds of unresolved sources (mostly quasars and radio-galaxies) are detected smoothly distributed in the sky plane. Furthermore a polarized extragalactic source showing a striking extended morphology is also present and marked in Fig. 4.1, the bright radio galaxy Cen A, with a north-south extension of about 8° of its structured emitting lobes.

There are also isolated Galactic structures on a range of scales. Peaks in the normalized polarization gradient signal are seen throughout the Galactic plane up to Galactic latitudes of $|b| \approx 25^\circ$ corresponding to bright supernova remnants (SNRs) and nearby H II regions. While the brightness of the former is mainly due to their intrinsic polarization, the latter are traced out by Faraday rotation along the line of sight to the observer induced by their thermal electrons. Indeed nearby (distance ~ 200 pc) and extended H II regions are seen towards the inner Galaxy, such as Sh 2-27 around the O-class star ζ Ophiuchi (at $l \sim 8^\circ$, $b \sim 23^\circ$) and Sh 2-7 excited by the nearby star δ Sco (at $l \sim 350^\circ$, $b \sim 22^\circ$).

The outstanding characteristic is that most of the polarization gradients come from a network of filaments, forming clearly separated and extended regions well outside the Galactic plane. The typical width of these filamentary structures matches the angular resolution. Furthermore different morphological patterns of these filaments are seen. In Fig. 4.2 we show an example of the observed morphology for the normalized spatial gradients of polarized synchrotron emission, as a result of fluctuations in the ISM induced by different type of shocks (Burkhart et al. 2012). The panel depicts a complex region above the Galactic plane centred at $(l, b) \approx (278^\circ, +22^\circ)$ and displays filamentary struc-

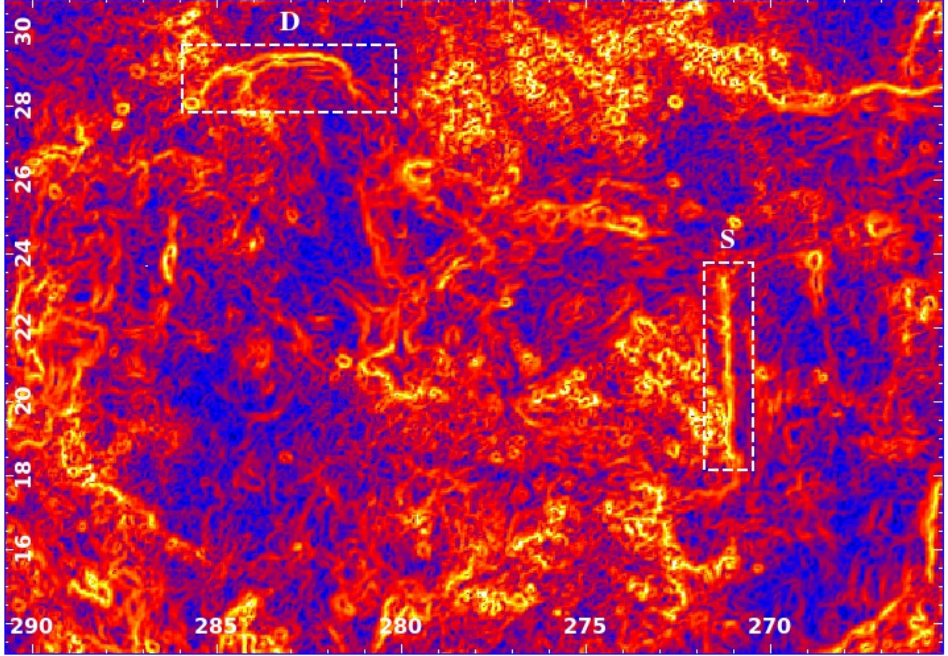


Figure 4.2 – *Different observed morphologies for different MHD turbulence cases* “double-jumps” (D boxed region) and “single-jump” (S boxed region) filaments due to strong and weak shocks, respectively. Intensity scale runs from 0.2 (black) to 2000 (white).

tures over a wide range of angular scales, up to about 6 degrees, with no correspondence to Stokes I. This extended pattern of filaments is due to the presence of discontinuities in the interstellar gas density and magnetic field. In particular, we note the presence of two evident structures which are also seen in MHD simulations (for a comparison see Fig. 4 of Burkhart et al. 2012) and are interpreted as due to different kinds of discontinuities in the warm, ionized ISM: a “double-jump” profile (box D) and a “single-jump” profile (box S), corresponding to the case of a strong and a weak shock along the line of sight, respectively. Moreover changes of the $|\nabla\mathbf{P}|/|\mathbf{P}|$ brightness along the filaments due to variations of the magnitude of turbulent fluctuations along the line of sight are recognized.

Complex large-scale structures (such as the nearby and shell-like G 353-34) are seen up to intermediate ($|b| \approx 40^\circ$) Galactic latitudes. A prominent arc-like feature is observed within the longitude range $270^\circ \lesssim l \lesssim 290^\circ$. The base of this magnetic structure is around $l = 270^\circ$ and it extends up as an arc from the Galactic plane up to about $(l, b) = (285^\circ, 45^\circ)$ with an overall length of $\sim 50^\circ$. Up to this point the structure is traced by the high polarization gradient intensity exhibiting a complex morphology: mostly filamentary at Galactic latitudes below 20° and mainly patchy, small-scale rich towards higher latitudes. High intensity values of radio polarization gradients are seen towards the 3rd Galactic quadrant at high and negative Galactic latitudes, forming a very extended and patchy

pattern up to $b = -70^\circ$ which is not spatially coincident with the nearby ($d \lesssim 500$ pc) region of higher interstellar polarization pointed out by Berdyugin et al. (2004).

4.3.1 The polarization horizon

In order to constrain the impact of depolarization, to perform a proper comparison of data with numerical simulations and to convert angular scales to spatial scales, we need to estimate the distance to which polarized emission is detected.

Such a spatial depth is referred to as the “polarization horizon” and has been used in previous works (see e.g. Duncan et al. 1997, Gaensler et al. 2001, Landecker et al. 2002, Uyaniker et al. 2003). This quantity is a function of the instrumental features (i.e. the beam size, the observing frequency) as well as of the physical conditions of the probed medium (causing an intrinsic degree of depolarization). The smaller the beam and/or the higher the observing frequency, the farther the polarization horizon; the brighter and/or more coherent is the synchrotron emission, the farther is the corresponding polarization horizon. Recently Carretti et al. (2013) derived an estimate of about 2 – 3 kpc for the “polarization horizon” of these S-PASS data, from the analysis of depolarized regions at low latitudes towards the inner Galaxy. However the polarization horizon depends on the viewing direction in the Milky Way and we consider the all-sky $|\nabla\mathbf{P}|/|\mathbf{P}|$ intensity, so we need to find estimates for the maximum spatial depth up to intermediate Galactic latitudes ($|b| \lesssim 30^\circ$) and towards the outer regions ($260^\circ \lesssim l \lesssim 330^\circ$). In order to estimate a lower limit for the polarization horizon we cross-check the radio catalogue¹ of Galactic supernova remnants (Green 2009) with detections in the Stokes I and $|\nabla\mathbf{P}|$ S-PASS maps and we consider SNRs with a minimum angular size matching the S-PASS angular resolution. We use the $|\nabla\mathbf{P}|$ map because for sources with a large intrinsic polarisation component it acts as an edge detection algorithm, making the source detection towards regions with strong diffuse emission easier. Also, we note that the non-detection of polarisation from a SNR may be due to internal depolarisation in the SNR itself, constituting a limitation of the adopted method. Thus we decide to not use non-detections to constrain the upper limit of the polarization horizon.

We find 4 SNRs satisfying our criteria (see Table 4.2) and suggest a lower limit for the polarization horizon of about 3 kpc away from the Galactic centre, which is in agreement with the above estimate of Carretti et al. (2013) and is used throughout the following sections. At this distance, the presence of radio polarization gradient features down to an angular resolution of $\sim 11'$ corresponds to a linear scale of < 10 pc for the filament widths, and therefore for the ISM fluctuations in the disk and the halo traced by these filaments. Note however that the earlier detection of $|\nabla\mathbf{P}|/|\mathbf{P}|$ filaments at arcmin resolution by Gaensler et al. (2011) implies a typical width of ≈ 1 pc, if a polarization horizon of about 3 kpc is assumed for their data.

¹ The catalogue is available at <http://www.mrao.cam.ac.uk/surveys/snrns/>

4.3.2 Galaxy-scale variations in $|\nabla\mathbf{P}|/|\mathbf{P}|$

The above lower limit of about 3 kpc for the polarization horizon constrains our data to probe the nearby, major large-scale Galactic features: the Local arm (Orion Spur) towards the outer region (i.e. $210^\circ \lesssim l \lesssim 280^\circ$) and the Carina-Sagittarius arm located at a distance of about 2 kpc (Georgelin et al. 2000) between the Centaurus-Scutum spiral arm (~ 3.5 kpc) and the Sun towards the 4th Galactic quadrant. Also some emission from the nearest side of the Centaurus-Scutum spiral arm towards the Galactic center and the Perseus arm towards the outer region (i.e. $l \lesssim 250^\circ$) cannot be excluded. Moreover out of the Galactic disk our estimate of about 3 kpc for the polarization horizon indicates a negligible amount of depolarization. Indeed, at Galactic latitudes $|b| \gtrsim 45^\circ$ this path length corresponds to a height $\gtrsim 2.1$ kpc, which is consistent with the scale heights of the relevant ISM components, the synchrotron-emitting thick disk (Beuermann et al. 1985, Kobayashi et al. 2004) and the scale height of the free electron density (Gaensler et al. 2008, Schnitzeler et al. 2012).

In this data set, regions of high $|\nabla\mathbf{P}|/|\mathbf{P}|$ with no Stokes I correlation effectively trace the loci of compression or rarefactions of the magnetic fields and/or the warm ionized gas in the ISM, as well as abrupt changes in direction of the magnetic field. Because the spiral arms constitute the most extended and synchrotron emitting Galactic structures where these compressions and rarefactions take place, a spatial dependence of the $|\nabla\mathbf{P}|/|\mathbf{P}|$ intensity with Galactic latitude and longitude is expected.

In order to focus on the diffuse emission, we mask the Galactic plane ($|b| \leq 2.5^\circ$) where depolarization effects are strong. The resulting map displays a diffuse foreground, and a background consisting of extragalactic discrete sources and noise. We explore the dependence on Galactic latitude by looking at the distribution of the $|\nabla\mathbf{P}|/|\mathbf{P}|$ intensity over four latitude ranges (see Fig. 4.3). The distribution peak position of the $|\nabla\mathbf{P}|/|\mathbf{P}|$ intensities decreases with distance from the Galactic plane, but not the distribution width. In addition, the intensity counts are approximately represented by a log-normal distribution and the log-normal fit to the $|\nabla\mathbf{P}|/|\mathbf{P}|$ intensity distribution of the latitude bin $|b| \lesssim 15^\circ$, which mostly probes the diffuse foreground emission, shows a reduced- χ^2 of 2.09. Increasing deviations from a log-normal distribution are found with Galactic latitude.

We highlight the presence of a longitude dependence of the $|\nabla\mathbf{P}|/|\mathbf{P}|$ emissivity by using the first two moments (i.e. the mean and standard deviation) of the $|\nabla\mathbf{P}|/|\mathbf{P}|$ distribution. We select lines of sight out of the Galactic disk over the latitude range $5^\circ \lesssim |b| \lesssim 10^\circ$ to limit the impact of depolarization. We sample the range of Galactic longitude with 5° sized squared bins, from which the mean and standard deviation of the $|\nabla\mathbf{P}|/|\mathbf{P}|$ intensity are calculated and displayed in Fig. 4.4. We use the mean and standard deviation of $|\nabla\mathbf{P}|/|\mathbf{P}|$ map as tracers of the diffuse emission and the presence of compact sources (e.g. SNRs, H II regions), respectively. Both the profiles are characterized by the presence of peaks corresponding to nearby extended structures (e.g. the Vela SNR) as well as large scale Galactic structures (e.g. the Carina-Sagittarius spiral arm), and a longitude dependence is seen with mean intensity gradually decreasing towards the outer region. Towards the anti-centre (i.e. $l \lesssim 240^\circ$), no relevant diffuse emission is detected and few compact sources are seen. These directions mostly probe the local arm synchrotron diffuse emis-

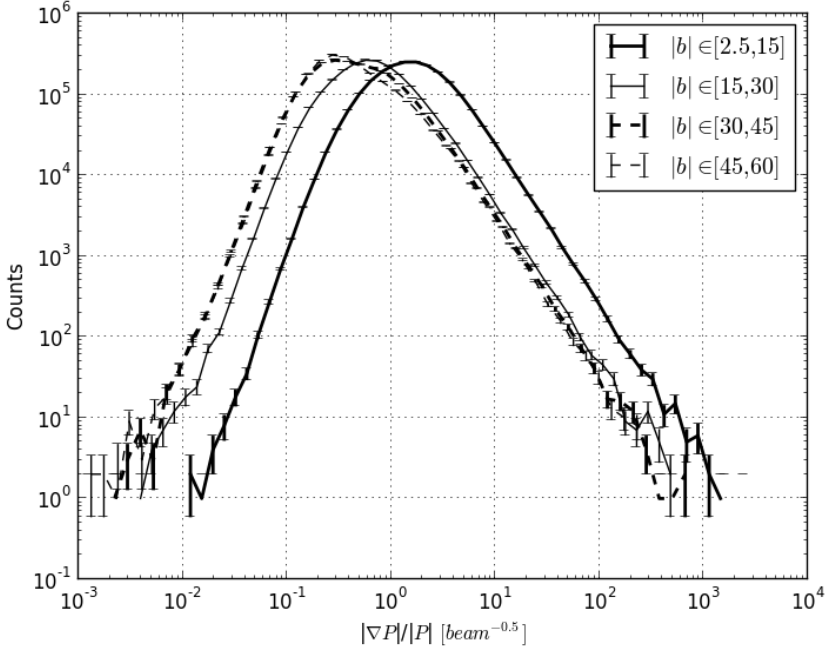


Figure 4.3 – Distributions of the $|\nabla\mathbf{P}|/|\mathbf{P}|$ intensity of the masked map at four ranges of Galactic latitude ($|b|$). Statistical errors in each intensity bin are also shown.

sion and so both the $|\nabla\mathbf{P}|/|\mathbf{P}|$ mean and standard deviation have low values, perhaps due to depolarization of the far end of the arm. A sudden jump in both moments is found around $l \sim 260^\circ$, corresponding to the extended and nearby Gum Nebula and Vela SNR complex. Two minima are seen at $l_{MIN,0} = (277.5^\circ \pm 2.5^\circ)$ and $l_{MIN,1} = (327.5^\circ \pm 2.5^\circ)$, corresponding to the observed tangential directions (see Table 2 of Vallée 2008) of the Carina ($282^\circ \pm 2^\circ$) and Norma ($328^\circ \pm 3^\circ$) spiral arms. The low values of the mean and standard deviation may be explained due to depolarization of the far end of the arms or by the alignment between the line of sight and the direction of the large scale magnetic field. The latter option would imply a drop of the synchrotron emissivity.

4.3.3 Thermal electron density and magnetic features

The presence of Faraday rotation effects in these data are evident when comparing the $|\nabla\mathbf{P}|/|\mathbf{P}|$ map with $H\alpha$ map. In this way is possible to highlight (nearby) extended structures with relevant density and/or magnetic fluctuations. To this aim, we use the all-sky $H\alpha$ map of Finkbeiner (2003), which has an angular resolution (of $6'$) similar to that of the $|\nabla\mathbf{P}|/|\mathbf{P}|$ map. We now report on some structures induced by density and/or magnetic

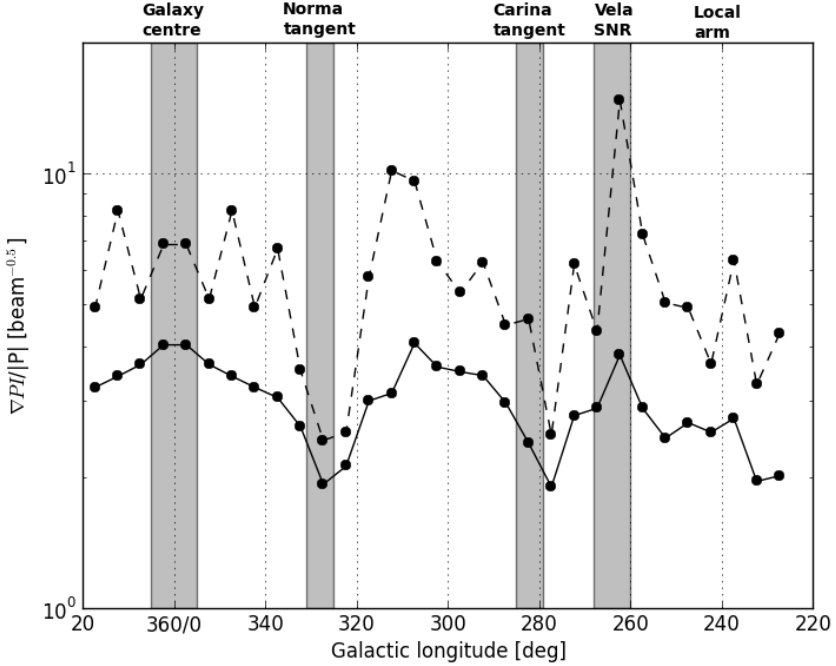


Figure 4.4 – The mean (solid lines) and standard deviation (dashed lines) profiles towards the Galactic disk ($5^\circ \lesssim |b| \lesssim 10^\circ$) for the $|\nabla\mathbf{P}|/|\mathbf{P}|$ intensity as a function of Galactic longitude. The Stokes I profile is indicated by crosses and is scaled by a factor of 7 for display purposes. The ranges of Galactic longitudes corresponding to the main Galactic features and spiral arms are also indicated. Data points are obtained from square regions of size 5° .

fluctuations.

4.3.3.1 Nearby H II regions

Nearby H II regions are extended objects with prominent electron density fluctuations, for which a correspondence with H α intensity is expected. Indeed a clear correlation of the $|\nabla\mathbf{P}|/|\mathbf{P}|$ and H α intensity patterns is seen towards the nearby H II regions Sh 2-27 and Sh 2-7, as shown in Fig. 4.5. The H α intensity contours clearly trace features with higher $|\nabla\mathbf{P}|/|\mathbf{P}|$ intensity both at the edges and towards the centre. A weak radio continuum feature is seen only for Sh 2-27 and the degree of correlation between the $|\nabla\mathbf{P}|/|\mathbf{P}|$ and the Stokes I intensity is $|\rho_p| = 0.30, 0.53$ for Sh 2-27 and Sh 2-7, respectively. The higher degree of correlation found towards Sh 2-7 can be explained due to the overlapping with the Galactic central spur, a feature detected with S-PASS in Stokes I and polarization (Carretti et al. 2013), and possibly emanating from the Galactic centre. The interpretation of the observed morphology in terms of ISM turbulent fluctuations is therefore supported

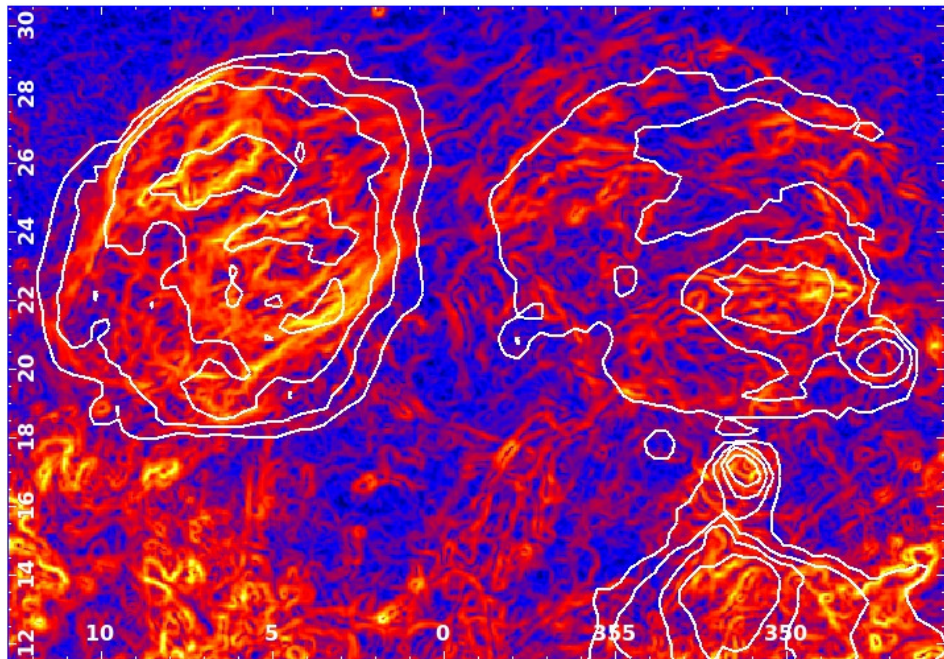


Figure 4.5 – The bubble-like $|\nabla\mathbf{P}|/|\mathbf{P}|$ morphology of the nearby H II regions Sh 2-27 (on the left) and Sh 2-7 (on the right) is shown together with the contours of the H α intensity from the all-sky map of Finkbeiner (2003). The units of contours are 1, 13, 25, 50 and 100 Rayleigh. Colour scale is the same as in Fig. 4.2.

only for Sh 2-27. This bubble-like feature is crossed and filled by filaments exhibiting a “single-jump” morphology, suggesting the presence of weak shock and/or strong turbulent fluctuations (Burkhart et al. 2012).

4.3.3.2 Nearby, old SNRs

We find an evident correlation of $|\nabla\mathbf{P}|/|\mathbf{P}|$ and H α intensity patterns for two extended shells likely due to nearby ($d_{SNR} \lesssim 500$ pc), old ($t_{SNR} \approx 1$ Myr) SNRs: the Antlia (McCullough et al. 2002) and G 353-34 (Testori et al. 2008) SNRs. The radio features are seen as incomplete shells around the center and partially filled by fainter gradients in polarized emission. Moreover the Antlia SNR feature is seen in a field with a complex pattern of $|\nabla\mathbf{P}|/|\mathbf{P}|$ intensity with no H α correspondence. The H α intensity contours show prominent arc features along the old radio shell. Unlike the younger SNRs listed in Table 4.2, both these evolved objects show prominent H α and weak radio continuum features, and an impressive morphology of filaments in polarization gradients is seen matching the H α features (see Fig. 4.6). These extended and nearby structures in polarization gradients and H α are surrounded by and likely interacting with complex environment in the ISMs,

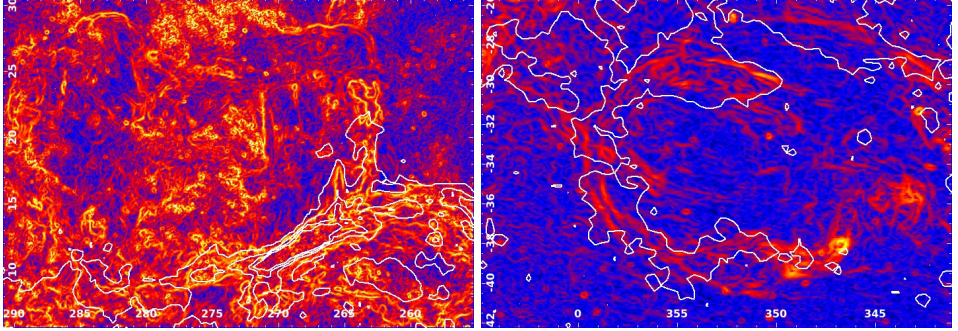


Figure 4.6 – The $|\nabla\mathbf{P}|/|\mathbf{P}|$ morphologies of the old SNRs Antlia (left) and G 353-34 (right) are shown together with the contours of the $H\alpha$ intensity from the all-sky map of Finkbeiner (2003). The units of contours for Antlia and G 353-34 are 0.1, 20, 40, 80, 160 and 0.1, 1.5, 8, 16, 32 Rayleigh, respectively. Intensity scale runs from 0.2 (black) to 2000 (white) and from 0.2 (black) to 1000 (white) for Antlia and G 353-34, respectively.

as suggested by the depolarization seen towards the brightest $H\alpha$ features along the two shells.

4.3.3.3 $|\nabla RM|$ features A,B,C

We note the presence in the $|\nabla\mathbf{P}|/|\mathbf{P}|$ map (see labels A,B,C in Fig. 4.1) of three structures with no corresponding radio continuum emission. An elongated bubble-like feature (labelled A) is depicted at $(l, b) \approx (6^\circ, -29^\circ)$ with a linear size of about 2° . $|\nabla\mathbf{P}|/|\mathbf{P}|$ and $H\alpha$ intensity correlate, but the $H\alpha$ intensity peaks at $(l, b) \approx (8^\circ, -30^\circ)$. A high normalized polarization gradient filament is seen crossing the feature and displays a single-jump morphology as shown in Fig. 4.7.

A long (~ 8.4 deg) and thick (~ 0.9 deg) linear structure (labelled B) extends from $(l, b) \approx (346^\circ.6, -14^\circ.8)$ to $(l, b) \approx (339^\circ.3, -17^\circ.1)$, and is prominent in both the $|\nabla\mathbf{P}|/|\mathbf{P}|$ and $H\alpha$ maps, as displayed in Fig. 4.7. The morphology of the $|\nabla\mathbf{P}|/|\mathbf{P}|$ intensity consists of two filaments, both showing a single-jump morphology, slightly diverging towards the southern edge. The mean width of the upper and lower filaments is about $14'$ and $21'$, respectively. The $|\nabla\mathbf{P}|/|\mathbf{P}|$ intensity correlates with $H\alpha$, showing a peak of ~ 12 R at $(l, b) \approx (343^\circ.0, -16^\circ.0)$. The $H\alpha$ contrast of the structure with respect the background is ~ 2 around the peak position, decreasing to ~ 1.3 over the rest of the feature. The mean $H\alpha$ contrast corresponds to an emission measure (EM) of about 4.4 pc cm^{-6} . The polarization horizon of the $|\mathbf{P}|$ map places an upper limit of about 3 kpc to the distance, implying a length of $\lesssim 440$ pc, a width of $\lesssim 50$ pc, and an height of $\lesssim 900$ pc above the Galactic plane. Such extended structures are observed in numerical simulations with sub-Alfvénic magnetic field strengths (see Burkhart et al. 2012). Linear features may be organized by large scale magnetic fields and observed perpendicular to the field orientation.

Finally, two prominent shell-like features are seen in $|\nabla\mathbf{P}|/|\mathbf{P}|$ towards the 3rd Galactic

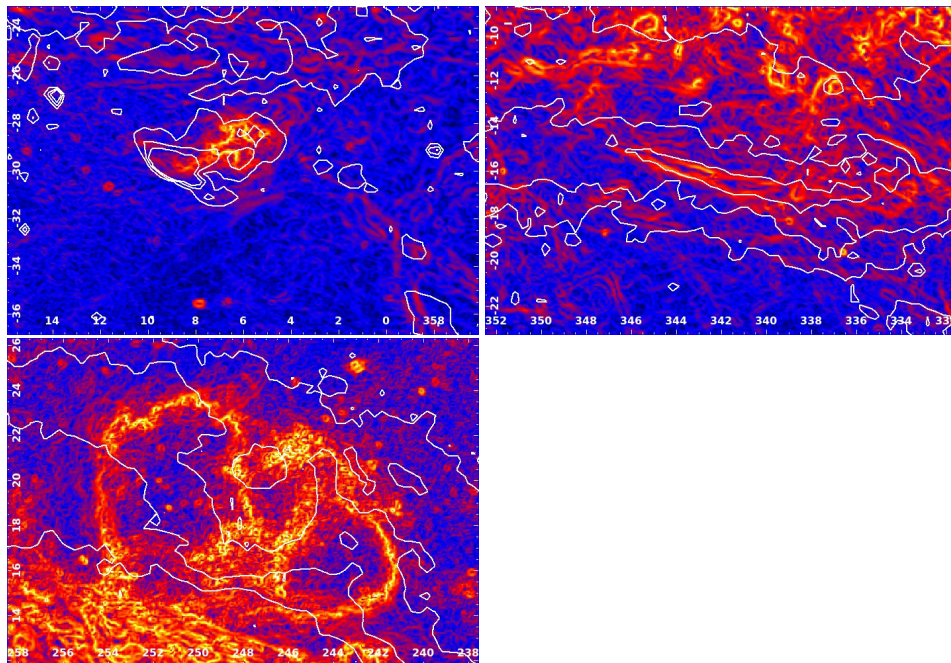


Figure 4.7 – The $|\nabla\mathbf{P}|/|\mathbf{P}|$ morphologies of the $|\nabla\mathbf{RM}|$ features labelled A, B, and C in Fig. 4.1 are shown together with the contours of the $H\alpha$ intensity from the all-sky map of Finkbeiner (2003). The units of the $H\alpha$ contours for feature A (top left panel), B (top right panel) and C (bottom left panel) are 0.1, 2, 3, 4, 16 and 3, 4, 7, 16, 50 and 3, 5, 8, 16, 32 Rayleigh, respectively. Colour scale is the same of Fig. 4.2.

quadrant. The loops are not symmetric, are characterized by high normalized polarization gradients and have centres at $(l, b) \approx (251^\circ, 20^\circ)$ and $(l, b) \approx (242^\circ.5, 17^\circ.5)$, with radii of about 3° and 2° , respectively. Along with the extended filaments tracing the edges, a mottled pattern of high $|\nabla\mathbf{P}|/|\mathbf{P}|$ intensity is also seen on small ($\lesssim 0.5^\circ$) scales. No correlation with $H\alpha$ intensity is found for these structures or their surroundings, thus disfavouring the presence of a relevant enhancement of the electron density due to an e.g. $H\text{II}$ region. Moreover the $|\nabla\mathbf{P}|/|\mathbf{P}|$ filaments are characterized by a single-jump morphological pattern, suggesting the presence of a weak shock in the medium.

4.4 ISM turbulent regimes

Polarization gradients are useful means to study turbulence and to constrain the Mach numbers of diffuse and ionized gas because, they are sensitive to variations of the free electron density and magnetic field strength. Variations of both the free electron density and magnetic field strength can be induced by strong shocks, thus the polarization

gradients are effective tracers of transonic and supersonic type turbulence. In addition, turbulence naturally induces discontinuities even in the incompressible limit, and thus polarization gradients can also indicate subsonic regimes.

The statistical determination of the sonic Mach number is possible because of the relationship between turbulence regimes and probability distribution functions (PDFs) of the image intensity distribution (Burkhart et al. 2012). The probability distribution function of an image distribution gives the frequency of occurrence of intensities values, and can be described by the main statistical moments: mean, variance, skewness and kurtosis. The higher order moments (skewness and kurtosis) measure the degree of deviation of the PDF from a Gaussian, and are sensitive to the imprints of turbulence encoded in the image intensity distribution. For this reason, their use constitutes a common diagnostic for astrophysical turbulence.

The first and second order statistical moments (mean and variance) used here are defined as follows: $\mu_\xi = \frac{1}{N} \sum_{i=1}^N (\xi_i)$ and $\nu_\xi = \frac{1}{N-1} \sum_{i=1}^N (\xi_i - \bar{\xi})^2$, respectively, with N the total number of elements and ξ_i the distribution of intensities. The 3rd and 4th order moments, skewness and kurtosis respectively, are defined as:

$$\gamma_\xi = \frac{1}{N} \sum_{i=1}^N \left(\frac{\xi_i - \bar{\xi}}{\sigma_\xi} \right)^3, \quad (4.4)$$

$$\beta_\xi = \frac{1}{N} \sum_{i=1}^N \left(\frac{\xi_i - \bar{\xi}}{\sigma_\xi} \right)^4 - 3, \quad (4.5)$$

where σ_ξ is the standard deviation. In this section, we investigate the presence of any large scale spatial dependence of the ISM turbulence regime as seen in the $|\nabla\mathbf{P}|/|\mathbf{P}|$ map. In order to search for spatial variations of the interstellar sonic Mach number, we select 11 $25^\circ \times 25^\circ$ sub-fields in the $|\nabla\mathbf{P}|/|\mathbf{P}|$ map, as shown in Fig. 4.8. These regions cover the relevant extended features seen in the map of spatial gradient of linear polarization, and sample a wide range of Galactic longitude and latitude. A small test region showing no extended emission was also chosen to characterize the noise statistics.

We show correlations between the first and second order moments of $|\nabla\mathbf{P}|/|\mathbf{P}|$ of the twelve selected regions in the top panel of Figure 4.9, and the correlation between the third and fourth order moments in the bottom panel of Figure 4.9. Tight correlations exist for the moments of all twelve maps, and interesting trends are seen with respect to Galactic latitude and level of noise. In general the noise maps have very low values of all four moments and the low values of the higher order moments indicate that the noise is Gaussian in nature. Regions with more structure exhibit higher values of the four moments, and hence departures from Gaussianity. In all fields towards the plane, the values of the moments are very high while the off-plane regions show a range of moments, which may indicate systematic variations of the ISM turbulence regime.

Figure 4.9 shows the moments for the S-PASS $|\nabla\mathbf{P}|/|\mathbf{P}|$ data. However if we would like to compare the S-PASS moments with ideal MHD simulations we must keep in mind two limitations concerning the observational data and simulated observations. First, the simulations cannot be normalized by the linear polarization map because they contain

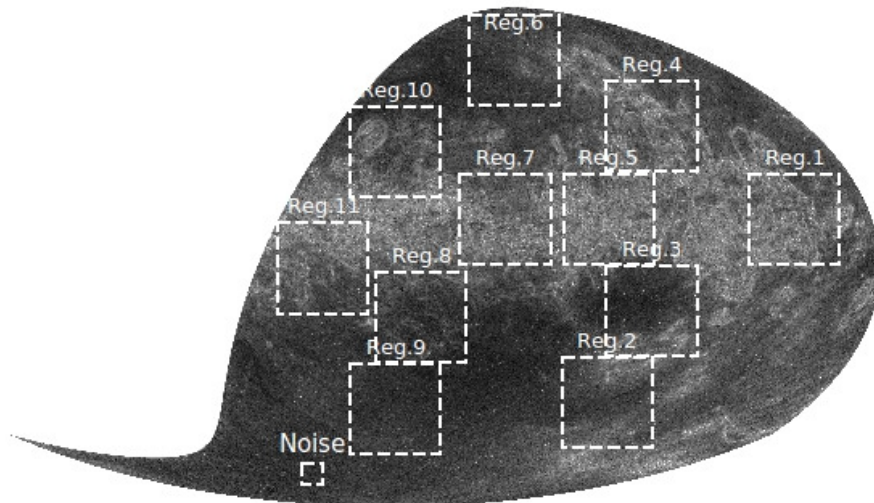


Figure 4.8 – The selected boxed regions of the $|\nabla\mathbf{P}|/|\mathbf{P}|$ map for the statistical determination of the sonic Mach number.

only “Faraday thin” structures (i.e. the emission and Faraday rotation take places in spatially separated regions) and have no intrinsic background polarization fluctuations. Thus as in the case of the ideal synthetic observations used by Gaensler et al. (2011), one must work with statistics of the $|\nabla\mathbf{P}|$ map only. Second, the observed polarization gradient fluctuations can only be interpreted in terms of turbulence once one has confirmed that the polarization signal is due to foreground Faraday rotation. In this scenario, there should be little correlation between the fluctuations of $|\mathbf{P}|$ and Stokes I. In the case that \mathbf{P} or $|\nabla\mathbf{P}|$ or $|\nabla\mathbf{P}|/|\mathbf{P}|$ matches the morphology seen in Stokes I, the polarized emission has a substantial intrinsic component and therefore does not necessarily describe the foreground turbulence along the line of sight.

We show the Pearson correlation coefficients of $|\mathbf{P}|$ with Stokes I in Table 4.3 for each region. We use the Pearson coefficient because a linear relationship between Stokes I and $|\mathbf{P}|$ is expected in the Faraday thin approximation. We see that in general there does not exist strong correlations between $|\mathbf{P}|$ with Stokes I in these maps.

Since there does not exist strong correlation between $|\mathbf{P}|$ and Stokes I, we can assume that the bulk of the emission and features seen in $|\nabla\mathbf{P}|/|\mathbf{P}|$ arise from (foreground) Faraday fluctuations in the turbulent ISM. Moreover for cases which are properly described by the Faraday thin approximation, $|\nabla\mathbf{P}|/|\mathbf{P}|$ will tend to $|\nabla\mathbf{P}|$ and the quantitative comparison with simulations is meaningful. Thus we can make a comparison between the statistics of $|\nabla\mathbf{P}|$ of the S-PASS observations and the MHD turbulence simulations of Burkhart et al. (2012), since the emission in both arises from turbulent fluctuations of n_e and B along the line of sight. This is the aim of the next subsection.

Table 4.3 – Main properties of the selected regions and their correlation degree of the $|\mathbf{P}|$ with Stokes I (column 3), as derived by the Pearson’s coefficient (ρ_p) which assumes a linear relationship. The degree of correlation between $|\mathbf{P}|$ and $|\nabla\mathbf{P}|/|\mathbf{P}|$ is indicated in columns 4–5 by the Pearson and Spearman’s rank (ρ_s) coefficients. The noise test field and region 9 correspond to noise dominated fields indicated in Fig. 4.9 by the black cross and X symbol, respectively. The Faraday thin regions used in Sect. 4.4.1 for the quantitative comparison with the MHD simulations are also shown.

Field	(l, b) coord.	$ \rho_p $	$ \rho_p $	$ \rho_s $	Notes
Reg.1	$240^\circ, 0^\circ$	0.09	0.31	0.63	
Reg.2	$269^\circ, -50^\circ$	0.35	0.20	0.69	
Reg.3	$278^\circ, -25^\circ$	0.12	0.18	0.70	
Reg.4	$278^\circ, +25^\circ$	0.12	0.29	0.61	
Reg.5	$297^\circ, 0^\circ$	0.46	0.15	0.48	Faraday thin
Reg.6	$310^\circ, +46^\circ$	0.37	0.45	0.60	
Reg.7	$327^\circ, 0^\circ$	0.16	0.21	0.49	Faraday thin
Reg.8	$350^\circ, -28^\circ$	0.06	0.18	0.11	Faraday thin
Reg.9	$357^\circ, -56^\circ$	0.52	0.36	0.37	Noise dominated
Reg.10	$358^\circ, +19^\circ$	0.19	0.23	0.47	Faraday thin
Reg.11	$19^\circ, -14^\circ$	0.09	0.17	0.26	Faraday thin
Noise	$74^\circ, -76^\circ$	0.23	0.18	0.17	Noise dominated

4.4.1 Moments of $|\nabla\mathbf{P}|$ and the Sonic Mach Number

To test the goodness of the “Faraday thin” approximation for the selected regions, we look at the correlation degree between $|\mathbf{P}|$ and $|\nabla\mathbf{P}|/|\mathbf{P}|$. To this aim we use both the Pearson and the Spearman’s rank (ρ_s) correlation coefficients. As discussed in Sect. 4.2.1, a negligible correlation is expected between $|\mathbf{P}|$ and $|\nabla\mathbf{P}|/|\mathbf{P}|$ in the Faraday thin regime with no intrinsic background polarization fluctuations. However, intrinsic background polarization fluctuations affect our data, so we assume $|\rho| < 0.5$ as a threshold for low/mild correlation.

The relationship between Pearson and Spearman’s rank correlation coefficients of $|\mathbf{P}|$ and $|\nabla\mathbf{P}|/|\mathbf{P}|$ for each region is displayed in Table 4.3. A sample of 7 regions is selected: two are noise dominated and two/three fields lie towards to/off the Galactic plane, respectively. The noise (dominated) regions display the lowest degree of correlation for both the correlation coefficients. For each selected region, we check the degree of correlation between $|\nabla\mathbf{P}|$ and $|\nabla\mathbf{P}|/|\mathbf{P}|$ maps, finding mild/high values (i.e. > 0.5) of the Spearman’s rank correlation coefficient. We then assume the Faraday thin approximation to hold for these few regions which sample a wide range of Galactic longitude and latitude. The small test region showing no extended emission is included to characterize the noise statistics. In order to search for spatial variations of the interstellar sonic and number, results from the statistical analysis of signal distributions of boxed $25^\circ \times 25^\circ$ sized sub-fields in the

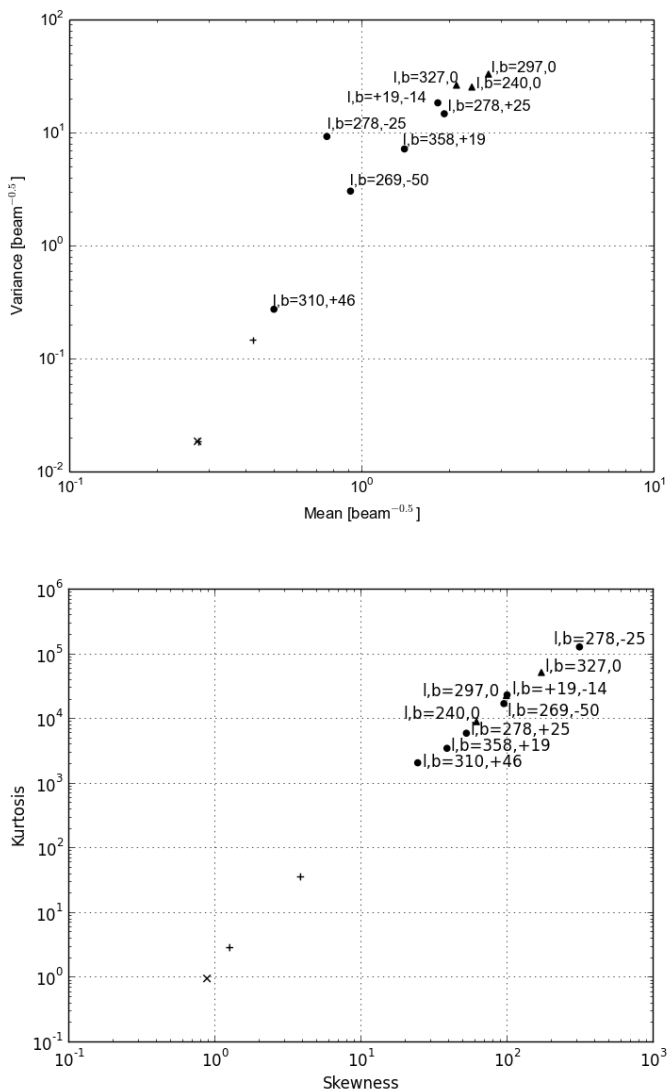


Figure 4.9 – The mean vs. variance (top) and skewness vs. kurtosis (bottom) for selected regions of the $|\nabla\mathbf{P}|/|\mathbf{P}|$ map. Noise dominated regions are indicated by crosses, the X symbol referring to the noise test region. Regions close to and off the Galactic plane are marked by filled squares and points, respectively.

$|\nabla\mathbf{P}|$ map are then matched with numerical simulations of isothermal compressible MHD turbulence, since the emission in both arises from turbulent fluctuations of n_e and B along

the line of sight.

Following Burkhart et al. (2012), we perform a statistical determination of the sonic Mach number by using the probability distribution function moments of the image distribution. In the framework of polarization gradients, the relationship between the moments of the $|\nabla\mathbf{P}|$ map and the sonic Mach number has been studied by Burkhart et al. (2012). As a consequence of the shock fronts creating more discontinuities and sharper gradients, a systematic increase of all four moments with increasing sonic Mach number is found.

In the analysis that follows, we employ the same set of MHD simulations that was used in the study by Burkhart et al. (2012), to estimate the sonic Mach number in S-PASS data. The database of 3D numerical simulations of isothermal compressible (MHD) turbulence is generated by using the MHD code of Cho & Lazarian (2003), and varying the input values for the sonic and Alfvénic Mach number. We scale the simulations to physical units, adopting typical parameters for warm ionized gas. We assume an average density of 0.1 cm^{-3} (Gaensler et al. 2011). The simulations are assumed to be fully ionized and we do not include the effects of partial ionization. To make the maps of $|\nabla\mathbf{P}|$, we first calculate the line of sight rotation measure at each pixel, then take the gradient of this rotation measure map and convert it to $|\nabla\mathbf{P}|$. For more information and details on these simulations, we refer the reader to Cho & Lazarian (2003) and Burkhart et al. (2012).

An additional effect that must be considered when applying the moments to estimate the sonic Mach number in $|\nabla\mathbf{P}|$ data is the issue of the telescope resolution. It is clear from the analysis of Burkhart et al. (2012) that smoothing changes the distribution of maps of $|\nabla\mathbf{P}|$. As the resolution of maps of Stokes Q and U decreases, so do the moments. Thus one needs to take the smoothing of the data into account when comparing PDFs of $|\nabla\mathbf{P}|$. We address this issue in the current study by applying 4-pixel smoothing (equivalent to $10.75'$ smoothing assuming that a scaling of one of our pixels at 512×512 resolution is 0.048 degrees) to the simulated $|\nabla\mathbf{P}|$ maps. This conversion is appropriate because the actual beam size of interest is a combination of the size scale of the beam in relation to the size scale of the turbulent injection. Given that the S-PASS maps we investigate are 25×25 degrees wide with a polarization horizon of ≈ 3 kpc, this means we are sampling emission in these boxes up to scales of ≈ 1 kpc. This is larger than the scale of the injection of turbulence in the Galaxy, but compatible to the large scale driving of turbulence in our simulations.

4.4.1.1 Moments analysis: results

After smoothing the MHD simulations, we apply the moment map analysis (see Burkhart et al. 2012) to both the simulations (using the aforementioned smoothing and scaling) and the S-PASS selected Faraday thin regions. The moment maps are made using a moving box kernel of 64×64 pixels and calculating the skewness and kurtosis at every point in the maps. The simulated maps of $|\nabla\mathbf{P}|$ have the advantage that their moments can directly relate back to the sonic Mach number; therefore we can estimate the accuracy of our analysis. We find that our simulation's moment maps and the sonic Mach number agree to 78–98% accuracy level for sonic Mach number ranges from 0.5 to 10. Since the moments are an effective diagnostic of supersonic turbulence, we determine which pixels have sonic

Table 4.4 – Summary of high order moments analysis obtained from selected “Faraday thin” regions. Regions 9 corresponds to noise dominated field indicated by black marker in Fig. 4.10. The last column shows the percentage of lines of sight with sonic Mach number greater than unity.

Field	(l, b) coordinates	Mean mJy beam ^{-1.5}	Variance [mJy beam ^{-1.5}] ²	Skewness	Kurtosis	# LOS ($M_s > 1$)
Reg.5	297°, 0°	0.058	0.041	1.70	4.60	33%
Reg.7	327°, 0°	0.16	0.11	1.56	3.42	20%
Reg.8	350°, -28°	0.041	0.030	2.26	9.09	28%
Reg.9 (Noise)	357°, -56°	0.015	0.0062	0.76	1.18	0.3%
Reg.10	358°, +19°	0.099	0.081	2.13	6.90	36%
Reg.11	19°, -14°	0.088	0.093	3.03	19.65	36%
Noise	74°, -76°	0.014	0.0062	0.75	0.75	0.1%

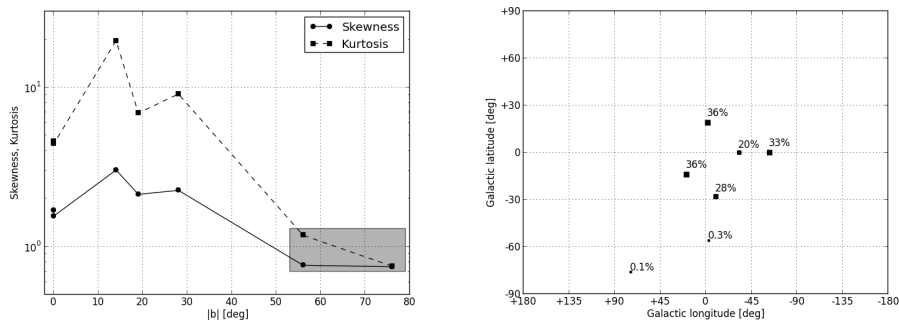


Figure 4.10 – The skewness and kurtosis as a function of Galactic latitude (top) for the “Faraday thin” selected regions of the $|\nabla P|$ map. Noise dominated regions are indicated by the shaded box. The spatial variations of the percentage of lines of sight with sonic Mach number greater than unity of each region (bottom) is also displayed.

Mach numbers greater than unity. We apply the criteria that if a pixel has values of skewness and kurtosis higher than 1.1 and 1.58, respectively, then that pixel has a sonic Mach number greater than unity. Otherwise it is subsonic or undetermined. Finally, pixels with values of skewness and kurtosis in the ranges than 2–4 and 10–20 correspond to a sonic Mach number $M_s = 2$. Table 4 lists the results of this thresholding for the S-PASS regions. Columns 3-6 show the all-map values of the skewness and kurtosis while column 7 shows the percentage of pixels with sonic Mach number greater than unity. Regions with a lot of noise, such as the Noise region but also Reg. 9, have very low overall percentages of higher Mach number gas.

A tight correlation is found between mean and variance and between skewness and kurtosis, with the highest sonic Mach numbers correspond to highest values of moments with lowest corresponding to low Mach numbers. We find this correlation behaviour of the four main moments also in the simulations, regardless of smoothing. Noise dominated regions show systematically low values of the mean, the variance, and to a lesser extent the skewness and kurtosis. In order to highlight any spatial dependence of the higher order moments for the selected regions in our data, we plot the calculated all-map skewness and kurtosis as a function of Galactic coordinates in Fig. 4.10. A clear correlation of both skewness and kurtosis as a function of Galactic latitude is seen, with the mid Galactic latitude regions showing slightly higher skewness and kurtosis. However, this trend implies only a weak increase of the percentage of pixels with sonic Mach number higher than one, as shown in Table 4.4. As a consequence, no systematic clustering of the sonic Mach number values as a function of Galactic latitude is found, but significant spatial variation indicating higher sonic Mach number in the WIM as is seen in the lower panel of Fig. 4.10.

4.5 Discussion

The distribution peak position of the $|\nabla\mathbf{P}|/|\mathbf{P}|$ intensities at Galactic latitudes $|b| < 15^\circ$ differs systematically from the peak positions at higher latitude ranges. The evident shift towards lower intensity values for higher Galactic latitudes observed towards the inner regions relates to the vertical extension of the Carina-Sagittarius spiral arm. Assuming a distance of ~ 2 kpc to this arm, the corresponding height above the Galactic disk is $\lesssim 500$ pc, in agreement with the typical vertical extension of other arms (Feitzinger & Spicker 1986) and the scale height of the arms in the Taylor & Cordes (1993) model of the free electron density.

Moreover, the $|\nabla\mathbf{P}|/|\mathbf{P}|$ intensity shows a dependence on both Galactic longitude and latitude. We find that $|\nabla\mathbf{P}|/|\mathbf{P}|$ emission is roughly approximated by a log-normal distribution, with deviations towards small $|\nabla\mathbf{P}|/|\mathbf{P}|$ fluctuations. A log-normal distribution is expected for pure density perturbations in a 3D turbulent and isothermal flow (see e.g. Vázquez-Semadeni 1994) and is observed for density tracers in the WIM such as the emission measure (Hill et al. 2008). However, the presence of magnetic fields in the WIM also influences the PDF of the perturbations (Kowal et al. 2007, Molina et al. 2012, Burkhart & Lazarian 2012b). Therefore, our result may be explained by the sensitivity of the $|\nabla\mathbf{P}|/|\mathbf{P}|$ emission to both density and magnetic fluctuations. In addition, the presence in our data of a polarization horizon at a distance of about 3 kpc also affects the observed PDF of $|\nabla\mathbf{P}|/|\mathbf{P}|$. As a consequence, most of the diffuse polarized emission seen in the $|\nabla\mathbf{P}|/|\mathbf{P}|$ map is generated within the nearest spiral arm, while the emission measure which is only sensitive to density perturbations can probe away of the Galactic plane the entire line of sight. Thus, the shorter pathlength limits the number of the observed independent fluctuations and affects the convergence to a Gaussian.

Spatial variations of the sonic Mach number are observed in the Faraday thin selected fields towards and out of the Galactic plane at medium latitudes. These variations may be consistent with turbulence in the WIM being driven by supernova explosions (see simulations by Hill et al. 2012), but they may also be explained by the presence of spatially extended and nearby objects triggering turbulence in (and interacting with) the surrounding medium. These features affect the statistical inference of the turbulent regime in some of the target regions. Since it is not possible to separate their contribution from the bulk of the $|\nabla\mathbf{P}|$ features, they were not masked.

Finally, we report the detection of a prominent spur-like feature (see Sect. 4.3) clearly seen towards the edge of the 3rd Galactic quadrant in the $|\nabla\mathbf{P}|/|\mathbf{P}|$ map but not traced by $H\alpha$ intensity. Because of the high latitude extinction it is not likely to be responsible for the $H\alpha$ non-detection, thus disfavouring a thermal electron density enhancement. Moreover this magnetic structure has no radio continuum counterpart, suggesting that the direction of the magnetic field is mainly pointed towards the observer. The large angular size of this magnetic feature, which is specific of to the $|\nabla\mathbf{P}|/|\mathbf{P}|$ map, suggests the structure is nearby. These characteristics, along with its shape, support its association with Loop I, a local feature of the ISM (Berkhuijsen et al. 1971, Heiles 1979) associated with an expanding SNR remnant (Spoelstra 1972, Heiles 1998, Wolleben 2007).

4.6 Summary and Conclusions

Normalized spatial gradients of the polarization vectors have been used for the first time to map the entire southern sky. The large sky coverage allows the exploration of cases not treated by the previous studies of Gaensler et al. (2011) and Burkhart et al. (2012). The S-PASS $|\nabla\mathbf{P}|/|\mathbf{P}|$ map displays a wealth of filamentary structures with typical widths down to the angular resolution. The emission is characterized by a polarization horizon of about 3 kpc, implying density and magnetic fluctuations down to a linear scale < 10 pc given the angular size of the S-PASS beam. An extended and patchy pattern of $|\nabla\mathbf{P}|/|\mathbf{P}|$ intensity is found within the 3rd and 4th Galactic quadrants at high ($b \lesssim -60^\circ$) latitudes towards the south Galactic pole.

Two different morphologies (i.e. “single” or “double” jump profiles) corresponding to different MHD turbulence cases (i.e. low or high sonic Mach numbers) are observed, thus supporting the predictions of numerical simulations (Burkhart et al. 2012). Normalized spatial gradients of the polarization vector are effective tracers of extended and Faraday rotating features, such as H II regions and evolved SNRs. Indeed we clearly recognize the two known old SNRs Antlia and G 353-34, and find them to be mildly supersonic (see e.g. McCullough et al. 2002). In addition, by combining the information from both the $|\nabla\mathbf{P}|/|\mathbf{P}|$ and H α intensity maps we can highlight the presence of both electron density and magnetic structures, in agreement with simulations (Burkhart et al. 2012).

Although multiple scales of energy injection are expected in the ISM (Nota & Katgert 2010), instabilities triggered by supernova events and Galactic shear in the ISM mainly generate and sustain MHD turbulence (MacLow 2004, Hill et al. 2012). Observational studies of MHD turbulence in the warm and ionized ISM also indicate a spectral index matching with that of Goldreich & Sridhar (1995) theory of Alfvénic turbulence, consistent with a weakly compressible medium. This is the case for transonic turbulence as shown by Hill et al. (2008) who estimated the sonic Mach number by comparing statistics of H α WHAM data with simulations. By applying a moment analysis to a number of fields, we confirm the earlier result of these authors, finding most lines of sight to be consistent with $M_s \lesssim 2$ (see Table 4.4).

The use of the spatial gradient of linear polarizations combined with a robust statistical analysis, makes mapping of the sonic and Alfvénic Mach numbers spatial variations in the WIM a feasible and mandatory aim of forthcoming radio observations at high angular resolution. These studies will allow us to gain complementary insights of MHD turbulence and shocks in the ionized ISM over a wide range of plasma β -parameter regimes. In order to gain a complete picture on Mach numbers and spatial variations in the WIM, complete sky coverage is needed, requiring a corresponding high resolution and sensitivity survey of the northern sky.

Acknowledgments This work has been carried out in the framework of the S-band Polarisation All Sky Survey collaboration (S-PASS). The Parkes Radio Telescope is part of the Australia Telescope National Facility, which is funded by the Commonwealth of Australia for operation as a National Facility managed by CSIRO. The research leading to these results has received funding from the European Union’s Seventh Framework Pro-

gramme (FP7/2007-2013) under grant agreement number 239490. This work is part of the research programme 639.042.915, which is (partly) financed by the Netherlands Organisation for Scientific Research (NWO). Support for B.B. and A.L. comes from the NSF grant AST 1212096, and the Center for Magnetic Self-Organization in Laboratory and Astrophysical Plasmas (CMSO). B.B. acknowledges Vilas Associate Awards and the hospitality of the International Institute of Physics (Natal). B.M.G. acknowledge the Australian Research Council (ARC) and the Centre for All-sky Astrophysics (CAASTRO).

Contributions This paper represents the combined work of the S-PASS (the S-band Parkes All-Sky Survey) team members listed as authors. E.C., M.H., G.B., N.M.Mc.ŠG., L.S.-S., B.M.G., M.J.K. and S.P. carried out the original observations. The simulations were carried out by B.B. and A.L.. M.I. led the writing of the paper and the analysis of the data. M.I. and M.H. determined the strategy to compare to the simulations. B.B., A.L. and M.H. were also involved in interpretation of the comparison of simulations and observations.

Bibliography

- Armstrong J.W., Rickett B.J., Spangler S.R. 1995, ApJ, 443, 209
- Berdyugin A., Piirola V. & Teerikorpi P. 2004, A&A, 424, 873
- Berkhuijsen E.M., Haslam C.G.T. & Salter C.J. 1971, A&A, 14, 252
- Beuermann K., Kanbach G., Berkhuijsen E.M. 1985, å, 153, 17
- Boulares A. and Cox D.P. 1990, ApJ, 365, 544
- Burkhart B., Stanimirović S., Lazarian A., Kowal G. 2010, ApJ708, 120
- Burkhart B., Lazarian A., Gaensler B.M. 2012, ApJ, 749, 145
- Burkhart B. and Lazarian A. 2012. Astrophysical MHD turbulence: confluence of observations, simulations, and theory. Proceedings of the International Astronomical Union, 8, pp 325-336
- Burkhart B. & Lazarian A. 2012b, ApJ, 755, 19
- Carretti E., Haverkorn M., McConnell D., Bernardi G., Cortiglioni S., McClure-Griffiths N.M., Poppi S. 2009, RevMexAA (SC) 36, 9
- Carretti E. 2010, in ASP Conf. Ser. 438, ed. R. Kothes, T.L. Landecker, & A.G. Willis, 276
- Carretti E., Crocker R.M., Staveley-Smith L., Haverkorn M., Purcell C., Gaensler B.M., Bernardi G., Kesteven M.J., Poppi S. 2013, Nature 493, 66
- Chepurnov A., Lazarian A., Stanimirović S., Heiles C., Peek J.E.G. 2010, ApJ, 714, 1398
- Chepurnov A. & Lazarian A. 2010, ApJ, 710, 853
- Cho J. Lazarian A. 2003, MNRAS, 345, 325
- Cox D.A. 2005, ARA&A, 43, 337
- Dodson R., Legge D., Reynolds J.E., McCulloch P.M. 2003, ApJ, 596, 1137
- Duncan A.R., Stewart R.T., Haynes R.F., Jones K.L. 1995, MNRAS, 277, 36
- Duncan A.R., Haynes R.F., Jones K.L., Stewart R.T. 1997, MNRAS, 297, 279
- Elmegreen B.G. & Scalo J. 2004, ARA&A, 42, 211
- Feitzinger J.V. & Spicker J. 1986, PASJ, 38, 485
- Ferrière K.M. 2001, Rev. Mod. Phys., 73, 1031
- Finkbeiner D.P. 2003, ApJS, 146, 407
- Gaensler B.M., Dickey J.M., McClure-Griffiths N.M., Green A.J., Wieringa M.H., Haynes R.F. 2001, ApJ, 549, 959
- Gaensler B.M., Madsen G.J., Chatterjee S. and Mao S.A. 2008, PASA, 25, 184
- Gaensler B.M., Haverkorn M., Burkhart B., et al. 2011, Nature 478, 214
- Georgelin Y.M., Russeil D., Amram P. et al. 2000, A&A, 357, 308
- Ghavamian P., Winkler P.F., Raymond J.C. & Long K.S. 2002, ApJ, 572, 888
- Giacani E.B., Dubner G.M., Green A.J., Goss W.M., Gaensler B.M. 2000, AJ, 119, 281
- Goldreich P. & Sridhar S. 1995, ApJ, 438, 763
- Green D.A. 2009, Bulletin of the Astronomical Society of India 37, 45
- Haslam C.G.T., Klein U., Salter C.J., Stoffel H., Wilson W.E., Cleary M.N., Cooke D.J., Thomasson P. 1981, A&A, 100, 209
- Haverkorn, M.; Gaensler, B. M.; McClure-Griffiths, N. M.; Dickey, John M.; Green, A. J. 2004,

- ApJ, 609, 776
- Haverkorn M., Katgert P., de Bruyn A.G. 2004, A&A, 427, 169
- Haverkorn M., Brown J.C., Gaensler B.M. and McClure-Griffiths N.M. 2008, ApJ, 680, 362
- Heiles C. 1979, ApJ, 229, 533
- Heiles C. 1998, LNP Vol. 506: IAU Colloq. 166: The Local Bubble and Beyond, 506, 229
- Hill A.S., Benjamin R.A., Kowal G., Reynolds R.J., Haffner L.M., & Lazarian, A. 2008, ApJ, 686, 363
- Hill A.S., Joungh M.R., Mac Low M.-M., Benjamin R.A., Haffner L.M., Klingenberg C., Waagan K. 2012, ApJ, 750, 104
- Hinshaw G., Weiland J.L., Hill R.S., et al. 2009, ApJS, 180, 225
- Hobbs G., Lorimer D.R., Lyne A.G. & Kramer M. 2005, MNRAS, 360, 974
- Iacobelli M., Haverkorn M., Orru E., Pizzo R.F. et al. 2013, A&A, 558, 72
- Jonas J.L., de Jager G., Baart E.E. 1985, A&AS, 62, 105
- Jonas J.L., Baart E.E. & Nicolson G.D. 1998, MNRAS, 297, 977
- Kowal G., Lazarian A., Beresnyak A. 2007 ApJ, 658, 423
- Kobayashi T., Komori Y., Yoshida K., Nishimura J. 2004, ApJ, 601, 340
- Landecker T.L., Uyaniker B., Kothes R. 2002, Conf. Proc. 609, Astrophysical Polarized Backgrounds, ed. S. Cecchini, S. Cortiglioni, R. Sault, & C. Sbarra (Melville, NY: AIP), 9
- Lazarian, A., Vishniac E.T. 1999, ApJ, 517, 700
- Lazarian A., Kowal G., Vishniac E., de Gouveia Dal Pino E. 2011, Planet. Space Sci., 59, 537
- Lazarian A. and Pogosyan D. 2012, ApJ, 747, 5
- Mac Low M.-M. 2004, Astrophys. Space Sci. 289, 323
- Manchester R.N., Hobbs G.B., Teoh A. & Hobbs M. 2005, AJ, 129, 1993
- McCullough P.R., Fields B.D. and Pavlidou V. 2002, ApJ, 576, 41
- McKee C.F., Ostriker E.C. 2007, ARA&A, 45, 565
- Milne D.K. 1970, AuJPh 23, 425
- Minter A.H., Spangler S.R. 1996, ApJ, 458, 194
- Molina F.Z., Glover S.C.O., Federrath C. & Klessen R.S. 2012 MNRAS, 423, 628
- Nota T. & Katgert P. 2010, A&A, 513, 65
- Pogosyan D. & Lazarian A. 2009, Rev. Mexicana Astron. Astrofis., 36, 54
- Reich P., Testori J.C., Reich W. 2001, A&A, 376, 861
- Sajina A., Partridge B., Evans T., Stefl S., Vechik N., Myers S., Dicker S., Korngut P. 2011, ApJ, 732, 45
- Schlickeiser R. 2011, ApJ, 732, 96
- Schnitzeler D.H.F.M., Katgert P., de Bruyn A.G. 2007, A&A, 471, 21
- Schnitzeler D.H.F.M., Katgert P., de Bruyn A.G. 2009, A&A, 494, 611
- Schnitzeler D.H.F.M. 2012, MNRAS, 427, 664
- Sofue Y., Reich W., Reich P. 1989, ApJ, 341, 47
- Soukup J.E. & Yuan C. 1981, ApJ, 246, 376
- Spoelstra T.A.T. 1972, A&A, 21, 61
- Taylor J.H., Cordes J.M. 1993, ApJ, 411, 674
- Testori J.C., Reich P., Reich W. 2008, A&A, 484, 733
- Tucci M., Martínez-González E., Toffolatti L., González-Nuevo J., & De Zotti G. 2004, MNRAS, 349, 1267

- Uyaniker B., Landecker T.L., Gray A.D., Kothes R. 2003, ApJ, 585, 785
Vallée J.P. 2008, AJ, 135, 1301
Vázquez-Semadeni E. 1994, ApJ, 423, 681
Vinokur M. 1965, Annales d'Astrophysique 28, 412
Wardle J.F.C. & Kronberg P.P. 1974, ApJ, 194, 249
Wieringa M.H., de Bruyn A.G., Jansen D., Brouw W.N. and Katgert P. 1993, A&A, 268, 215
Wolleben M. 2007, ApJ, 664, 349



The all-sky structure function portrait
of Galactic MHD turbulence

M. Iacobelli, D.H.F.M. Schnitzeler, M. Haverkorn

to be submitted to A&A

Abstract

Aims. We study turbulence in the Galactic magnetized interstellar medium by measuring fluctuations between the rotation measures (RMs) of extragalactic sources along different lines of sight.

Methods. A new catalogue of accurate Faraday depths of extragalactic sources obtained from S-PASS/ATCA observations is used along with the earlier NVSS rotation measure catalogue to calculate all sky structure functions of RM over an angular range of 1–12 degrees.

Results. We present an all-sky map of rotation measures of extragalactic sources as well as maps for both the structure function amplitudes and slopes. Steeper structure functions correspond to nearby and extended objects characterized by strong H α emission. No flattening is seen for structure function slopes towards the arms at low Galactic latitudes. However, a systematic flattening is found in both the NVSS and S-PASS samples away from the Galactic plane. In some fields of view, the structure function slopes are consistent with 2D turbulence, while none of them correspond to 3D turbulence. The flat and low amplitude structure functions observed towards the Galactic poles can be explained by a combination of the intrinsic contribution of the RMs of the extragalactic sources and the Galactic RMs.

5.1 Introduction

The diffuse interstellar medium of the Galaxy is a turbulent and magnetized plasma, thus magnetohydrodynamic (MHD) turbulence plays an essential role for the dynamics of the ISM (see e.g. the review of Elmegreen & Scalo 2004). Fluctuations due to interstellar turbulence can be traced by observations of different quantities, such as the velocity field, the magnetic field as well as particle densities and are usually studied through measurement of the velocity field (see e.g. Lazarian & Pogosyan 2006) or density (see e.g. Armstrong et al. 1995). In particular, fluctuations in the warm and ionized ISM of the thermal electron density (n_e) are measured by propagation effects of radio waves, such as e.g. the scattering or dispersion measure. These fluctuations are observed over an impressive range of spatial scales, spanning 12 orders of magnitude and hinting at a turbulent MHD cascade with a Kolmogorov spectrum, in agreement with the prediction of the Goldreich & Sridhar (1995) theory of Alfvénic turbulence.

However, also magnetic fields trace the MHD turbulence in the ISM. The presence of turbulent fields has been demonstrated by investigations of spatial variations of the diffuse synchrotron emission (Lazarian & Pogosyan 2012), e.g. by the angular power spectra of the diffuse, total and polarized synchrotron emission (see e.g. La Porta et al. 2008, Iacobelli et al. 2013a). Recently, the spatial gradient of the polarization vector (see e.g. Gaensler et al. 2011, Burkhart et al. 2012, Iacobelli et al. 2013b) has also been used to image turbulent fluctuations in both the thermal electron density and magnetic fields and their spatial variations. However these approaches require deep, wide-field imaging at high angular resolution of the Galactic diffuse emission.

Alternatively, the rotation measure (RM) constitutes a valuable diagnostic of interstellar MHD turbulence. Fluctuations of RMs of extragalactic sources indicate variations in the composite quantity $n_e B_{\parallel}$, where again n_e is the thermal electron density and B_{\parallel} is the component along the line of sight of the magnetic field. RM power spectra and/or structure functions characterize the physics of the fluctuations. A power law power spectrum provides the signature of turbulence. However, RM power spectra require that the rotation measures are sampled on a regular grid. RM maps do not have regular sampling and therefore structure functions are a good alternative to study power law behaviour in the fluctuations.

Earlier studies of RM structure functions provided a statistical framework for interpretation of RM fluctuations as a function of the angular scale (Simonetti et al. 1984, Simonetti & Cordes 1986, Minter & Spangler 1996). Furthermore, the structure function profiles were found to increase up to a break and then a flattening was observed. The turnover point has been associated with the outer angular scale of the MHD turbulent cascade and values of a few degrees were typically measured. Recently, Stil et al. (2011) presented the first map of the structure function features over most (80%) of the sky. Large-scale trends of structure function amplitudes and slopes were shown, where both amplitude and slope increase towards the Galactic plane. Structure function slopes are flat at high latitudes (Mao et al. 2010), confirming results from a North Galactic Pole field by Simonetti et al. (1984).

In this paper we present a new sample of accurate RMs over the entire southern sky, which includes declinations below -40 degrees that were not included in the analysis by Stil et al. (2011). The goal of this paper is to analyse the amplitudes and slopes of structure functions for the entire sky, by combining the results that Stil et al. (2011) derived from the NVSS RMs for declinations $\delta > -40^\circ$ with S-PASS data below $\delta = 0^\circ$. We focus on the implications for the MHD turbulence of the ISM, while a discussion about the large-scale structure of the Galactic magnetic field will appear in a separate paper (Schnitzeler et al. in prep.).

In Sect. 5.2 we present an overview of the new RM data and RM maps, the editing performed and the comparison with earlier catalogues. In Sect. 5.3 we present the structure function calculations and we address the reliability of the results. Next, in Sect. 5.4 we present the all-sky maps for both the structure function amplitudes and slopes and discuss science with the structure function contour maps. Finally, we present our conclusions in Sect. 5.5.

5.2 RM data overview

In the following we briefly describe the S-PASS/ATCA observations (in the remainder of the text “S-PASS”) and calibration of these observations, while a comprehensive discussion will appear in Schnitzeler et al. (in prep.).

We describe the identification and rejection of sources with a high intrinsic component of RM. Next we assess the quality of the S-PASS RMs by comparing this catalogue with the catalogue by Mao et al. (2010), which covers latitudes within 12 degrees of the North

Table 5.1 – Observational properties of S-PASS data.

Observing date	23 – 26/03/12,17/07/12
Bandwidth	$\Delta\nu = 1.7$ GHz
Channel width	8 MHz
FWHM of the synthesized beam	$FWHM = 1' \times 2'$
FWHM of the RM spread function	$FWHM = 87$ rad m ⁻²
RM synthesis noise level	0.44 mJy beam ⁻¹

and South Galactic Poles, and by comparing with the NVSS RM catalogue by Taylor et al. (2009). Finally, we complement the S-PASS RMs with RMs from the catalogue by Taylor et al. (2009) and we show in Fig. 5.1 an all-sky plot of RMs from the S-PASS/ATCA and NVSS catalogues with the H α intensity map of Finkbeiner (2003) as background. In this paper we adopt the following notation: positive and negative RM values correspond to blue and red markers, respectively.

5.2.1 The observations

The S-band Parkes All-Sky Survey (S-PASS) mapped the southern sky at 2.3 GHz using the Parkes radio telescope (Carretti et al., in prep.). We selected compact sources from this survey for follow-up observations with the Australia Telescope Compact Array (ATCA). The ATCA is a six-element east-west interferometer with a short north-south spur, which is located near the town of Narrabri in New South Wales, Australia. Each antenna is 22 m in diameter, and is equipped with cryogenically-cooled receivers. The observations make use of the newly installed Compact Array Broadband Backend (Wilson et al. 2011), which covers frequencies between 1.3 and 3.1 GHz instantaneously. Observational parameters are provided in Table 5.1.

The new observations with the ATCA provide a much larger bandwidth, 1.7 GHz versus the 256 MHz of bandwidth that was available with the old ATCA receivers and correlator, which allows us to determine RMs with a theoretical accuracy of at least 1.5 rad m⁻². Also, the ATCA observations have much improved angular resolution compared to the 9 arcminute beam that was used by the Parkes survey, which makes it easier to identify the source of the emission. The selected candidates all have a polarized flux >5 mJy at 2.3 GHz, which is at least five times the noise level of the S-PASS maps, and a degree of polarization $P/I > 1\%$. All candidates furthermore have counterparts in the NVSS/SUMSS/MGPS catalogues (Condon et al. 1998, Mauch et al. 2003, Murphy et al. 2007).

4700 candidates that we selected from the Parkes S-PASS survey were observed between the 23-26th of March 2012 and on the 17th of July 2012; splitting the observations over

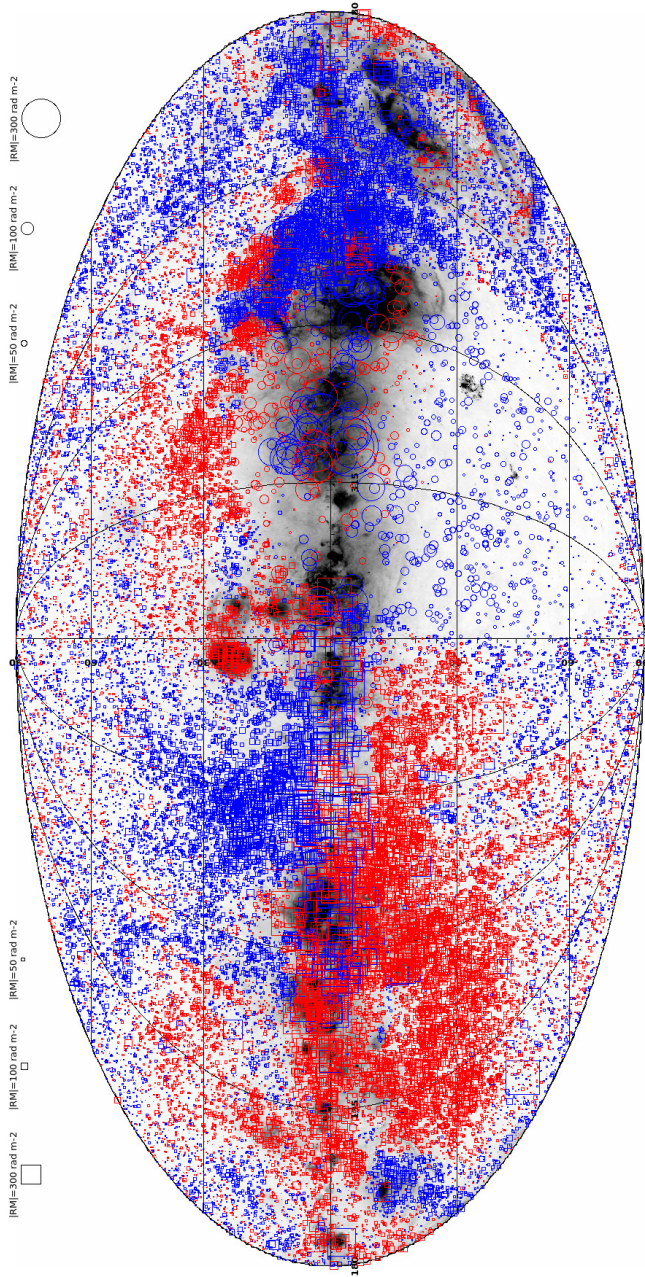


Figure 5.1 – Rotation measures over-plotted on a grey scale map of $H\alpha$ intensities. The NVSS and S-PASS rotation measures are indicated by squares and circles, respectively. Positive and negative RM values correspond to blue and red markers, respectively. The $H\alpha$ intensities in the background range from 0 (white) to 80 (black) Rayleigh with an arcsinh scale.

two epochs avoids observing candidates that lie within 40 degrees of the Sun during the first observing epoch. Candidates were observed in the hybrid H168 configuration in snapshot mode for 36 seconds each, reaching a theoretical sensitivity of 0.2 mJy and producing a synthesized beam of $\sim 1 \times 2$ arcminutes at 2.1 GHz. Because of the layout of the ATCA and because we observed in snapshot mode the instantaneous uv -coverage on baselines including antenna six is poor, and we did not include this antenna in our analysis. To reduce the data volume we averaged the original 1 MHz channels to 8 MHz channels. Data were self-calibrated and flagged using the `miriad` software package (Sault et al. 1995). The bandpass, absolute flux, and leakages were calculated from the primary calibrator PKS 1934-638. Candidates brighter than 200 mJy in total intensity were used for phase self-calibration, and these calibration solutions were passed on to fainter candidates that could not be self-calibrated. We then applied RM-synthesis (Brentjens & De Bruyn 2005) to coherently sum the polarization vectors of the individual frequency channels. The theoretical RM spread function has a full width at half maximum (FWHM) of 87 rad m^{-2} , and rotation measures of at least 14000 rad m^{-2} can be detected. This paper uses the first version of the calibration pipeline. In the remainder we will not refer to the single-dish S-PASS observations anymore, and we will refer to “S-PASS sources observed with the ATCA” as “S-PASS sources”.

5.2.2 Catalogue filtering: the outliers issue

For our analysis we select S-PASS sources that are sufficiently bright, highly polarized and resembling a point source in Faraday space. To identify automatically these lines of sight we use the following criteria:

- a polarized signal-to-noise ratio of the detection $S/N > 5$,
- an amplitude of the polarized signal $|P| > 4 \text{ mJy}$,
- an amplitude of the fractional polarization $P/I > 0.5 \%$,
- a flux ratio between the brightest and second brightest peak in the RM synthesis spectrum $P_1/P_2 > 3$.

2610 S-PASS candidates passed the selection criteria for being reliable sources. The constraint adopted for the flux ratio of the peaks allows us to select sources characterized by the presence of a dominant peaked feature in the RM synthesis spectrum. The high quality of the source detection and the RM determination is evident by inspecting the RM spectrum, as shown in Fig. 5.2.

The observed rotation measure of extragalactic sources contains contributions from all the Faraday depth components along the line of sight, viz. the intrinsic RMs of the sources, the RM of intergalactic space (and possibly intervening clusters), the Galactic RM, and the ionospheric RM. As Sun & Han (2004) showed, a single large RM can corrupt the slope and amplitude of the fitted structure function, and these RM outliers have to be removed. Note that this rejection step can not be avoided also in case of high source densities, which limit the statistical impact of single RM values as was the case of

e.g. Stil et al. (2011) with the NVSS data. To this aim we follow the method of Inoue & Tabara (1981): first we calculate the mean and standard deviation of all RMs within 6 degrees of each sight-line, then we remove that line of sight if its RM is more than 3 sigma removed from the mean RM. As shown in figure 5.3 and Table 5.2, these outliers fall in two categories:

- a clustering at low Galactic latitudes $|b| \lesssim 20^\circ$ corresponding to $H\alpha$ bright features and around Galactic longitudes $l \sim 250^\circ, 300^\circ, 0^\circ$ possibly associated to Gum nebula/Vela SNR and $H\text{II}$ region complexes (Galactic origin),
- a number of outliers lie far from the Galactic plane and are not associated with bright $H\alpha$ foreground features: these sources must have large intrinsic RMs. B2221-116 that we show in Figure 5.2 is an example of this type of outlier.

Table 5.2 – List of rejected objects identified in the Parkes Radio Sources Catalogue (Wright & Otrupcek 1990). Origin of rejection as due to a large intrinsic (I) or foreground (F) RM component is also indicated.

Obj. Name	(l, b) coordinates	Origin
	205.26,-48.55	F
B0451-282	229.09,-37.02	F
	267.16,12.53	F
B1058-656	291.85,-6.17	F
B1127-145	275.35,43.64	I
B1145-397	289.46,20.86	F
	294.71,1.98	F
B1247-149	302.38,47.67	I
B1348-055	328.71,54.34	I
B1547-021	5.84,37.92	I
B1554-140	356.28,28.87	F
	5.78,21.05	F
	16.48,6.89	F
	12.71,5.45	F
	359.16,-3.24	F
	353.26,-5.82	F
B1847-796	314.73,-26.87	I
	18.21,-5.32	F
B1946-536	344.58,-30.06	I
B0357-247	220.84,-47.14	F
B0502-696	280.79,-34.76	F
B0506-612	270.62,-36.07	I
	223.28,0.65	F
	271.36,10.84	F
B1000-427	273.11,9.85	F

Table 5.2 – *Continued from previous page*

Obj. Name	(<i>l, b</i>) coordinates	Origin
B1158-652	297.81,-2.71	F
	319.41,1.07	F
B1602-174	355.56,25.27	F
B1602-174	354.98,25.19	F
B0524-708	281.81,-32.67	F
	225.47,1.09	F
	257.68,15.01	F
B0913+003	231.27,31.67	F
B1322-015	320.18,59.93	I
B1617-041	9.29,30.69	F
B1614-099	3.55,27.80	F
B1617-111	3.02,26.49	F
	330.25,-2.67	F
	0.68,5.98	F
	17.65,-15.53	F
B2021-040	40.31,-22.25	F
	30.14,-7.20	F
	30.46,-5.22	F
B0436-203	218.34,-37.89	F
B0540-628	272.19,-31.93	I
	217.93,-6.54	F
B1635-141	4.17,21.03	F
B1635-141	3.33,21.73	F
	334.20,-46.19	I
B2145-449	354.84,-49.78	I
B2207-069	53.54,-46.61	I
B2206-237	29.39,-53.35	I
B2215-508	343.43,-52.71	I
B2221-116	50.14,-52.06	I
B0218-683	291.16,-46.94	I
B0218-220	204.62,-68.81	I
B0010-049	97.53,-65.37	I
B0000-307	12.70,-78.83	I
B0005-594	313.20,-57.13	I
B0057-180	135.65,-80.45	I
B0058-138	132.89,-76.28	I
	282.45,-73.78	I
B0140-699	296.85,-47.35	I
B0157-363	248.99,-73.02	I
B0239-070	180.18,-56.87	I
B0312-034	184.58,-48.16	F
	190.51,-52.42	I

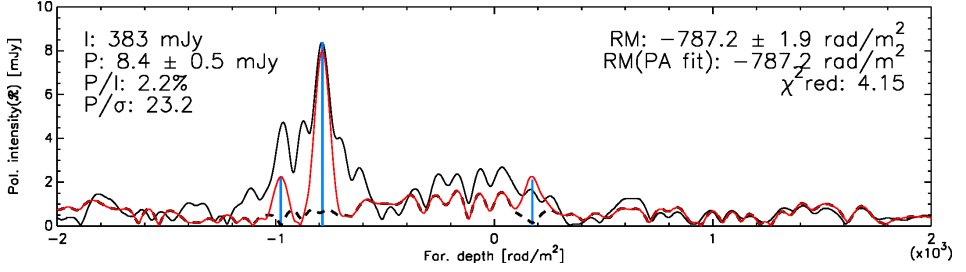


Figure 5.2 – RM spectrum of source B2221-116 showing a high intrinsic RM contribution. The raw and cleaned RM spectra are indicated by the black and the red solid line, respectively. The clean components are shown in blue, while the residuals after cleaning are traced by the dashed black line. The values mentioned in the left column show the measured total and polarized intensity of the brightest RM component, the polarization fraction, and the polarization signal to noise ratio. The values in the right column show the Faraday depth (RM) of the peak in the RM spectrum, the RM derived from fitting position angles versus the square of the wavelength and the reduced χ^2 of the latter fit.

Table 5.2 – Continued from previous page

Obj. Name	(l, b) coordinates	Origin
B0304-122	194.40, -54.87	I

After the removal of outliers the S-PASS/ATCA catalogue consists of 2490 extragalactic sources (see Fig. 5.1).

5.2.3 RM comparison with the Mao catalogue

In order to understand the quality of the S-PASS RMs and to check for systematic effects we compare our S-PASS RMs with the catalogue compiled by Mao et al. (2010). Using the Mao et al. (2010) catalogue as a reference has the advantage of having accurate (median RM error of 5 rad m^{-2}) and reliable RMs for many sources within 12 degrees of the North and South Galactic Poles (472 and 341 RMs respectively). The North Galactic Pole region that was observed by Mao et al. (2010) was not covered by S-PASS. Therefore we can only compare S-PASS RMs with lines of sight from the catalogue by Mao et al. (2010) that lie towards the South Galactic Pole (SGP).

In Figure 5.4 we compare the S-PASS RMs with the RMs found by Mao et al. towards the South Galactic Pole. We compare RMs around the SGP region of sources with positions which differ less than 4 arcminutes from each other in the S-PASS and Mao data sets. The distribution of $\Delta RM = RM_{S-PASS} - RM_{Mao}$ has a mean and standard deviation of $-1.12 \pm 5.62 \text{ rad m}^{-2}$, calculated in a way that is robust against outliers (i.e. clipping away outliers using the median and the median absolute deviation). Then we assess the

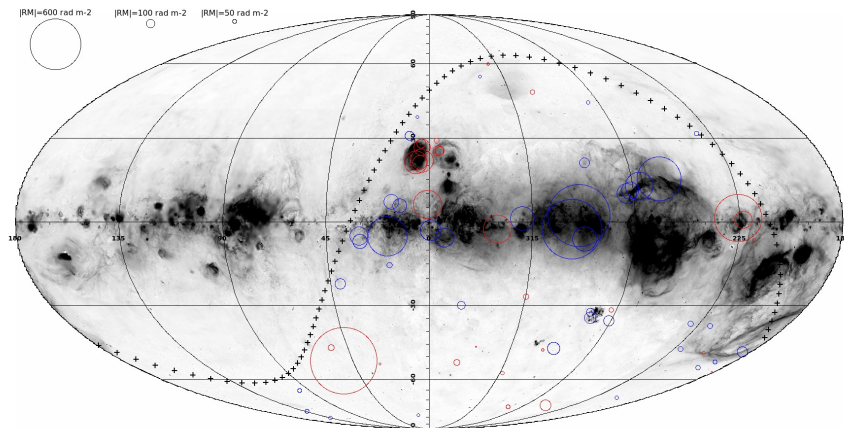


Figure 5.3 – *The spatial distribution of sources identified as outliers, overplotted on the $H\alpha$ map by Finkbeiner (2003). Positive and negative RM values correspond to blue and red markers, respectively. The black crosses indicate the celestial equator which limits the coverage of the RM data. The $H\alpha$ intensities in the background range from 0 (white) to 80 (black) Rayleigh with an arcsinh scale.*

impact of the measurement errors in the S-PASS RMs and the RMs from the Mao catalogue on the variance of the RM difference between these catalogues. From a Monte Carlo simulation of the variance in ΔRM due to the measurement errors of the individual lines of sight we find that the combined measurement errors alone ($\sigma_{err} = 2.65 \text{ rad m}^{-2}$) cannot fully explain the observed RM variance. A systematic trend is visible in Fig. 5.4 at low values in the distribution of RM difference between the S-PASS sources that are also in the catalogue by Mao et al. (2010). However, the small average value and standard deviation of the RM difference between sources from our catalogue and the catalogue by Mao et al. indicates that the RM values in these catalogues agree well with each other.

5.2.4 RM comparison with the NVSS catalogue

The NVSS catalogue of RMs of extragalactic sources consists of 37543 entries (Taylor et al. 2009), covering the sky above $\delta > -40^\circ$ and providing a source density of one source per square degree. The median RM error from the NVSS RM catalogue (10.80 rad m^{-2}) is much larger than the median RM error in the catalogue by Mao et al. (5.00 rad m^{-2}). The larger errors reflect the lower accuracy of the position angle measurements at the NVSS frequencies. In addition, these RMs have been calculated by a linear least-squares fit of the polarization angle as a function of the square of the wavelength and suffer from the $n\pi$ -ambiguity problem. Because only two wavelengths were used the NVSS RMs are unreliable when the RM magnitude is larger than a few hundred rad m^{-2} (Taylor et al. 2009). These limitations are partially compensated by the very large source density and not using sources near the mid-plane, where high RMs are expected. However, due to

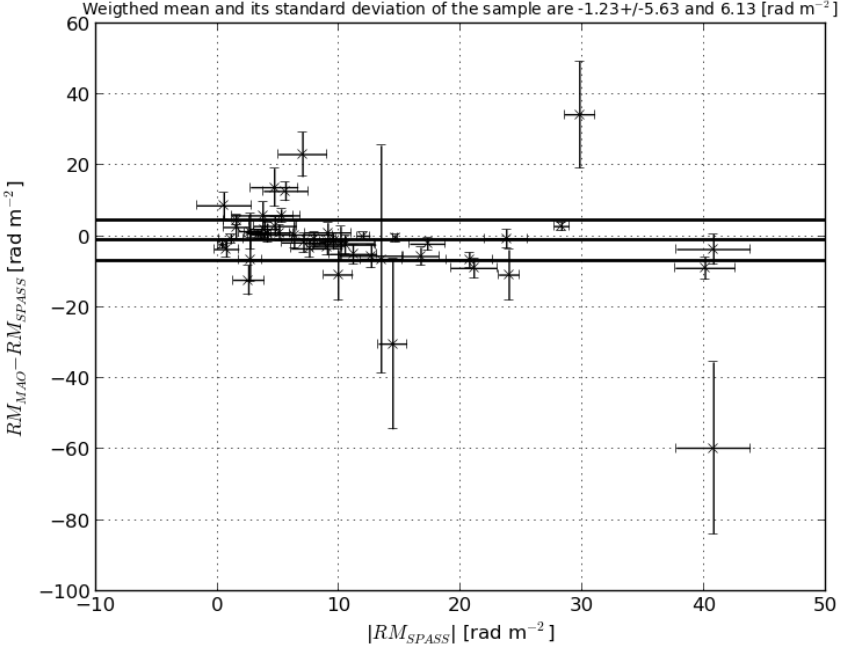


Figure 5.4 – The RM difference between sources within 12 degrees of the South Galactic Pole that are both in the catalogue by Mao et al. and in S-PASS.

the large NVSS sky coverage, the RM comparison between the S-PASS and the NVSS catalogues allows us to compare the quality of the S-PASS RMs and NVSS RMs at a range of Galactic longitudes and latitudes, which also includes lines of sight towards complex ISM structures and H II regions. Indeed the impact of H α structures at high latitudes is negligible, therefore we could not use the above comparison with Mao et al. (2010) to assess their effect on the RMs and structure functions. Because of the absence of bright H α features towards the SGP, we did not remove outliers from the Mao catalogue. In order to compare the S-PASS RMs with the NVSS RMs, we use the S-PASS data set which still includes outliers.

1482 S-PASS RMs could be cross-correlated with NVSS RMs, using source positions in NVSS and S-PASS which were not allowed to be further than 9 arcmin away from each other. In Figure 5.5 we show the RM difference as a function of longitude instead of RM, to avoid cluttering the plot. The RM difference has a mean and standard deviation of -1.62 and 10.84 rad m⁻². No systematic scatter is found towards bright H α features, e.g. the disk, the Gum nebula and the nearby and extended H II regions. However, a bunch of scattered sources with highly positive RMs difference is seen towards the Gum nebula at $l \in [250^\circ, 270^\circ]$. These outliers are likely caused by the $n\pi$ ambiguity affecting the NVSS

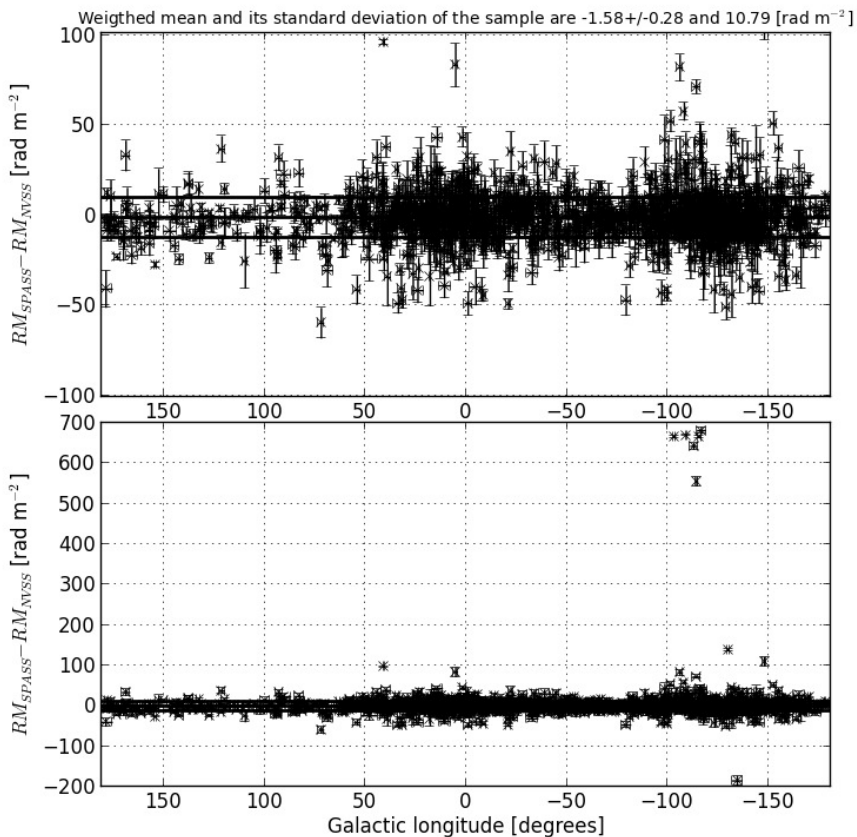


Figure 5.5 – The all-sky distribution of RM difference between S-PASS and NVSS cross-correlated sources in the region of overlap ($-40^\circ < \delta < 0^\circ$) as a function of Galactic longitude. The outliers at $RM = +600 \text{ rad m}^{-2}$ seen in the bottom panel correspond to lines of sight that pass through the Gum nebula.

RMs determination towards this complex ISM feature which makes large intrinsic RMs, into small values in NVSS.

Finally to estimate how much the measurement errors in both the S-PASS and NVSS RMs contribute to the variance of the RM difference between these catalogues we follow the same method adopted for the RM comparison with the data of Mao et al. (2010). Again we find that the combined measurement errors alone (4.86 rad m^{-2}) cannot fully explain the observed RM variance.

5.3 Structure function calculations

The second order RM structure function ($D_{RM}(\delta\theta)$) is defined as

$$D_{RM}(\delta\theta) = \langle [RM(\theta) - RM(\theta + \delta\theta)]^2 \rangle \quad (5.1)$$

for pairs of lines of sight towards directions θ and $\theta + \delta\theta$, where the angle brackets indicate the ensemble average for any line of sight calculated for all lines of sight of a region of a specified size. Pairs of lines of sight are distributed uniformly in $\log(\delta\theta)$ between a fixed minimum and maximum angular distance (see for example Figure 5.8). As Haverkorn et al. (2004) showed, the measurement uncertainties in RM offset the structure function amplitudes. Assuming that the measurement errors in RM (σ_{RM}) follow a Gaussian distribution, this offset can be calculated and removed as follows:

$$D_{RM}(\delta\theta) = D_{RM}^{OBS}(\delta\theta) - D_{\sigma_{RM}}(\delta\theta) \quad (5.2)$$

The radius of the region over which we calculate the structure function, the bin width as well as the number of bins that we use to calculate the structure function are crucial parameters for calculating and comparing structure functions features and are related to the catalogue source density. Because one of the aims of the present analysis is to perform a comparison with the results of Stil et al. (2011), the values adopted by Stil et al. (2011) to calculate structure functions are a good starting point. In this section we first investigate how different source densities affect the structure function amplitudes and slopes that we calculate, due to the different source density between the S-PASS and NVSS catalogues.

5.3.1 The size of the sampling regions, and the width of the structure function bins

With a source density of one line of sight per square degree Stil et al. (2011) calculated structure functions for all lines of sight within 5 degrees of each grid point on the sky, sampling angular distances between 1 and 10 degrees with 16 $\delta\theta$ bins that are uniformly spaced in $\log(\delta\theta)$. Because the sampling region is not very big no corrections were applied for the the RM gradient related to the large-scale magnetic field.

However, the surface density of S-PASS lines of sight is almost an order of magnitude smaller than the surface density of NVSS RMs. In order to compensate for the smaller surface density of S-PASS lines of sight we increase the bin size ($\delta\theta$). Then we only have to increase the size of the sampling region slightly (from 5 degrees to 6 degrees) to have enough lines of sight so that we can reliably calculate structure functions from our S-PASS data. To characterize the structure function profile we assume the turnover point to occur at $\delta\theta \leq 1^\circ$ similar to Stil et al. (2011). In that case we only have to fit the structure function slope and amplitude beyond the turnover point, which can be done with fewer, and wider, bins than those used by Stil et al. (2011). Thus we only use 5 bins to fit the structure function beyond the turnover point, sampling separations between 1 and 12 degrees, and using a uniform distribution in $\log(\delta\theta)$. Even if in some parts of the sky the

turnover point occurs on angular scales above 1 degree, the average distance between S-PASS lines of sight of about 8 degrees means that this will not affect the S-PASS structure functions strongly.

An approximate range of values for the optimum radius can be found by inspecting the source density all-sky maps which describe the spatial variations of the source surface density for different radii. We calculated source densities on a rectangular grid on the sky, using circles with radii between 5-12 degrees. Increasing the size of the sampling region reduces the number of sampling regions with very small numbers of lines of sight in them, but at the cost of losing resolution on the sky. In addition, large-scale RM gradients that affect structure functions slopes and amplitudes become more important when the sampling region is too large. In order to minimize the number of rejected regions and obtain a dense sampling of the plane of the sky, a range of 6–8 deg for the optimum radius is derived and we selected a value of 6 degrees which gives us better resolution on the sky. To understand how well we can measure the slope and amplitude of structure functions using the surface density of S-PASS lines of sight, we select a number of lines of sight from the catalogue by Mao et al. (2010) from the region $b < -84^\circ$, calculate the structure function slope and amplitude from this sample, corresponding to a sampling region with a radius of 6 degrees, and we repeat this 500 times with different source selections to estimate the uncertainties in the slope and amplitude. By selecting different numbers of lines of sight over the region $b < -84^\circ$ we can study how accurate the structure function slopes and offsets are for different surface densities of lines of sight (see Fig. 5.6).

To summarize, for our analysis the smallest angular separation is fixed to be $\delta\theta_{MIN} = 1^\circ$. The largest angular separation ($\delta\theta_{MAX}$) is dictated by the size of the sampling region of the adopted grid and we find $\delta\theta_{MAX} = 12^\circ$ to be optimal. The linear dimension of the region we consider is not much larger than that considered by Stil et al. (2011), so we did not correct RMs of lines of sight for large-scale gradients in RM before calculating structure functions. On average the sampling regions contain 15 lines of sight. We discard sampling regions with fewer than 10 sources and structure function bins with fewer than 5 sight-line pairs to correct each bin in the structure functions for measurement errors.

5.3.2 Comparison with NVSS structure functions

In order to perform a comparison with slopes and amplitudes derived by Stil et al. (2011) we use a Cartesian grid of points separated by half the size of the sampling region, or 3 degrees, to derive contour maps of RM structure function amplitudes and slopes. In Fig. 5.7 we display the final spatial sampling corresponding to the adopted parameters. To be sure that the structure functions are calculated for regions that fall completely within the area covered by S-PASS we only consider pixels with $\delta < -6^\circ$, which is indicated by the black solid line. We use the reduced χ^2 as a parameter to judge the goodness of the fitted structure function and identify which lines of sight are properly modelled. As displayed in Fig. 5.7 most regions on the sky can be fitted well by the structure functions and our choice of parameters for the fitting, but a number of poorly fitted lines of sight are also seen. Furthermore 43 structure function profiles with negative slopes are found in S-PASS data, while these lines of sight cannot be identified based on their χ^2 values.

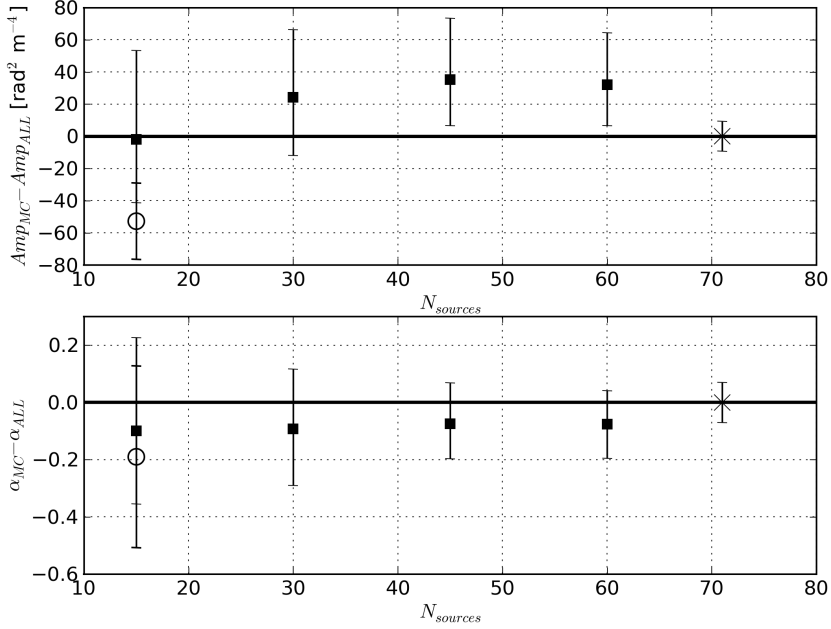


Figure 5.6 – Plot of the amplitude and slope differences between the Monte Carlo (MC) simulation outcomes and the RMs structure function values for different surface densities. Structure functions are calculated by selecting lines of sight from the catalogue by Mao et al. (2010) that lie within 6 degrees of the South Galactic Pole. The comparison with the S-PASS structure function values is also shown by the empty black circle, while the cross indicates the value for the full Mao sample for lines of sight within 6 degrees of the South Galactic Pole.

Structure functions with negative slopes are seen around $(l, b) \approx (342^\circ, -6^\circ)$, which is not surprising due to the complex medium probed by these lines of sight towards the nebula RCW 114 (Welsh et al. 2003), as well as around $(l, b) \approx (316^\circ, 60^\circ)$. Finally we find a number of lines of sight exhibiting negative slopes towards high Galactic latitudes around $(l, b) \approx (6^\circ, -66^\circ)$. Negative slopes are not physical and may be due to the presence of outliers in the RM data (Sun & Han 2004). Thus we check the RMs distribution towards these peculiar lines of sight, finding no deviation at the 3 sigma level of large RM values. However, we note these slopes are consistent with zero within 2σ and we consider negative slopes to be due to statistical fluctuations of the RMs sample.

To show the quality of the slopes and amplitudes we obtain, we display in Fig. 5.8 a structure function profile towards the Gum nebula at $(l, b) \approx (252^\circ, -9^\circ)$ and we compare with the one derived by Stil et al. (2011) and shown in their Figure 8. The structure function profile towards this line of sight does not show any break up to an angular scale

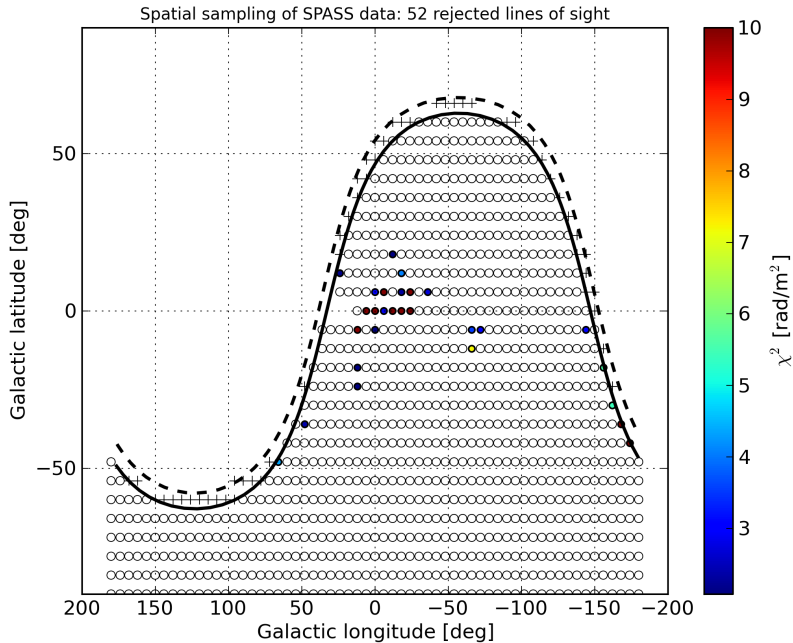


Figure 5.7 – The spatial sampling for the calculation of the structure functions corresponding to the $R = 6^\circ$ optimum sampling radius. The declination limit ($\delta = -6^\circ$) at which structure functions are calculated and the overall sampling of the S-PASS RMs data are indicated by the black solid and dashed lines, respectively. The goodness of the fit for each line of sight is indicated by the color bar. Empty circles indicate lines of sight with a reduced- χ^2 lower than 2.

of 10° and has a low value of the χ^2 due to the linear relationship between the data points. The results from the fits to the NVSS and S-PASS data are listed in Table 5.3 and indicate a good agreement, with the amplitudes (A) and slopes (α) matching within 2σ .

5.4 Observational results

In this section we present all-sky contour maps of structure function slopes and amplitudes that we calculated from the S-PASS and NVSS RMs. Then we compare S-PASS structure functions on either side of the Galactic plane with with SGPS structure functions towards the Galactic plane in order to check whether the contrast in structure function slopes and amplitudes that Haverkorn et al. (2008) found towards arms/interarm regions in the Galactic plane is also visible further from the Galactic plane. Finally we interpret the results from our structure functions analysis in term of interstellar turbulence.

Table 5.3 – Comparison between S-PASS and NVSS RMs structure function amplitudes and slopes towards the Gum nebula.

	$\log_{10} A$	α
Stil et al. (2011)	3.72 ± 0.04	1.14 ± 0.09
This paper	3.51 ± 0.07	1.14 ± 0.14

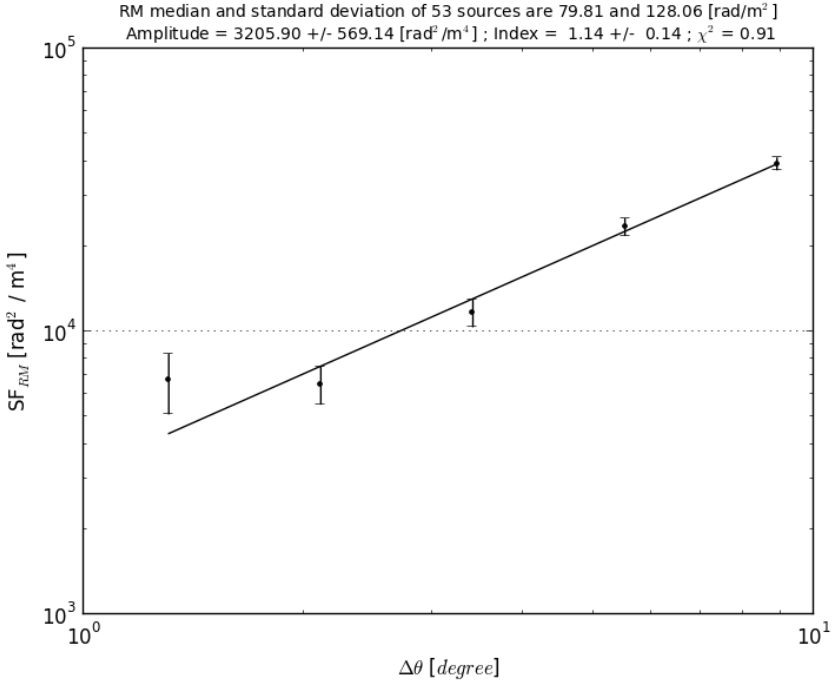


Figure 5.8 – The S-PASS measured structure function towards $(l, b) \approx (252^\circ, -9^\circ)$.

5.4.1 Structure functions contour maps

Both the S-PASS and NVSS structure functions were calculated on rectangular grids with spacings of 6 and 5 degrees, respectively. In order to have smoother contours, we linearly interpolated the values of amplitudes and slopes on a denser grid with a spacing of 1 degree. The amplitude and slope contour maps for both S-PASS and NVSS are displayed in Fig. 5.9, with the Finkbeiner (2003) $H\alpha$ intensity map plotted in the background. As shown in Fig. 5.7 only data below $\delta = 0^\circ$ have been sampled and contours above this declination, which are due to the sparse sampling, are not used in the following. Note that the structure functions are severely oversampled at high Galactic latitudes. The use of contour levels to display structure function features implies a selection from the bulk of

detected features. Both Galactic and extragalactic extended structures (e.g. H II regions, the radio loops) are seen in the RM data but depending on the choice of the contour levels only some structures will finally appear. In order to perform a comparison with the results of Stil et al. (2011), we adopt the same contour levels of Stil et al. (2011).

The contour maps of structure function amplitude and slope reveal different morphologies. The contour map of structure function amplitude relates to the intensity of the MHD turbulence. As expected, larger amplitudes are seen towards the Galactic plane, with a fair correlation with the diffuse H α emission. However, a weak correlation is seen with nearby, extended and H α bright features. The structure function slope relates to the outer scale of the MHD turbulent cascade. Several features with the steepest slopes in the contour map are associated with nearby objects such as the Gum nebula and the Sh 2-27 H II region around $(l, b) \approx (6.3^\circ, 23.6^\circ)$. Moreover, compact features with moderate slopes are found in the NVSS map towards the anti-centre at positive, high Galactic latitudes while there is no H α bright counterpart. The NVSS slopes show a general trend in Galactic latitude, with flatter structure function slopes towards the Galactic poles. This trend is also apparent in the S-PASS map, which in addition shows a path with small structure function slopes between about $-20^\circ < l < -60^\circ$ and $0^\circ > b \gtrsim -50^\circ$. Flat slopes in structure function can have different origins: either the fluctuations are purely white noise, or the probed scales are all above the saturation scale of turbulent fluctuations. Lastly, towards the Galactic poles, the intrinsic RM of the extragalactic background sources is not negligible with respect to the Galactic contribution (see Schnitzeler et al. 2010), which can also explain a flat structure function slope (e.g. Leahy 1987). A flattening of the structure functions slope is also seen in the S-PASS slopes around $(l, b) \approx (45^\circ, -25^\circ)$. The comparison with the NVSS RMs shows a clearly delineated filament where the RMs are up to $+200 \text{ rad m}^{-2}$ (extremely high at this Galactic latitude) embedded in a region where the RMs are generally $\approx -50 \text{ rad m}^{-2}$. Indeed Hill et al. (2013) reported the presence of enhancements in RMs which correlate with the H α intensities and are associated with the complex region around the Smith Cloud, a high velocity cloud.

5.4.2 Comparison with the SGPS structure functions

Using 148 RMs from the Southern Galactic Plane Survey (SGPS; McClure-Griffiths et al. (2005), Haverkorn et al. (2006)), Haverkorn et al. (2008) found a striking difference in the structure function slopes towards Galactic spiral arms and interarm regions. While the SGPS only covers latitudes between $\pm 1.5^\circ$ of the Galactic plane, we can use the S-PASS structure functions to investigate the transition between the Galactic plane and the lower Galactic halo.

In Fig. 5.10 we compare the S-PASS and SGPS slopes and amplitudes as a function of the Galactic longitude towards the disk in the 4th Galactic quadrant. The structure function values for the SGPS data are taken from Haverkorn et al. (2008). The amplitudes agree within the errors, showing no trend with Galactic longitude. However, the slopes reveal different profiles for the two data sets. While SGPS structure function slopes are flat towards the arm regions, the S-PASS slopes are positive. Moreover, S-PASS structure functions tend to flatten towards the interarm 3 region in correspondence to a local min-

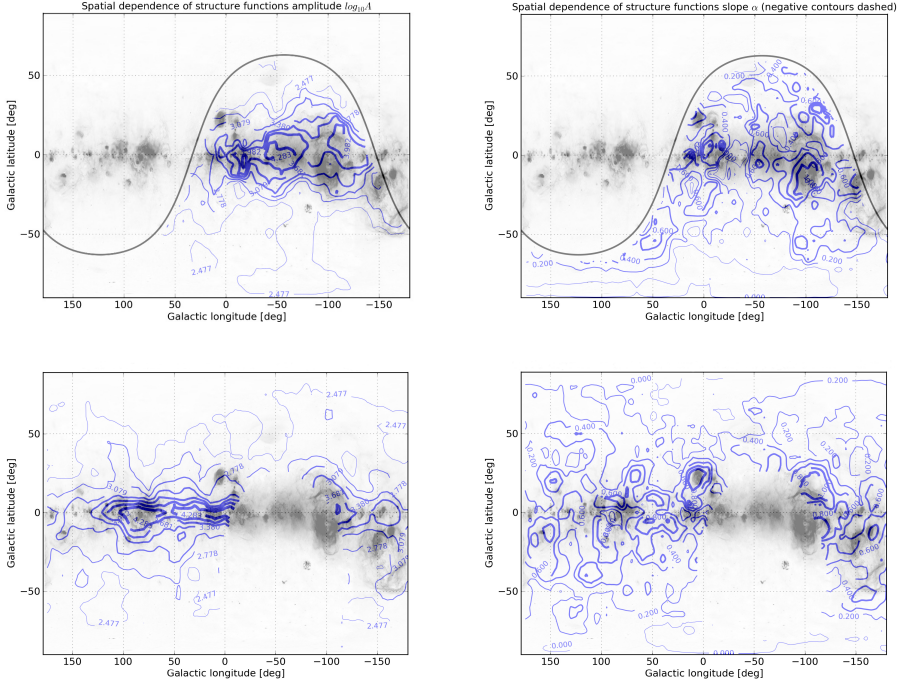


Figure 5.9 – Composite image showing the structure function amplitudes and slopes in the left and right panels, respectively. The S-PASS and NVSS results are displayed in the upper and lower plots, respectively. The $H\alpha$ intensity map by Finkbeiner (2003) is shown in the background for a comparison with the structure function contours. The $H\alpha$ intensities in the background range from 0 (white) to 80 (black) Rayleigh with an arcsinh scale. The contour levels for both amplitude and slope are marked along the contours, the contour thickness increases with the values. In the S-PASS plots the declination limit $\delta = 0^\circ$ is indicated by the solid black line.

imum of SGPS RMs (Brown et al. 2007) while the SGPS structure function slopes are positive. SGPS RMs of extragalactic sources from the Southern Galactic Plane Survey have been calculated by a linear least-square fit of the polarization angle as a function of the square of the wavelength, using 12 separate bands. Haverkorn et al. (2008) calculated structure functions for the spiral arm and interarm regions separately (in the longitude ranges indicated in figure 5.10), correcting for large-scale RM gradients, and discarding 27 outliers towards bright $H\alpha$ features. Although large-scale RM gradients that can affect structure functions were subtracted from the SGPS data but not from the S-PASS data, there is no reason why this would explain the differences between the two surveys. Because the SGPS structure functions were calculated over a much smaller range in Galactic latitude than the S-PASS structure functions, the difference between the SGPS and S-PASS structure function slopes indicates that these slopes only become flat close to the

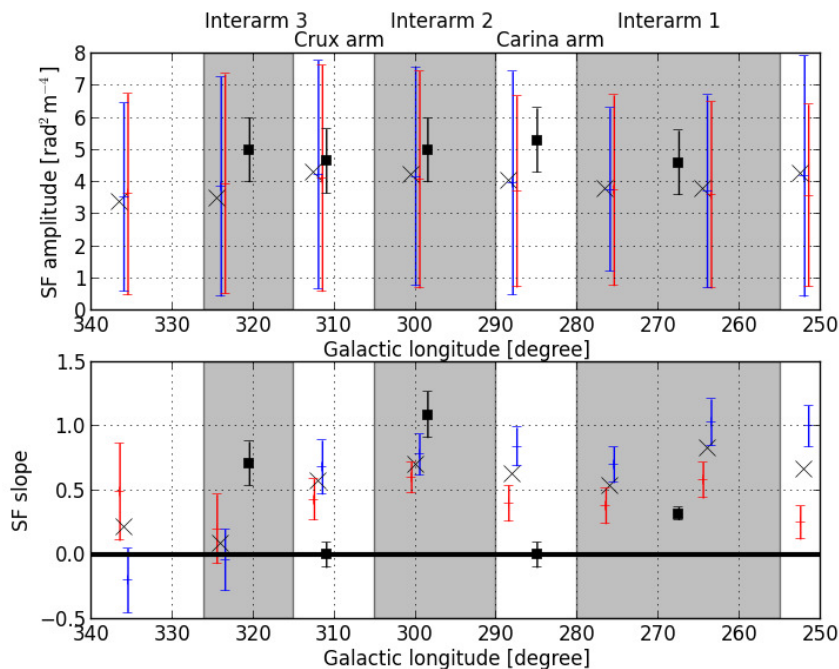


Figure 5.10 – Structure function amplitudes and slopes from the S-PASS (black \times) and SGPS (black squares) data towards the disk in the 4th Galactic quadrant. The S-PASS data at $b = -6^\circ$ (blue plus) and $b = +6^\circ$ (red plus) are plotted to check for trends. The location of the arm and interarm features as defined in Haverkorn et al. (2008) are also indicated.

Galactic disk.

5.4.3 Contour maps and ISM turbulence

A large-scale trend is seen in both the NVSS and S-PASS contour maps of amplitude and slope, but with a different morphology of contours. Amplitudes increase with decreasing distance to the Galactic plane, thus indicating increasing turbulent fluctuations towards the Galactic plane. This behaviour of the amplitude of turbulent fluctuations matches with the idea of sources triggering turbulence being mostly located in or around the Galactic plane, supporting the idea of a supernova-driven turbulent ISM (see e.g. MacLow 2004, Hill et al. 2012).

Local, extended $H\alpha$ bright features do not leave imprints on the structure function amplitude. Therefore the line of sight path-length and the size of the turbulent cells are the relevant parameter for characterizing the intensity of turbulence, in agreement with the statistical description by a sum of stochastic fluctuations. The smoothness of the con-

tours as a function of the Galactic longitude observed towards intermediate/high Galactic latitudes can also be related to the size of the turbulent cells along the line of sight. At a constant Galactic latitude away from the Galactic plane (so that the lines of sight probe only the Galactic halo and the finite extent of the Milky Way disk does not play a role) different lines of sight have the same path length, thus to average out fluctuations of structure functions amplitude a large number of turbulent cells is needed. Assuming a scale height of about 1.5 kpc for the thermal electron density (Gaensler et al. 2008, Schnitzeler et al. 2012) and a number of cells $\gtrsim 10$ an upper limit of 150 pc for the cell size away from the Galactic plane is derived to smooth out fluctuations on the largest scales. This upper limit agrees with values obtained for the outer scale of turbulence in the halo of both the Milky Way (see e.g. Chepurnov et al. 2010) and nearby galaxies (see e.g. Houde et al. 2013).

Also the contour map of structure function slopes exhibits systematic steeper values at Galactic latitudes $\lesssim 40^\circ$, but the contours are much less regular as a function of Galactic longitude. We note that the trend seen in the NVSS and S-PASS contour maps of the structure functions slope resembles that seen by Carretti et al. (2010), who identify a transition from thick to thin disk around a Galactic latitude of 20–40 deg. Thus, the observed variations of the structure function slope would indicate the transition between the disk and the halo. However a quantitative comparison between our results and those by Carretti et al. (2010) is not straightforward because the data sets probe the component of the magnetic field and its fluctuations along and normal to the line of sight, respectively, and because of the different lengths of the line of sight through the medium.

Over the range of angular scales 1–12 degrees 3D Kolmogorov-like turbulence with a power-law slope of $5/3$ is rarely observed, which was found previously by Minter & Spangler (1996) and Stil et al. (2011). Because of the adopted Cartesian grid the lines of sight at high Galactic latitudes are highly correlated and have systematically flat slopes, thus introducing a bias in the distribution. In order to avoid such a bias we only plot slopes of lines of sight with $|b_{lim}| \lesssim 75^\circ$. The distribution of the S-PASS structure function slopes is more symmetric than the NVSS one, while both are centred on low values of ~ 0.36 as shown in Fig. 5.11. The centres of the distributions are consistent with the expected slopes $\alpha_{2D} = 2/3 = 0.67$ and $\alpha_{3D} = 5/3 = 1.67$ of the 2D (Thompson, Moran & Swenson 1991) and 3D (Goldreich & Sridhar 1995) MHD turbulence within 1.3σ and 5.4σ , respectively. The systematic offset as well as the widths of the distributions disfavour 3D MHD turbulence. Furthermore the few lines of sight with slopes consistent with 3D MHD turbulence are seen towards local structures, thus being not representative of the turbulence in the diffuse ISM.

The observed low values of structure function slopes that is consistent with 2D MHD turbulence may be explained by assuming a filamentary morphology of turbulent structures in the diffuse ISM. Filamentary structures are generally observed in the multi-phase ISM from radio to optical wavelengths. Numerical studies (see e.g. Padoan et al. 2001, Burkhart et al. 2012) show that transonic and supersonic isothermal MHD turbulence can produce complex network of shocks, which shapes both the neutral and ionized ISM into sheets and filamentary features. Several mechanisms of filament formation involving turbulent flows have been discussed in literature. Both the warm neutral and ionized

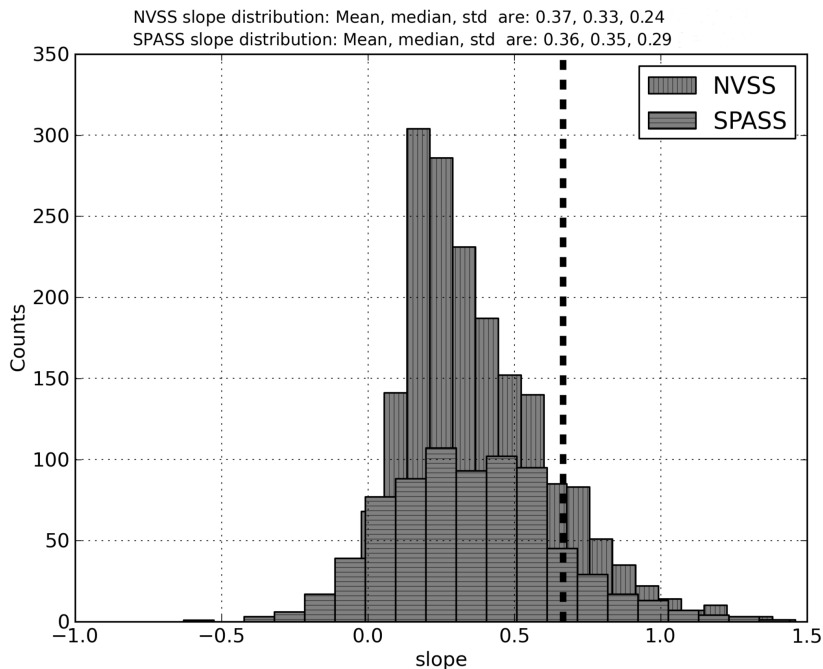


Figure 5.11 – Distributions of structure function slopes from the S-PASS and NVSS data for Galactic latitudes $|b_{\text{lim}}| \lesssim 75^\circ$. The expected slope of the 2D MHD turbulent cascade is also indicated by the black dashed line.

ISM phases show 2D turbulent structures and Foster et al. (2013) claimed that both the neutral, partially ionized and the ionized ISM phases influence the RMs of extragalactic sources. Therefore this partially ionized medium may explain the low correlation of the contour maps with the $\text{H}\alpha$ emission. A filamentary morphology could cause 2D turbulence, which has a flatter structure function slope than Kolmogorov-like turbulence. We note that the flattening of structure function slopes below the α_{2D} and α_{3D} values could result from line-of-sight effects modulating the angular correlation function. Line-of-sight effects have been applied to explain the structure functions and angular power spectra of total intensity, polarized intensity and optical polarization (see e.g. Cho & Lazarian 2002, 2010), but not RM structure functions.

Earlier observations of density and magnetic turbulent fluctuations suggest that the turbulence in the ISM is three-dimensional on small (i.e. $\lesssim 10$ pc) scales but flattens on larger scales (see e.g. Minter & Spangler 1996). Such a flattening has been interpreted in terms of two-dimensional turbulence, implying that motions are dominated by two-dimensional structures up to the scales of energy injection (i.e. the outer scale of the MHD cascade). A further flattening of spectra towards larger (i.e. > 100 pc) scales may

suggest the presence of an inverse cascade of magnetic helicity. The presence of helicity in the turbulent, multiphase ISM is not surprising. Relevant helicity fluctuations originate in strong SNR-driven shocks interacting with background interstellar turbulence (Balsara et al. 2001, Balsara & Kim 2005). According to this interpretation, the RM structure functions over the angular range 1–12 degrees, which corresponds to a range of spatial scales of ~ 0.1 –5 kpc at low latitudes and for a radial exponential scale length of the magnetic field of ~ 12 kpc (Beck et al. 2013), would probe the inverse MHD turbulent cascade sustained by the magnetic helicity, rather than magnetic energy.

Finally, we note that flat slopes are dominant only towards the Galactic poles. At high latitude the lines of sight mostly probe the local turbulence and turbulence in the halo. The flattening of the slopes towards high Galactic latitudes can be justified by the presence of a relevant intrinsic contribution in the RMs of the extragalactic sources along with the foreground Galactic contribution. The former explanation is favoured because the variance of the RMs due to the intrinsic contribution of the extragalactic sources is comparable to the one of the Galactic contribution at high Galactic latitudes (Schnitzeler et al. 2010) and the stochastic nature of these fluctuations implies flat structure functions with a spatially smooth distribution. Because of the absence of fluctuations in the amplitudes the latter explanation implies the local turbulence is weak (because of the observed low amplitudes) and the number of turbulent cells along the line of sight large.

5.5 Summary and Conclusions

We presented a new sample of RMs below declination $\delta = 0^\circ$ obtained in the framework of the S-PASS survey project. We assessed their accuracy by comparing this catalogue with the Taylor et al. (2009) and Mao et al. (2010) RM catalogues. We used both the NVSS and S-PASS RM catalogues to make a RM all-sky map displaying a wealth of structures both in terms of RM sign and amplitude. We investigated the fluctuations of RMs over the entire southern sky by calculating the second order structure functions of RMs and we find trends in agreement with the previous results of Stil et al. (2011) who only analysed RMs at declinations $\delta > -40^\circ$.

Steeper structure functions are seen towards nearby and extended objects such the Gum nebula and the H II region Sh 2-27. We compared the S-PASS with the SGPS structure functions towards the Galactic plane, finding no flattening for structure function slopes towards the arms when moving towards the Galactic plane. While the structure function slopes we derive from S-PASS and the structure function slopes from the NVSS RMs are inconsistent with 3D MHD turbulence, the median of the distribution is consistent with 2D MHD turbulence at the 1.3 sigma level. This result could be due to a much smaller outer scale for magnetic field fluctuations, as suggested by observations and numerical simulations (see e.g. Minter & Spangler 1996, Schekochihin et al. 2004), possibly combined with line-of-sight effects (Cho & Lazarian 2010). A constant outer scale of fluctuations will result in a variable angular outer scale for turbulence that extends along a line of sight, which can cause flattening of the structure function slope as well. Additionally, effects like 2-dimensional turbulence (Minter & Spangler 1996) may

play a role as well in specific parts of the ISM. Alternatively, the RM structure functions over the angular range 1–12 degrees may probe the inverse MHD turbulent cascade sustained by the magnetic helicity, rather than magnetic energy, in agreement with theoretical models of interstellar MHD turbulence driven by supernova explosions. If confirmed, the presence of an inverse MHD cascade of magnetic helicity in the ISM at large (i.e. 0.1–5 kpc) spatial scales, thus shaping the large-scale Galactic magnetic field, provides a clue for theoretical efforts to understand the MHD dynamo processes in the Galaxy.

Acknowledgments We thank Dr. J. Stil for providing the structure functions derived from the NVSS RM catalogue. The research leading to these results has received funding from the European Union’s Seventh Framework Programme (FP7/2007-2013) under grant agreement number 239490. This work is part of the research programme 639.042.915, which is (partly) financed by the Netherlands Organisation for Scientific Research (NWO). This research has made use of the SIMBAD database, operated at CDS, Strasbourg, France.

Contributions D.H.F.M.S. carried out the original observations. M.I. performed the analysis under the supervision of D.H.F.M.S. and M.H.. All authors were collectively involved in the discussion and interpretation of the results.

Bibliography

- Armstrong J.W., Rickett B.J., & Spangler S.R. 1995, *ApJ*, 443, 209
- Balsara D.S., Benjamin R. & Cox D.P. 2001, *ApJ*, 563, 800
- Balsara D.S., Kim J. 2005, *ApJ*, 634, 390
- Beck R., Wielebinski R. 2013, in *Planets, Stars and Stellar Systems. Volume 5: Galactic Structure and Stellar Populations*, ed. T.D. Oswalt & G. Gilmore, 641
- Brentjens, M.A., de Bruyn A.G. 2005, *A&A*, 441, 1217
- Brown J.C., Haverkorn M., Gaensler B.M., Taylor A.R., Bizunok N.S., McClure-Griffiths N.M., Dickey J.M., Green A.J. 2007, *ApJ*, 663, 258
- Burkhart B., Lazarian A., Gaensler B.M. 2012, *ApJ*, 749, 145
- Carretti E., Haverkorn M., McConnell D., Bernardi G., McClure-Griffiths N.M., Cortiglioni S., Poppi S. 2010, *MNRAS*, 405, 1670
- Chepurinov A., Lazarian A., Stanimirović S., Heiles C., Peek J.E.G. 2010a, *ApJ*, 714, 1398
- Cho J., Lazarian A. 2002, *ApJ*, 575, 63
- Cho J., Lazarian A. 2010, *ApJ*, 720, 1181
- Condon J.J., Cotton W.D., Greisen E.W., Yin Q.F., Perley R.A., Taylor G.B., Broderick J.J. 1998, *AJ*, 115, 1693
- Elmegreen B. & Scalo J. 2004, *ARA&A*, 42, 211
- Finkbeiner D.P. 2003, *ApJS*, 146, 407
- Foster T., Kothes R. and Brown J.C. 2013, *ApJ*, 773, 11
- Gaensler B.M., Madsen G.J., Chatterjee S., Mao S.A. 2008, *PASA*, 25, 184
- Gaensler B.M., Haverkorn M., Burkhart B., Newton-McGee K.J., Ekers R.D., Lazarian A., McClure-Griffiths N.M., Robishaw T., Dickey J.M., Green A.J. 2011, *Nature*, 478, 214
- Goldreich P. & Sridhar S. 1995, *ApJ*, 438, 763
- Haverkorn M., Gaensler B.M., McClure-Griffiths N.M., Dickey J.M., Green A.J. 2004, *ApJ*, 609, 776
- Haverkorn M., Gaensler B.M., McClure-Griffiths N.M., Dickey J.M., Green A.J. 2006, *ApJS*, 167, 230
- Haverkorn M., Brown J.C., Gaensler B.M., McClure-Griffiths N.M. 2008, *ApJ*, 680, 362
- Hill A.S., Joungh M.R., Mac Low M.M., Benjamin R.A., Haffner L.M., Klingenberg C. Waagan K. 2012, *ApJ*, 750, 104
- Hill A.S., Mao S.A., Benjamin R.A., Lockman F.J., McClure-Griffiths N.M. 2013, *ApJ*, in press
- Houde M., Fletcher A., Beck R., Hildebrand R.H., Vaillancourt J.E., Stil J.M. 2013, *ApJ*, 766, 49
- Iacobelli M., Haverkorn M., Orrú E., Pizzo R.F., Anderson J., Beck R., Bell M.R., Bonafede A., Chyzy K., Dettmar R.J. and 78 coauthors 2013a, *A&A*, 558, 72
- Iacobelli M., Burkhart B., Haverkorn M., Lazarian A., Carretti E., Staveley-Smith L., Gaensler B.M., Bernardi G., Kesteven M.J., Poppi S. 2013b, submitted to *A&A*,
- Inoue M. & Tabara H. 1981, *PASJ*, 33, 603
- La Porta L., Burigana C., Reich W. & Reich P. 2008, *A&A*, 479, 641

- Lazarian A. & Pogosyan D. 2006, *ApJ*, 652, 1348
Lazarian A. & Pogosyan D. 2012, *ApJ*, 747, 5
Leahy J.P. 1987, *MNRAS*, 226, 433
MacLow Mordecai-Mark 2004, *Ap&SS*, 289, 323
Mao S.A., Gaensler B.M., Haverkorn M., Zweibel E.G., Madsen G.J., McClure-Griffiths N.M., Shukurov A., Kronberg P.P. 2010, *ApJ*, 714, 1170
Mauch T., Murphy T., Buttery H.J., Curran J., Hunstead R.W., Pietrzynski B., Robertson J.G., Sadler E.M. 2003, *MNRAS*, 342, 1117
McClure-Griffiths N.M., Dickey J.M., Gaensler B.M., Green A.J., Haverkorn M., Strasser S. 2005, *ApJS*, 158, 178
Minter A.H., Spangler S.R. 1996, *ApJ*, 458, 194
Murphy T., Mauch T., Green A., Hunstead R.W., Pietrzynska B., Kels A.P., Sztajer P. 2007, *MNRAS*, 382, 382
Padoan, P., Juvela M., Goodman A.A., Nordlund A. 2001, *ApJ*, 553, 227
Sault R.J., Teuben P.J. & Wright M.C.H. 1995, in *ASP Conf. Ser. 77, Astronomical Data Analysis Software and Systems IV*, ed. R.A. Shaw, H.E. Payne, & J.J. Hayes (San Francisco, CA: ASP), 433
Schekochihin A.A., Cowley S.C., Taylor S.F., Maron J.L., McWilliams J.C. et al. 2004, *ApJ*, 612, 276
Schnitzeler D.H.F.M. 2010, *MNRAS*, 409, 99
Schnitzeler D.H.F.M. 2012, *MNRAS*, 427, 664
Simonetti J.H., Cordes J.M., Spangler S.R. 1984, *ApJ*, 284, 126
Simonetti J.H., Cordes J.M. 1986, *ApJ*, 310, 160
Stil J.M., Taylor A.R., Sunstrum C. 2011, *ApJ*, 726, 4
Sun X.H. & Han J.L. 2004, in *Proc. Conf. on the Magnetized Interstellar Medium*, held in Antalya, Turkey, 2003 September 8–12, ed. B. Uyaniker, W. Reich, & R. Wielebinski (Katlenburg-Lindau: Copernicus GmbH), 25
Taylor A.R., Stil J.M., Sunstrum C. 2009, *ApJ*, 702, 1230
Thompson A.R., Moran J.M., & Swenson G.W. 1991, *Interferometry and Synthesis in Radio Astronomy*, Krieger Publ. Corp., Florida
Welsh B.Y., Sallmen S., Jelinsky S., Lallement R. 2003, *A&A*, 403, 605
Wilson W.E., Ferris R.H., Axtens P., et al. 2011, *MNRAS*, 416, 832
Wright A., Otrupcek R. 1990, *Parkes Catalog, 1990, Australia telescope national facility*

Final remarks and perspectives



6.1 Summary

Radio observations are an essential tool for investigations of Galactic magnetism and magnetohydrodynamic (MHD) turbulence of the ISM. Radio observations can reveal insights on both the atomic neutral and ionized phases of the ISM. Indeed magnetic fields permeates the ISM and influence both these phases, directly via the Lorentz force on charged particles and indirectly through the ion-atom scattering and diffusion. Furthermore a linear relationship between the mean of binned RMs of the extragalactic sources towards the Galactic plane and the H I column density has been recently pointed out by Foster et al. (2013), suggesting the diffuse magneto-ionic medium to be dominated by the partially-ionized Warm Neutral Medium (WNM) phase. In this framework the cartography of the structures of both the neutral and ionized phases of the ISM is mandatory.

In Chapter 2 we show the capability of low-frequency radio observations and RM synthesis to diagnostic local structures in the magneto-ionic medium. We claim the first radio detection of the Local Bubble edges towards the second Galactic quadrant at about 100 pc, in agreement with the recent mapping of Lallement et al. (2014). The nearby, bubble-like feature could be a relic or, following Foster et al. (2013), a structure related to a density enhancement in both the neutral and ionized medium. In both cases many more features are expected to be found by deep and wide-field RM synthesis studies at low-frequencies, allowing a 3D mapping of the solar neighbourhood and helping to address their origin. We show evidence for these structures being in a turbulent state and the characterization of the turbulence will provide clues to understand their origin and physics. In the context of this thesis a further step would be to combine the RM synthesis and the spatial gradients of the polarization vector techniques, to constrain both the sonic and (possibly) the Alfvénic Mach numbers of the different structures detected in Faraday depth space. Note that RM synthesis applied to low-frequency polarization data is sensitive to Faraday thin structures, thus allowing a direct comparison with simulations.

Valuable technical and observational as well as theoretical progresses have been done over the last decade, thus improving the knowledge of the MHD interstellar turbulence. In particular thanks the new generation of radio telescopes operating at low frequencies such as LOFAR we can now gain a sharper view of the magnetic fields structure and the interplay with the warm ionized medium (WIM) phase both in the Milky way and in the external galaxies. The new (LOFAR, ASKAP, MWA) and recently upgraded (WSRT, GMRT) facilities will allow to perform high-sensitivity and high-resolution radio observations over a wide field of view, allowing investigations of the diffuse synchrotron emission and its fluctuations, as outlined in Chapters 2 and 3, with unprecedented accuracy. Low-frequency radio observations are indeed sensitive to small Faraday depths from weak interstellar (and intergalactic) magnetic fields. Moreover the low frequency synchrotron emission arises from aged and low energy cosmic-ray electrons which propagates far away from the sources, thus allowing to better trace the magneto-ionic structures in the ISM and address the fluctuations in terms of MHD turbulence and weak magnetic fields. Therefore we expect to detect many nearby magnetic-ionic structures as the one discussed in Chapter 2 and recover patterns of synchrotron fluctuations in detail. Finally,

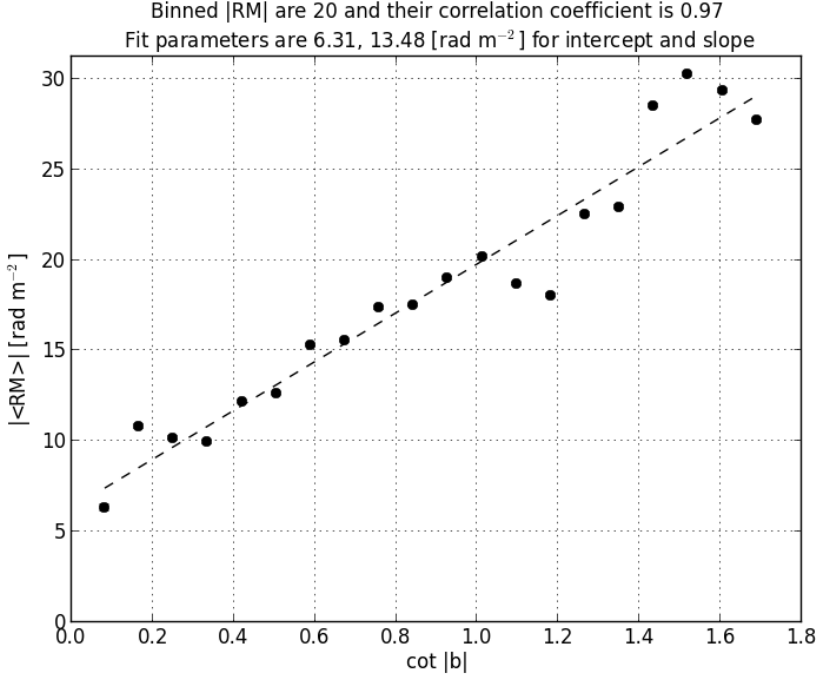


Figure 6.1 – The linear trend of the absolute values of averaged RMs for extragalactic sources binned as a function of $\cot |b|$, from which a scale height for the magnetic field of $h_B = (2459 \pm 720)$ pc is obtained.

the development of an observational approach combining multi-wavelength data from both imaging and spectroscopy is crucial to constrain a wide set of parameters (such as the gas and thermal electron densities, magnetic field components, the sonic and Alfvénic Mach numbers, the outer scale of turbulence and the Reynolds number) along the line of sight and for gaining an adequate description of a multi-phase, turbulent medium such as the interstellar one.

In Chapters 4 we find the interstellar turbulence in the isothermal WIM to be organized in a network of elongated, filamentary structures, reflecting its anisotropy on scales $\gtrsim 10$ pc. This observational result matches with the one found by (Gaensler et al. 2011) at scales $\lesssim 10$ pc. The presence of highly anisotropic structures in the WIM is also suggested by the detection of scintillation arcs in observations of scattering of pulsar radio emission (Rickett et al. 2011) at small ($\lesssim 1$ AU) spatial scales. Noteworthy our result is based on approach sensitive to both the density and magnetic field fluctuations, which may suggest the presence of a correlation between the fluctuations in these quantities. The observational evidence for the spatial structure in the ionized ISM being a network of filaments due to highly anisotropic turbulence is also supported by the theory of compressible

MHD turbulence (Lithwick & Goldreich 2001). The presence of a fully developed web of filamentary structures as seen (Chapter 4) over the entire southern sky may also relate with the propagation distance in the diffuse ISM of interstellar turbulence. As noted by Spangler (2007), the ion-neutral atomic collisions constitute a turbulence damping mechanism and the associated scale length is very short ($\lesssim 1$ pc), thus an efficient propagation mechanism of the interstellar MHD turbulence is needed. A network of filaments with highly-ionized gas (i.e. with a negligible ion-neutral collisional damping) allows for a diffusion of turbulent energy over longer distances. Further observational and numerical studies are needed to characterize the propagation distance of interstellar turbulence and clarify the relationship with the structures highlighted by the spatial gradient of the polarization vector.

Finally, the new, accurate S-PASS/ATCA RMs catalogue covering the 3rd and 4th Galactic quadrant is revealing the all-sky picture of the large-scale magnetic field of the Galaxy, as well as its turbulent properties. Several relevant spatial symmetries of both RMs sign and amplitude are seen in the all-sky RMs map shown in Chapter 5, allowing to improve the modelling of the field structure (Schnitzeler et al. (in prep.)). As an example, we show in Fig. 6.1 the linear relationship between the RMs amplitudes and the Galactic latitude from which a scale height for the magnetic field of $h_B = (2459 \pm 720)$ pc is obtained by assuming a scale of height for the thermal electrons $h_e = (1587 \pm 300)$ pc and an amplitude of about $2 \mu\text{G}$ for the regular field. This value is larger than earlier estimates (see e.g. Inoue & Tabara 1981) but in agreement with the scale height of the thermal electrons (see e.g. Gaensler et al. 2008) and the diffusion scale height of cosmic ray electrons in the solar neighbourhood (see e.g. Biermann et al. 2010).

In Chapter 5 we focus on the all-sky portrait of the interstellar turbulence derived from the second order structure functions of RMs, finding a systematic flattening away from the Galactic plane at angular scales larger than 1° . In some fields of view, the structure function slopes are consistent with 2D turbulence, while none of them correspond to 3D turbulence. The presence of a 2D spatial structure of the interstellar turbulence is suggested by observations of the thermal electron density fluctuations. A 2D or a fractal structure is also invoked to explain the propagation of turbulence away from the injection sites and matches with the portrait presented in Chapter 4. The spatial pattern of structure functions amplitude and slopes may also suggest the presence of an inverse MHD cascade of magnetic helicity in the ISM at large (i.e. 0.1–5 kpc) scales, thus shaping the large-scale Galactic magnetic field. Interestingly, the above estimate of the magnetic field scale of height support the presence of magnetic fields structures on the large spatial scales suggested by our structure functions results, providing a clue for the theoretical efforts to understand the MHD dynamo processes in the Galaxy as well as the confinement and propagation of cosmic-rays.

6.2 The LOFAR Magnetism key science project

Measuring radio waves at low frequencies offers a new window for astrophysics and cosmology, and the LOw Frequency ARray (LOFAR) is an innovative radio telescope with

multi-disciplinary capabilities (Van Haarlem et al. 2013) ready to open this window. One of the LOFAR key science projects (KSP) is the Magnetism Key Science Project (MKSP), whose aim is to make use of the LOFAR polarimetric capabilities to investigate weak, cosmic magnetic fields in a variety of astrophysical sources, to finally understand the origin of cosmic magnetism (Beck et al. 2013). The MKSP science goals concern the following fundamental and still unanswered scientific questions:

- the origin of the first magnetic fields, to discriminate between two major scenarios: magnetic field generated during the formation of proto-galaxies, or as relics from the early Universe before the galaxies were formed (for a review see e.g. Widrow 2002).
- the origin of large-scale fields from small scale seed fields: the amplification of fields is usually investigated in the framework of magnetohydrodynamic (MHD) dynamo processes but the physics of the galactic dynamo is far from being understood, with the preservation of total helicity, which leads to a quenching of dynamo action, being an unsolved issue (Brandenburg & Subramanian 2005).
- the presence of a large-scale network of intergalactic magnetic fields and its description, which relates to the above points of magnetic fields generation and amplification as well as to the study of the largest gravitationally bound structures in the universe, namely the clusters of galaxies.
- the importance of magnetic fields for the physics of galaxies and galaxy groups/clusters; magnetic fields are a fundamental ingredient of the interstellar medium (ISM) of the Galaxy (for a review see e.g. Ferrière 2001), having an energy density that is comparable to the energy density in cosmic rays and in the turbulent motions of the interstellar gas. Also, magnetic fields influence star formation by affecting the removal of angular momentum from proto-stellar clouds, thus playing a role in the formation and evolution of galaxies and clusters.
- the topology and the properties of magnetic fields and their feedback to the interstellar medium and the interstellar turbulence in our Galaxy.

To investigate the above fundamental astrophysical questions on the distribution of magnetic fields in the Universe the LOFAR MKSP project will utilise different observational approaches. The surveys will provide diffuse emission from the Milky Way and from nearby galaxies, tracking the propagation of long-lived cosmic-ray electrons through magnetic field structures, to search for radio halos around spiral and dwarf galaxies and for magnetic fields in intergalactic space. Targeted deep-field observations of selected nearby galaxies and suspected intergalactic filaments allow sensitive mapping of weak magnetic fields. In addition high-resolution observations of proto-stellar jets and giant radio galaxies will reveal structures on small physical scales and at high red-shifts, while pulsar RMs allow to map large-scale magnetic structures of the Galactic disk and halo in detail.

For these studies based on wide-field imaging at high angular resolution and high dynamic range the much better sensitivity and angular resolution of the new generation radio telescopes are needed. The main advantages to utilise low-frequency radio observations are due to the frequency dependence of both the synchrotron emission processes as well as the propagation effects in the magneto-ionic medium, which enhance the detectability of weak magnetic fields and their fluctuations. Furthermore, at low frequencies the contribution of the thermal emission is negligible and radio waves closely trace the non-thermal (i.e. cosmic rays and magnetic fields) components of the ISM. However, several technical issues (such as the depolarization effects, the ionospheric effects and a suited, high-precision polarization calibration) affect low-frequency radio observations making a fully exploitation of the LOFAR polarimetric capabilities challenging. Anyway, these observational efforts will focus on the understanding of the magnetic fields in galaxies and will boost our knowledge of the interstellar turbulence.

Bibliography

- Beck R., Anderson J., Heald G., Horneffer A., Iacobelli M., Köhler J., Mulcahy D., Pizzo R., Scaife A., Wucknitz O., LOFAR Magnetism Key Science Project Team 2013, AN 334, 548
- Biermann P.L., Becker J.K., Caceres G., et al. 2010, ApJ, 710, 53
- Brandenburg A. & Subramanian K. 2005, Phys. Rep., 417, 1
- Ferrière K.M. 2001, Rev. Mod. Phys., 73, 1031
- Foster T., Kothes R. and Brown J.C. 2013, ApJ, 773, 11
- Gaensler B.M., Madsen G.J., Chatterjee S. and Mao S.A. 2008, PASA, 25, 184
- Gaensler B.M., Haverkorn M., Burkhart B., et al. 2011, Nature 478, 214
- Inoue M. & Tabara H. 1981, PASJ, 33, 603
- Lallement R., Vergely J.L., Valette B., Puspitarini L., Eyer L., Casagrande L. 2014, A&A, 561, 91
- Lithwick Y. & Goldreich P. 2001, ApJ, 562, 279
- Rickett B., Stinebring D., Coles B., Jian-Jian G. 2011, in American Institute of Physics Conference Series, 1357, 97
- Spangler S.R. “The Propagation Distance and Sources of Interstellar Turbulence”, in “SINS-Small Ionized and Neutral Structures in the Diffuse Interstellar Medium”, Haverkorn M. and Goss W.M. editors, Astr. Soc. Pac. Conference Series 367, 307–314 (2007)
- Widrow L.M. 2002, Rev. Mod. Phys., 74, 775

Nederlandse Samenvatting

Introductie

Magnetisme in het universum manifesteert zich over een gigantisch bereik qua schaal-grootte. Magnetische velden bestaan vanaf kleine objecten, zoals planeten, sterren en nevels tot sterrenstelsels en clusters van sterrenstelsels. In het algemeen geldt hoe groter het object, hoe zwakker het magnetisch veld. Ongeacht hun sterkte spelen magnetische velden een significante rol in al deze omgevingen met invloed op een breed spectrum van fenomenen, zoals poollicht op planeten en sterrenvlammen. Deze fenomenen die gedomineerd worden door magnetische velden zijn de eerste die in de afgelopen eeuw bestudeerd werden. Vervolgens werd het onderzoek uitgebreid naar magnetische velden op een grotere schaal.

Dit proefschrift behandelt de interactie tussen het interstellair magnetisch veld en het turbulente warme interstellair medium in de Melkweg. Het doel van de volgende hoofdstukken is een overzicht te bieden over het ontstaan van onze huidige kennis over het interstellair medium en het beschrijven van enkele fundamentele concepten die bijzonder relevant zijn om dit proefschrift te begrijpen.

De geschiedenis van het interstellair medium

“Het is ondertussen welbekend dat de ruimte tussen de sterren verre van leeg is, het bevat zowel gas als kleine stofdeeltjes.” (van de Hulst 1946)

De uitspraak hierboven herinnert ons eraan hoe jong het concept van het interstellair medium is en toont hoe de sterrenkundigen tegen ons melkwegstelsel (en het universum) aankeken. Tot de 19de eeuw beschouwden sterrenkundigen onze melkweg als het gehele universum, gevormd door een gigantische hoeveelheid sterren in een vacuum. Ondanks dat waarnemingen door de Herschels een systematische aanwezigheid van nevels aan de hemel aan het licht bracht werd dit niet geaccepteerd als bewijs voor het diffuse interstellair medium.

Aan het begin van de 20ste eeuw toonden spectroscopische studies van sterren voor het eerst aan dat er zich tussen de sterren een diffuus medium bevindt. Hartmann (1904) toonde aan dat er in sterrenspectra “stationaire Ca II lijnen” verschenen waarvoor later door Plaskett & Pearce (1930) een correlatie aangetoond werd tussen sterkte van deze

“stationaire lijnen” en de afstand. Hiermee werd voor het eerst aangetoond dat er tussen de sterren een medium bestond dat het licht van deze sterren absorbeert. Vervolgens werd dit bewijs uitgebreid met studies van absorptie (Barnard 1919) en roodverkleuring (Trumpler 1930). Op dat moment werd er nog steeds van uit gegaan dat het interstellair medium homogeen en diffuus was, wat snel veranderde in de late jaren '30 met de komst van hoge resolutie spectroscopische waarnemingen van heldere sterren. Met deze waarnemingen werd aangetoond dat deze sterren omringd werden met gas dat zich bijzonder dynamisch en complex gedraagt. Het bestaan van een algemeen, diffuus, absorberend interstellair medium had een sterke invloed op een van de belangrijkste problemen in de sterrenkunde, namelijk het bepalen van afstanden tot de sterren met behulp van helderheidsmetingen (en dus studies naar de structuur van onze Melkweg).

In 1913 ontdekte Victor Hess met behulp van ballonvluchten ioniserende straling vanuit de hemel. Vervolgens, in 1927 toonde J. Clay aan dat deze straling het gevolg is van geladen deeltjes die met hoge energie de atmosfeer binnen komen. Hiermee werd een ander aspect van het interstellair medium ontdekt: kosmische straling. Tenslotte achtten Alfvén (1939) en Fermi (1949) de aanwezigheid van een magnetisch veld in het interstellair medium noodzakelijk om de versnelling en het insluiten van kosmische straling te verklaren. Dit idee werd bevestigd via de waarneming van gepolariseerd licht door Hall (1949) en Hiltner (1949a,b) en via de waarneming van het galactisch radio continuum door Reber (1944). Het waargenomen gepolariseerde licht werd verklaard met de aanwezigheid van ellipsoïde stofdeeltjes die door het magnetische veld georiënteerd worden (Davis & Greenstein 1951). Het Galactisch radiocontinuum wordt veroorzaakt door de versnelling van elektronen tot relativistische snelheden in een magnetisch veld, wat radiostraling veroorzaakt (Kiepenheuer 1950).

In de late jaren '40 was algemeen gekend dat het interstellair medium bestaat uit een gasvormig mengsel van atomen, ionen en moleculen (bijvoorbeeld Adams 1941) en uit stofdeeltjes (bijvoorbeeld Hall 1949). Naast deze complexe mengeling van materie bestaat het interstellair medium ook uit kosmische straling en magnetische velden: de moderne visie op de interstellair ruimte begon door te dringen. Uiteindelijk werd hier in de jaren '60 nog een hete en geïoniseerde component aan toegevoegd met de ontdekking van de Röntgen achtergrondstraling.

Het galactische ecosysteem en magneto-hydrodynamische turbulentie

Ondanks de uitgebreide kennis van vele aspecten van het interstellair medium mist er nog een algemeen model. Het grootste probleem hieromtrent is dat alle stukjes van deze interessante puzzel op een complexe manier met elkaar verbonden zijn. Het interstellair medium is bijzonder complex en dynamisch waarbij materie in meerdere fasen georganiseerd is. Gelukkig kan de status van materie door enkele parameters beschreven worden: de temperatuur, de dichtheid en de ionisatie. Het interstellair medium bestaat zowel uit neutrale materie als geïoniseerde materie, zie Tabel 6.3.

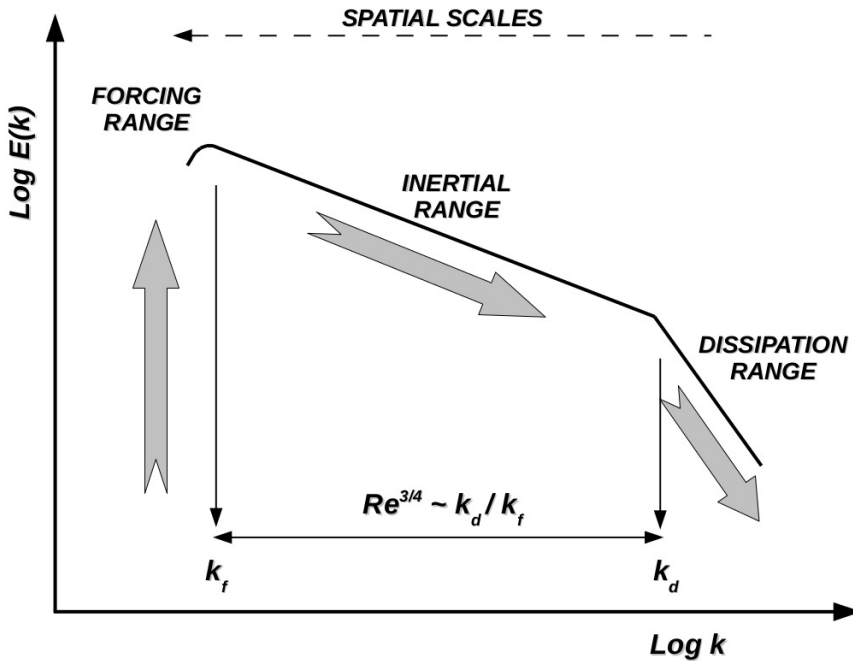
Tabel 6.1 – Fases van het interstellair medium: temperatuur, dichtheid en ionisatie.

Fase	T [K]	n_H [cm ⁻³]	ξ
Heet gas	$\gtrsim 10^{5.5}$	0.004	~ 1
Warm geïoniseerd gas	~ 8000	0.1	~ 0.9
Warm neutraal gas	~ 8000	0.5	~ 0.2
Koud neutraal gas	~ 100	50	$\lesssim 10^{-3}$

Door de cyclus van materie en energie wordt tegenwoordig algemeen aangenomen dat het interstellair medium een belangrijke rol speelt in de evolutie van onze Melkweg. De elementaire componenten en eigenschappen van het interstellair medium hebben een fundamentele invloed op de levenscyclus van een sterrenstelsel en de sterren erin. Name-lijk, de interactie tussen de sterren en het lokale interstellair medium beïnvloedt zowel de fysische als de chemische processen die de fundamentele evolutie van het sterrenstelsel bepalen. Daarnaast kan het interstellair medium beschouwd worden als een elektrisch geleidende vloeistof bestaande uit een turbulent kosmisch plasma.

Door de chaotische bewegingen in het interstellair plasma bestaat er een diepe wisselwerking tussen het turbulente plasma en het galactisch magnetisch veld. Deze wisselwerking zorgt voor een complexe veldstructuur die op zijn beurt zorgt voor een gigantisch transport van massa, energie, impuls en magnetisme. De turbulente bewegingen onder invloed van het magnetisch veld kunnen beschreven worden door een set wiskundige vergelijkingen die onderdeel maken van de nog onvolledige theorie, magneto-hydrodynamische (MHD) turbulentie genaamd. De fundamentele rol van MHD turbulentie in de verschillende fases van het interstellair medium heeft invloed op zowel de structuurvorming, de evolutie en de magnetisatie. Turbulentie is noodzakelijk om de omzetting van een deel van de kinetische energie in magnetische energie via zowel grote als kleine structuren en dynamo mechanismen. Als gevolg, heeft het onderzoek naar MHD turbulentie in astrofysische plasma's betrekking tot betrekking op bijzonder complexe niet-lineaire fenomenen zoals hoogst chaotische stromingen, fractale stromingen en gemagnetiseerde stromingen.

Het fenomeen is kwalitatief beschreven via het concept van een turbulente waterval (zie Fig. 6.4) waar de energie geïnjecteerd wordt op een gigantische schaal L_{out} en vervolgens via niet-lineaire processen zonder dissipatie getransporteerd wordt naar kleinere structuren met typische grootte van l_{diss} waar dissipatie plaats vindt. In het interstellair medium wordt de turbulente magneto-hydrodynamische waterval voortgedreven door verschillende bronnen (zoals supernova-explosies of sterke sterrenwinden). De energie wordt in het medium gebracht op verschillende ruimtelijke schalen (vermoedelijk 1 - 100 parsec) met de supernova uitbarstingen als grootste bijdrage. De dissipatie schaalgrootte (mogelijk ~ 500 km) en mechanisme is nog ter discussie.



Figuur 6.2 – Schematische voorstelling van de ruimtelijke energieverdeling van een turbulente waterval. De aandrijving ($k_f \sim 1/L_{out}$) en dissipatie ($k_d \sim 1/l_{diss}$) golfgetallen die de grootte en het bereik in inertiaalruimte bepalen zijn ook aangeduid. De energiestroming is van grote naar kleine schalen zoals aangeduid met de pijlen.

Samengevat, verschillende fysische processen zoals straling (zowel opwarming als koeling), magnetische velden, zwaartekracht en turbulentie zijn belangrijk in het interstellair medium. Om de evolutie van de melkweg te begrijpen zijn studies naar hun rol en interacties noodzakelijk. Het betreft hier grote wetenschappelijke vragen met betrekking tot interstellair turbulentie zoals: hoe magnetische velden versterkt, ondersteund en gevormd worden, hoe energietransport naar kleinere schalen zonder dissipatie via niet-lineaire processen verloopt, hoe de hieropvolgende kleinschalige dissipatie verloopt, de impact van deze processen op de voortplanting van kosmische straling en hoe het interstellair medium gestructureerd is. Om een realistisch globaal model van het interstellair medium te vormen dienen deze kwesties verklaard worden.

Radiowaarnemingen en interstellair MHD turbulentie

Interstellair turbulentie manifesteert zich via fluctuaties in ruimte of tijd van fysische grootheden zoals de dichtheid en snelheid van deeltjes of de sterkte van het magnetisch

veld. Metingen ter plekke zijn enkel mogelijk in het zonnestelsel en waarnemingen van het interstellair medium zijn tot op heden een uitdaging.

Radiowaarnemingen vormen de grootste bron van informatie over de interstellair turbulente en interstellair magnetische velden. Het is *de facto* mogelijk om radiowaarnemingen te gebruiken om de fluctuaties van zowel dichtheid, snelheid en om magnetische velden in zowel neutraal als geïoniseerd interstellair medium te detecteren. Deze fluctuaties manifesteren zich via de mechanismen die emissie en voortplanting van elektromagnetische golven in een gemagnetiseerd plasma bepalen.

Wanneer vrije kosmische elektronen zich met relativistische snelheden door het magnetisch veld in de Melkweg bewegen zullen zij synchrotronstraling produceren. De hoeveelheid straling is afhankelijk van de sterkte van het magnetisch veld en kan bijgevolg gebruikt worden als een indicatie van het plaatselijke magnetisch veld. Gezien de straling zich in het lage frequentiebereik bevindt (< 1 GHz) is het mogelijk om met een radiotelescoop metingen te verrichten. Uit metingen is gebleken dat het vlak van de Melkweg een sterke bron is van radiostraling wat impliceert dat er in het vlak van de Melkweg zich een sterk magnetisch veld bevindt.

Hiernaast is de voortplanting van de synchrotronstraling in het gemagnetiseerd en geïoniseerd interstellair medium onderhevig aan twee belangrijke effecten: dispersie en Faradayrotatie. De gevolgen van deze effecten hangt af van de dichtheid aan vrije, niet-relativistische elektronen en de sterkte van het magnetisch veld langs de zichtlijn tussen de bron en de waarnemer. Bijgevolg is het mogelijk om via deze manier variaties in dichtheid van deeltjes en magnetische veldsterkte langs de zichtlijn tussen de bron en de waarnemer te bepalen.

Waarnemingen van radiostraling dragen vitale informatie over dichtheid, snelheidsvelden en hun variaties. Met name emissie van de neutrale waterstoflijn (rond 1420 MHz) is eenvoudig met een radiotelescoop waar te nemen en staat ons toe om een kaart te maken van deze variaties in onze melkweg. Daarnaast is het mogelijk om deze waarnemingen te verrichten op sterrenstelsels buiten onze Melkweg en op die manier de verdeling van atomair waterstof in het sterrenstelsel te bepalen en hieruit de rotatiesnelheid van dat sterrenstelsel als functie van afstand tot het centrum te bepalen.

Wanneer de waterstofemissie gebeurt in de aanwezigheid van een sterk magnetisch veld, dan zal de emissielijn zich splitsen in twee verschillende lijnen, het zogenoemde Zeeman effect. De afstand tussen beide emissielijnen is gecorreleerd met de sterkte van het aanwezige magnetisch veld. Op deze manier kan via radiowaarnemingen het magnetisch veld in de melkweg bepaald worden. Daarnaast wordt deze techniek ook gebruikt om te meten hoe sterk het magnetisch veld in sterren, moleculaire wolken en masers is.

Dit proefschrift

Systematische radiowaarnemingen van magneto-hydrodynamische turbulente in het interstellair medium zijn een uitdaging en vereisen toegang tot bijzonder hoog-presterende radiotelescopen. De nieuwste apertuur-synthese radiotelescopen, zoals bijvoorbeeld LOFAR (Van Haarlem et al. 2013) maken het mogelijk om waarnemingen van magneto-

hydrodynamische turbulentie met tot nog toe ongeziene resolutie te verrichten. Naast het wetenschappelijk gedeelte van dit promotieproject, heb ik ook gewerkt als een commissaris aan LOFAR tijdens de opleveringsfase, wat betreft het testen van de software en het verrichten van data-analyse.

Dit proefschrift bestaat uit 4 waarnemingsprojecten in verband met MHD turbulentie in warm geïoniseerd interstellair medium. Deze studies hebben betrekking op twee complementaire wetenschappelijke theses. De eerste betreft het in kaart brengen van de magneto-ionische structuren in het interstellair medium (Hoofdstuk 2) en het karakteriseren van MHD turbulentie in het diffuse, warme geïoniseerde interstellaire medium (Hoofdstukken 3, 4 en 5). Het onderzoek beschreven in Hoofdstuk 3 is gebaseerd op de resultaten van de opleveringsfase van LOFAR.

In hoofdstuk 2 wordt ingegaan op het locale warme geïoniseerde interstellaire medium in de richting van de rand van de Melkweg. De waarnemingen zijn verricht in de richting van het Fan gebied, een gebied dat bijzonder helder is in synchrotronstraling. De radiostraling uit dit gebied vertoont op verschillende plaatsen een interessante variatie aan plekken met bijzonder weinig Faraday depolarisatie. Deze waarnemingen zijn in overeenstemming met eerdere radiowaarnemingen van synchrotronstraling uit de diffuse interstellaire medium. Een zwakke voorgrondbel wordt geassocieerd met dit systeem en wordt geïnterpreteerd als een overblijfsel van een Strömgren-bol. Turbulentie in zowel de bel als in de achtergrondcomponent wordt afgeleid van het ruimtelijke spectrum van de gepolariseerde emissie.

In hoofdstuk 3 wordt onderzoek gedaan naar de karakteristieken van een interstellaire magneto-hydrodynamische waterval in de richting van het Fan gebied. Dit gebeurt door de ruimtelijke fluctuaties in synchrotronstraling te onderzoeken. Hierbij zijn de scherpste en diepste beelden van het Fan gebied tot nog toe gemaakt en gebruikt. In deze gegevens wordt diffuse continuum emissie gevonden in de primaire telescoopbundel. Deze waarnemingen zijn voor LOFAR de eerste beelden van galactische fluctuaties in de diffuse synchrotronemissie in de buurt van 160 MHz. Hiervan wordt afgeleid dat de bovengrens van de interstellaire MHD turbulente waterval op ~ 20 pc ligt. Deze komt overeen met eerdere schattingen in de literatuur. De ondergrens voor de verhouding tussen willekeurige en geordende magnetische veldsterkte is consistent met andere plaatsen in het interstellair medium. Hieruit leiden we een waarde af als functie van galactische coördinaten.

In hoofdstuk 4 wordt ingegaan op de ruimtelijke variatie van het Mach getal (M_s) van de interstellaire MHD turbulentie. Hiervoor is de eerste kaart van variaties in lineair gepolariseerde synchrotron emissie in het zuidelijke halfrond gemaakt. Op deze kaart zijn sterke fluctuaties in de dichtheid van magnetische fluctuaties als gevolg van magnetische turbulentie in de warme geïoniseerde fase van het interstellair medium te zien. Deze vertonen een typische uitgerekte structuur met de korte as gelijk aan de resolutie van de telescoop en worden geassocieerd met turbulentie in het warme, geïoniseerde interstellair medium. Om een goede schatting voor het Mach getal te verkrijgen werd er een hogere

orde momentenanalyse toegepast op de waarnemingen en op het gesimuleerde isotherme interstellair medium met MHD turbulentie. Hieruit werd afgeleid dat de bovengrens voor het Mach getal gelijk is aan $\lesssim 2$, wat overeen komt met de visie dat het turbulente interstellaire medium onder het transsonic regime valt. Hierbij zijn systematische verschillen in Mach getal als functie van plaats in de Melkweg waargenomen. Een belangrijk aspect van dit onderzoek is dat de benadering van dit probleem vooral gevoelig is voor fluctuaties van het magnetisch veld in een plasma met laag Mach getal.

Uiteindelijk wordt in hoofdstuk 5 de dichtheid van thermische electronen en (in mindere mate) van het magnetisch veld over de hele hemel afgeleid. De turbulentie in het gemagnetiseerde interstellaire medium in de Melkweg wordt gemeten aan de hand van rotatiesnelheden van vele bronnen buiten de melkweg in verschillende richtingen. Uit deze waarnemingen wordt een kaart gemaakt van de rotaties van deze bronnen over de volledige hemel alsook een kaart met amplitudes en hellingen van structuurfuncties. In beide datasets (NVSS en S-PASS) werd een systematische afplating gevonden naarmate er verder van het vlak van de Melkweg waargenomen wordt. In sommige waarnemingen was de structuur van de variaties consistent met 2-dimensionale turbulentie terwijl geen enkele overeen kwam met 3-dimensionale turbulentie.

Bibliografie

- Adams W.S. 1941, PASP, 53, 209
Alfvén H. 1939, Phys. Rev. Lett., 55, 425
Barnard E.E. 1919, ApJ, 49, 1
Davis Jr. L. & Greenstein J.L. 1951, ApJ, 114, 206
Fermi E. 1949, Phys. Rev. Lett., 75, 1169
Hall J.S. 1949, Science 109, 166
Hartmann J. 1904, ApJ, 19, 26
Hiltner W.A. 1949a, ApJ, 190, 471
Hiltner W.A. 1949b, Science 109, 165
Kiepenheuer K.O. 1950, Phys. Rev. A, 79, 738
Plaskett J.S., Pearce J.A. 1930, MNRAS, 90, 243
Reber G. 1944, ApJ, 100, 279
Trumpler R.J. 1930, PASP, 42, 214
van Haarlem M.P., Wise M.W., Gunst A.W., Heald G., McKean J.P., Hessels J.W.T., de Bruyn A.G.,
Nijboer R., Swinbank J., Fallows R. et al. 2013, A&A, 556, 2
van de Hulst H.C. 1946, Recherches Astronomiques de l'Observatoire d'Utrecht, 11, 2

Sommario in Italiano

Introduzione

La presenza di campi magnetici nell' universo è osservata su di un esteso intervallo di scale spaziali. Campi magnetici esistono nei pianeti, nelle stelle e nelle nebulose come pure nelle galassie e nei gruppi di galassie. In linea di massima, maggiore è la dimensione del sistema fisico in questione e minore è l' ampiezza del campo magnetico associato. Nonostante l' ampiezza dei campi magnetici nei sistemi astrofisici, la loro presenza gioca un ruolo importante ed è alla base di molti fenomeni osservati come ad esempio le aurore nelle atmosfere dei pianeti ed i brillamenti (eruzioni) stellari. In effetti proprio questi fenomeni regolati dai campi magnetici furono i primi ad essere studiati a partire dal secolo scorso, e solo successivamente i campi magnetici distribuiti su scale maggiori nell' universo furono osservati. Questa tesi tratta l' interazione tra i campi magnetici interstellari e la fase ionizzata e turbolenta del mezzo interstellare (l' ISM) galattico e lo scopo di questo sommario è di illustrare l' origine dell' attuale idea dell' ISM galattico ed i concetti fondamentali per la comprensione del lavoro svolto.

Excursus storico della visione dell' ISM

“Ora è un fatto ben noto che lo spazio tra le stelle non è vuoto ma contiene materia gassosa come pure minuscole particelle solide.” (van de Hulst 1946)

Questa affermazione suggerisce quanto recente sia il concetto dell' ISM e riporta alla visione che gli astronomi avevano della struttura della nostra galassia, la Via Lattea, e più in generale dell' universo. Fino al XIX secolo il mainstream di molti astronomi è stato quello di considerare la nostra galassia come fosse l' intero universo, cioè formato da un enorme numero di stelle poste nel vuoto. Tale visione era messa in difficoltà dalla scoperta fatta dagli astronomi della famiglia Herschel circa la presenza sistematica di oggetti estesi nel cielo (le nebulose), ma tale scoperta non veniva riconosciuta come prova sperimentale dell' esistenza di materia diffusa tra le stelle.

Tuttavia all' inizio del XX secolo gli studi spettroscopici della luce stellare (gli spettri stellari) fornirono la prova osservativa dell' esistenza di un mezzo diffuso distribuito nello spazio tra le stelle: Hartmann (1904) rivelò la presenza di “righe stazionarie” dell' elemento Calcio ionizzato (Ca II) negli spettri stellari ed in seguito Plaskett & Pearce (1930)

mostrarono la correlazione tra le intensità di tali “righe stazionarie” e la distanza delle stelle, da cui si evinceva la presenza di un ISM pervasivo e non circoscritto in prossimità delle stelle. Gli studi concernenti l’estinzione (assorbimento) (Barnard 1919) e l’arrossamento (Trumpler 1930) della luce stellare fornirono altre prove fondamentali per la presenza di un ISM diffuso. Sino ad allora l’ISM era considerato diffuso ed omogeneo, ma questa concezione era destinata a cambiare velocemente negli anni 30 a seguito di studi spettroscopici ad alta risoluzione di stelle luminose che rivelarono moti complessi dei gas tra le stelle. In particolare, l’esistenza di un ISM diffuso e capace di assorbire la luce delle stelle ebbe conseguenze per uno dei problemi più importanti in astronomia, ovvero la determinazione delle distanze delle stelle mediante la misura della loro luminosità. A sua volta la difficoltà nel determinare le distanze delle stelle rendeva problematico lo studio della struttura della Via Lattea.

Nel 1913 conducendo degli esperimenti durante ascensioni in mongolfiera Victor Hess scoprì l’esistenza di una radiazione ionizzante e nel 1927 J. Clay dimostrò che l’origine di tale radiazione era dovuta a particelle cariche di elevata energia, in tal modo scoprendo un altro ingrediente principale dell’ISM: i raggi cosmici. In seguito, Alfvén (1939) prima e Fermi (1949) poi invocarono la presenza di campi magnetici nello spazio interstellare per spiegare il confinamento e l’accelerazione nella galassia di tali particelle. Queste previsioni teoriche trovarono riscontro nelle osservazioni dell’emissione radio della Via Lattea condotte da Reber (1944) e della luce stellare polarizzata condotte da Hall (1949) e Hiltner (1949a,b). L’emissione radio fu attribuita da Kiepenheuer (1950) alla presenza nei raggi cosmici di elettroni relativistici in moto nei campi magnetici interstellari, in grado di emettere onde radio mediante radiazione di sincrotrone. La polarizzazione della luce stellare venne spiegata da Davis & Greenstein (1951) come dovuta alla presenza di grani di polvere allungati ed allineati rispetto la direzione del campo magnetico interstellare.

Dunque alla fine degli anni 40 gli astronomi consideravano l’ISM costituito da un mix di gas parzialmente ionizzati nella fase atomica e molecolare (si veda ad es. Adams 1941), microscopiche particelle solide (chiamate polveri) (si veda ad es. Hall 1949) e particelle relativistiche (i raggi cosmici), tutto immerso in campi magnetici interstellari: la moderna visione dell’ISM stava formandosi. Infine, negli anni 60 una nuova componente venne individuata: un gas molto caldo e per lo più ionizzato capace di emettere raggi-X.

L’ecosistema Galattico e la MHD turbulenta

Nonostante la conoscenza di molte caratteristiche dell’ISM un modello globale non è ancora stato sviluppato, la causa principale essendo che le tessere di questo affascinante enigma si intrecciano tra loro. L’ISM è un sistema fisico complesso, dinamico a multi-fase. La natura multi-fase della fase gassosa dell’ISM è solitamente descritta mediante pochi ma essenziali parametri: la temperatura, la densità e lo stato di ionizzazione. Sia le fasi neutre e ionizzate sono presenti nella descrizione dell’ISM, come mostrato nella Tabella 6.3.

Oggi giorno è ampiamente riconosciuto che il mezzo interstellare ha un ruolo centrale nell’evoluzione delle galassie, per via del ciclo evolutivo della materia ed energia dell’

Tabella 6.2 – Fasi gassose dell’ ISM diffuso e valori tipici dei principali parametri: temperatura e densità del gas e livello di ionizzazione.

Phase	T [K]	n_H [cm ⁻³]	ξ
Caldo gas coronale	$\gtrsim 10^{5.5}$	0.004	~ 1
Tiepido gas ionizzato	~ 8000	0.1	~ 0.9
Tiepido gas neutro	~ 8000	0.5	~ 0.2
Freddo gas neutro	~ 100	50	$\lesssim 10^{-3}$

ISM. I costituenti e le caratteristiche fondamentali dell’ ISM sono collegate al ciclo vitale di una galassia e delle sue stelle. Infatti l’interazione tra le stelle e l’ISM influenza i processi fisici e chimici, guidando in tal modo l’evoluzione della Galassia. Uno dei principali aspetti riguardante la dinamica dell’ ISM è il suo stato turbolento, che è anche regolato dal ciclo di materia ed energia. Inoltre, l’ISM si può descrivere come un fluido elettricamente conduttore, che quindi costituisce un enorme e turbolento plasma cosmico.

A causa dei moti caotici nel plasma ISM esiste una profonda interazione tra l’ ISM ed i campi magnetici galattici. Infatti il plasma dell’ ISM è altamente conduttore e le linee del campo magnetico sono congelate nei movimenti turbolenti del fluido, originando una configurazione spaziale del campo magnetico complessa come pure delle fluttuazioni dell’ ampiezza di tale campo su una vasta gamma di scale spaziali. I moti turbolenti in presenza di campi magnetici favoriscono il trasporto di massa, momento, ed energia. La descrizione di tali moti turbolenti in presenza di campi magnetici è affidata ad un insieme di equazioni che definiscono una teoria ancora incompleta chiamata magnetoidrodinamica (MHD) turbolenta. Il ruolo fondamentale della MHD turbolenta nelle diverse fasi dell’ ISM riguarda sia la formazione delle strutture, che l’evoluzione e la magnetizzazione. Infatti la turbolenza è necessaria per generare le strutture su una vasta gamma di scale spaziali e di originare meccanismi di dinamo al fine di convertire una frazione di energia cinetica in energia magnetica. Perciò ci si occupa di MHD turbolenta nei plasmi astrofisici, indagando su fenomeni complessi e non lineari. Come conseguenza, la firma caratteristica della MHD turbolenta è la presenza di flussi altamente irregolari, frattali e magnetizzati.

La fenomenologia è qualitativamente rappresentata mediante il concetto di una cascata turbolenta (si veda la Fig. 6.4), dove l’ energia viene iniettata attorno una generica grande scala (L_{out}) e quindi viene trasferita senza dissipazione da processi non-lineari a scale più piccole fino a raggiungere una piccola scala tipica (l_{diss}), dove ha luogo la dissipazione. Nell’ ISM la cascata turbolenta è alimentata da diverse sorgenti di energia (ad esempio esplosioni di supernovae, forti venti stellari) e l’ energia viene iniettata a diverse scale spaziali (probabilmente nel range 1–100 pc). Le esplosioni di supernova forniscono il maggior contributo energetico, mentre la scala di dissipazione (forse dell’ ordine di \sim

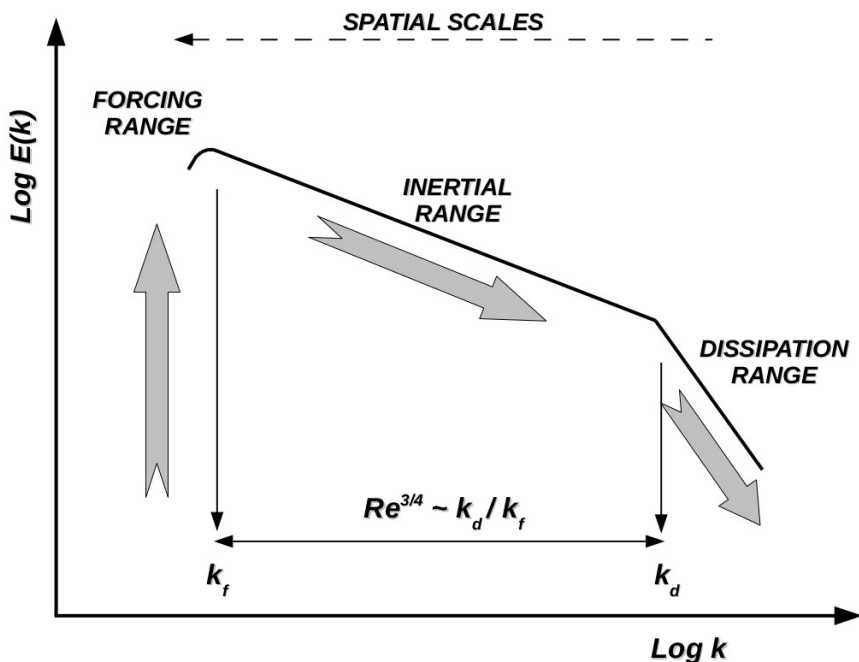


Figura 6.3 – Rappresentazione schematica dello spettro di energia spaziale di una cascata turbolenta. Le scale di immissione di energia ($k_f \sim 1/L_{out}$) e quella di dissipazione ($k_d \sim 1/l_{diss}$) sono indicate dai rispettivi numeri d'onda che definiscono l'estensione dell'intervallo inerziale lungo il quale avviene il trasferimento di energia. Il flusso di energia diretto dalle grandi verso le piccole scale è indicato dalle frecce.

500 Km) ed i meccanismi di dissipazione sono ancora incerti.

In sintesi, diversi importanti processi fisici, quali il riscaldamento e il raffreddamento radiativo, i campi magnetici, l'auto-gravità e la turbolenza sono presenti nell'ISM. Pertanto le indagini del loro ruolo e la loro interazione sono necessarie per capire l'evoluzione delle galassie. Alcune delle principali questioni scientifiche concernenti la turbolenza interstellare sono: il modo in cui i campi magnetici sono amplificati, sostenute e generati; il modo in cui l'energia viene trasferita senza dissipazione per processi non lineari a scale più piccole ed infine è dissipata, l'impatto sulla propagazione e il confinamento dei raggi cosmici, il modo in cui l'ISM è strutturato. La risposta a queste questioni è necessaria per sviluppare un modello globale realistico dell'ISM.

La radioastronomia e la turbolenza interstellare

La caratteristica distintiva della turbolenza interstellare è costituita dalla presenza di fluttuazioni spaziali e temporali di grandezze fisiche quali la densità e la velocità delle particelle e l'intensità del campo magnetico. Misurazioni in-situ possono essere fatte solo nel sistema solare ed in generale le osservazioni della turbolenza interstellare sono difficili.

Le osservazioni radioastronomiche sono un importante strumento per investigare sia la turbolenza interstellare che i campi magnetici. Infatti utilizzando osservazioni radio è possibile misurare nelle fasi ionizzate e/o neutre dell'ISM le fluttuazioni di concentrazione e velocità delle particelle come pure dell'intensità del campo magnetico. I traccianti di queste fluttuazioni sono i meccanismi che regolano l'emissione e la propagazione di onde elettromagnetiche in un plasma magnetizzato.

Gli elettroni relativistici dei raggi cosmici che si muovono nei campi magnetici galattici emettono una radiazione detta luce di sincrotrone e la quantità di tale luce emessa dipende dalla forza del campo magnetico sperimentato dalle particelle. Fluttuazioni della forza del campo magnetico appaiono come fluttuazioni di intensità della radiazione ricevuta dal radiotelescopio. Le energie tipiche degli elettroni dei raggi cosmici e la forza del campo magnetico galattico danno origine ad una emissione luminosa continua nelle basse radio frequenze < 1 GHz.

Inoltre la propagazione della luce di sincrotrone in un plasma magnetizzato come l'ISM è soggetta a due effetti importanti: la dispersione e la rotazione di Faraday. L'impatto di questi effetti sulla radiazione propagantisi nell'ISM dipende dalla densità degli elettroni liberi (non relativistica) e la grandezza del componente del campo magnetico lungo la linea di vista. Quindi fluttuazioni della densità delle particelle e forza del campo magnetico lungo la linea di vista possono essere studiate.

Infine, le righe spettrali di emissione radio costituiscono dei traccianti importanti della concentrazione di particelle, delle loro velocità e delle fluttuazioni di tali quantità. Infatti, la riga di emissione radio dell'idrogeno neutro permette di tracciare fluttuazioni sia della concentrazione di particelle che delle loro velocità. A causa di piccole variazioni di energia degli atomi di idrogeno interstellare, fotoni con frequenza intorno a 1420 MHz sono emessi e poi rilevati a terra con i radiotelescopi. Inoltre lo studio di tale riga di emissione consente agli astronomi di mappare la distribuzione dell'idrogeno atomico delle galassie e il loro tasso di rotazione in funzione della distanza dal centro della galassia.

Utilizzando osservazioni radioastronomiche è quindi possibile effettuare studi spettroscopici delle righe di emissione di specie atomiche ed anche eseguire misurazioni della separazione Zeeman dei livelli atomici. La presenza di un campo magnetico lungo la linea di vista determina infatti una suddivisione di una linea ad una certa frequenza in due componenti, la separazione essendo proporzionale alla forza del campo magnetico. Grazie a tale fenomeno metodo è possibile effettuare una misura diretta della grandezza del campo magnetico lungo la linea di vista nella sorgente ed è attualmente utilizzato per indagare campi magnetici nelle stelle (ad esempio il Sole), nubi molecolari e regioni con emissione maser.

Questa tesi

Le osservazioni radioastronomiche di turbolenza interstellare sono impegnative e per raggiungere la necessaria accuratezza richiedono strumenti con elevate prestazioni. La nuova generazione di radio-telescopi come LOFAR (Van Haarlem et al. 2013) consentono studi della turbolenza interstellare con una precisione senza precedenti. Nel quadro dell'attività scientifica di questo progetto di dottorato, ho anche lavorato come commissario di LOFAR eseguendo riduzione dei dati e test del software durante la fase finale di setup dello strumento. In questa tesi, presento quattro studi osservazionali sulla turbolenza MHD nel tiepido ed ionizzato ISM riguardo due casi scientifici complementari: la mappatura delle strutture magneto-ioniche nell'ISM (capitolo 2) e la caratterizzazione della turbolenza MHD nella fase tiepida e ionizzata dell'ISM (capitoli 3, 4 e 5). Si noti che lo studio descritto nel capitolo 3 è basato sui risultati della mia attività di commissario.

Nel Capitolo 2 presentiamo uno studio del vicino mezzo interstellare ionizzato, in direzione dell'anti-centro della Via Lattea. Il campo di indagine è una peculiare regione galattica caratterizzata da una brillante radiazione di sincrotrone (chiamata la regione "Fan"). In questa regione abbiamo rilevato diffusa, emissione di sincrotrone a bassa frequenza da diverse strutture Faraday sottili (cioè con trascurabile depolarizzazione Faraday interna) con diverse morfologie, in accordo con gli studi di RM-synthesis effettuati in precedenza della diffusa radio emissione Galattica di sincrotrone. Associamo una componente di primo piano debole con la Bolla Locale e studiamo la natura di una ulteriore struttura a forma di bolla, favorendo lo scenario di una antica regione ionizzata da venti stellari. Lo stato turbolento sia della bolla che della componente di fondo è suggerito dallo spettro di potenza spaziale dell'emissione polarizzata.

Nel Capitolo 3 caratterizziamo la turbolenza interstellare in direzione della regione "Fan", attraverso lo studio delle fluttuazioni spaziali della radiazione di sincrotrone. Presentiamo l'immagine più profonda di tale regione e troviamo una emissione radio continua e diffusa all'interno del fascio primario, che costituisce il primo rilevamento LOFAR delle fluttuazioni dell'emissione galattica diffusa di sincrotrone a circa 160 MHz. Un limite massimo di ~ 20 pc per la scala di iniezione di energia nella cascata MHD turbolenta del mezzo interstellare è derivata, in accordo con le stime precedenti presenti in letteratura. Presentiamo anche dei limiti inferiori del rapporto tra le componenti random ed ordinata dell'intensità del campo magnetico, trovando valori compatibili con quelli stimati in altre direzioni dell'ISM. I valori presentati non escludono la possibilità di una variazione spaziale del rapporto tra le componenti random ed ordinata dell'intensità del campo magnetico in funzione di coordinate galattiche.

Il Capitolo 4 discute le variazioni spaziali del numero di Mach sonico (M_s) della turbolenza MHD interstellare. Presentiamo la prima mappa dell'intero cielo meridionale del gradiente spaziale della emissione di sincrotrone linearmente polarizzata, rivelando rapidi cambiamenti della densità di elettroni liberi e fluttuazioni magnetiche nella fase tiepida e ionizzata dell'ISM. Tali fluttuazioni sono osservate in funzione della posizione

Galattica e sono dovute alla turbolenza MHD. Le strutture allungate con larghezze tipiche dell'ordine della risoluzione angolare sono associate con turbolenza nell'ISM ionizzato. Al fine di vincolare il numero di Mach sonico applichiamo un'analisi statistica dei momenti superiori per l'emissione radio polarizzata osservata e quella isoterma simulata in condizioni di turbolenza magneto-idrodinamica ideale. Un limite massimo di $\lesssim 2$ per il numero di Mach sonico viene trovato, supportando il modello di un ISM turbolento in regime transonico. Inoltre nessuna variazione sistematica del numero di Mach sonico è osservata in funzione delle coordinate galattiche. Una delle caratteristiche principali di questa indagine riguarda il metodo adottato, che è soprattutto sensibile alle fluttuazioni del campo magnetico in un plasma con bassi valori del parametro M_s .

Infine, nel Capitolo 5 viene presentato uno studio esteso a tutto il cielo delle fluttuazioni della densità di elettroni termici e (in misura minore) del campo magnetico. Studiamo la turbolenza nel mezzo interstellare galattico magnetizzato misurando le fluttuazioni tra le misure di rotazione (RMs) di sorgenti extragalattiche lungo diverse linee di vista e presentiamo una mappa dell'intera volta celeste delle misure di rotazione di sorgenti extragalattiche. Inoltre mostriamo mappe per le ampiezze e pendenze della funzione di struttura delle RMs del precedente catalogo NVSS e di quello nuovo S-PASS, trovando un sistematico appiattimento lontano dal piano galattico. In alcuni campi di vista, le pendenze delle funzioni di struttura sono coerenti con turbolenza bi-dimensionale, mentre nessuno di loro corrisponde alla turbolenza tri-dimensionale.

Bibliografia

- Adams W.S. 1941, *PASP*, 53, 209
Alfvén H. 1939, *Phys. Rev. Lett.*, 55, 425
Barnard E.E. 1919, *ApJ*, 49, 1
Davis Jr. L. & Greenstein J.L. 1951, *ApJ*, 114, 206
Fermi E. 1949, *Phys. Rev. Lett.*, 75, 1169
Hall J.S. 1949, *Science* 109, 166
Hartmann J. 1904, *ApJ*, 19, 26
Hiltner W.A. 1949a, *ApJ*, 190, 471
Hiltner W.A. 1949b, *Science* 109, 165
Kiepenheuer K.O. 1950, *Phys. Rev. A*, 79, 738
Plaskett J.S., Pearce J.A. 1930, *MNRAS*, 90, 243
Reber G. 1944, *ApJ*, 100, 279
Trumpler R.J. 1930, *PASP*, 42, 214
van Haarlem M.P., Wise M.W., Gunst A.W., Heald G., McKean J.P., Hessels J.W.T., de Bruyn A.G.,
Nijboer R., Swinbank J., Fallows R. et al. 2013, *A&A*, 556, 2
van de Hulst H.C. 1946, *Recherches Astronomiques de l'Observatoire d'Utrecht*, 11, 2

English Summary

Introduction

Cosmic magnetism is a phenomenon observed across a huge range of spatial scales. Magnetic fields exist on planets, stars and nebulae up to galaxies and clusters of galaxies. As a rule of thumb, the larger the typical size of the object, the lower the magnitude of its magnetic field. Regardless of their magnitude, magnetic fields play a relevant role in all of these environments and contribute to a wide spectrum of phenomena such as e.g. planetary auroras and stellar flares. Indeed these cosmic magnetic field driven phenomena were the first to be studied in the last century. Then the investigation of the large scale magnetic fields in the universe began. This thesis deals with the interplay between interstellar magnetic fields and turbulent warm phase of the Galactic interstellar medium (ISM). The genesis of the current view of the ISM along with fundamental concepts relevant for an understanding of this thesis, form the scope of the following sections.

Historical overview of the ISM

“It is now a well established fact that the space between the stars is not empty but contains gaseous matter as well as tiny solid particles.” (van de Hulst 1946)

The above statement recalls how recent the concept of the ISM is and relates to the way astronomers viewed how our galaxy (and the Universe) was structured. Up to the 19th century the mainstream thinking of many astronomers was to consider our Galaxy to be the entire universe, formed by a huge number of stars in a vacuum. The systematic presence of extended objects in the sky (called nebulae) was discovered by the Herschels, but it had not been recognized as observational evidence for the existence of a diffuse interstellar medium.

However, at the beginning of the 20th century spectroscopic studies of starlight provided the first observational evidence for the existence of a diffuse medium filling the space between stars: Hartmann (1904) revealed the presence of “stationary Ca II lines” and later Plaskett & Pearce (1930) showed the correlation between the strengths of “stationary lines” and distance, thereby indicating a pervasive interstellar medium. Two other pieces of evidence for the presence of a diffuse ISM were provided by studies of extinction (Barnard 1919) and reddening (Trumpler 1930). At that time the ISM was still considered

homogeneous and diffuse but this view quickly changed in the late 1930s following high-resolution spectroscopic observations towards bright stars, which revealed complex gas kinematics. Notably, the existence of a general, diffuse and absorbing ISM impacted one of the foremost problems in astronomy, i.e. to determine distances to stars from measure of brightness and thus for galactic structure studies.

In 1913 Victor Hess discovered ionizing radiation from the sky in balloon flights and in 1927 J. Clay proved that this radiation was due to high energy charged particles, which led to the discovery of another main ingredient of the ISM: the cosmic rays. Subsequently, the presence of a magnetic field in the interstellar space was invoked by Alfvén (1939) and Fermi (1949) in order to explain the cosmic ray confinement and acceleration. These theoretical ideas were observationally supported by the discoveries of polarized starlight by Hall (1949) and Hiltner (1949a,b) and the Galactic radio continuum emission by Reber (1944). The former was explained by Davis & Greenstein (1951) due to the presence of elongated dust grains aligned in the interstellar magnetic field, the latter was attributed by Kiepenheuer (1950) to relativistic cosmic-ray electrons gyrating in magnetic fields thus emitting radio waves by the synchrotron process.

Therefore, by the late 1940s, the ISM was known to consist of a mixture of atomic, ionized and molecular (see e.g. Adams 1941) gas as well as dust particles (see e.g. Hall 1949), along with cosmic rays and magnetic fields: the modern view of the ISM was emerging. Finally, a hot and ionized component was found in the 1960s with the discovery of a soft X-ray background.

The Galactic ecosystem and MHD turbulence

Notwithstanding the knowledge of many ISM features, a global model is still lacking with the main difficulty being that pieces of this fascinating puzzle are interwoven. The ISM is complex, dynamic and multi-phase. The multi-phase nature of the ISM is usually described by a few parameters: the temperature, the density and the ionization state. Both neutral and ionized phases are considered in the description of the ISM, as shown in Table 6.3.

Nowadays it is widely recognized that the interstellar medium plays a central role in the evolution of the Galaxy, because of the cycle of matter and energy. The basic components and properties of the ISM relate to the life cycle of a galaxy and its stars. Indeed the interplay between stars and the ISM affects both the physical and chemical processes, driving the evolution of the Galaxy. A major aspect concerning the dynamics of the ISM is its turbulent state, which is also regulated by the cycle of matter and energy. In addition, the ISM can be described as an electrically conducting fluid, constituting a huge, turbulent cosmic plasma.

Due to the chaotic motions in the ISM plasma, there exists a deep relationship between the ISM and Galactic magnetic fields. Indeed, the ISM plasma is highly conducting and the magnetic field lines are frozen into the turbulent fluid motions, giving rise to a complex field structure as well as strength fluctuations over a wide range of spatial scales. Turbulent motions in the presence of magnetic fields favour the transport of mass,

Table 6.3 – Phases of the diffuse ISM and its main parameters: temperature, gas density and degree of ionization.

Phase	T [K]	n_H [cm ⁻³]	ξ
Hot coronal gas	$\gtrsim 10^{5.5}$	0.004	~ 1
Warm ionized gas	~ 8000	0.1	~ 0.9
Warm neutral gas	~ 8000	0.5	~ 0.2
Cold neutral medium	~ 100	50	$\lesssim 10^{-3}$

momentum, energy and magnetic fields. The description of such turbulent motions in presence of magnetic fields is entrusted to a set of equations defining a still incomplete theory called magnetohydrodynamic (MHD) turbulence. The fundamental role of MHD turbulence in the different phases of the ISM concerns both structure formation, evolution and magnetization. Indeed turbulence is necessary to generate structure over a huge range of spatial scales and to set up dynamo mechanisms that to convert a fraction of kinetic to magnetic energy. When dealing with MHD turbulence in astrophysical plasmas, complex and non-linear phenomena naturally arise. As a consequence, the characteristic signature of MHD turbulence is the presence of highly-irregular, fractal and magnetized flows.

The phenomenology is qualitatively depicted by the concept of a turbulent cascade (see Fig. 6.4). The energy is injected at a large scale L_{out} and then transferred without dissipation by non-linear processes to smaller scales down to a typical scale (l_{diss}) where dissipation finally takes places. In the ISM, the MHD turbulent cascade is driven by several sources (e.g. supernova explosions, strong stellar winds). The energy is injected at different spatial scales (likely in the range 1–100 pc), with the supernova explosions providing the major contribution, while the dissipation scale (perhaps at scales ~ 500 km) and associated mechanisms are still debated.

In summary, several major physical processes, such as radiative heating and cooling along with magnetic fields, self-gravity, and turbulence play a role in the ISM. Therefore investigations of their role and interplay are required to understand Galaxy evolution. Major scientific questions concerning interstellar turbulence include: how are magnetic fields amplified, sustained and shaped; how is the energy transferred without dissipation by non-linear processes to smaller scales and then dissipated; how do magnetic fields impact on the propagation and confinement of cosmic rays; how is the ISM structured. Solving these matters is mandatory for developing a realistic global picture of the ISM.

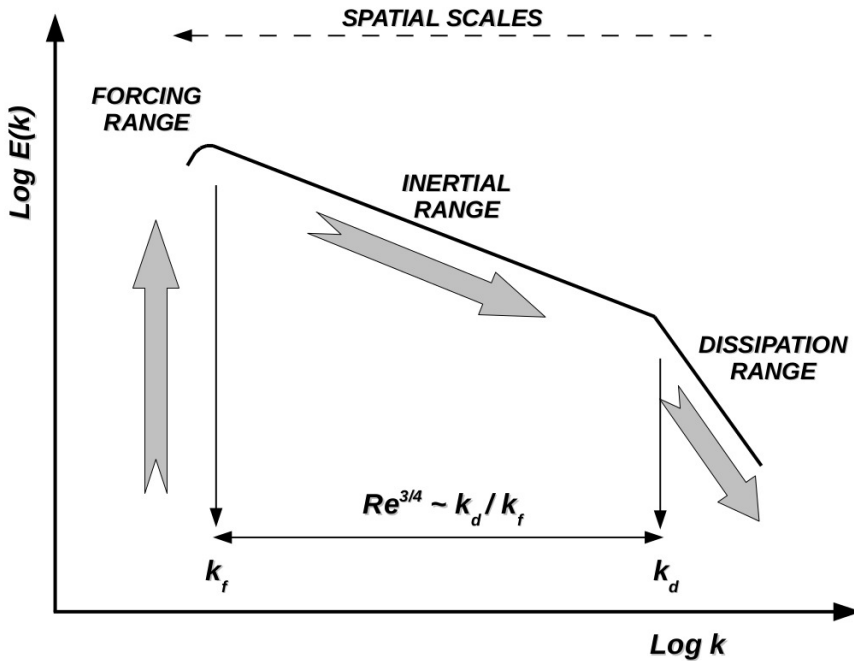


Figure 6.4 – Schematic representation of the spatial energy spectrum of a turbulent cascade. The forcing ($k_f \sim 1/L_{out}$) and dissipation ($k_d \sim 1/l_{diss}$) wave-numbers defining the extension of the inertial range are also marked. The direction of energy flow, from large to small scales, is indicated by the arrows.

Radio observations and interstellar MHD turbulence

The signature of interstellar turbulence is the presence of spatial and temporal fluctuations of physical quantities such as particle density and velocity, the magnetic field strength. In-situ measurements can only be done in the Solar system and observations of interstellar turbulence are challenging.

Radio observations are a major probe of the interstellar turbulence as well as of magnetic fields. By using radio observations it is possible to detect fluctuations in both density, velocity and magnetic fields in either the neutral and/or ionized ISM phases. The tracers of these fluctuations are the mechanisms which regulate the emission and propagation of electromagnetic waves in a magnetized plasma.

Relativistic cosmic rays electron moving in Galactic magnetic fields emit a kind of light called synchrotron-light and the amount of light emitted depends on the magnetic field strength experienced by the particles. Fluctuations of the magnetic field strength will appear as fluctuations of the intensity received by the radio-telescope. The typical

energies of the cosmic rays electrons and strength of the Galactic magnetic fields give rise to a bright continuum emission in the low frequency < 1 GHz radio regime.

Furthermore, the propagation of synchrotron-light in the magnetized and ionized ISM is subject to two important effects, namely dispersion and Faraday rotation. The impact of these effects on the propagating light depends on the density of the free (non relativistic) electrons and the magnitude of the magnetic field component along the line of sight. Fluctuations of particle density and magnetic field strength along the line of sight can thus be traced.

Finally, radio line emission is a tracer of density, velocity fields and their fluctuations. Indeed, the radio line emission of neutral hydrogen allows to trace fluctuations of both density and velocity fields. Small energy variations of interstellar hydrogen atoms, produce photons with frequencies around 1420 MHz which are detected with radio-telescopes. This allows astronomers to map the distribution of atomic hydrogen in galaxies as well as the galaxies rotation rate as a function of distance from the galaxy center.

By using radio observations it is thus possible to detect line emission from atomic species and also perform measurements of Zeeman splitting of atomic levels. The presence of a magnetic field along the line of sight causes a line at a certain frequency to split into two components, the separation being proportional to the magnetic field strength. This method allows for a direct measure of the magnitude of the magnetic field along the line of sight in the source and it is currently used to investigate magnetic fields in stars (e.g. the Sun), molecular clouds and maser spots.

This thesis

Observational investigations in the radio domain of MHD turbulence in the ISM are challenging and require high performance facilities. New generation aperture array radio telescopes such as LOFAR (Van Haarlem et al. 2013) allow observational studies of the interstellar turbulence with unprecedented accuracy. In the framework of the scientific activity of this Ph.D. project, I also worked as a commissioner of LOFAR, performing data reduction and software testing. In this thesis, I present four observational studies on the MHD turbulence in the warm ionized ISM regarding two complementary science cases: mapping of the magneto-ionic structures in the ISM (Chapter 2) and characterizing the MHD turbulence of the diffuse warm ionized ISM (Chapters 3, 4 and 5). Note that the study described in Chapter 3 is based on the results of my commissioning activity.

In Chapter 2 we present a study of the local, warm ionized ISM towards the Galactic anti-center. The target field is a peculiar synchrotron bright Galactic region (called the Fan region) and we detect diffuse, low-frequency synchrotron emission from several Faraday thin (i.e. with negligible internal Faraday depolarization) structures with different morphologies, in agreement with earlier RM synthesis studies of the Galactic diffuse synchrotron emission. We associate a faint foreground component with the Local Bubble and investigate the nature of a bubble structure, favouring the scenario of a Strömgren

sphere relic. The turbulent state of both the bubble and the background component is suggested by the spatial power spectrum of the polarized emission.

In Chapter 3 we characterize the interstellar MHD turbulent cascade towards the highly polarized Fan region, by studying the spatial fluctuations in synchrotron emission. We obtain the deepest image of the Fan region to date and find diffuse continuum emission within the primary beam, which constitutes the first LOFAR detection and imaging of the Galactic fluctuations of diffuse synchrotron emission around 160 MHz. An upper limit of ~ 20 pc for the outer scale of the interstellar MHD turbulent cascade is derived, which matches with previous estimates in literature. Lower limits of the ratio of random to ordered magnetic field strength consistent with magnetic field ratios at other places in the ISM are also found and we claim a variation of the ratio of random to ordered field as a function of Galactic coordinates.

Chapter 4 discusses the spatial variations of the sonic Mach number (M_s) of the interstellar MHD turbulence. The first map of the spatial gradient of the linearly polarized synchrotron emission of the entire southern sky is shown, revealing rapid changes of the density and magnetic fluctuations in the warm and ionized phase of the ISM due to magnetic turbulence as a function of Galactic position. The elongated structures with typical widths down to the angular resolution are associated with turbulence in the warm, ionized ISM. In order to constrain the sonic Mach number we apply a high order moments analysis to the observations and to the simulated diffuse, isothermal ISM with ideal magneto-hydrodynamic turbulence. An upper limit of $\lesssim 2$ for the sonic Mach number is found, supporting the view of a turbulent ISM in a transonic regime. Moreover no systematic variations of the sonic Mach number are observed as a function of Galactic coordinates. A major feature of this investigation is that the adopted approach is mainly sensitive to the magnetic field fluctuations in a plasma with low- M_s .

Finally, in Chapter 5 a study of the all-sky thermal electron density and (to a lesser extent) of the magnetic field fluctuations is presented. We study turbulence in the Galactic magnetized interstellar medium by measuring fluctuations between the rotation measures (RMs) of extragalactic sources along different lines of sight and we show an all-sky map of rotation measures of extragalactic sources as well as maps for both the structure function amplitudes and slopes. A systematic flattening is found in both the NVSS and S-PASS samples away from the Galactic plane. In some fields of view, the structure function slopes are consistent with 2D turbulence, while none of them correspond to 3D turbulence.

Bibliography

- Adams W.S. 1941, *PASP*, 53, 209
Alfvén H. 1939, *Phys. Rev. Lett.*, 55, 425
Barnard E.E. 1919, *ApJ*, 49, 1
Davis Jr. L. & Greenstein J.L. 1951, *ApJ*, 114, 206
Fermi E. 1949, *Phys. Rev. Lett.*, 75, 1169
Hall J.S. 1949, *Science* 109, 166
Hartmann J. 1904, *ApJ*, 19, 26
Hiltner W.A. 1949a, *ApJ*, 190, 471
Hiltner W.A. 1949b, *Science* 109, 165
Kiepenheuer K.O. 1950, *Phys. Rev. A*, 79, 738
Plaskett J.S., Pearce J.A. 1930, *MNRAS*, 90, 243
Reber G. 1944, *ApJ*, 100, 279
Trumpler R.J. 1930, *PASP*, 42, 214
van Haarlem M.P., Wise M.W., Gunst A.W., Heald G., McKean J.P., Hessels J.W.T., de Bruyn A.G.,
Nijboer R., Swinbank J., Fallows R. et al. 2013, *A&A*, 556, 2
van de Hulst H.C. 1946, *Recherches Astronomiques de l'Observatoire d'Utrecht*, 11, 2

Publications

Galactic interstellar turbulence in the southern sky seen through spatial gradients of the polarization vector. Interstellar turbulence in the southern sky

Iacobelli M., Burkhart B., Haverkorn M., Lazarian A., Carretti E., Staveley-Smith L., Gaensler B.M., Bernardi G., Kesteven M.J., Poppi S.
Submitted to Astronomy & Astrophysics (Chapter 4)

The brightness and spatial distributions of terrestrial radio sources

Offringa A.R., de Bruyn A.G., Zaroubi S., Koopmans L.V.E., Wijnholds S.J., Abdalla F.B., Brouw W.N., Ciardi B., Iliev I.T., Harker G.J.A. et al.
MNRAS (2013) 435, 584

Studying Galactic interstellar turbulence through fluctuations in synchrotron emission. First LOFAR Galactic foreground detection

Iacobelli M., Haverkorn M., Orrú E., Pizzo R.F., Anderson J., Beck R., Bell M.R., Bonafede A., Chyzy K., Dettmar R.-J. et al.
Astronomy & Astrophysics (2013) 558, 72 (Chapter 3)

LOFAR: The LOw-Frequency ARray

van Haarlem M.P., Wise M.W., Gunst A.W., Heald G., McKean J.P., Hessels J.W.T., de Bruyn A.G., Nijboer R., Swinbank J., Fallows R. et al.
Astronomy & Astrophysics (2013) 556, 2

The LOFAR view of cosmic magnetism

Beck R., Anderson J., Heald G., Horneffer A., **Iacobelli M.**, Köhler J., Mulcahy D., Pizzo R., Scaife A., Wucknitz O. et al.
Astron. Nachr. (2013) 334, 548

Calibrating high-precision Faraday rotation measurements for LOFAR and the next generation of low-frequency radio telescopes

Sotomayor-Beltran C., Sobey C., Hessels J.W.T., de Bruyn G., Noutsos A., Alexov A., Anderson J., Asgekar A., Avruch I.M., Beck R. et al.
Astronomy & Astrophysics (2013) 552, 58

LOFAR detections of low-frequency radio recombination lines towards Cassiopeia A

Asgekar A., Oonk J.B.R., Yatawatta S., van Weeren R.J., McKean J.P., White G., Jackson N., Anderson J., Avruch I.M., Batejat F. et al.
Astronomy & Astrophysics (2013) 551, 11

Initial deep LOFAR observations of epoch of reionization windows. I. The north celestial pole

Yatawatta S., de Bruyn A.G., Brentjens M.A., Labropoulos P., Pandey V.N., Kazemi S., Zaroubi S., Koopmans L.V.E., Offringa A.R., Jelić V., et al.
Astronomy & Astrophysics (2013) 550, 136

Synchronous X-ray and Radio Mode Switches: A Rapid Global Transformation of the Pulsar Magnetosphere

Hermesen W., Hessels J.W.T., Kuiper L., van Leeuwen J., Mitra D., de Plaa J., Rankin J.M., Stappers B.W., Wright G.A.E., Basu R. et al.
Science (2013) 339, 436

Rotation measure synthesis at the 2 m wavelength of the Fan region: unveiling screens and bubbles

Iacobelli M., Haverkorn M., Katgert P.
Astronomy & Astrophysics (2013) 549, 56 (Chapter 2)

Radio and X-ray properties of galactic supernova remnants G7.7-3.7 and G344.7-0.1

Giacani E., Loiseau N., Smith M.J.S., Dubner G., **Iacobelli M.**
AIP Conf. Ser. (2010) 1248, 39

Splitting Neutrino masses and Showering into Sky

Fargion D., D'Armiento D., Lanciano O., Oliva P., **Iacobelli M.**, de Sanctis Lucentini P.G., Grossi M., de Santis M.
Nucl.Phys. B (2007) 168, 292

Curriculum Vitae

I was born in the beautiful city of Rome, where I received my education. After I graduated in a school for science (high school education) I studied physics at “La Sapienza” university. Because of my interest in astrophysics and space science, I focused on this field of the activity. In order to improve and develop new skills I had several research experiences. In 2002–2003 I was involved in an Earth observation project proposed in the framework of the Success Student Contest (a competition for European university student from all disciplines to propose an experiment that can be conducted on-board the International Space Station (ISS)) under the supervision of Prof. Alessandro Cacciani. The aim of the experiment was the investigation of the atmospheric sodium layer at 90 km in the Mesosphere, with the collaboration of JPL Laboratory (Pasadena) for the construction of the image sensor and with a planned collaboration with the Earthshine project at the Big Bear Solar Observatory and Caltech in California. In 2004 I performed photometric asteroseismology on a Rapid Oscillating star, asteroseismology being the topic of my practical astrophysics course thesis. Then I decided to focus on cosmic rays physics. This was the topic of my master thesis and I performed a study on inclined air showers and in particular the Up going Tau air showers under the supervision of Dr. Daniele Fargion. After I graduated I applied at the ENEA (Italian National agency for new technologies, Energy and sustainable economic development) research institute to be involved in a laser physics project. The aim of this project was the development of a Thomson spectrograph in order to estimate the velocity distribution for different ions species in laser’s produced plasmas. Finally, in 2009 I spent a year of trainee at the European Space Astronomy Centre (ESAC) under the supervision of EASC scientists Matthias Ehle and Matteo Guainazzi. During my trainee I was a member of the XMM-Newton Science Operations Centre (SOC) and I gained a valuable experience with X-ray data reduction and increasing my interest in high-energy astrophysics.

Then I started my duty as a Ph.D. student at Leiden observatory under the supervision of Dr. Marijke Haverkorn. The purpose of my doctoral studies was twofold. I worked as a commissioner of the LOw Frequency ARray (LOFAR), a new generation aperture array radio telescope performing data reduction and software testing. Also, I investigated the interstellar turbulence in the warm ionized medium of the Galaxy regarding two complementary science cases: mapping of the magneto-ionic structures in the interstellar medium and characterizing the hydromagnetic turbulence of the diffuse interstellar medium. The approach to investigate the interplay of the Galactic magnetism with the diffuse and turbulent magneto-ionic medium of the Milky Way was observational. During my PhD I attended several international and national meetings where I presented my work.

Acknowledgements

These few lines are aimed to give thanks to all people who contribute to make this important life experience successful. Of course, I am grateful to my promotor Huub Röttgering and my supervisor Marijke Haverkorn. Then a special thank is for you, Peter: you guided me through a difficult period of my Ph.D experience and your life. I have no words to explain my respect for you.

I thank my collaborators Emanuela Orrú, Roberto Pizzo, Blakesley Burkhart, Gianni Bernardi and Dominic Schnitzeler for their precious support and patience. I am also in debt with expertise at ASTRON for their kind support and guidance. A special thank to the MKSP people for their support and enjoyable discussions and meetings. Thanks to my colleague Carl Shneider for the nice days we had. Travelling and attending conferences was a pleasure. The Netherlands for being a tolerant and welcoming country. People at Karalis for the delightful Italian atmosphere and the delicious food, isn't true Carl? I am also grateful to the great office mates and all colleagues which contribute the Sterrewatch to be such an amazing melting-pot both culturally as well as scientifically. Steven thanks for your prompt support to translate this thesis summary to Dutch. Thanks to the "computer group" as well as the support staff for their kind help.

Lights and shadows have characterized these years and allowed me to grow up but at a price for my dearest loved ones. I thank my father and my mother which supported me unconditionally over these years. My wife, Carmen, for your indescribable, pure love and your patience. I dedicate this work to you and I apologize for not having been with you all the time you needed. Last but not least, I thank all my friends spread in Italy and Europe: I hope to meet you again altogether.

“Life is a play that does not allow testing. So, sing, cry, dance, laugh and live intensely, before the curtain closes and the piece ends with no applause.”

– Charles Chaplin

